THE INFLUENCE OF THE MICROSTRUCTURAL SHAPE ON THE MECHANICAL BEHAVIOUR OF INTERPENETRATING PHASE COMPOSITES

A Thesis Submitted to the College of
Graduate Studies and Research
in Partial Fulfilment of the Requirements
for the Degree of Master of Science
in the Department of Civil and Geological Engineering
University of Saskatchewan
Saskatoon

By
Gregory Albert Del Frari

COPYRIGHT

ABSTRACT

The microstructure-property relationship for interpenetrating phase composites (IPCs) is currently poorly understood. In an attempt to improve this understanding this study focussed on one particular part of this relationship: the effect of phase shape on the elastic and plastic behaviour. A review of previous research showed that investigations had linked phase shape to the elastic and plastic behaviour of various inclusion reinforced composites, but that no similar work had been completed for IPCs.

To study the complex response of the IPC microstructure under load, a numerical modelling analysis using the finite element method (FEM) was undertaken. Two three-dimensional models of IPCs were created, the first consisting of an interconnected spherical phase with the interstitial space forming the other interconnected phase, and the second replacing the spherical phase with an interconnected cylindrical phase. With the simulation of a uniaxial tension test under elastic and plastic conditions, these two models exhibited different responses based on the shape of the phases.

Results from an analysis of the macroscopic behaviour identified that the cylindrical model produced greater effective properties than the spherical model at the same volume fraction. The influence of phase shape was connected to the increased contiguity of the superior phase within the IPC for the cylindrical model, which allowed similar levels of long-range continuity with smaller amounts of the superior phase (compared to the spherical model).

An examination of microstructural stress distributions showed that preferential stress transfer occurred along paths of low compliance. This provided an explanation of how the improved contiguity of the stiffer (or stronger) phase could enhance the macroscopic effective properties of an IPC. Contiguity of the stronger phase was particularly important for plastic behaviour, where early yielding of the weaker phase requires the stronger phase to carry nearly all the load within itself.

ACKNOWLEDGMENTS

I would like to begin by thanking Dr. Leon Wegner, my faculty supervisor on this project, for his suggestion of this topic, his guidance during research and his financial support. I take full responsibility for any mistakes within this thesis but certainly the level of accuracy which has been attained has been due to Dr. Wegner's diligence. I would also like to thank Dr. Mel Hosain, Dr. Wegner, Dr. Bruce Sparling, Dr. Pufahl, Ms. Maureen Limet, Ms. Joanne Skeates and Mr. Dale Pavier for their inspiration, encouragement and readiness to help during my work as a sessional lecturer. I consider this experience to be amongst the most valuable and rewarding of my graduate studies.

For support during times of frustration and stress I owe a debt of gratitude to numerous friends. Special thanks are offered to Lisa Yang, Kevin Heppner, Tanya De Rosairo, Kris Jackson, Mark Polachic, Anna Paturova and Stephen Wood. To Emma Boghossian and Amit Pashan, I can not possibly offer sufficient thanks. I do not think there has been a happy moment during my graduate studies that does not contain the two of you.

Finally, I would like to thank those whose support, encouragement and love has never been in doubt; my aunts, uncles, cousins, grandparents, brothers and especially Sandra and my parents. You are the foundation upon which any success I have obtained has been built and the reason I can face the future without fear.

This thesis is dedicated with love to my parents,

Bernard Reno Del Frari

and

Lynn Marie Del Frari.

TABLE OF CONTENTS

LIST OF TABLES

LIST OF FIGURES

LIST OF NOTATIONS

a	centre-to-centre distance between spheres
A	correction constant for volume fraction in Eq. 4.2
A_{top}	top surface area
b	length of all prism unit cell base edges
B	correction constant for contiguity in Eq. 4.2
C_{sp}	contiguity of the stiffer (or stronger) phase
C_{α}	contiguity of the α-phase
CI_{sp}	coupled influence of the stiffer (or stronger) phase
E	Young's modulus
E_c	Young's modulus of cylinder constituent phase
E_{mf}	Young's modulus of the more flexible phase
E_s	Young's modulus of sphere constituent phase
E_{sp}	Young's modulus of the stiffer phase
E_{sur}	Young's modulus of surrounding phase
F_a	reaction force due to applied displacement at master node
F_c	degree of continuity
F_s	degree of separation
G	shear modulus
G_1	lower shear modulus phase in Hashin-Shtrikman (H-S) bounds
G_2	higher shear modulus phase in H-S bounds
G_u	upper H-S bound on the shear modulus
G_l	lower H-S bound on the shear modulus
h	height of prism unit cell
K	bulk modulus
K_1	lower bulk modulus phase in H-S bounds
K_2	higher bulk modulus phase in H-S bounds
K_u	upper H-S bound on the bulk modulus
K_l	lower H-S bound on the bulk modulus
l_o	half the height of the prism unit cell (h/2)
M_{α}	matricity of the α-phase

n_{bc}	number of random points in the back cylinder
n_c	number of random points in the cylinders
n_{hp}	number of random points in the half prism unit cell
n_i	number of random points at the cylinder intersection
n_{tc}	number of random points in the top cylinder
n_{total}	total number of random points
r	radius of spheres
s_α	skeleton line length in α-phase
s_β	skeleton line length in β-phase
S_α	separation of the α-phase
$S_v^{\alpha\alpha}$	surface area between parts of the α-phase
$S_v^{\alpha\beta}$	surface area between the α-phase and β-phase
$u_{x(LeftBottom)}$	x-displacement of the left-bottom surface
$u_{x(LeftFront)}$	x-displacement of the left-front surface
$u_{x(RightBottom)}$	x-displacement of the right-bottom surface
$u_{x(RightFront)}$	x-displacement of the right-front surface
$u_{y(LeftBottom)}$	y-displacement of the left-bottom surface
$u_{y(LeftFront)}$	y-displacement of the left-front surface
$u_{y(RightBottom)}$	y-displacement of the right-bottom surface
$u_{y(RightFront)}$	y-displacement of the right-front surface
$u_{z(LeftBottom)}$	z-displacement of the left-bottom surface
$u_{z(RightBottom)}$	z-displacement of the right-bottom surface
$u_{z(Top)}$	z-displacement of the top surface
$u_{x(TLB)}$	x-displacement of the master node (top-left-back corner)
$u_{z(TLB)}$	z-displacement of the master node (top-left-back corner)
V_{box}	volume of the Monte Carlo simulation box
V_{hp}	volume of the half prism unit cell
V_α	volume of the α-phase
V_β	volume of the β-phase
δ_a	applied displacement at master node
ε_a	strain due to applied displacement at master node

ν_c	Poisson's ratio of cylinder constituent phase
ν_s	Poisson's ratio of sphere constituent phase
ν_{sur}	Poisson's ratio of surrounding phase
σ_a	stress due to applied displacement at master node
σ_{eff}	effective stress
$\sigma_{eff(norm)}$	normalised effective stress
$\sigma_{P1(mf)}$	first principal stress in a pure sample of the more flexible phase
$\sigma_{P1(sp)}$	first principal stress in a pure sample of the stiffer phase
σ_y	yield strength
ϕ	volume fraction
ϕ_1	volume fraction of lower property phase for H-S bounds
ϕ_2	volume fraction of higher property phase for H-S bounds
ϕ_c	volume fraction of cylindrical phase
ϕ_{hp}	volume fraction of half prism unit cell
ϕ_s	volume fraction of spherical phase
ϕ_{sp}	volume fraction of stiffer (or stronger) phase
ϕ_α	volume fraction of the α-phase
$\phi_{\alpha c}$	continuous volume fraction of the α-phase
$\phi_{\alpha s}$	separated volume fraction of the α-phase

CHAPTER ONE

INTRODUCTION

1.1 BACKGROUND

Interpenetrating phase composites (IPCs) are fundamentally different from other composite materials due to the geometry of their microstructures. Most common composites consist of a reinforcing constituent (or phase) that is isolated within a continuous matrix phase. The reinforcing phase generally has the material properties desired for the composite, but because of processing difficulties, other less desirable properties or cost, a pure sample of this phase cannot be used. The matrix phase is usually chosen based on its bonding ability and thermal compatibility with the reinforcing phase, as well as low cost. Its mechanical properties are often less desirable to those of the reinforcing phase (though this is becoming less often the case with the development of metal matrix and ceramic matrix composites). This can pose problems, since as the continuous phase the matrix often dominates the behaviour of the composite. Two large families of conventional composite materials exist: particle reinforced composites, such as concrete, and fibre reinforced composites, such as glass fibre reinforced polymer (GFRP). The main difference between these two families is the shape of the reinforcing phase. In particle reinforced composites, the reinforcing phase consists of more or less equi-dimensional particles; in concrete, the reinforcing phase is the aggregate. In fibre reinforced composites, the reinforcing phase has a high aspect ratio, such that one dimension of the phase is much greater than the others. In GFRP, the glass fibres, either in discontinuous short lengths or one-dimensionally continuous long lengths, form the reinforcing phase.

IPCs consist of two or more three-dimensionally interconnected phases, so there are not easily definable reinforcing and matrix phases based on states of isolation and continuity (see Fig. 1.1). This dual continuity of the phases removes the previous problem of matrix dominated behaviour. The stiffer or

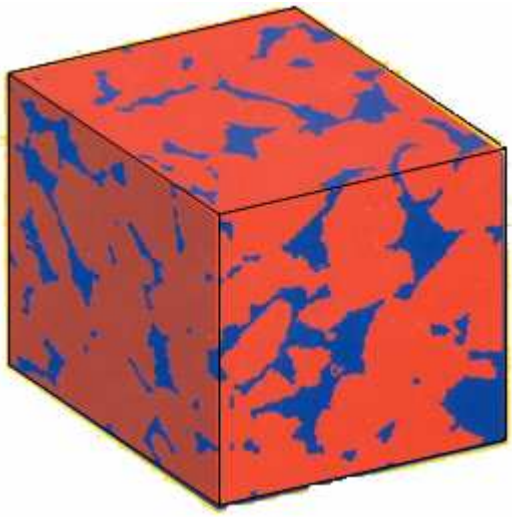

Figure 1.1: An interpenetrating phase composite (from Torquato, 2002)

stronger phase is now continuous, allowing it to more significantly influence the behaviour of the composite. The continuity of the other phase also allows it to have a significant influence. In this way, IPCs offer the possibility of truly composite behaviour, where two usually incompatible properties for pure materials can exist within a single composite. Each phase offers its own benefits due to its complete continuity.

A good example of a potential application of this work is in electronics packaging. Shen (1998) describes the possible use of an aluminium silicon-carbide (Al/SiC) IPC for attachment to delicate electronic circuitry. The thermal conductivity of the aluminium is needed to dissipate the heat generated during use of the electronics; however, the thermal expansion of pure aluminium would break the delicate circuit connections, destroying the device. In contrast, a SiC attachment would expand only a small amount, preventing breakages at the connections, but would not be able to prevent the build-up of intense heat within the device. The desired material should consist of a combination of these properties, making an IPC of Al/SiC an attractive solution.

1.2 OBJECTIVE AND SCOPE

Despite the potential benefits of using IPCs, there are few current applications for these materials. One of the major reasons for this is their

relatively unknown behaviour. The unique interpenetrating microstructure of IPCs is complex, making its performance difficult to predict. The following study focuses on a determination of:

1. The effect of microstructural phase shape on the linear elastic behaviour of IPCs. This was examined through changes to the effective Young's modulus of the overall composite and local stress distribution variations within the microstructure.
2. The effect of microstructural phase shape on the non-linear plastic behaviour of IPCs, in this case examined through changes to the effective yield strength of the composite and stress distribution variations within the microstructure.

The shapes chosen for investigation were those of interconnected spheres and interconnected cylinders, both surrounded by a second phase with more flexible and weaker properties. The former is comparable to the non-IPC particle reinforced composite and the latter is similar to the non-IPC fibre reinforced composite.

Numerous other variables, in addition to phase shape, affect the behaviour of IPCs. In order to focus on shape, it was necessary to control these other variables. To do this, a periodic arrangement of the phases was used in the study so that parameters of the microstructural geometry (shape, size distribution, spatial distribution and orientation of the phases) could be easily defined. However, this means that various randomly arranged IPCs are not well represented in this study. All sphere and cylinder pieces were uniform in size, so that size distribution had no affect. A single spatial distribution – a hexagonal close-packed (HCP) system – was also chosen so that its influence was controlled. The HCP system also provides an isotropic response that allows the direction dependence of results to be ignored. The orientation of the phases could not be completely removed as a variable, since it is dependent upon both the chosen shape and spatial distribution. This can be seen by considering first the sphere shape, which is equi-dimensional and therefore has no orientation

dependence, and then the cylinder shape, whose orientation is set by the HCP system (this is examined in more detail in Chapter 3; see Fig. 3.1 and 3.6). While other orientations of the cylinder shape are possible, no other orientation will allow the creation of an IPC with an HCP system. Orientation may therefore be viewed as controlled by the spatial distribution. The overall composition of the IPCs, or the amount of each phase in them, was varied over an applicable range of volume fractions in order to generalise the results.

Besides the parameters of the microstructural geometry, other variables had to be considered. The material properties of the constituent phases were assumed to be elasto-plastic, matching the basic behaviour of ductile materials. Various different values for the stiffness and strength of each phase were examined in order to generalise the applicability to a range of potential phases as much as possible. However, no case assuming a constituent to be purely elastic to failure was analysed and the results of this thesis should be applied to IPCs containing a brittle phase with caution. The interface between the phases also needed to be simplified due to the complexity of the interaction of IPCs under load. In the investigation described here, a perfect bond between the phases was assumed such that strain compatibility was required across the interface. This is generally the desirable interfacial condition from the processing of IPCs.

In addition to controlling the variables considered in this research, it should be reiterated that only the basic elastic and plastic behaviours were studied. The investigation focussed on the determination of simple effective properties for IPCs, such as the Young's modulus and the yield strength. The more severe plastic behaviour occurring near failure due to fracture or fatigue was not considered in this study. The effects of time-dependent behaviour from creep and relaxation were also not examined. Most important to the behaviours that were studied is that no thermal influences were considered. The creation of thermal residual stresses due to thermal expansion mismatch of the phases during processing can significantly influence IPC behaviour. This phenomenon

is discussed in the next chapter through the research of others, but was not studied as part of this thesis.

1.3 METHODOLOGY

In order to determine the influence of phase shape on IPC behaviour, two unit cell models, one containing a sphere and the other a cylinder, were created. Each unit cell was based on the HCP system and was limited by the scope just stated. The co-continuous, three-dimensional nature of these models is sufficiently complex to require the solution to be determined through numerical methods. For the purposes of this study, the computer software package ADINA (ADINA R&D, Inc. 2002a) was used to solve for the composite behaviour in response to a simulated uniaxial tension test. ADINA's solutions are found by application of the finite element method (FEM). The solutions to linear elastic behaviour focussed on changes to the IPC's effective Young's modulus, while those for non-linear plastic behaviour focussed on changes to the effective yield strength.

Modelling results provided data about the influence of several variables on composite behaviour. Different ratios of the constituent phase properties allowed general trends to be determined when various types of constituents are used. A range of volume fractions for the phases provided insight into the effect of phase composition on the mechanical behaviour of an IPC. The influence of phase shape became apparent when the volume fractions and phase property ratios in each of the two models were set to be the same. This influence was initially determined based on the macroscopic behaviour (either the effective Young's modulus or effective yield strength), but it was also confirmed through a study of the mechanisms acting at the microstructural level. Finally, a parameter to help describe the effect of phase shape was developed. The purpose of this parameter was to account for the effect of phase shape in an equation that describes IPC behaviour.

1.4 LAYOUT OF THESIS

The remainder of this thesis provides the details of the research just outlined. The second chapter is a literature review of previous research relevant to IPCs. Its first two sections describe various methods that have been used to study IPCs. Each method is briefly outlined and an analysis of its usefulness is provided. These sections are written as an introductory reference for planning research on IPCs. In the third section of the literature review, the results of previous research on the elastic and plastic behaviour of composites are discussed. This section gives a background on the current state of knowledge about IPC mechanical behaviour. It also provides a subsection on the influence of thermal residual stresses, which, although not considered in this study, can be a significant determinant of behaviour.

The third chapter describes the development of the models used in this research. The material in this chapter is intended to simply provide a better understanding of how the models work; however, if the software programs in the appendices are used, it should also allow the models to be recreated.

The fourth chapter discusses the results found by the models and how they were validated. Validation was a multiple step process to ensure sufficient accuracy of the results. After validation, the effect of phase shape on the elastic behaviour of IPCs is discussed through two separate methods. The first method draws initial results from the macroscopic behaviour. Confirmation of these results is then sought by examining the mechanisms at the microstructural level. A similar procedure is used to discuss the effect of shape on the plastic behaviour of IPCs.

Finally, in the fifth chapter, a brief summary of the research is given, which leads to conclusions regarding the effect of phase shape on the elastic and plastic behaviour of IPCs. Recommendations are also provided on the future direction of research in creating a mechanistic model for IPCs.

CHAPTER TWO

LITERATURE REVIEW

Research into the relationship between the microstructural geometry and the macroscopic behaviour of composite materials has been a topic of interest for nearly a century. However, the possibility of multiple phases being three-dimensionally continuous, as occurs within interpenetrating phase composites (IPCs), has been largely overlooked until the past decade; most researchers date the separate study of IPCs to a state-of-the-art paper by Clarke (1992). This situation is now rapidly changing as the growing importance of IPCs is leading researchers to develop methods to predict their performance. This chapter, therefore, describes the various approaches researchers are using to characterise the microstructures of IPCs, the methods that are being used to predict their behaviour and the factors which influence that behaviour. This objective has been broken into its three distinct parts, with Section 2.1 examining the methods of microstructural characterisation, Section 2.2 discussing the benefits and limitations of various prediction methods, and Section 2.3 describing some of the factors that influence the basic mechanical behaviour of IPCs. This separation of review material into these three sections should aid in the analysis of each part of the microstructure-behaviour relationship and emphasize the importance of considering each one in the proper development of IPC research.

2.1 CHARACTERISATION OF MICROSTRUCTURAL GEOMETRY

2.1.1 Experimental Characterisation Methods

The proper characterisation of an experimental specimen's microstructure is highly dependent on the technology and methods used to describe that microstructure. The most common means of observing the nature of composite microstructures is through two-dimensional sectioning of a sample followed by observation through some type of microscopy. Optical microscopy

is generally used for coarser microstructures, where the phases are fairly easy to distinguish with moderate magnification (e.g. Liu and Köster 1996, Agrawal et al. 2003, San Marchi et al. 2003). For finer microstructures or more detailed analyses, scanning electron microscopes (SEM) or transmission electron microscopes (TEM) are more useful (e.g. Daehn et al. 1995, Peng et al. 2000, Wegner and Gibson 2000b).

Unfortunately, these methods provide two-dimensional representations whose accuracy in representing the actual three-dimensional material is dependent upon the number and orientation of the chosen sections. Characterisation of a three-dimensional microstructure is particularly important for IPCs, where the co-continuous geometry of the microstructure is dependent upon visualisation in three dimensions. Fredrich et al. (1995) attempted to improve their characterisation of sandstone and granite where the pore space was filled with a fluorescent epoxy by creating numerous thin sections. When studied under a laser scanning confocal microscope, three-dimensional images of each small section were created. Adjacent sections were then combined to provide larger three-dimensional representations of the pore structures. Flannery et al. (1987) determined a potential method involving the use of x-ray microtomography. In their method, x-rays are passed from a source through a specimen and the incident and transmitted intensities of the rays are detected. This can be used to produce two-dimensional representations along the paths of the x-rays. With numerous such representations taken at different angles, it is possible to non-destructively build a three-dimensional image of an experimental sample's microstructure. Coker et al. (1996) used this method with synchrotron x-rays in order to study the microstructure of Fontainebleau sandstone.

After finding a means to study the microstructure, the experimental researcher still must determine how to describe it. Most descriptions are largely qualitative judgements by the researcher, with only small amounts of quantitative data being listed. The preference for this system of description is due mainly to the complexity of depicting the microstructure in a numerical form;

however, it makes the characterisation highly subjective and dependent upon researcher experience. As examples, Liu and Köster (1996) studied alumina/aluminium IPCs with both optical microscope and TEM images, making note of the continuous appearance of the phases, the existence of silicon impurities, the progress of the reaction front and the volume fraction. Stainless steel/bronze composites considered in a project by Wegner and Gibson (2000b) were described using microstructural observations of volume fraction, the existence of voids along phase interfaces and tin rich regions within the bronze. In a study on the fracture behaviour of alumina/aluminium IPCs, Pezzotti and Sbaizero (2001) used SEM inspection to determine the absence of voids. Agrawal et al. (2003) used SEM and optical micrographs to determine the existence of co-continuous systems, phase volume fractions and the average phase grain size in alumina/copper and alumina/aluminium composites. With the exception of some information regarding phase volume fractions, all these microstructures are completely qualitatively characterised.

The preference for qualitative descriptions, while useful, poses a definite problem for other researchers who are attempting to make comparisons with their own research or who require detailed data for the creation of numerical models. Even when sufficient experimental results exist to contrast the accuracy of other test predictions, an insufficient amount of microstructural information may exist to draw a strong connection between the geometry of the microstructure and the overall behaviour. This is particularly troublesome for modelling studies, since the potential usefulness of a model's predictions become highly questionable when there are numerous limitations in accurately describing the microstructure. This problem is exacerbated in IPC research since the microstructures of these composites are more complex and a greater number of assumptions must be made. In order to improve modelling predictions on the behaviour of IPCs, experimental research must provide more detailed and more quantitative depictions of realistic microstructures to allow validation.

As early as 1984, Camus et al. (1984) were discussing the quantification of interpenetrating microstructures through topological or fractal analysis. Although at the time of their writing the analysis of numerous sections by the researcher made laboratory work extremely tedious, computer imaging software can now sometimes perform these operations. As an example, Coker et al. (1996) used an edge-based segmentation algorithm on synchrotron x-ray microtomographic data to separate the material and pore phases of Fontainebleau sandstone. With this data they characterised the microstructure through a number of statistical correlation functions as defined by Torquato (1991). Peng et al. (2000, 2001), in addition to a qualitative analysis, noted the average cell and window diameters of their foamed alumina preform's microstructure. This allows some determination of the interconnection of the two phases.

2.1.2 Characterisation through Topological Parameters

An ideal means of quantifying a composite's microstructure would be through the use of topological parameters. These are dimensionless variables that describe geometric properties and are independent of the size of the microstructure that is considered. The volume fraction of the phases is a common example:

$$\phi_\alpha = \frac{V_\alpha}{V_\alpha + V_\beta}, \tag{2.1}$$

where ϕ_α is the volume fraction of the α-phase, and V_α and V_β are the volumes of the α and β-phases, respectively. Note that while the volumes of each of the phases are dependent upon the size of the sample, the volume fraction is not.

Unfortunately, no other standard topological parameters are in wide spread use and a variety of them can be found in the literature. Contiguity was defined by Gurland (1958) as the fraction of surface area shared by a grain of one phase with all other grains of the same phase. In equation form, this is

$$C_\alpha = \frac{2S_v^{\alpha\alpha}}{2S_v^{\alpha\alpha} + S_v^{\alpha\beta}}, \tag{2.2}$$

where C_α is the contiguity of the α-phase, $S_v^{\alpha\alpha}$ is the surface area between α-phase grains per unit volume and $S_v^{\alpha\beta}$ is the surface area between α and β grains. Lee and Gurland (1978) used the parameter “continuous volume fraction” in a study on sintered tungsten carbide/cobalt alloys. They defined continuous volume fraction as the volume fraction of one phase which is contiguous with itself. In mathematical form this is

$$\phi_{\alpha c} = C_\alpha \phi_\alpha, \tag{2.3}$$

where $\phi_{\alpha c}$ is the continuous volume fraction of α-phase.

Fan and Miodownik (1993a) defined complements to the previous two parameters. The separation (S_α) was defined as the fraction of surface area shared by a grain of one phase with all other grains of another phase, i.e.

$$S_\alpha = \frac{S_v^{\alpha\beta}}{2S_v^{\alpha\alpha} + S_v^{\alpha\beta}}. \tag{2.4}$$

In addition, the separated volume fraction ($\phi_{\alpha s}$) was defined as the volume fraction of one phase that is not contiguous with itself, calculated by

$$\phi_{\alpha s} = S_\alpha \phi_\alpha. \tag{2.5}$$

Fan and Miodownik further defined the degree of continuity and its complement, the degree of separation. The degree of continuity, F_c, is related to the entire continuous volume fraction for the composite (for both phases), while the degree of separation, F_s, is related to the entire separated volume fraction. For a two-phase composite these are, respectively,

$$F_c = \phi_{\alpha c} + \phi_{\beta c} \tag{2.6}$$

and

$$F_s = \phi_{\alpha s} + \phi_{\beta s}. \tag{2.7}$$

One final topological parameter that arises in the study of IPCs is matricity. Matricity was defined by Leβle et al. (1998) as the length of skeleton lines from one phase divided by the length of skeleton lines for both phases, as taken from numerous section images of the composite microstructure (see example image in Fig. 2.1):

$$M_\alpha = \frac{s_\alpha}{s_\alpha + s_\beta} \tag{2.8}$$

where M_α is the matricity of the α-phase, and s_α and s_β are the skeleton line lengths of the α and β-phases, respectively.

The physical significance of these parameters is important to understanding their utility. Contiguity is a measure of short-range continuity, since it is concerned with grain neighbours. A high contiguity necessarily means that there is a great deal of short-range continuity of that phase. This does not, however, mean that long-range continuity exists, since clusters of a single phase would have high contiguity. A well dispersed, highly contiguous phase would, however, have a greater probability of having long-range continuity than a phase without these two properties. This was explored by Aldrich and Fan (2001) for an alumina/nickel composite.

Along similar lines of argument, the continuous volume fraction is the

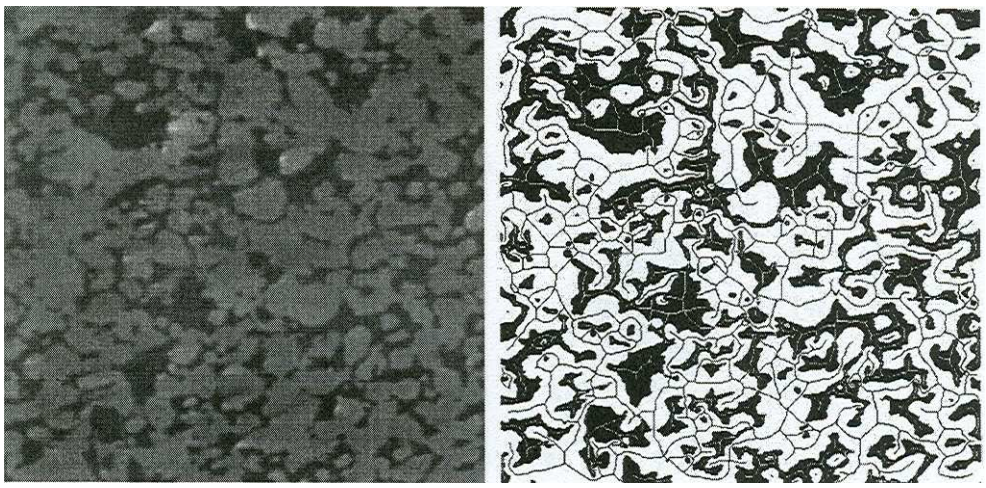

Figure 2.1. Micrograph of an IPC at left with skeleton lines used to determine matricity at right (from Leβle et al. 1999)

volume fraction of a phase that shows short-range continuity since it is dependent upon contiguity. The degree of continuity also denotes only short-range continuity, although in this case it includes all phases. Matricity is also a measure of short-range continuity, but in this case it is based on the size, orientation and number of two-dimensional sections that are used to determine a microstructure's matricity. By increasing the size, total number and number of orientations considered in representing the microstructure, a greater probability is created that the determined matricity denotes the long-range character.

It is also interesting to note that the statistical correlation functions defined by Torquato (1991) have the same physical meaning as these topological parameters, and their ability to represent long-range rather than simply short-range continuity is also dependent on the care taken in a section analysis. Those parameters based on separation simply imply the inverse of those based on contiguity: short-range discontinuity.

2.2 PREDICTION OF MACROSCOPIC MECHANICAL BEHAVIOUR

2.2.1 Bounds on the Mechanical Properties of General Composites

Important early analytical studies attempted to place bounds on the effective properties of any general composite material. These bounds are still valuable to current research as they provide some conception about the optimality of the composite, and a general solution against which more specific models can be tested. The general nature of the desired bounds meant that the original researchers attempted to make as few assumptions about the microstructure as possible. The most useful bounds for the work in this thesis are those by Hashin and Shtrikman (1963) for isotropic composites.

The derivation of these bounds begins with the assumptions of macroscopic isotropy and elastic behaviour. Macroscopic isotropy requires that the component phases be significantly smaller than the composite sample considered. When calculating the upper bound, Hashin and Shtrikman (1963) used variational calculus together with the theorem of minimum potential

energy, and the lower bound was found using the theorem of minimum complementary energy. Only the volume fractions of the phases were used as microstructural parameters, so the bounds are applicable to the elastic properties of any isotropic composite regardless of its microstructure. The upper Hashin-Shtrikman bounds were found to be

$$K_u = K_2 + \frac{\phi_1}{\left(\frac{1}{K_1 - K_2}\right) + \left(\frac{3\phi_2}{3K_2 + 4G_2}\right)} \tag{2.9}$$

and

$$G_u = G_2 + \frac{\phi_1}{\left(\frac{1}{G_1 - G_2}\right) + \frac{6(K_2 + 2G_2)\phi_2}{5G_2(3K_2 + 4G_2)}}, \tag{2.10}$$

where K, G and ϕ denote bulk modulus, shear modulus and volume fraction, respectively. The subscript “u” marks the upper bound, “1” the first phase parameters and “2” the second phase parameters. It is necessary when using these bounds that K_2 is greater than K_1 and G_2 greater than G_1. Similarly, the lower bounds are;

$$K_l = K_1 + \frac{\phi_2}{\left(\frac{1}{K_2 - K_1}\right) + \left(\frac{3\phi_1}{3K_1 + 4G_1}\right)} \tag{2.11}$$

and

$$G_l = G_1 + \frac{\phi_2}{\left(\frac{1}{G_2 - G_1}\right) + \frac{6(K_1 + 2G_1)\phi_1}{5G_1(3K_1 + 4G_1)}} \tag{2.12}$$

where K_l and G_l are the lower bounds for the effective bulk and shear moduli, respectively, and all other variables are as described above. In the same paper, Hashin and Shtrikman (1963) proved that these were the most restrictive bounds that could be found for any general isotropic composite without

incorporating information about the microstructural geometry in addition to the volume fraction.

There is an implicit statement of phase geometry in the exact solution of the Hashin-Shtrikman bounds (though this does not affect the generality of the previous solutions). Hashin (1962) created a model assuming a microstructure of composite spheres, in which a sphere of one phase is coated by a concentric sphere of the other phase. These concentric spheres in a wide range of sizes are then packed so that no void space exists between them (this requires sizes from a relatively large maximum to an infinitesimally small minimum, see Fig. 2.2). If the more flexible phase coats the stiffer phase, the result is the lower bound derived above, and if the stiffer phase coats the more flexible phase, the upper bound is achieved. The reason for this difference involves the connectivity of the stiffer phase. When placed as the coating, the stiffer phase is completely connected such that it is able to take the majority of the stress and reduce the deflections due to deformations of the more flexible phase. However, when placed in the centre, the stiffer phase is not connected and the composite behaviour is mainly dependent on the flexible phase.

2.2.2 Analogy Models

Similarities exist between numerous different physical properties and it is not uncommon for researchers to study physical phenomena that are relatively easy to model in order to better understand more complex phenomena. Such a

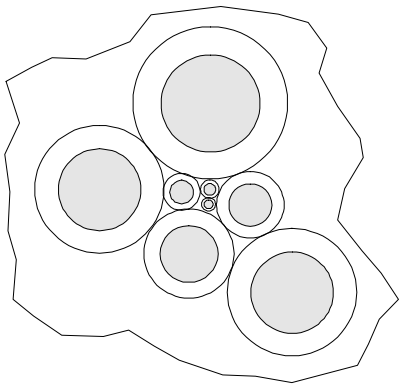

Figure 2.2. Composite spheres model

correlation exists between the failure of electrical networks consisting of a random arrangement of resistors and the failure of composite materials. Moukarzel and Duxbury (1994) used this parallelism to study the mechanical behaviour of IPCs using the numerical model of an electrical network composed of two different types of resistors (each resistor type representing a different phase). In this analogy, the electrical conductivity of the resistors is similar to the mechanical stiffness of the phases, and the maximum electrical current at which a resistor fails is similar to the fracture strength.

Their model used a process known as the multiple hottest bond algorithm in order to simulate the behaviour. In this system, a voltage is applied (a strain for mechanical comparison) and the current in each resistor is determined. Any resistor over its breakdown current (fracture strength) is removed from the system and the current in each resistor is again calculated. This process is repeated until no further resistors fail. The voltage is then increased slightly and the previous calculations are repeated incrementally until complete failure is achieved.

A cubic lattice of resistors was modelled with two different volume fractions of the two resistor types (the different phases). In the first case, the volume fractions of the resistors were equal (50% each) so that an interpenetrating network was created, and in the second case the volume fraction of the stronger (inclusion) resistor was only 15% so that a discontinuous two-phase network was created. For both cases, the current-voltage (stress-strain) behaviour was recorded for each step in the process, as well as the number of resistors that failed prior to complete failure (damage tolerance or ductility) and peak overall current (composite ultimate strength). Although the IPC models did not produce the highest peak overall current (ultimate strength) they showed a significantly larger number of failed resistors (enhanced ductility).

2.2.3 Self-Consistent Models

Composites containing random microstructures and exhibiting isotropic behaviour are well suited for self-consistent models. These models consist of a circular cell, which includes both of the actual phases of the composite, embedded within a general homogeneous medium (see Fig. 2.3). The properties of the constituent phases are applied to their respective parts of the embedded cell, while initially assumed properties must be given to the homogeneous embedding medium. With boundary conditions applied sufficiently distant from the embedded cell, an iterative procedure may be used to solve for the composite's effective behaviour. Iteration is required since the general homogeneous embedding medium's properties must be determined through improvements with each solution step. Some confusion has arisen about the use of this model since several researchers have used only one phase in the embedded circular cell and given the other phase properties to the embedding medium. Christensen (1979) noted that this is an improper use of the underlying mathematics of the self-consistent method and readers are cautioned to carefully analyse the models used in this method.

Leβle et al. (1998, 1999) expanded the use of self-consistent models into the analysis of IPCs. Their method was based on the self-consistent models originally developed by Dong and Schmauder (1996) and the use of the topological parameter matricity (see Section 2.1.2). Dong and Schmauder's models were two-dimensional with applied plane stress, plane strain or axisymmetric boundary conditions and were solved using the FEM. The volume fractions of the phases could be varied by changing the radii of each phase

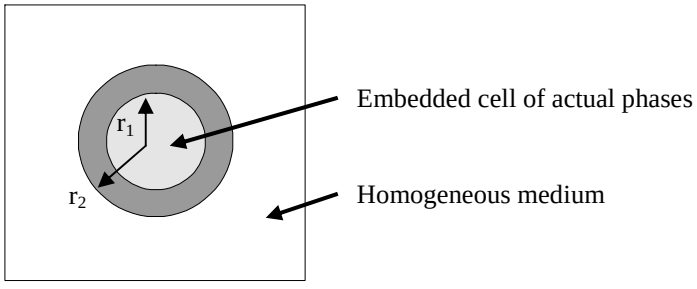

Figure 2.3. Self-consistent model

within the embedded cell (see Fig. 2.3). Matricity was incorporated through the use of two self-consistent models where the skeleton line length of the α-phase was equal to the circumference of the outer phase in the first model, and the skeleton line length of the β-phase equal to the circumference of the outer phase in the second model (in one model the α-phase was at the centre and was surrounded by the β-phase, in the other model these positions were switched). The matricity was given a weighting factor that was based on the diameter of the embedded cell within each model. Effective composite results were then determined by solving both models and weighting the determined stress and strain values at each integration point by the diameter of the embedded cell.

Hoffman et al. (1999) used self-consistent modelling to determine the effective bulk modulus of an alumina/aluminium IPC. Although not described in detail, the only geometric parameters they appear to have used are the volume fractions of the phases. The effective bulk modulus, along with properties of the constituent phases, was then used in several analytical equations to calculate the yield and creep behaviour. This information was used in the determination of mechanisms for thermal residual strains and stresses created in IPCs during processing.

2.2.4 Unit Cell Models

In direct contrast to self-consistent models, unit cell models are better able to describe composite materials with ordered periodic microstructures rather than random microstructures. They are also useful in depicting internal stress and strain distributions that occur within the microstructures of loaded composites. These capabilities are possible through the representation of large, often complicated microstructures with single building blocks (unit cells) of those structures. Proper boundary conditions on the cell surfaces replicate the existence of the surrounding material using the geometry within the cell. The surrounding material therefore takes on an ordered arrangement based on the

template geometry from the unit cell. For IPCs, three-dimensional unit cells are required since their geometry is defined by its three-dimensional dual continuity.

A common unit cell for modelling IPCs is the anisotropic simple cubic microstructure (see Fig. 2.4). This model was used by Ravichandran (1994) to study the stress-strain behaviour of IPCs with two ductile phases. The cell was separated into a combination of parallel and series components which were then solved using Newton's bisection method (Moore, 1979). Phase constraint was introduced by assuming that pieces of the more compliant phase were rigidly sandwiched between layers of the less compliant phase. Daehn et al. (1995) used the simple cubic unit cell to model the stress-strain behaviour of an interpenetrating network of brittle alumina and ductile aluminium. As is common in similar studies of metal-ceramic composites, the brittle ceramic was modelled as elastic and the ductile metal as elasto-plastic. Since they desired isotropic material behaviour, they used Reuss (isostress) and Voigt (isostrain) averaging to provide an aggregate response from the anisotropic results obtained using the FEM. Shen (1998) used this unit cell in his study of the coefficient of thermal expansion (CTE) for a brittle silicon-carbide and ductile aluminium IPC. A similar model with discrete and continuous phases considered the CTE for metal-matrix and ceramic-matrix composites in which various levels of continuity were considered. Shen noted that the simple shape and distribution assumed for the IPC (i.e. the simple cubic unit cell) was justified by previous work that showed the effective CTE to be insignificantly affected by these geometric parameters (Shen et al. 1994a). He also noted, however, that this was not the case for effective elastic and plastic properties, where shape and distribution had a marked affect on composite performance (Shen et al. 1994b, 1995). Analytical solutions were found using the simple cubic unit cell for the piezoelectric and elastic properties studied by Bowen et al. (2001) and Feng et al. (2003), respectively. Feng's model largely improved the work of Ravichandran (1994) by extending its applicability to multiple continuous and discrete phases.

The anisotropy of the simple cubic unit cell differs from the usual isotropic properties found in the experimental testing of IPCs. This led Wegner and Gibson (2000a) to develop the isotropic hexagonal close-packed (HCP) microstructure seen in the unit cell of Figure 2.5. The HCP unit cell was used to model two ductile phases with a simulated uniaxial tension test and solved using the FEM. Results were found for elastic and plastic behaviour, and in Wegner and Gibson (2000b), comparisons to experimental data were used to determine the effect from thermal residual stresses. A uniform heating regime was also used to determine the effective CTE. In addition to the IPC model, a discrete particle reinforced model for non-IPCs was used to consider the effect of an interpenetrating geometry. Wegner and Gibson (2000a) noted that a perfect bond was assumed between the two phases; this assumption is also likely true of all the discussed unit cell models.

2.3 FACTORS INFLUENCING MACROSCOPIC MECHANICAL BEHAVIOUR

2.3.1 Factors Influencing Thermal Residual Stresses

Thermal residual stresses are commonly caused during the processing of composite materials. Although they are rarely of direct interest to IPC research, they can have a profound effect upon composite behaviour and are therefore of indirect interest to numerous studies on effective properties. There are two basic mechanisms for their creation; the first is related to the difference

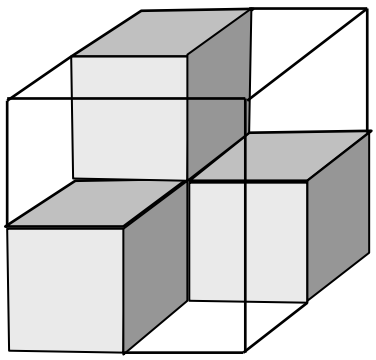

Figure 2.4. Simple cubic unit cell

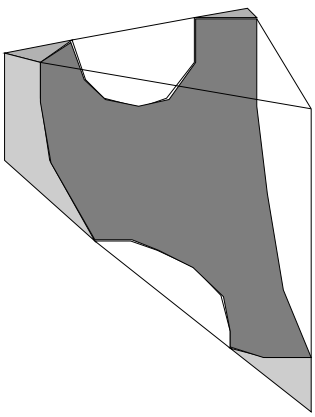

Figure 2.5. HCP unit cell

between the coefficients of thermal expansion (CTEs) of the constituent phases, and the second to the dissimilar cooling rates in different locations within the material. The latter mechanism regarding location was to some extent alleviated in the following studies so that only the former mechanism is considered further. During cooling from the manufacturing temperature, both phases of a composite will contract. The phase with the higher CTE (more compliant) will want to contract to a greater extent than the phase with the lower CTE (less compliant). This difference causes the less compliant phase to constrain the more compliant phase, such that compressive stresses and tensile stresses are created in the less and more compliant phases, respectively. These stresses are referred to as thermal residual stresses and their existence in a newly manufactured composite produces an initially loaded state.

Many of the same factors which influence composite effective behaviour also influence thermal residual stresses. As mentioned above, the mechanism of interest is related to the difference between the CTEs of the constituent phases. However, the CTEs are not the only variables that affect the creation of thermal residual stresses. Other material properties and the geometry of the microstructure also have a significant influence. Skirl at al. (1998) recorded overall strains in an alumina/aluminium (Al_2O_3/Al) IPC at various different volume fractions of the ceramic and metal phases. They noted that the total thermal residual strain in the IPCs increased in direct proportion to an increase in the volume fraction of the metal phase. A more detailed study carried out by Agrawal et al. (2003) used neutron diffraction measurements to determine the stresses in each of the phases for both an alumina/copper (Al_2O_3/Cu) IPC and an Al_2O_3/Al IPC. They found that the tensile stresses developed in the Cu phase of the Al_2O_3/Cu IPC were much higher than those developed in the Al phase of the Al_2O_3/Al IPC (620 MPa compared to 112 MPa), despite the fact that the ratio between the CTEs for Cu and Al_2O_3 was smaller than the ratio of the CTEs between Al and Al_2O_3 (2.54 Cu to Al_2O_3 and 3.65 Al to Al_2O_3). Although this appears inconsistent from the mechanism described previously, it

can be understood when it is noted that for the Al_2O_3/Cu IPC the volume fraction of Cu was 30%, whereas in the Al_2O_3/Al IPC the volume fraction of Al was 70%. The much smaller amount of Cu in the first IPC was therefore of much smaller dimensions and more greatly constrained than the Al of the second IPC. A more minor link was also noted between the different stiffnesses and melting temperatures for the two metals.

In the study of IPCs, the dual continuity of the phases requires a further examination of microstructural parameters besides simply the volume fraction. Shen (1998) noted that the thermal residual stresses in his simple cubic unit cell model of a silicon carbide/aluminium composite were greatly affected by the level of continuity for each phase. Hoffman et al. (1999) attempted to explain the thermal residual stresses found by Skirl et al. (1998) through two mechanisms. The first mechanism was dominant at low temperatures (near the end of cooling) where permanent strain was induced through yielding of the metal phase due to constraint from the ceramic phase. At higher temperatures and lower stresses (near the metal's melting point) the second mechanism involving time-dependent behaviour was dominant. In this mechanism, diffusion creep leading to the relaxation of the metal was accounted for during the creation of thermal residual stresses. A reasonable correlation was found between this study and the experimental work of Skirl et al. (1998) if a combination of the mechanisms was used. The majority of permanent deformation in the aluminium was attributed to time-dependent behaviour at elevated temperatures with only a minor effect due to yielding near room temperature.

Agrawal et al. (2003) modelled their thermal residual stresses through the use of a simple cubic unit cell and the concept of an effective processing temperature. This allowed them to avoid the necessarily complex equations used by Hoffman et al. (1999). Unfortunately, neither of these studies isolates the effect that dual continuity has on the creation of thermal residual stresses but only produces models able to predict their distribution.

2.3.2 Factors Influencing Elastic Behaviour

The behaviour of IPCs in their elastic range of response is a key concern in understanding their performance under usual service conditions. Unless the IPC is intended for single use, it is generally desirable that the loads it is likely to encounter on a regular basis are in its elastic range such that when the load is removed all the deformation is removed. Determining this behaviour is, however, complex due to the multiple continuity of the phases in IPCs. While purely elastic behaviour would require all phases to be elastic (if one phase were acting plastically then the removal of load would still not allow the material to return to its initial form), a more complex situation is possible with IPCs where a continuous phase of significantly greater strength could hold almost all the load and create a pseudo-elastic condition. Several ceramic/metal and ceramic/polymer IPCs have the potential to meet this condition.

The effect of constituent phase properties and volume fractions on effective elastic properties was determined for any general isotropic composite by Hashin and Shtrikman (1963). They were able to analytically solve for upper and lower bounds on the effective bulk and shear moduli of two-phase composites using variational principles and elastic theory (see Section 2.2.1). This also applies to IPCs so long as they consist of two phases and behave in an isotropic manner. A plot of the bounds for the effective Young's modulus against the volume fraction of the less compliant phase is shown in Figure 2.6. To make this plot, the bounds from Equations 2.9 to 2.12 were used with the following relationship, which relates them to the Young's modulus:

$$E = \frac{9KG}{3K + G}, \tag{2.13}$$

where E, K and G denote the Young's modulus, bulk modulus and shear modulus, respectively. Whether the solution is for the upper or lower bound of the Young's modulus is directly dependent upon whether the upper or lower bounds for the bulk and shear moduli are input into Equation 2.13. The bounds

are plotted for two different modular ratios of the constituent phases, the blue bounds for a ratio of 2 and the red bounds for a ratio of 5.5.

The first point to note is that the effective Young's modulus increases with an increase in the volume fraction of the less compliant phase. This is true for both modular ratios and makes physical sense since, as the volume fraction of the less compliant phase increases, it takes up an increasing amount of the space and the composite should begin to act more like the stiffer phase.

The relative difference between the constituent material properties shifts the entire range of potential behaviour defined by the bounds as well as the spread between the upper and lower bounds. For the modular ratio of 2, shown by the blue lines, the bounds are tight, indicating that the elastic behaviour of any isotropic composite can be predicted to a great degree of accuracy knowing only the volume fractions of the phases. This is not the case when the modular ratio is increased to 5.5. The greater space between the red bounds allows the effective Young's modulus of a composite to vary over a significant range at a

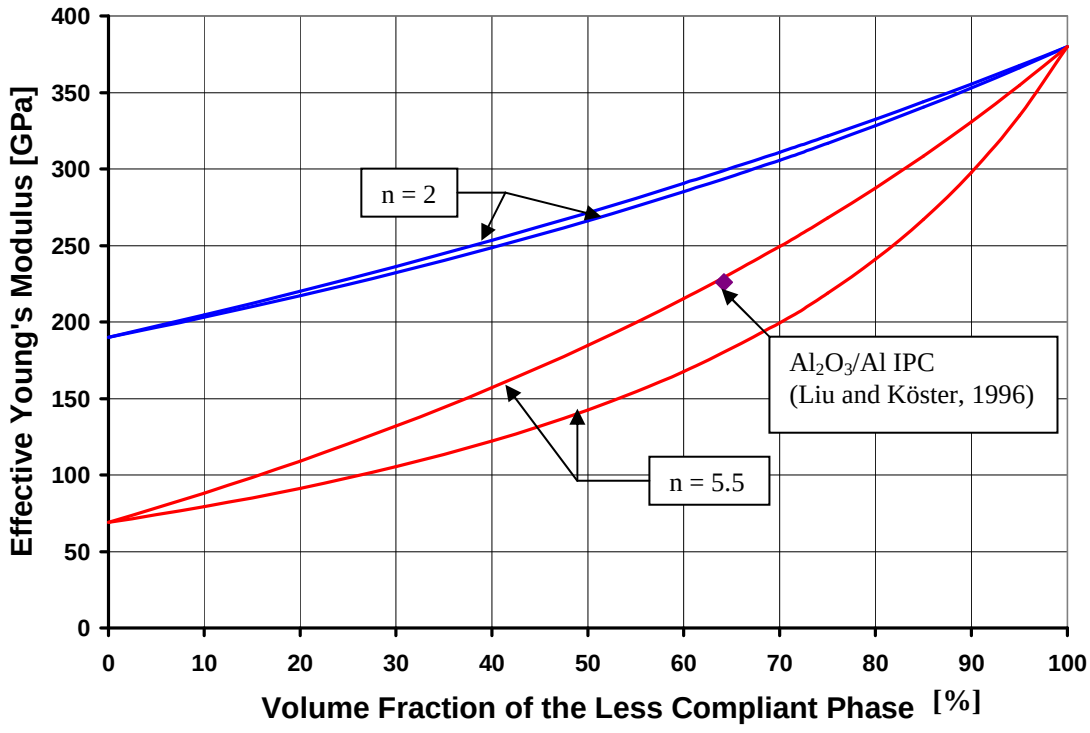

Figure 2.6. The Hashin-Shtrikman bounds on elastic behaviour (n = modular ratio of phases)

particular volume fraction. In this case, further information about the microstructural geometry is necessary to make more accurate predictions.

The use of these bounds for an interpenetrating microstructure can be seen when compared to the data from Liu and Köster (1996) for their Al_2O_3/Al IPC, denoted by the purple diamond. This IPC had a volume fraction of 64.2% Al_2O_3 and the Young's moduli of the constituents differed by a ratio of 5.5. It can be seen from Figure 2.6 that this plots near the upper bound and the interpenetrating geometry has produced the optimum response for this volume fraction of these materials.

The thermal residual stress derived from processing an IPC has been found to have some effect on its elastic behaviour. The numerical work of Daehn et al. (1995), considering an Al_2O_3/Al IPC with a simple cubic microstructure, showed a minor difference in overall stress-strain behaviour if thermal residual stresses were or were not considered (the volume fractions for each phase were 50%). The only point of significant change was the strain at which yielding occurred. With the inclusion of thermal residual stresses, the strain at yield increased, leading to a decrease in the slope of the elastic region and therefore a decrease in the effective Young's modulus. Dong et al. (1999) used the self-consistent model of Leβle et al. (1998, 1999) to find the stress-strain behaviour of a tungsten/copper (W/Cu) IPC. Their work showed a significant decrease in the effective Young's modulus when thermal residual stresses were considered but only when the volume fraction of Cu was greater than 40%. The decrease in the effective Young's modulus with the consideration of thermal residual stresses was further confirmed by the findings of Wegner and Gibson (2000b), who compared their experimental work on a stainless steel/bronze IPC to a hexagonal close-packed unit cell model. They noted that thermal residual stresses could account, at least in part, for their IPC's Young's modulus being below the Hashin-Shtrikman lower bound.

The continuity of the constituent phases also influences the elastic behaviour of IPCs. Wegner and Gibson (2000a) studied interpenetrating and

non-interpenetrating IPCs over the same volume fraction range with hexagonal close-packed unit cells. The unit cells that interpenetrated showed a much more significant increase in their effective Young's modulus as the volume fraction of the stiffer phase was increased. This result had to be balanced against the previously mentioned finding of a stiffness reduction due to thermal residual stresses (Wegner and Gibson (2000b)). They theorised that an increased effective Young's modulus was possible due to the interconnection of the stiffer phase, but that this also applied an increased constraint to the more flexible phase causing enhanced thermal residual stresses. The effect of continuity on composite stiffness was therefore found to be based on the relative importance of these two mechanisms. Dong et al. (1999) agreed that increased continuity would produce a small increase the effective stiffness of the composite; however, they theorised that a slightly different mechanism was acting on the thermal residual stresses. In their self-consistent model of a brittle-ductile IPC, the effect due to thermal residual stresses was found significant only over a volume fraction greater than 40% of the ductile phase (above which they suggest an interpenetrating ductile phase exists). This was assumed to be due to plastic flow in the connected ductile phase caused by the thermal residual stresses induced by the connected brittle phase. Peng et al. (2001) noted that the effective Young's moduli of their experimental Al_20_3/Al IPCs best fit predictions by Tuchinskii's (Peng et al. 2001) lower bound equation for an interpenetrating microstructure rather than those of the Halpin-Tsai (Peng et al. 2001) equation for discontinuously reinforced composites. This again notes that the continuity of the phases has an effect on the elastic behaviour.

Phase continuity has been shown to have an effect on the elastic behaviour; however, continuity is itself dependent upon a number of microstructural parameters, such as the phase shape, size distribution and spatial distribution. No known study of these parameters has been made for IPCs; however, Shen et al. (1994b) studied phase shape and spatial distribution for two-phase particle reinforced composites. The findings of this study are a guideline for the application of a shape study to IPC research. In the study on

reinforcement phase shape, Shen et al. (1994b) used two-dimensional axisymmetric unit cell models to show that shape had a significant effect on composite behaviour. Increasing composite stiffness over that of the matrix alone occurred in greater amounts with each of the following particle reinforcement shapes: the double-cone (diamond cross-section), the sphere, the truncated cylinder (hexagonal cross-section), the unit cylinder and the whisker. This increased stiffness was attributed to the ability of the matrix to transfer its load to the reinforcement. The whisker has the greatest surface area through which the matrix could transfer its load by shear and therefore had the greatest stiffness. This effective surface area decreases from unit cylinder, to truncated cylinder, to sphere and to double-cone. It is interesting to note that Shen et al. (1994b) did not find that any of the shapes was more effective at constraining the matrix (reducing its strain) in the elastic range.

Shen et al. (1994b) also found that reinforcement spatial distribution had a significant effect on composite behaviour (though less of an effect than shape) through the use of two-dimensional plane strain models. Distributions representing uniformly sized particles in horizontally and vertically aligned periodic arrangements showed the greatest effective stiffening, while distributions of uniformly sized particles in an offset periodic arrangement showed the least stiffening. These results were linked to the reinforcement's ability to constrain the matrix. This is studied in more detail in the next section where the composite's plastic behaviour showed a similar but more definite effect from the reinforcement spatial distribution.

2.3.3 Factors Influencing Plastic Behaviour

Plastic behaviour is the permanent deformation that commonly occurs in ductile materials after loads have exceeded the elastic range. Near the failure of such materials, plastic conditions usually exist and a proper understanding of them is essential to predicting their maximum response. Accurate determination of this behaviour is difficult, as mathematical models tend to be quite complex. In addition, with IPCs pseudo-plastic conditions often exist due to the differing

behaviours of phases made from ceramics, metals or polymers. In general, the variables that affect elastic behaviour also affect plastic behaviour.

Unlike elastic behaviour, no general bounds have been determined for the plastic behaviour of composite materials. The effect due to the volume fractions and properties of the phases must therefore be based upon the collective results of numerous studies. Basic theory suggests that effective plastic properties will increase with the volume fraction of the stronger phase, based simply on the fact that the more of this phase that is within the composite, the more its behaviour will dominate the effective behaviour (this assumes that no significant flaws exist in the microstructure). This was confirmed by the self-consistent models of Leβle et al. (1999) and the experimental and unit cell models of Wegner and Gibson (2000a, 2000b). In all three of these studies, the effective yield strengths of the IPCs were found to increase with increasing amounts of the stronger phase.

Comparable to the trend for elastic properties discussed in the previous section, the plastic properties of IPCs are shifted by the relative difference between the properties of the constituents, while producing similar stress-strain behaviours. Daehn et al. (1995) confirmed this in a numerical sensitivity study of the influence of the yield strength of the aluminium phase on the yield strength of an Al_2O_3/Al IPC. It was found that the composite's point of yielding was shifted with changes to the ductile phase's yield strength while producing similar curves before and after yielding. As discussed earlier, the Hashin-Shtrikman bounds demonstrate that increasing the relative difference between the constituent phase elastic properties increases the range of potential composite behaviour (the bounds become less restrictive). Without general bounds, the same statement is difficult to verify for plastic properties. However, the analogy model of Moukarzel and Duxbury (1994) showed that an interpenetrating structure became more and more significant with an increasing relative difference between the constituents. This indirectly shows that the range of potential composite behaviour increases with increasingly different

phases, since microstructural geometry is only important when the limits of behaviour are far apart (consider the two sets of bounds in the Fig. 2.6).

All studies into the effect of thermal residual stresses on plastic behaviour have shown it to have little influence. There is, however, some difference in research observations as to whether this minor influence shifts the stress-strain curve of IPCs upwards or downwards. The simple cubic unit cell model of brittle/ductile phases in the study by Daehn et al. (1995) predicted a slight shift in yield strength such that the stress-strain curve was shifted downward when thermal residual stresses were present, but this was considered insignificant. The results of the brittle/ductile self-consistent models of Leβle et al. (1999) and Dong et al. (1999) agreed that the total effect of thermal residual stresses was insignificant but that overall stress-strain behaviour was shifted slightly upwards. The HCP unit cell model of Wegner and Gibson (2000b) used two ductile phases and found slightly downward shifted deformation behaviour that agreed more closely to the work of Daehn et al. (1995). Reasons for these opposite but relatively small influences due to thermal residual stress were connected to continuity, which is discussed below.

Current research has determined that continuity has an influence on the plastic behaviour of IPCs that is likely well in excess of the influence it has on elastic behaviour. In the self-consistent models of Leβle et al. (1999) and Dong et al. (1999) the matricities of the phases (which control continuity in their models) were varied while the volume fractions were kept constant. Stress-strain behaviour, especially after yielding, was found to differ by large amounts as continuity was shifted between the extremes of each phase forming inclusions within a particle reinforced composite. The IPC and non-IPC unit cell models of Wegner and Gibson (2000a) noted that continuity produced distinctly different results at yielding. The IPC model produced much higher yield strengths as the continuity of the stronger phase was increased.

This strong influence from continuity on plastic behaviour was used by all these researchers to explain the minor effect from thermal residual stresses.

Both Leβle et al. (1999) and Dong et al. (1999) focussed on an increased plasticity of the ductile phase in their models, due to a continuous microstructure, to explain their IPCs' slightly enhanced behaviour. In their theory, a slight improvement in behaviour is created by isotropic hardening of the ductile phase as thermal residual stresses induce an initial plastic deformation. This leads to an increase in the yield strength at which plastic behaviour begins (though in this author's opinion this theory only works if there is some mechanism by which the thermal residual stresses could reduce to zero prior to loading). Wegner and Gibson (2000b) attributed the only slightly downward shifted stress-strain behaviour to the continuity of the stronger phase in their IPC. Numerical results determined that thermal residual stresses were sufficient to induce plasticity in the weaker phase, but were far below the yield strength of the stronger phase. A reduction in overall behaviour as the IPC was loaded should then be expected due to the reduced strength that could be contributed from the weaker phase. This reduction, however, was assumed to be largely offset by the dominant behaviour of the almost unaffected continuous stronger phase.

Moukarzel and Duxbury (1994) studied the effect of a continuous microstructure on plastic behaviour by considering the damage induced in their electrically analogous system at failure. Their model with an interpenetrating system produced more damaged resistors prior to complete failure than a non-interpenetrating system. This suggested greater ductility in the interpenetrating system due to an increased redundancy of paths for current flow (in their model paths for current flow were analogous to paths for stress distribution). Based on their results, IPCs obtain enhanced ductility through a reduction in the importance of any single connection within the stronger phase.

As with elastic behaviour, no study has currently been performed to determine the effect of geometric parameters of the microstructure on IPCs under plastic conditions. Again, however, a study by Shen et al. (1995) considered the effects of phase shape and spatial distribution on the plastic

behaviour of two-phase particle reinforced composites. The same two-dimensional axisymmetric and plane strain unit cell models were used for the shape and distribution studies, respectively. Non-linear conditions were considered by applying a sufficient load to obtain plastic behaviour in the matrix (the reinforcement was assumed to remain elastic). The effect of reinforcement shape on plastic behaviour was even more pronounced than that shown for elastic behaviour. Composite strengthening with shape followed the same pattern as was observed for stiffness: the double-cone showed the lowest strengthening, then the sphere, truncated cylinder, unit cylinder and finally the whisker, which showed the greatest strengthening. In this case, Shen et al. (1995) determined that matrix constraint was occurring, as some reinforcement shapes were able to produce a notable reduction of the strain in the matrix. Two important constraining mechanisms were identified:

1. The ability of the reinforcement to interrupt the path of high plastic strain; and
2. The ability of the reinforcement to restrict the size of the high and moderate plastic flow paths.

The whisker shape showed the greatest ability to meet these two points and therefore provided the highest constraint to the matrix material. Since any reduction in the deformation of the weak matrix phase increases the load carrying capacity of the composite, the whisker produced the greatest strengthening to the composite.

The effect of reinforcement spatial distribution also had a more significant effect on composite plastic behaviour than on elastic behaviour (again this effect was less than that shown by the phase shape). Distributions containing horizontally and vertically aligned periodic microstructures again produced the most enhanced effective plastic properties, while distributions with offset periodic microstructures again showed the least. The relative level of strengthening was based on the ability of the distribution to constrain the matrix by means of the previously listed two mechanisms. Of the two important points

for constraint, the offset distributions were better able to interrupt the path of high strain, while the aligned distributions showed a greater ability to restrict the size of the overall strain path. It is the greater volume of matrix material that is under moderate strain that leads to the weaker reinforcing of the offset distributions. Neither unit cell was definitively better on both of the constraining points, showing why reinforcement shape was shown to have a more significant effect than distribution.

2.4 SUMMARY OF RESEARCH ON INTERPENETRATING PHASE COMPOSITES

Several methods have been used to study IPCs and several means used to describe their microstructures. Unfortunately, many of these studies have failed to either properly describe the microstructures that they assumed or have used representations of these microstructures that are overly simplistic. The focus of researchers on the prediction of IPC behaviour rather than on characterising microstructures has made the comparison of the results of various studies difficult, as microstructural differences remain unknown. This lack of microstructural data has led to a great deal of inefficiency in the attempt to understand the behaviour of IPCs. It is therefore highly important that researchers choose appropriate methods to use and characterise their microstructures carefully.

The great benefit of an experimental study is that realistic results may be found for an actual IPC's behaviour. In general, the greatest problem that occurs with experimental work is that the microstructural analysis is considered only briefly or entirely in a qualitative manner such that comparisons to other research are difficult. In particular, the increased complexity inherent in the geometry of IPCs requires an increase in the amount of data used to characterise these materials. The topological parameters from Section 2.1.2 along with methods of Aldrich and Fan (2001) are suggested as good guidelines for the procedure needed in an IPC microstructural analysis.

Early studies on prediction of IPC behaviour used simplified methods so that the complexity of the microstructural geometry could be avoided. One of these simplified methods is the use of general bounds on the effective behaviour. General bounds, such as the Hashin-Shtrikman bounds (1963), offer an excellent means of understanding some of the simple influences on effective response, as well as a means to test the accuracy of experimental work or more detailed models. Analogy models have also been used to determine broad behavioural patterns in IPCs. Unfortunately, like general bounds they are also quite limited and cannot produce exact results.

While the previous simplified methods provided a good understanding of basic IPC behaviour, they consisted of too many simplifying assumptions to be able to accurately predict the response of an actual IPC. Improvements in predictions have been obtained with self-consistent models and unit cell models. Self-consistent models have proven to be relatively simple and provide good global results for the behaviour of IPCs with random microstructures. These models do not, however, provide a good representation of ordered microstructures and cannot be used to study the local conditions at a point within a composite. For cases where an IPC has an ordered microstructure or local behaviour within the microstructure is of interest, unit cell models are more appropriate. The use of a fully described microstructure with the unit cell model also allows the highest accuracy for characterisation of the microstructure.

Using the various prediction methods, researchers have determined a number of important factors that influence the behaviour of IPCs. This was studied for thermal residual stresses, elastic properties and plastic properties. Thermal residual stresses are created as a result of relative differences in the properties of the constituent phases. Research considered in Section 2.3.1 noted the importance of the constituent CTEs, stiffnesses and melting temperatures in the development of thermal residual stresses. In addition, the microstructural geometry also has a strong influence through the level of constraint applied to the more compliant phase by the less compliant phase.

The influence of constituent properties and volume fractions on the elastic behaviour of general composites, including IPCs, has long been understood; more recently the effects from thermal residual stresses and continuity have been determined. The bounds determined by Hashin and Shtrikman (1963) denote the limitations of elastic behaviour for all isotropic composites. With the use of these bounds, it can be seen that constituent properties influence the range of potential composite behaviour (the greater the difference between the constituents the greater the range of behaviour for a composite containing them). In general, an increase in the volume fraction of the less compliant phase causes an upward shift of the stress-strain curve for an IPC, denoting improved behaviour. Increased microstructural continuity was also theoretically found to directly increase the elastic modulus. In experimental programs, however, several studies have shown that elastic properties, such as the effective Young's modulus, slightly decrease with increases in continuity. The source for this inconsistency has been linked to the creation of increased thermal residual stresses due to the continuous microstructure, ultimately leading to a lower elastic modulus.

The variables that affect the elastic behaviour of IPCs are also important for their plastic behaviour. Assuming no significant flaws exist within an IPC's microstructure, the constituent phase properties and volume fractions have a similar influence on the plastic behaviour to what was previously noted for the elastic behaviour. The greater the volume fraction of the stronger phase, the higher the effective yield strength of the IPC, and the larger the relative difference in phase properties, the greater the range of potential effective behaviour. For plastic behaviour, thermal residual stresses were found to be unimportant due to the continuity of the microstructure. The exact mechanism for this is currently undetermined; however, all studies have shown either an increase in yield strength or an increase in post-yielding stresses related to the continuous nature of IPCs.

Previous researchers have shown that long-range continuity has an important influence on the mechanical behaviour of IPCs, but they have only

rarely noted the effect of microstructural parameters on continuity. Among such parameters are the shape, size distribution and spatial distribution of the phases, which affect the location and amount of interconnection in a three-dimensionally continuous microstructure. For two-phase particulate composites (non-IPCs), Shen et al. (1994b, 1995) attempted to determine the effect of phase shape and spatial distribution on the elastic and plastic behaviours. These geometric parameters were found to enhance the behaviour of particulate composites in direct relation to their ability to allow the reinforcement to constrain the weaker matrix material. Given this importance to non-IPCs, it is the purpose of this research to extend the understanding of how the microstructural geometry influences the mechanical behaviour of composites to IPCs, specifically the effect of phase shape on elastic and plastic properties.

CHAPTER THREE

NUMERICAL MODELLING PROGRAM

Interpenetrating phase composites (IPCs) are distinguished from other composite materials by the continuous three-dimensional geometry of all their constituent phases. No other restrictions are placed on them, so the number of potential microstructures that are interpenetrating is quite large. To study the effect phase shape has on the behaviour of IPCs, this modelling program considered two different microstructures in which only the shape differed; the phase size and spatial distributions were kept constant.

To meet these requirements, a microstructure resembling the hexagonal close-packed (HCP) system of uniformly sized, intersecting spheres was considered. The HCP system provides an isotropic spatial distribution so the direction of testing does not need to be considered and the uniformly sized spheres supply a constant size distribution. This model provides one phase shape as spherical with the other phase taking on the shape of the interstitial space. A second model involving a uniformly sized cylindrical phase shape with an HCP microstructure was also created. A cylindrical shape is oriented along its length, so it differs significantly from the equi-dimensional nature of the sphere shape. A comparison of these two shapes should therefore provide extreme results of the influence of phase shape on IPC properties. The interfacial bond between the two phases for both model geometries was assumed to be perfect so that debonding was not taken into account. Both of these geometries, as well as the steps required to model them using the finite element method (FEM) are considered in this chapter.

3.1 GEOMETRY OF THE SPHERICAL MODEL

The long range order of the spherical hexagonal close-packed (HCP) microstructure can be seen by considering Figure 3.1. The microstructure consists of repeating layers of spheres with the spheres in adjacent layers fitting into the gaps of the previous layer, the same gaps being used with every

second layer. If the plan view of the HCP microstructure is considered, a further level of order can be seen (see Fig. 3.2). The black equilateral triangular region near the centre of Figure 3.2, when symmetrically mirrored at its right boundary, creates the red triangle (symmetrically mirroring simply flips the region within the black triangle about the right boundary). The same process can be used about the lower left boundary to create the blue triangle. Continuing this process about the boundaries of the red and blue triangles, the entire area within the black hexagon is soon defined.

Considering again the black triangle shown in Figure 3.2, if the upper left boundary is symmetrically mirrored out of the hexagon, the region within the green triangle is created. Note that the sphere at the centre of Figure 3.2 is arbitrary since all spheres have similar adjacent spheres in the same locations. Therefore the sphere in the upper left corner with the green triangle can also be thought of as being surrounded by a hexagon and the symmetric mirroring process used to complete it. Since this can be carried out for all the spheres on the two planes shown in Figure 3.2 (the upper plane of seven spheres and the lower plane of three), the HCP microstructure is sufficiently modelled by simply using the black triangular region.

Cutting the black triangular region of Figure 3.2 through the equatorial planes of the upper and lower layers of spheres and looking at it in three

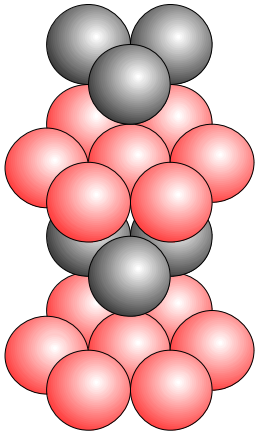

Figure 3.1. Exploded view of the spherical hexagonal close-packed (HCP) system

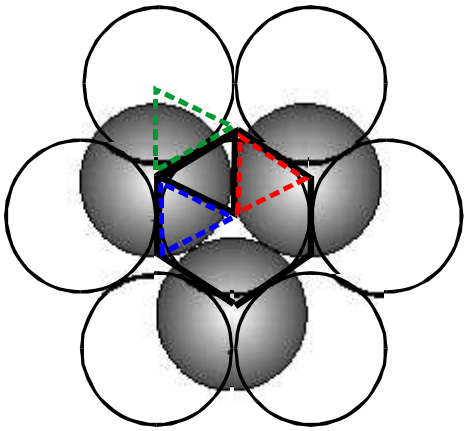

Figure 3.2. Plan view of the spherical HCP system (shaded spheres = lower layer; open spheres = upper layer)

dimensions, the prism unit cell in Figure 3.3 is created. The material above and below this unit cell can be created by symmetrically mirroring the unit cell (flip the unit cell about both the top and bottom planes). The prism unit cell of Figure 3.3 is therefore able to represent the entire HCP microstructure outwards in all directions if symmetric boundary conditions are applied to all five of its faces.

A final simplification to this model can be made by considering Figure 3.4, where a plane has been cut through the prism unit cell perpendicular to a line joining the sphere centres. If the top half of the unit cell is rotated about the central axis of the bottom surface (shown in red), it creates the bottom half of the unit cell; this is an anti-symmetric boundary condition. In summary, the half prism unit cell with four faces having symmetric boundary conditions and one face having an anti-symmetric boundary condition is able to represent the entire three-dimensional HCP microstructure. This process was used to model the IPC microstructure based on the spherical shape and is essentially the same as that used by Wegner & Gibson (2000a, 2000b). A similar process will be used to model the cylindrical shape in Section 3.2.

The spherical geometry of the IPC model follows the HCP microstructure just described, but one further consideration is needed. The spheres in Figure

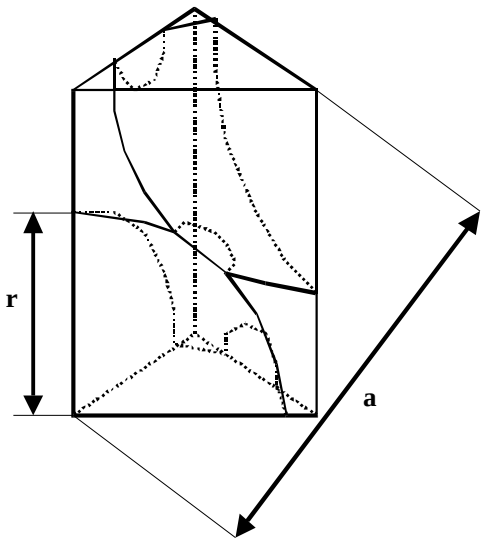

Figure 3.3. Prism unit cell of the spherical system

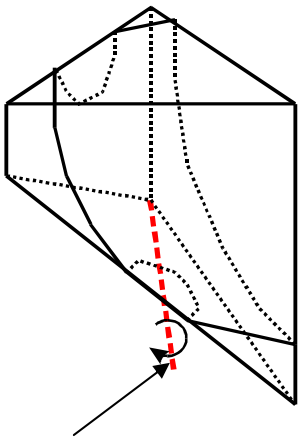

Figure 3.4. Half prism unit cell of the spherical system

3.3 are required to remain within a certain range of possible sizes. If they are reduced in size while prism dimensions remain constant such that they no longer touch, then the material modelled would no longer be an IPC since the sphere phase would not be continuous. On the other hand, if the spheres are increased in size, the surrounding material will eventually become isolated into small pockets and again the model will no longer represent an IPC. The final consideration that needs to be made is the range of sphere sizes that will produce an IPC model. This range of sizes is discussed in terms of the spherical volume fraction that will produce an IPC model. How the behaviour of the IPC changes with volume fraction is also of interest, so the entire range of applicable volume fractions is studied.

Within the prism unit cell (Fig. 3.3) are two pieces of spheres, each one-twelfth of a whole sphere minus the volume of material that is lost at their intersection (see Fig. 3.5). The volume fraction of spheres within the prism unit cell can be found by determining the volume of sphere material within the unit cell, then the volume of the prism unit cell and finally dividing the former by the latter. Note that the volume fraction of sphere material is the same in the half prism unit cell as in the prism unit cell since the ratio of sphere to unit cell volume is the same. This problem can be solved analytically to produce the following equation for spherical volume fraction: (the derivation is shown in Appendix A)

$$\phi_s = 8\sqrt{2}\cdot\pi\left(\frac{r}{a}\right)^3\left[\frac{-5}{6}+\frac{3}{4}\left(\frac{a}{r}\right)-\frac{1}{16}\left(\frac{a}{r}\right)^3\right], \tag{3.1}$$

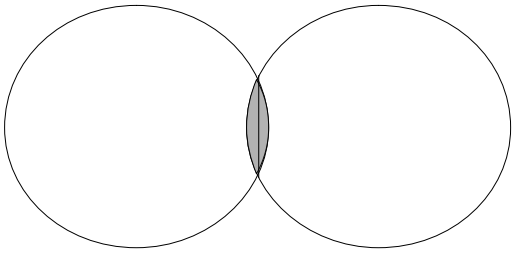

Figure 3.5. Two intersecting spheres showing the volume lost at the intersection (grey)

where ϕ_s is the volume fraction of spheres in prism or half prism unit cells, “r” is the radius of the spheres and “a” is the centre-to-centre distance between spheres (for r and a see Fig. 3.3).

To understand the volume fraction range that will allow adjacent spheres to come in contact, yet not be so large as to prevent the surrounding phase from remaining interconnected, consider again Figure 3.3. The lower bound of the volume fraction range is where the spheres just come into contact. This occurs when the radius of the sphere equals half the centre-to-centre distance between the adjacent spheres,

$$r = \frac{a}{2}. \tag{3.2}$$

The upper bound of the volume fraction range is where the spheres take all the space along one edge of the half prism unit cell; in this case, the surrounding phase would not be interconnected but would only exist in pockets (consider, for example, the closest top edge in Fig. 3.3). This condition is met when

$$r = \frac{a}{\sqrt{3}}. \tag{3.3}$$

Substituting Equations 3.2 and 3.3 into Equation 3.1, the lower bound volume fraction is found to be 74.05% of the spherical phase, and the upper bound to be 96.41% of the spherical phase. For practical purposes, this model was created over the range of 75% to 95% to avoid dealing with the extremely small regions that were created in the sphere material near the lower bound and in the surrounding material near the upper bound.

3.2 GEOMETRY OF THE CYLINDRICAL MODEL

The geometry of the cylindrical IPC model, like that of the spherical IPC model, follows the basic HCP microstructure. However, to include cylinders in place of the spheres, the appearance of the model was changed significantly. In order to visualize this new geometry, imagine nodes that are located at the centres of the spheres shown in Figure 3.1. The cylindrical system was created

by connecting each adjacent node with a line that formed the axis of a cylinder. All cylinders were of equal length and equal radius (equal length because all adjacent nodes are an equal distance apart, and equal radius because the unit cell should model a homogeneous, isotropic composite). As seen in Figure 3.6, in the absence of the surrounding material, the cylindrical microstructure is a space frame.

The cylindrical system was also modelled using the half prism unit cell, since the spatial distribution of the intersection points of cylinder axes were the same as those of the sphere centres. Thus, only the shapes of the phases within the unit cell were changed. The cylindrical half prism unit cell contained the halves of two cylinders of equal length minus a few pieces of those cylinders which fall outside the unit cell near the top right corner (see Fig. 3.7).

Similar to the previous case with the sphere, the volume fraction range over which this cylinder shape model can represent an IPC must be determined. To solve this problem in the same way as was done for the sphere would require calculation of the volume of the portions of the cylinders that fall outside the unit cell. Although relatively simple in appearance, to do this for the unit cell in Figure 3.7 involves solving numerous complex equations, making another method more desirable. As an alternative, a Monte Carlo simulation or single point probability function was used to determine the volume fraction of

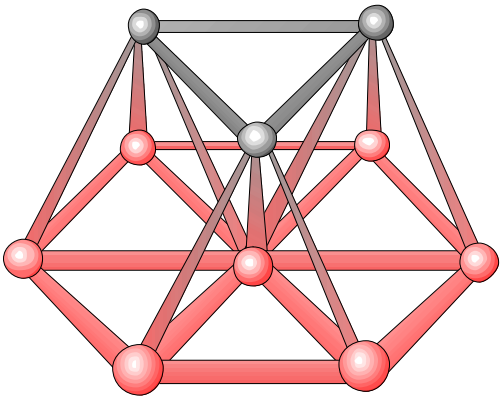

Figure 3.6. Cylindrical system
(small spheres denote nodes where cylinders interconnect)

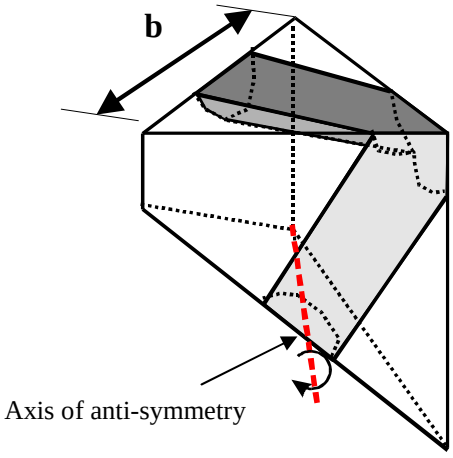

Figure 3.7. Half prism unit cell of the cylindrical system

the cylinders as the radius of the cylinders was varied. The C++ program used to run this simulation and details of its development are provided in Appendix B. Only a simple discussion of the program's methodology is provided here.

The Monte Carlo simulation created for this work produced groups of three random numbers used to define the coordinates of points within a box shown in Figure 3.8. Within the box is the half prism unit cell with its cylinders oriented along the top and back surfaces. Using this geometry, the box was separated into five regions: the total space in the box, space in the unit cell, space in the back surface cylinder, space in the top surface cylinder and space at the intersection of the cylinders. Each region was separated by equations that defined the location of boundary coordinates.

The volume fraction of the cylinders within the half prism unit cell is approximately equal to the number of random points within the cylinders divided by the total within the unit cell. The problem is therefore simplified to a determination of how many of the random points fall within each of the five

Point 1: Top-left-back corner $(0,0,h)$

Point 2: Top-front corner $\left(\frac{b}{2},\frac{\sqrt{3}b}{2},h\right)$

Point 3: Top-right-back corner $(b,0,h)$

Point 4: Bottom-left-back corner $\left(0,0,\frac{3h}{4}\right)$

Point 5: Bottom-front corner $\left(\frac{b}{2},\frac{\sqrt{3}b}{2},\frac{h}{2}\right)$

Point 6: Bottom-right-back corner $\left(b,0,\frac{h}{4}\right)$

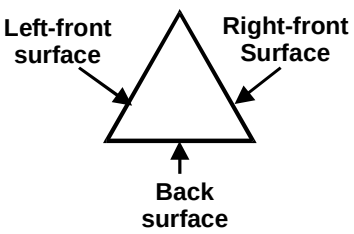

(a) Top view of the unit cell

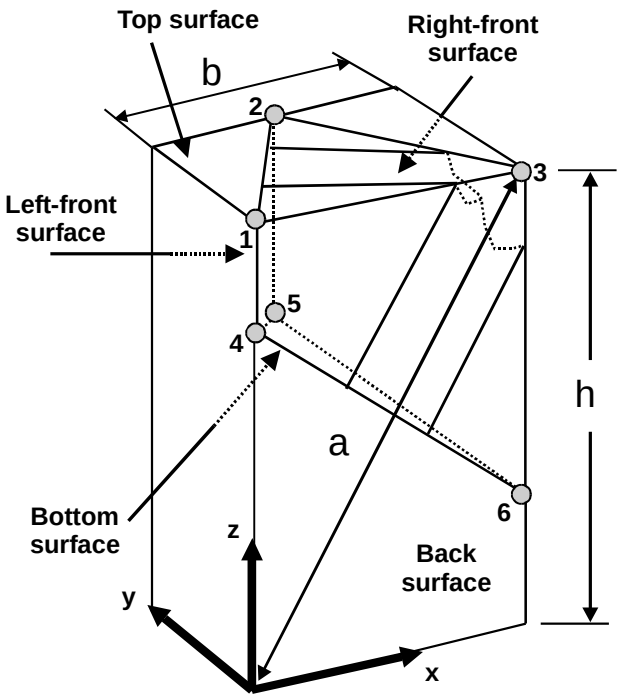

(b) Isometric view of the unit cell

Figure 3.8. Box for Monte Carlo simulation with half prism unit cell inside

regions. To do this, the coordinates for each generated random point were tested against the boundary equations to determine which region contained each point. The points in each region were then counted and the ratio of those within the cylinders to the total number in the unit cell was used to determine the volume fraction. In equation form, this is

$$\phi_c = \left(\frac{n_c}{n_{hp}} \right) \cdot 100 \,, \tag{3.4}$$

where ϕ_c is the volume fraction of cylinders in half prism unit cell, n_{hp} is the total number of random points in the half prism unit cell, and n_c is the number of random points in cylinders. n_c is defined as

$$n_c = n_{bc} + n_{tc} - n_i \,, \tag{3.5}$$

where n_{bc} is the number of random points in back cylinder, n_{tc} the number of random points in the top cylinder, and n_i the number of points at the cylinder intersection.

Any time the Monte Carlo method is used, it is necessary to ensure that a sufficient number of random points are used to achieve an accurate answer. This was done by running the simulation for the same volume fraction several times, while increasing the number of random points. As the number of random points increases, the accuracy of the results should increase, but at a decreasing rate such that they converge towards the correct solution. As an example, the simulation was run at the maximum cylinder volume fraction and the result for four different numbers of random points is graphed in Figure 3.9. It can be seen from the figure that the volume fraction of the cylinders converges towards a value of approximately 90.7% with a difference in the results for 10 million and 100 million random points being less than 0.02%. A satisfactory level of accuracy is therefore obtained with about 10 million points.

Another test was run on the Monte Carlo simulation in order to verify that the random number generator for C++ (Microsoft Corporation, 2003) was sufficiently random that results could be considered unbiased. The test was a

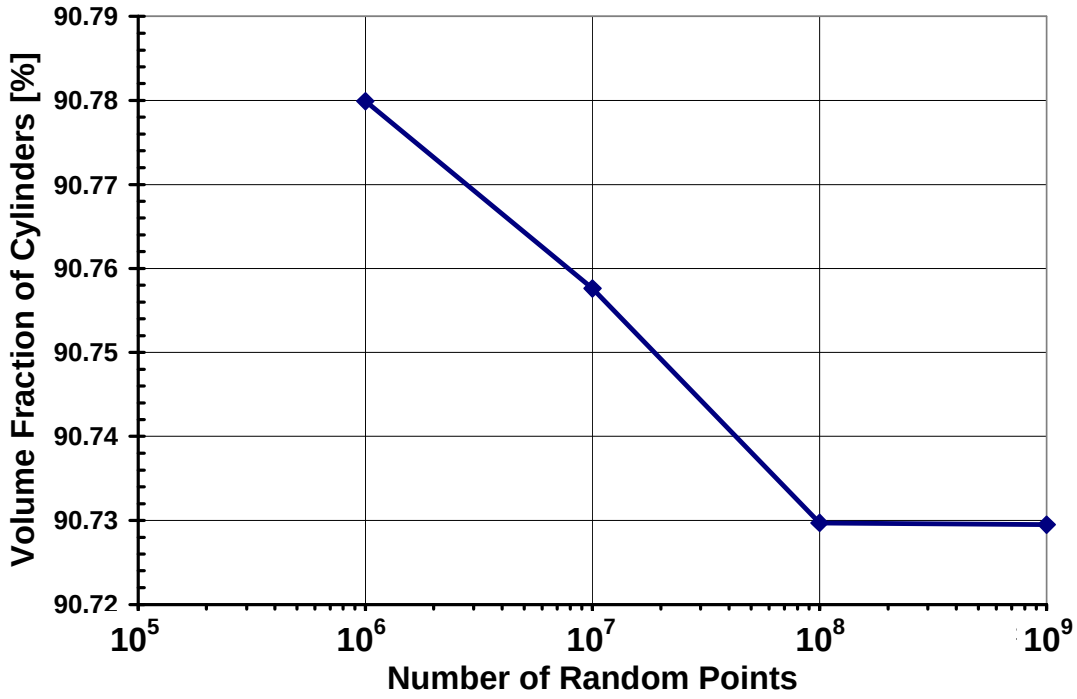

Figure 3.9. Convergence of the volume fraction of cylinders with an increasing number of random points

comparison between the volume fraction of the half prism unit cell within the box (see Fig. 3.8), and the exact solution based on the dimensions of the unit cell and box. The exact solution was found using the following equation:

$$\phi_{hp} = \left[\frac{V_{hp}}{V_{box}}\right] \cdot 100\,, \tag{3.6}$$

where V_{hp} is the volume of half prism unit cell (which is equal to half the volume of the prism unit cell, see Appendix A). V_{box} is the volume of the box, which is defined as

$$\begin{aligned} V_{box} &= (b)\left(\frac{\sqrt{3}}{2}b\right)\left(\frac{3h}{4}\right), \\ V_{box} &= \frac{3\sqrt{3}}{8}b^2 h \end{aligned} \tag{3.7}$$

where “b” is the length of a top surface edge and “h” the height of prism unit cell (see Fig. 3.8). This was then compared to the following result from the Monte Carlo simulation:

$$\phi_{hp} = \left[\frac{n_{hp}}{n_{total}} \right] \cdot 100 \,, \tag{3.8}$$

where n_{total} is the number of total points (all points fall within box). Both methods produced the result that 33.32% of the volume of the box is the half prism unit cell. This verifies that the random number generator in C++ is sufficiently unbiased for the purposes of this simulation.

The Monte Carlo method was then used to find the limits at which the cylinder HCP microstructure could be used to model an IPC. Since the cylinders become interconnected as soon as any cylinder material is added to the composite, the theoretical lower volume fraction limit for an interpenetrating geometry is zero. The upper limit can be visualised by considering the diameter of the top cylinder along the top surface (see Fig. 3.10). As more cylinder material is added to the composite the diameter of the top cylinder grows until it takes up the entire top surface (this is when the diameter equals “b”, the length of the top left-front edge). In this case, the surrounding material is no longer continuous upwards, and both phases no longer interpenetrate. If a cylinder diameter of “b” is input into the Monte Carlo simulation, a maximum cylinder volume fraction of approximately 90.73% is obtained. Although the cylinder model theoretically works between 0% and 90%, to avoid element distortion problems near these extremes the model was tested between approximately 2% and 84%.

3.3 BOUNDARY CONDITIONS FOR THE MODELS

To use the HCP microstructure as a model for an IPC required both the proper volume fraction to ensure the interpenetration of both constituents (considered in previous sections), and the proper boundary conditions to ensure the model acted as though surrounded by the rest of the material. Symmetric surfaces, such as the top, back, left-front and right-front faces (see Fig. 3.8), required that their displaced positions remain in a plane and be parallel to their original positions in order to ensure geometric periodicity. It should also be noted that the given displacement to the top surface, discussed below, was

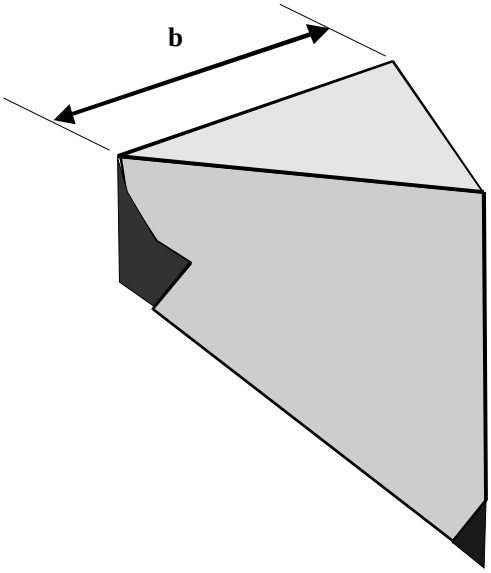

Figure 3.10. Cylinder HCP microstructure at its maximum volume fraction for interpenetration

applied symmetrically (other loading conditions may violate the symmetric boundary conditions). In the case of the bottom surface, an anti-symmetric boundary condition necessitates rotation about a central axis as displacement occurs. Although the rules are fairly simple, their application is complex and the details for each of these boundary conditions are considered in the rest of this section.

The top surface of the model was the most important boundary condition in determining its behaviour. It was given an applied displacement to simulate the IPC being placed in uniaxial tension or compression (see Fig. 3.11). This simulation was desirable if the model was to provide information on the effective elastic and plastic properties of the IPC and its overall stress-strain behaviour. To ensure that all nodes on the top surface symmetric boundary remained on a single plane, only one master node was given the applied displacement and all the other nodes were made its slaves through a constraint equation forcing them to displace the same as the master node. The node chosen to be the master was in the top-left-back corner. The reasons for choosing this node will become more apparent when the boundary conditions for the left-front and right-front surfaces are considered. The constraint equation applied to the nodes on the top surface was

$$u_{z(Top)} = u_{z(TLB)}, \tag{3.9}$$

where $u_{z(Top)}$ is the displacement in the z-direction of all nodes on the top surface and $u_{z(TLB)}$ is the z-direction displacement of the master node (in the top-left-back corner). Note that displacement in the z-direction indicates vertical extension or compression as defined by the axes in Figure 3.8.

The movement of the bottom surface was the most complicated boundary condition, since its anti-symmetry required rotation about a central axis running from the bottom-front corner to halfway along the bottom-back edge (see Fig. 3.4 and 3.7). To understand this movement, it is first necessary to consider the entire prism unit cell (see Fig. 3.3). If the prism unit cell is stretched with equal forces pulling at the top and bottom, nodes above the mid-height would move upwards and nodes below the mid-height would move down. Returning to the half prism unit cell, it should be noted that the axis of anti-symmetry sits at half the height of the prism unit cell. Therefore, bottom surface nodes to the right of the axis fall below half the height of the prism unit cell and would move down when stretched, and nodes to the left of the axis fall above half the height of the prism unit cell and would move up (see Fig.3.12). The axis of anti-symmetry itself remains fixed in the z-direction. Since the bottom surface must act such that the half prism unit cell when rotated 180 degrees will create the bottom half of the prism unit cell these downward and upward movements must be equal. To ensure this, the z-displacements of nodes to the right of the axis were made slaves to the negative z-displacements of nodes to the left of the axis through the following constraint equation:

$$u_{z(RightBottom)} = -u_{z(LeftBottom)}, \tag{3.10}$$

where $u_{z(RightBottom)}$ is the z-direction displacement of bottom surface nodes on the right side of the axis, and $u_{z(LeftBottom)}$ is the z-direction displacement of bottom surface nodes on the left side of the axis.

Taking the above discussion of vertical stretching further, it should be noted that this stretching would cause lateral contraction in relation to the constituent phases' Poisson's ratios. This lateral contraction means that for

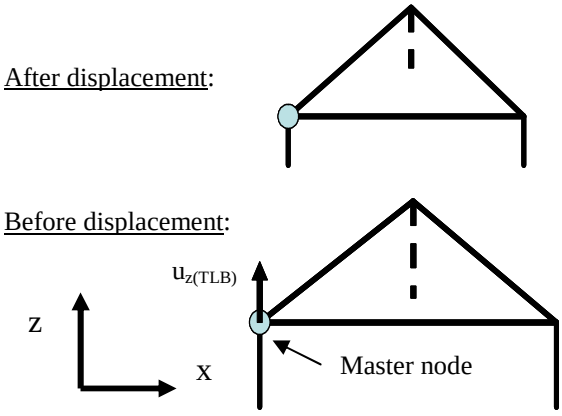

Figure 3.11. Top surface boundary condition

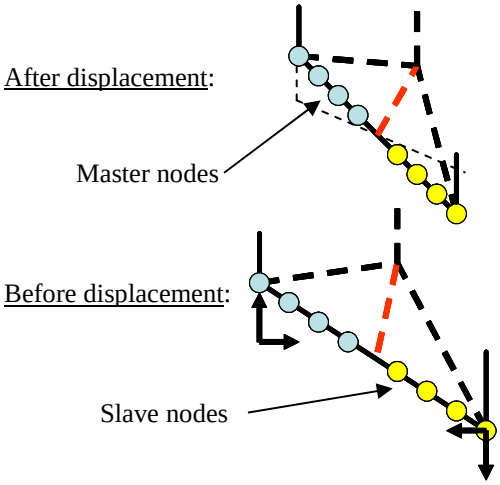

Figure 3.12. Bottom surface boundary condition

nodes on the right side of the axis, the x-displacement is towards the left and that for nodes on the left side it is towards the right. The y-displacements on both the right and the left of the axis are the same (if a node on the left moves forward a node on the right does also). Two more constraint equations can ensure that these x and y-displacements are met:

$$u_{x(RightBottom)} = -u_{x(LeftBottom)}, \tag{3.11}$$

$$u_{y(RightBottom)} = u_{y(LeftBottom)}, \tag{3.12}$$

where $u_{x(RightBottom)}$ is the displacement in the x-direction of the bottom surface nodes on the right side of the axis, and $u_{x(LeftBottom)}$ is the x-direction displacement for those nodes on the left side of the axis. The y-direction displacement of nodes on the bottom surface are denoted as $u_{y(RightBottom)}$ for those on the right side of the axis and $u_{y(LeftBottom)}$ for those on the left side of the axis.

The necessary means to keep the back surface symmetric boundary as a plane are the easiest to visualize in Figure 3.8. The global coordinate system that was chosen for the model places the back surface on the x-z plane so that the planar requirement was met by simply fixing the y-displacement. The x and z-displacements remain free so the model can still expand or contract as appropriate. This condition also does not contradict the y-direction constraint

placed on the bottom, where both right and left y-displacements still remain equal.

Maintaining the left-front surface as a plane requires control of varying amounts of x and y-displacement. Consider Figure 3.13, where the top-left-back corner moves completely in the x-direction and the top-front corner moves completely in the y-direction (these displacements are necessary since the left-front surface is a symmetric boundary condition and its displaced position must be parallel to its original position). At a node somewhere between these two corners, partial amounts of the x and y-displacements are required so that the node moves from the original plane and falls on the displaced plane (see inset of Fig. 3.13). Note that for this intermediate node, the x-component of the resultant displacement can be viewed as the x-displacement of the top-left-back corner minus a distance “a”. The distance “a” is related to the y-component of the resultant displacement such that the following constraint equation can be found for the x-displacement:

$$u_{x(LeftFront)} = u_{x(TLB)} + \frac{1}{\sqrt{3}} u_{y(LeftFront)}, \tag{3.13}$$

where $u_{x(LeftFront)}$ is the x-direction displacement of nodes on the left-front

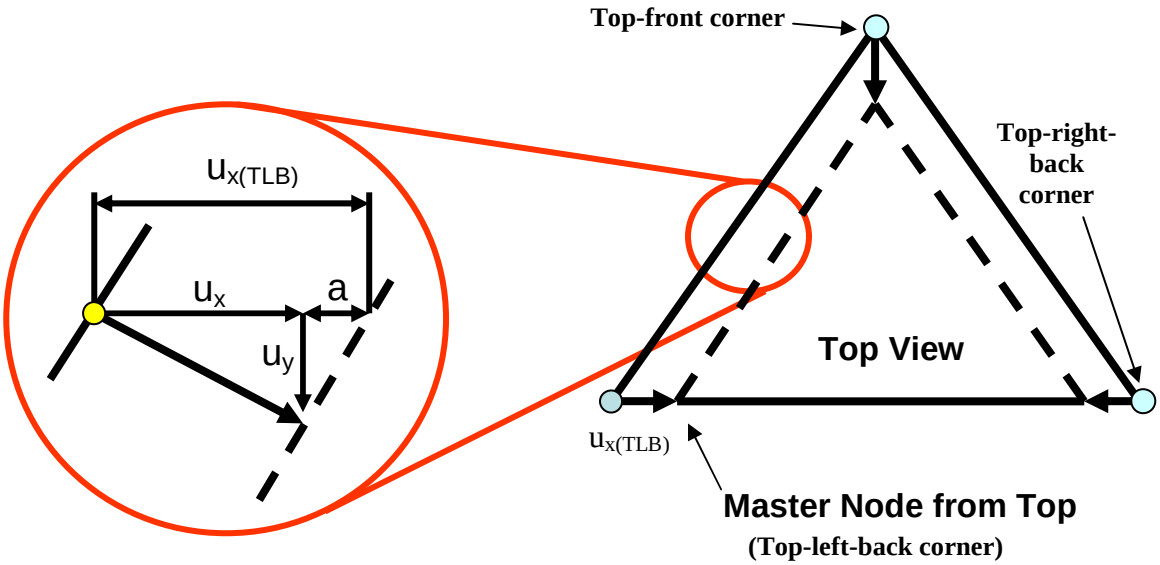

Figure 3.13. Left-front surface boundary condition

surface, $u_{x(TLB)}$ is the x-direction displacement of the master node (in the top-left-back corner), and $u_{y(LeftFront)}$ is the y-direction displacement of nodes on the left-front surface. With this constraint equation, the left-front surface should remain plane since for any given y-displacement the x-displacement conforms to the necessary value to place the node on a plane that is parallel to the original surface.

The right-front surface is quite similar to the left-front surface and should have a similar constraint equation, except using the x-displacement of the top-right-back corner in place of that from the top-left-back corner (see Fig. 3.13). Considering, however, that the x-displacement of the top-right-back corner should be the same as, but in the opposite direction to, that of the top-left-back corner, the following constraint equation was derived:

$$u_{x(RightFront)} = -u_{x(TLB)} - \frac{1}{\sqrt{3}} u_{y(RightFront)}, \tag{3.14}$$

where $u_{x(RightFront)}$ is the displacement in the x-direction of nodes on the right-front surface, $u_{x(TLB)}$ is the displacement in the same direction for the master node (again in the top-left-back corner), and $u_{y(RightFront)}$ is y-direction displacement of nodes on the right-front surface.

When applying the previous boundary conditions to the surfaces, some important situations along certain lines and nodes occur that need to be confirmed. The first involves the axis of anti-symmetry. Nodes on either side of the axis act in different directions for both the x and z-directions. This situation requires the x and z-displacements of the axis be fixed since it must act as the location about which the rotation occurs. At the back end of the axis, there is a point that is on the back surface; this is the hinge point. All three of its degrees of freedom are fixed because it is on both the axis (x and z-displacements are fixed) and on the back surface (y-displacements are fixed). The hinge point is an important condition since without it, rigid body translation remains possible.

Each edge provides an interesting case, since two surfaces meet along these lines, and therefore a combination of boundary conditions must be

satisfied. In particular, the vertical front, back-left and back-right edges are of interest since they have the added condition that they must remain perfectly vertical.

All boundary conditions were added directly to the nodes (the creation of the nodes is discussed in the next section). This was done through the use of a simple C++ program, which performed essentially two functions. The first function of the program was to locate all the surface nodes and note to which surface they belong, and the second function was the application of the appropriate boundary condition to those nodes. The details of this C++ program can be found in Appendix C.

3.4 DISCRETISATION OF THE MODELS

The solution to both the different phase shape IPC models was established using the finite element method (FEM), which requires the models to be divided into discrete pieces, or discretised. The conditions involved in the displacement of the bottom surface necessitate an accurately mapped discretisation since this boundary condition requires the pairing of nodes on the left and right sides of the axis of anti-symmetry. This means that the bottom nodes must be carefully placed so that each slave node is paired with a master node that is its exact mirror. To meet this need, the model was carefully divided into smaller volumes that were then discretised in a controlled way.

A view of the spherical model's half prism unit cell broken into smaller volumes or blocks is shown in Figure 3.14. The bottom surface, as needed, has the right side as a mirror of the left side (see Fig. 3.14(b)). Once this surface was set, the initial blocks were placed so that the various elements, when discretised, would fit together correctly. To create this system of blocks, 107 points were sited at predetermined positions, any arc lines for volumes with curved surfaces were defined, and groups of eight points were located for the vertices of each individual block. The region of surrounding material was separated into twenty-four blocks and the sphere region into thirty-eight, for a total of sixty-two initial blocks in the spherical model.

The half prism unit cell for the cylindrical model was handled in a similar way to that of the spherical model (see Fig. 3.15). The bottom surface of this model looks the same as the spherical model's (see Fig. 3.15(b)), so the same process was carried out with care taken to deal with the different geometry appropriately. The blocks for the cylindrical model were determined by 158 points, arc lines were input for curved surfaces, and groups of eight points were used to define each block. The region of the surrounding material had forty blocks and the cylinder region fifty-eight blocks, for a total in the cylindrical model of ninety-eight blocks.

Three-dimensional isoparametric brick elements with twenty-seven

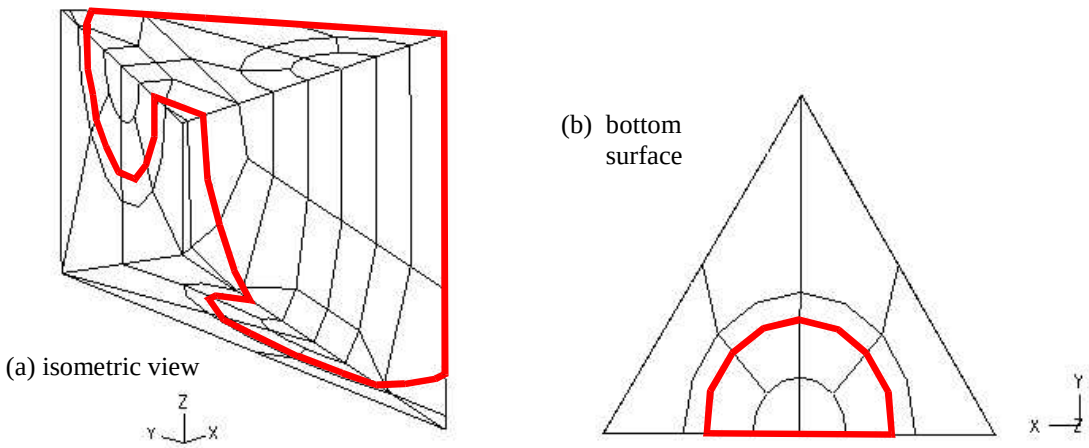

Figure 3.14. Initial blocks for discretisation of the spherical model (sphere ϕ = 85%)
- The red lines indicate the phase interface

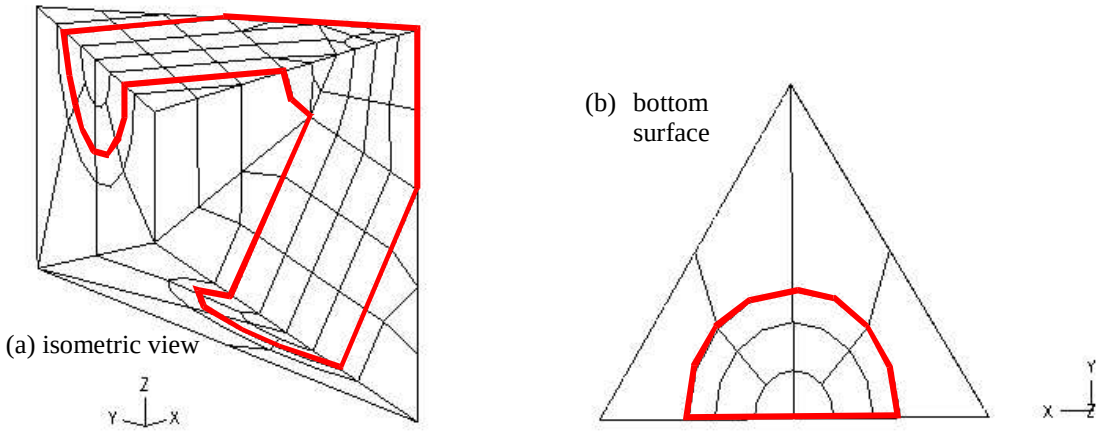

Figure 3.15. Initial blocks for discretisation of cylindrical model (cylinder ϕ = 39%)
- The red lines indicate the phase interface

nodes were used for discretisation. Each face of this element has four corner nodes, four nodes at the midpoints of the edges and one node at the centre of the face. In addition to the nodes on the faces, there is a single node in the interior of the element. This type of element is referred to as Lagrangian because it possesses nodes that do not lie at either corners or edges. The Lagrangian type of element was particularly useful for these models because it shows little reduction in accuracy due to angular distortion (Lee & Bathe, 1993), a problem in both models due to their geometry.

After each of the blocks was defined, they were automatically discretised by stating the number of subdivisions into which each block was to be divided along three of its edges. Each subdivision was then filled with the brick elements. Using this method, all the nodes within the unit cells, in addition to the 107 points for the spherical model or the 158 points for the cylindrical model, were defined. Both model geometries were analysed for three different levels of refinement: 1-1-1, 2-2-2 and 3-3-3, where each number in the refinement refers to the number of subdivisions along each edge of a block (see Fig. 3.16). With each increase in the level of refinement, the number of equations that need to be solved to obtain results increases significantly. Table 3.1 shows the number of elements, nodes and degrees of freedom for each refinement of both models. After validation of the model (see Section 4.1), the 3-3-3 refinement was used since its solutions were considered the most accurate and the time for solution not excessive.

The discretisation data for both the phase shape IPC models was created in two text files through the use of C++ programs. These programs are provided in Appendices D and E for the spherical and cylindrical models, respectively. Both programs contain the placement of initial nodes, complex lines and location of vertices for the mapped division of the basic geometry, as well as the necessary commands for further subdivision and element generation. The programs also contain the constituent material information described in the next section.

(a) Refinements for Spherical models

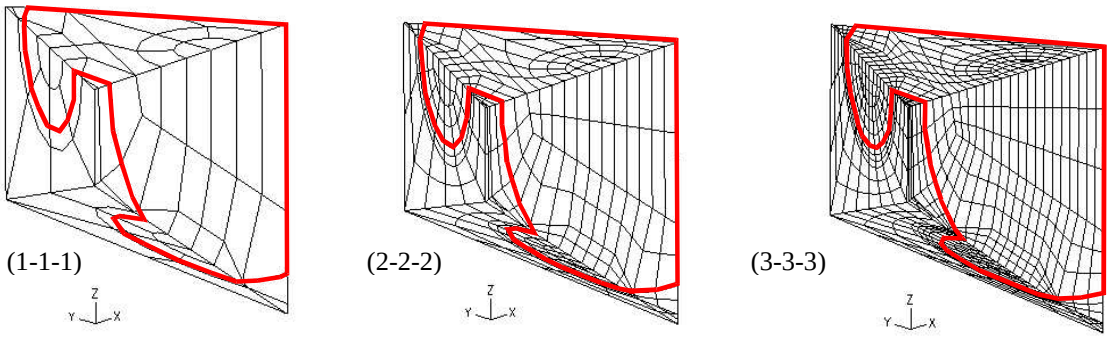

(b) Refinements for Cylindrical models

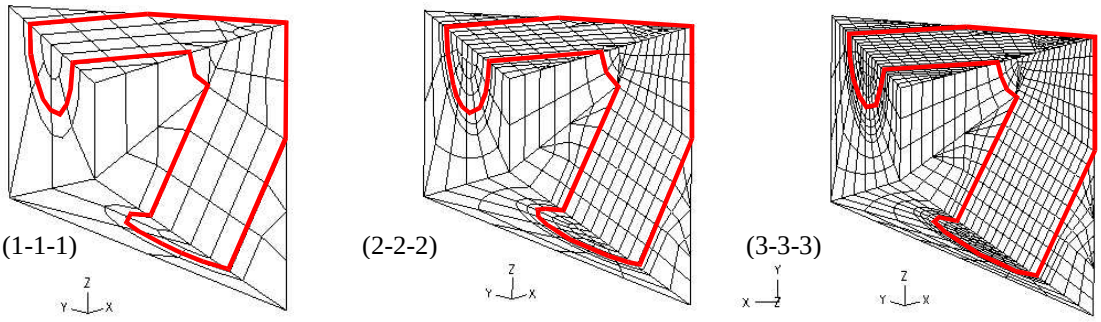

Figure 3.16. The three levels of refinement for both models

- Sphere volume fraction = 85%
- Cylinder volume fraction = 39%

3.5 CONSTITUENT MATERIALS FOR THE MODELS

As mentioned in Section 1.2, the objective of this research was to determine the effect that phase shape has on the elastic and plastic behaviour of an IPC. To do this, the constituent materials were modelled separately as linear elastic and non-linear plastic. The main focus of both material models was the characterisation of the behaviour through some representative properties. For the elastic behaviour, the effective Young's modulus of the composite was chosen and for the plastic behaviour the effective yield strength was chosen. Both of these properties were studied as the volume fraction of the phases and the phase property ratio (the modular ratio or yield strength ratio) were varied.

3.5.1 Material Properties for the Linear Elastic Analyses

The first step in the analysis of the models was to validate if the results they calculated were accurate. This was done through linear elastic simulations

Table 3.1. Elements, nodes and degrees of freedom in the models

Model	Refinement	Number of Elements	Number of Nodes	Degrees of Freedom
Spherical	1-1-1	62	657	1518
	2-2-2	496	4577	12068
	3-3-3	1674	14737	40578
Cylindrical	1-1-1	98	979	2380
	2-2-2	784	7013	18960
	3-3-3	2646	22807	63852

of a uniaxial tension test on all three refinements of both models (the refinements were described previously) and compared to the Hashin-Shtrikman bounds described in Section 2.2.1. The phases in the elastic models were assumed to be isotropic and have only small displacements during deformation. With these assumptions, only the Young's modulus and Poisson's ratios of the constituents were needed.

For the spherical IPC model, the simulations were carried out with a specific set of constituent material properties. The specific properties were taken from Wegner (1997), who used the same spherical model as used in this research to better understand the behaviour of several experimental IPC's. Wegner's material properties were set so that the sphere material was a 420 stainless steel and the surrounding material a bronze:

E_s = 210 GPa $\qquad$ E_{sur} = 110 GPa

ν_s = 0.29 $\qquad$ ν_{sur} = 0.33

By validating the results of the spherical model used in this research with the model from Wegner's research, it is also indirectly validating this model with his experiments. Since this study is only interested in the relative effect phase shape has on the behaviour of IPCs, it is not necessary to have experimental verification; however, this does provide an extra level of certainty about the model results.

To the author's knowledge, no experimental work such as that of Wegner (1997) for the spherical model can be used for comparison with the cylindrical

model. However, as mentioned, such experimental verification is not necessary for the purposes of this study. For the cylindrical IPC model validation, the ratio of the Young's moduli of the two constituent materials was set equal to two and the Poisson's ratios were held constant:

$E_c = 200$ GPa $\qquad E_{sur} = 100$ GPa

$\nu_c = 0.3 \qquad \nu_{sur} = 0.3$

After the models were validated, numerical experiments were simulated in uniaxial tension to determine the effect of phase shape on the effective Young's modulus of the IPC. For both models, three series of tests were analysed, each series consisting of a different modular ratio of the phases. The stiffer phase was either the sphere or cylinder, depending on the model considered, and had a Young's modulus kept at a constant value of 200 GPa. The more flexible phase was always the surrounding material and, depending upon the series, it had a Young's modulus of 100 GPa, 20 GPa or 2 GPa. This variation allowed modular ratios of 2, 10 and 100 to be studied. The Poisson's ratio for each phase was held equal to 0.3 for all analyses. Within each of the three test series, the volume fraction of the phases changed. The spherical model was tested at volume fractions of the sphere phase of 75%, 80%, 85%, 90% and 95%. The cylindrical model, with its much wider range of applicable IPC geometry, was tested at volume fractions of the cylinder phase of 2%, 16%, 39%, 64% and 84%. The results presented in Section 4.2 therefore describe IPC elastic behaviour for both the spherical and cylindrical models at different phase property ratios over the entire volume fraction ranges of each model.

As noted at the end of Section 3.4, the elastic constituent material information was input into both models through part of the C++ programs in Appendices D and E. The commands necessary to create linear elastic models are shown in Step 7 of the spherical discretisation program. More information on the formulation of the linear elastic FEM can be found in Bathe (1996).

3.5.2 Material Properties for the Non-linear Plastic Analyses

The same spherical and cylindrical models used for the linear elastic analyses were used for the non-linear plastic analyses, so further validation was considered unnecessary. The focus for the non-linear analyses was on determining the effect phase shape had on the effective yield strength of the IPC. In this case, two different series of tests were run at yield strength ratios for the constituents of 2 and 10. The surrounding material's yield strength was always that of the weaker phase, having a constant value of 110 MPa, and the stronger sphere and cylinder phases were given yield strengths of 220 MPa and 1100 MPa for each of the yield strength ratio series, respectively.

For the plastic model, it was assumed that the constituents were isotropic, showed kinematic non-linearity and their deformation behaviour could be approximated as bi-linear. Kinematic non-linearity assumes that large displacements and strains are likely to occur as the models begin to behave plastically. To assume a bi-linear stress-strain path, constituent properties other than the yield strength were needed. These included the Young's modulus, Poisson's ratio, strain hardening modulus (the slope of the stress-strain behaviour after yielding), and maximum allowable effective plastic strain. For both models, all these properties were held constant for all analyses. The Young's modulus of the surrounding phase was set at 100 GPa and that for the sphere or cylinder phase set at 200 GPa. It was considered to be reasonable that the phase with the greater strength would also have a greater stiffness, so a small difference in Young's modulus was introduced. The Poisson's ratios, strain hardening moduli and maximum allowable effective plastic strains for both phases were set equal to 0.3, 0.001, and 0.2, respectively. In each of the two yield strength ratio series, the five different volume fractions listed for each model in Section 3.5.1 were considered again for the plastic analyses.

Data for the non-linear plastic IPC models was created for the models using the commands in Step 7 of Appendix E for the cylindrical model. These commands could also be added to the program in Appendix D for the spherical

model. Further information about the formulation of non-linear analyses using the FEM can be found in Bathe (1996).

3.6 IMPLEMENTATION OF THE MODELS

To determine the effective material properties and deformation behaviour of the model IPCs, solutions were found using the commercial FEM software application ADINA, version 8.0 (ADINA R&D Inc., 2002a). As mentioned in Section 3.3, a simple uniform displacement was applied to the top surface of each model to simulate a uniaxial tension test. ADINA was used to predict the model response to this simulation, from which solutions for the effective Young's modulus and yield strength could be established. The results of these solutions are provided in Chapter 4. In this section, the procedure for completing a simulation and finding the solutions is described.

Simulation of a uniaxial tension test was carried out by applying a displacement in the z-direction to the node in the top-left-back corner. Since all other nodes on the top surface were constrained to this master node, a uniform vertical displacement across the entire surface was created (see Section 3.3 for more details about the application of this boundary condition). For the linear elastic analyses, the actual displacement used was not important, so to simplify later calculations, a uniform strain of 0.001 was chosen. In the non-linear plastic analyses, strain incrementally increased to a maximum of 0.005 or until ADINA was unable to converge towards a solution.

With the desired strain known, the appropriate displacement for use by ADINA was determined by multiplication of that strain with the distance between the top surface and the hinge point (see Section 3.3 for discussion of this boundary condition). The hinge point is fully fixed such that it is the only point in the model that is not displaced during the simulation. This makes it a desirable reference point for determining the displacement of all other points within the models, including the nodes on the top surface. For the simulations with elastic conditions, the required uniaxial tensile displacement was therefore given by

$$\delta_a = \varepsilon_a \cdot l_o , \tag{3.15}$$

where δ_a is the displacement in the z-direction to be applied to the master node on the top surface, ε_a is the desired applied strain to the master node on the top surface and l_o is half the height of the prism unit cell.

ADINA offers both direct and iterative solution methods. Based on information provided by ADINA R&D, Inc. (2002b), a direct solution method was used for the linear elastic analyses. All direct solution methods are based on the process of Gauss elimination, in which the set of simultaneous equations defining the problem are dealt with all at once. This requires significant amounts of memory for storage. To reduce the memory requirement, a sparse matrix solver was used. According to Bathe (1996), sparse solvers reduce memory requirements and the time to solution by removing operations on matrix elements that remain zero throughout the solution procedure. This is particularly relevant for large three-dimensional problems like those found with these spherical and cylindrical phase shape models.

For the plastic analyses, two nested iterative solution methods were used to solve for the IPCs' stress-strain behaviour. Since the behaviour was non-linear, it was necessary to assume that each succeeding point along the stress-strain curve had the properties of the previous point. By making this assumption, a system of simultaneous equations was created that could be solved by an iterative procedure known as the incomplete Cholesky conjugate gradient method. This provided a definition of the succeeding point, but due to the assumption of the properties of the previous point it was likely inaccurate. A correction was now completed so that a more accurate set of simultaneous equations was created, which again were solved using the incomplete Cholesky conjugate gradient method. The iterative process of solutions and corrections is referred to as the full Newton method, and it was continued until it reached an accurate solution for the succeeding point along the IPC's stress-strain curve. The non-linear plastic analyses therefore required the definition of a series of displacement increments. These increments used for this study are given in

Section 4.3.1. More information on this solution method and other iterative solution methods may be found in ADINA R&D, Inc. (2002b) and Bathe (1996).

After the models had been solved, the effective Young's modulus and yield strength of the IPC's could be determined. The first step in obtaining the effective Young's modulus was to find the reaction force on the top surface required to produce the applied displacement. Since all the nodes on the top surface were slaved to the master node in the top-left-back corner, its reaction was also the total reaction of the top surface. The applied stress was then established by dividing this reaction force by the area of the top surface,

$$\sigma_a = \frac{F_a}{A_{top}}, \tag{3.16}$$

where σ_a is the normal stress on the top surface, F_a is the reaction force at the master node due to the applied displacement, and A_{top} is the area of the top surface. The effective Young's modulus was then simply determined through the use of Hooke's law for uniaxial conditions,

$$E_{eff} = \frac{\sigma_a}{\varepsilon_a}, \tag{3.17}$$

where E_{eff} is the effective Young's modulus for the IPC and ε_a is the known applied strain.

The effective yield strength of both IPC models was obtained using the standard experimental criterion, which is the stress at a strain offset of 0.002. The effective yield strength was determined for each model through linear double interpolation of the stress-strain plot of the IPC's deformation behaviour with the offset line (a line parallel to the effective Young's modulus with its origin at the strain offset). In some cases, the models' simulations failed prior to reaching their offset yield strength due to the inability of ADINA's iterative solver to converge to a solution. It could not be definitively determined if these convergence failures were due to mathematical difficulties from the distortion of elements or the failure of the materials. The possible causes for the failures are

discussed in greater detail in Section 4.3. In these premature failure situations, the maximum stress that was reached was used in place of the yield strength, though it should be noted that significant error may exist as a result.

CHAPTER FOUR

NUMERICAL MODELLING RESULTS

The numerical models described in the previous chapter provided a method for determining the influence of phase shape on the mechanical behaviour of interpenetrating phase composites (IPCs). Prior to using the data generated by these models, it was first necessary to validate that they provided an accurate solution to the theoretical model and that they had comparable results to other sources from the literature. Several procedures were used for validation and are discussed in Section 4.1.

After the models' responses were validated, an examination of the linear elastic behaviour of IPCs was conducted; this is described in Section 4.2. This study was separated into two distinct subsections. The first subsection focussed on the macroscopic behaviour of the models, specifically considering the dependence of the effective Young's modulus on the elastic modular ratio, the volume fractions of the phases, and the phase shape. In the second subsection, the mechanisms within the microstructure that produced the macroscopic behaviour were analysed.

A similar procedure was followed for the study of the non-linear plastic behaviour of IPCs, described in Section 4.3. The first part of this study again considered the models' macroscopic behaviour; in this case, it was the effective yield strength of the IPCs that was of interest. The second part then sought explanation of the observed behaviours based on the mechanisms acting within the microstructure. The discussion of results in Sections 4.2 and 4.3 forms the basis for the conclusions presented in the next chapter regarding the effect of microstructural phase shape on the behaviour of IPCs.

4.1 VALIDATION OF NUMERICAL MODELS

4.1.1 Geometry and Boundary Condition Validation

An initial step after the completion of each model was a basic review of its geometry and boundary conditions to ensure that they were correct. This is a simple but often overlooked step in finite element analysis, and when not completed can lead to poor results due to misrepresentation of the IPCs. The intended geometry for both the spherical and cylindrical hexagonal close-packed (HCP) models was checked quickly by examining graphical outputs provided by the program ADINA (ADINA R&D, Inc., 2002a). Both models at each of their volume fractions were plotted so that all external surface nodes could be visually inspected and their correct positioning confirmed. Internal nodes along the interface between the two phases were also checked by making separate plots of each phase.

The boundary conditions were checked by examining the displaced geometry after solving the model simulations for the linear elastic case. It is important to note that the boundary conditions for both elastic and plastic simulations were the same, so the models were only examined from the elastic simulations. To ensure that results were as expected, nodes were chosen from each surface and edge such that each condition or combination of conditions could be tested. The independent degree of freedom displacements for each chosen node were then used to calculate the dependent degree of freedom displacements. Where discrepancies existed between the calculated behaviour and that which was expected, revisions to the boundary conditions were made until the model behaved properly. It is important to emphasize that this was not an attempt to manipulate the global results and implicitly control the macroscopic behaviour. Changes were always based on ensuring the correct behaviour of single nodes, not on the overall behaviour.

4.1.2 Discretisation Validation

The essential step in providing sufficient accuracy with the finite element method (FEM) is deciding the level of refinement for the discretised model. Two separate methods were used to examine three different refinements of both models so that the correct refinement level could be determined (the three refinements were previously discussed in Section 3.4). The first method considered the global or macroscopic behaviour of the models and the second method their local or microscopic behaviour. Both of these methods were applied to solutions under only linear elastic conditions. It was assumed that the best level of refinement for elastic conditions would also be the best refinement for plastic conditions.

In the validation method based on global behaviour, the effective Young's modulus was determined for both models at each of its volume fractions and for all three refinement levels. This method is based on the fact that increasing the level of refinement should increase the accuracy of the global result so that convergence to the exact solution should occur. This convergence is shown with example solutions for the spherical model and cylindrical model in Figures 4.1 (a) and (b), respectively. The improvement in accuracy for these examples is evidenced by the reduction in the effective Young's modulus with the increase in the number of nodes. The percentage decrease between each level of refinement is provided in Table 4.1. Using either the figures or the table, it can be observed that there is only a small

Table 4.1. Convergence of effective Young's modulus with increasing refinement

Model	Refinement	Effective Young's Modulus [GPa]	Difference [%]
Spherical (ϕ = 85%)	1-1-1	191.250	n/a
	2-2-2	191.229	0.0112
	3-3-3	191.225	0.0021
Cylindrical (ϕ = 39%)	1-1-1	132.285	n/a
	2-2-2	132.202	0.0624
	3-3-3	132.198	0.0035

improvement between the 1-1-1 refinement and the 2-2-2 refinement, and an even more minuscule change between the 2-2-2 and 3-3-3 refinements. While results are shown only for two examples, similar results were obtained for both models at each volume fraction (see Appendix F). This suggests that any of the refinements are sufficient for the determination of the macroscopic behaviour, though slight improvements in accuracy are possible at each additional

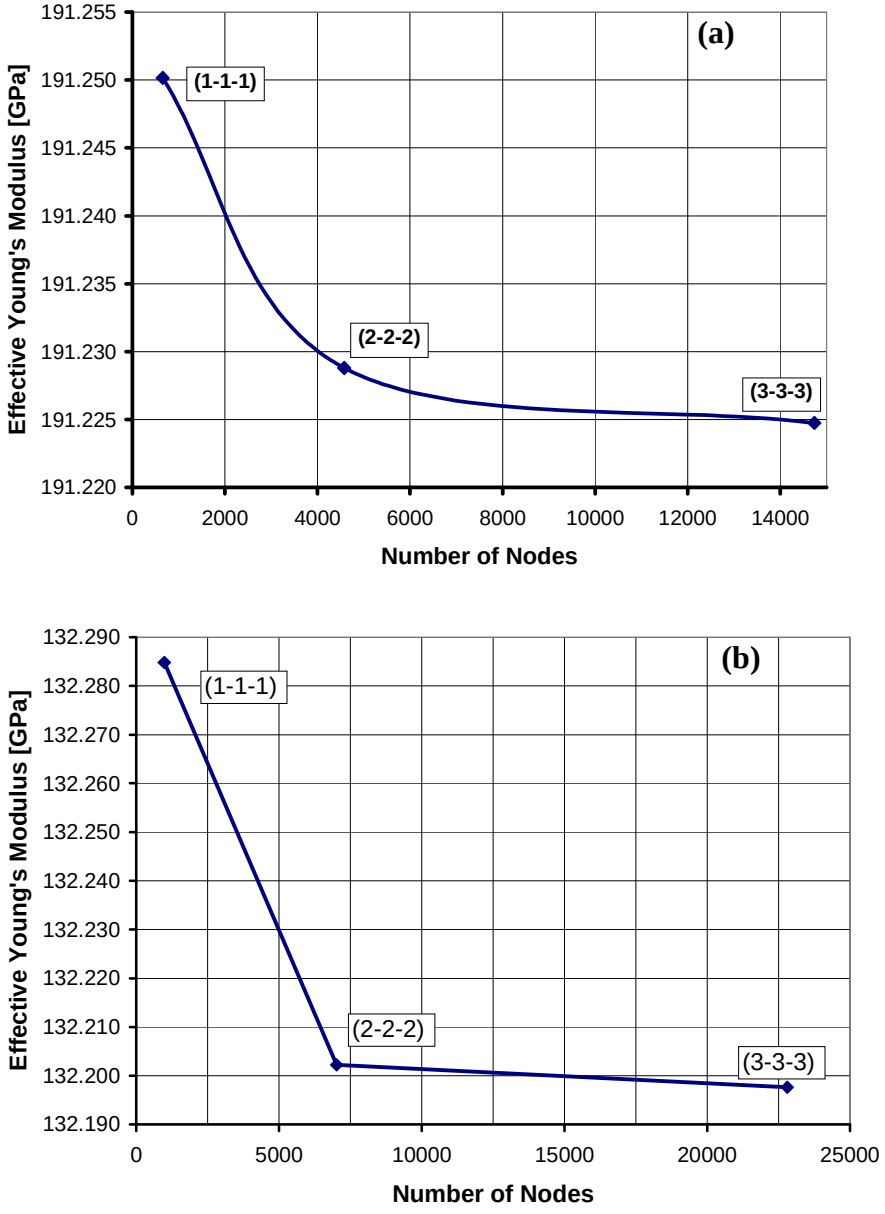

Figure 4.1. Convergence of effective Young's modulus with increasing levels of refinement:
(a) spherical model at a volume fraction of 85% and
(b) cylindrical model at a volume fraction of 39%

refinement level.

The second method of discretisation validation was through a consideration of the local behaviour within the models. This method involved examination of the effective stress distribution in the models provided by plots from ADINA. The purpose of these examinations was to identify the existence of discontinuities along element boundaries that suggest local errors in the FEM calculations. The effective stress distribution was chosen as the field variable for study based on its importance to the microstructural study in Section 4.3.

Example cases for both models are presented in Figure 4.2, showing the effective stress contour plot for the 1-1-1 refinement level. The stiffer and more flexible phases for each model can be clearly seen due to the large stress discontinuity at the phase interface. This discontinuity is expected since the constituent materials of the phases have different stiffness values, and since strain compatibility is ensured across the interface, the stress distributions should differ. Such effective stress discontinuities should not, however, exist within each separate phase where material properties are uniform.

Examples are shown in Figure 4.3 of discontinuities in the more flexible phase for each model at the 1-1-1 refinement level. These discontinuities exist due to an insufficient number of calculation points to adequately solve for the stress distribution in the local regions. The change in the stress distribution associated with increasing levels of refinement is considered by examining only the regions within the highlighted squares. As shown in Figure 4.4, the stress distribution becomes smoother and more continuous across element boundaries as the number of degrees of freedom in these regions increases due to refinement. This improvement has a beneficial effect on the global response of the model leading to slightly more accurate behaviour with each refinement level. This was shown by the convergence of the effective Young's modulus in the previous method. The improvement at the local level is more pronounced, as significant shifts in the region's stress distribution are observed with increasing levels of refinement.

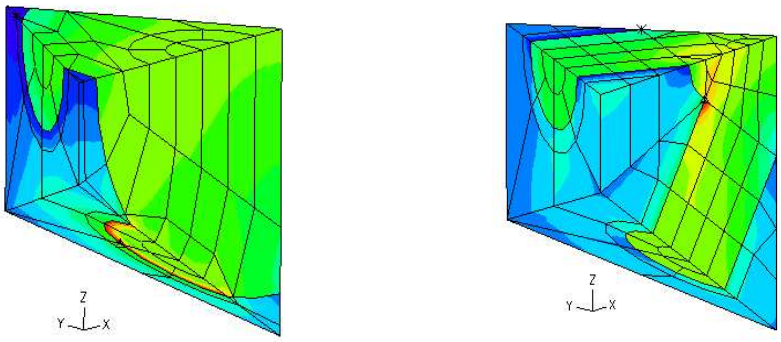

Figure 4.2. Effective stress distributions at the 1-1-1 refinement level:
(a) spherical model at ϕ = 85% and
(b) cylindrical model at ϕ = 39%

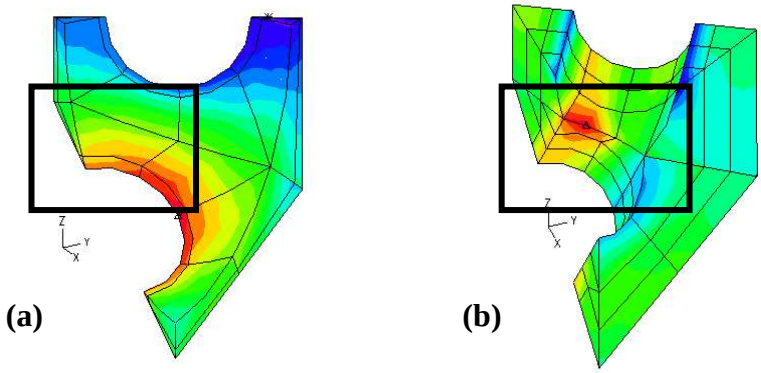

Figure 4.3. Effective stress distributions in the more flexible phase at the 1-1-1 refinement level:
(a) spherical model at ϕ = 85% and
(b) cylindrical model at ϕ = 39%

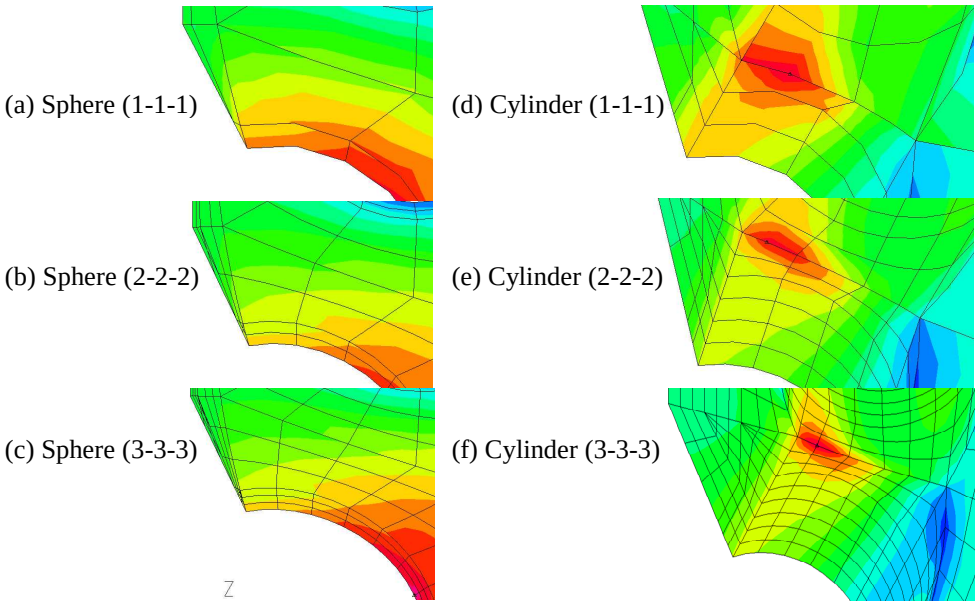

Figure 4.4. Increasing accuracy of effective stress distribution with increasing refinement

After consideration of both validation methods, the 3-3-3 refinement level for both models' discretisation was used in all further analyses. The global method determined that any of the three refinements would produce essentially the same level of accuracy for macroscopic values such as the effective Young's modulus. However, the local method showed significant improvement with the use of higher refinement levels in the microscopic representation for both models. In the second part of Section 4.2 and Section 4.3, a microstructural analysis requires good local accuracy, making the higher levels of refinement more desirable. Finally, simulation at increasing levels of refinement produced only a slight increase in the time to solution, making the 3-3-3 refinement the preferred choice.

4.1.3 Comparison of Results to Literature

Validation of the geometry and boundary conditions was based on a qualitative inspection of model behaviour that may allow mistakes to sneak through if insufficient care is taken. Even if this validation was successful, it still did not ensure that the results were a good representation of any real material. The discretisation validation improves the accuracy of the results but has no effect on certifying that the results are not accurate around an incorrect answer. To solve these problems, a comparison can be made to research that was previously reviewed in the second chapter.

A check for the validation of the geometry and boundary conditions of the models may be made by comparison of the results to the Hashin-Shtrikman bounds. These bounds, reviewed previously in Section 2.2.1, describe the range of possible elastic behaviour for any isotropic composite material. Since it was stated in Section 1.2 that both the spherical and cylindrical models are isotropic due to the use of the HCP system, they should both produce results that lie within the Hashin-Shtrikman bounds. Using the Equations 2.9 – 2.13, the Hashin-Shtrikman bounds on the effective Young's modulus may be computed.

Figure 4.5 shows a comparison of the Hashin-Shtrikman bounds with the data from both models. In this comparison, an elastic modular ratio of 2 was chosen in order that the bounds would be quite restrictive. The volume fractions of the stiffer phase for the spherical model were 75%, 80%, 85%, 90% and 95%, and those for the cylindrical model were 2%, 16%, 39%, 64% and 84%. The important point to note is that despite how tight the bounds are, the results for both models at all volume fractions are within them. This suggests that the models accurately represent an isotropic composite and provides some confidence that the validation of the geometry and boundary conditions was correct.

The final check for accuracy requires the comparison of results to those of an actual IPC. It should be noted that this is not strictly required, since the objective of this study was to determine the general influence of phase shape on IPCs rather than its influence on a specific IPC. However, in the case of the spherical model, an easily comparable case exists in the work of Wegner (1997). Wegner was able to obtain a close comparison of his model results to

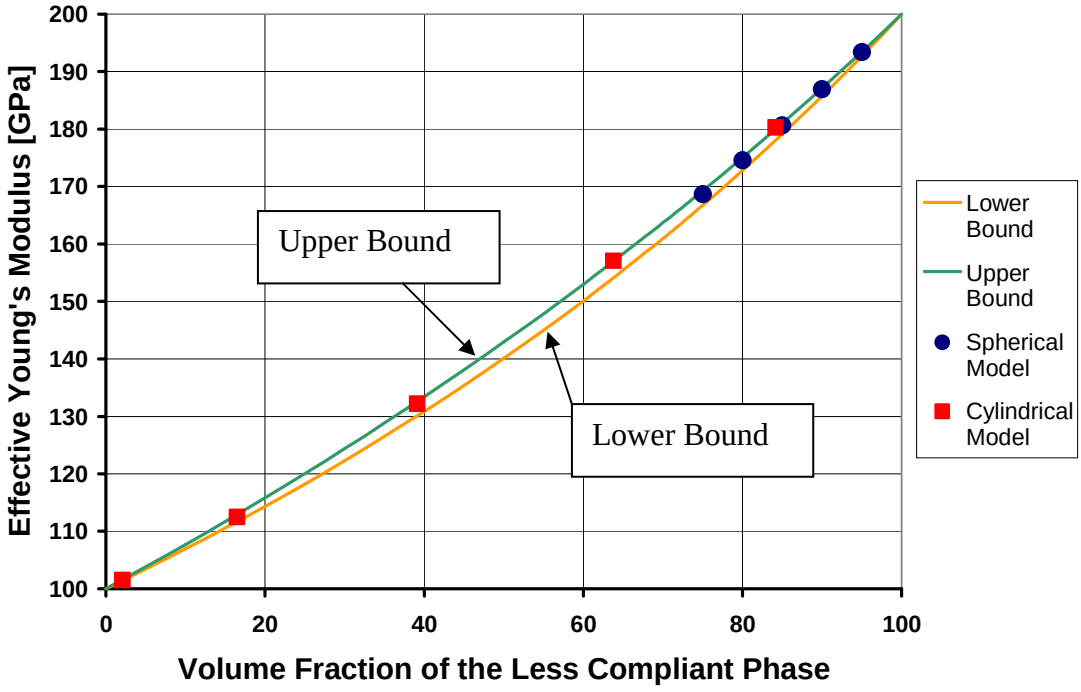

Figure 4.5. Comparison of both models' elastic results to the Hashin-Shtrikman bounds for a modular ratio of 2

Table 4.2. Comparison of the spherical models of this thesis and Wegner (1997)

Volume Fraction [%]	Thesis Model Young's Modulus [GPa]	Wegner's Model Young's Modulus [GPa]	Difference [%]
75	179.562	179.6	0.0210
83.2	189.067	188.9	0.0882
95	203.573	203.6	0.0135

those of an experimental IPC, so a close comparison to Wegner's model also guarantees a close comparison to an actual IPC.

Wegner analysed his spherical HCP model for stiffer phase volume fractions of 75%, 83.2% and 95% with an elastic modular ratio of 1.9. The effective Young's modulus results for the spherical model developed in this thesis for the same volume fractions and elastic modular ratio are shown with Wegner's in Table 4.2. At all three volume fractions, the difference between results is less than a tenth of a percent. This is an insignificant difference, and in the 75% and 95% volume fraction cases, the difference might be smaller, the comparison being limited by the precision in which Wegner listed his results. This provides some assurance that the accuracy of at least the spherical model results is comparable to that of actual IPCs.

4.2 LINEAR ELASTIC BEHAVIOUR OF INTERPENETRATING MICROSTRUCTURES

4.2.1 Macroscopic Behaviour

The initial stress-strain behaviour of the two ductile phase IPC is linear elastic and it is therefore of interest to determine how the interpenetrating microstructure might affect this low strain behaviour. The linear elastic range of behaviour was studied through a determination of the effective Young's modulus of the composite as several variables were changed. These variables included the phase elastic modular ratio and two geometric parameters of the microstructure: the volume fraction and shape of the phases.

A common way to display effective composite properties in relation to microstructural geometry and constituent properties is through a plot like those

shown in Figure 4.6. In both figures, the effective Young's modulus of the composite is plotted against the volume fraction of the stiffer phase. It is important to note that for all model simulations, the stiffer phase was always either the sphere or cylinder portion of each of the unit cells. The surrounding material was always the more flexible phase. Three different elastic modular ratios were considered by reducing the Young's modulus of the more flexible

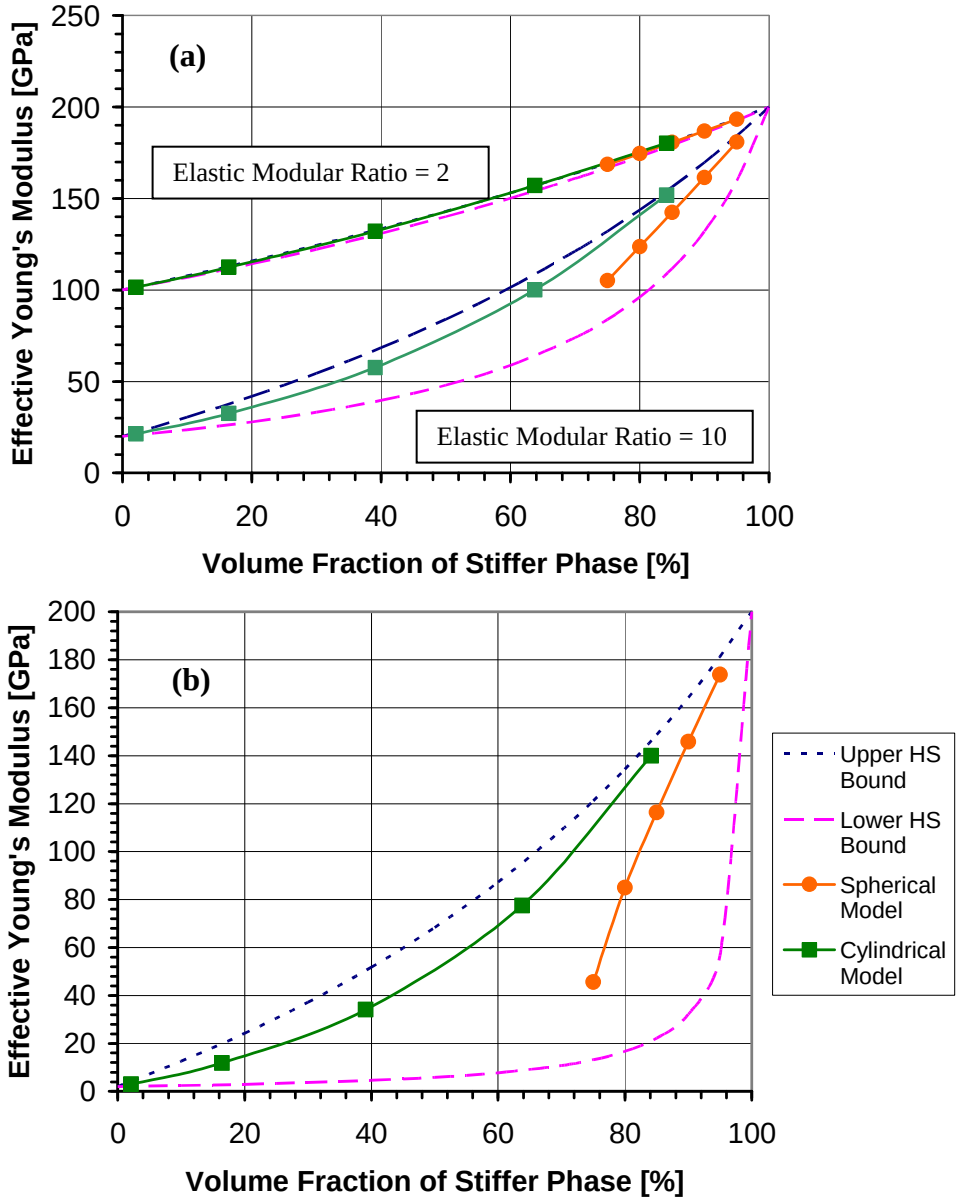

Figure 4.6. Effective Young's modulus versus the volume fraction of the stiffer phase
(a) for elastic modular ratios of 2 and 10, and
(b) for an elastic modular ratio of 100

phase while keeping the Young's modulus of the stiffer phase the same. Figure 4.6 (a) shows results for ratios of 2 and 10 while the results for a ratio of 100 are plotted separately in Figure 4.6 (b) to prevent the graphs from becoming too cluttered. The Hashin-Shtrikman upper and lower bounds are also plotted for each of the elastic modular ratios. As discussed in Section 2.2.1, these bounds provide the range of behaviour for isotropic composites and they were calculated using Equations 2.9 - 2.13. The raw data that was taken from the uniaxial tension simulations used to create Figure 4.6 can be found in Appendix G.

Considering first the influence of volume fraction, it can be seen from Figure 4.6 that the effective Young's modulus of the composite increases with greater amounts of the stiffer phase. This effect is due to the stiffer phase occupying a greater proportion of the composite's microstructure as its volume fraction increases and therefore having a more dominant influence on the overall composite behaviour. This trend occurs for both the spherical and cylindrical unit cells, as well as the upper and lower Hashin-Shtrikman bounds.

Studying each set of bounds more closely reveals that they all diverge through an intermediate volume fraction range and converge at either end of the range. The convergence is necessary since the ends of the volume fraction range denote samples of the pure constituent phases. At 0% volume fraction of stiffer phase, only the more flexible phase exists, and at 100% volume fraction, only the stiffer phase exists. Both bounds therefore converge upon the single property values of the pure phases at the extremes. The maximum divergence of the bounds occurs within the range where there is a majority of the stiffer phase, though the actual maximum value occurs at different points for each elastic modular ratio. Maximum divergence occurs at volume fractions of the stiffer phase of approximately 60%, 75% and 90% for the elastic modular ratios of 2, 10 and 100, respectively.

The properties of the constituent phases have a very noticeable effect on the Young's modulus of the composite. An increase in the elastic modular ratio

shifts the composite behaviour downwards, since there is increasing compliance of the more flexible phase. The Hashin-Shtrikman bounds also differ noticeably with changes in the elastic modular ratio. For a small modular ratio of 2, the bounds are quite restrictive, roughly approximating a linear relationship between the properties of the pure phases. When the modular ratio is increased to a high value of 10, the bounds have substantially diverged and no longer follow this rough linear behaviour between the phase properties (though the lower bound shows a much greater deviation from the straight line). At a modular ratio of 100, where the more flexible phase can be considered almost non-existent, the bounds are exceedingly divergent, with the lower bound offering little restriction on effective behaviour. Since all these bounds provide the range of possible behaviour for an isotropic composite, it can be seen that the elastic modular ratio strongly influences this range; essentially, the higher the elastic modular ratio, the greater the range of potential composite behaviour.

The microstructural shape of the phases also influences the behaviour of IPCs. This influence is imperceptible when the elastic modular ratio is small (e.g. at a value of 2). For low modular ratios, the phases of the composite are similar in terms of stiffness and the bounds on effective behaviour are restrictive. The effective Young's modulus of the composite can be predicted accurately knowing only the volume fraction of the phases by simply observing the values for the Hashin-Shtrikman bounds for a modular ratio of 2 at that volume fraction. Phase shape therefore has a negligible influence on IPCs with low elastic modular ratios.

With higher elastic modular ratios such as 10 or 100, the effect of phase shape becomes much more apparent. When comparing the results for the spherical and cylindrical unit cell models, it is important not to focus on the different volume fraction ranges they were tested on; different ranges were used due to geometric limitations as described in Sections 3.1 and 3.2. Instead, it should be noted that the results do not coincide over their common volume fraction range of 75% to 84%. Phase shape is therefore a geometric parameter

of the microstructure that causes variation of composite behaviour within the Hashin-Shtrikman bounds. It should also be noted that the model with the cylinder phase plots above the model with the sphere phase. Since this means that the cylinder model is able to obtain a greater effective Young's modulus than the sphere model at the same volume fraction, the cylindrical phase shape is more efficient than the spherical phase shape.

To study why the cylindrical shape is more efficient than the spherical shape, it is necessary to consider the topological parameter of contiguity. Contiguity, as described in Section 2.1.2, is the ratio of the surface area of a particle connecting it to pieces of the same phase divided by the total surface area of the particle. Gurland (1958) defined contiguity in the following equation form (it was previously listed as Equation 2.2):

$$C_\alpha = \frac{2S_v^{\alpha\alpha}}{2S_v^{\alpha\alpha} + S_v^{\alpha\beta}}, \tag{4.1}$$

where Gurland defined contiguity such that $S_v^{\alpha\alpha}$ was the surface area between separate particles of the α-phase and $S_v^{\alpha\beta}$ the interfacial surface area between a particle of the α-phase and the β-phase.

This definition can easily be applied to the spherical model, where each individual sphere may be viewed as a separate particle. Considering the spherical half prism unit cell (see Fig. 4.7), $S_v^{\alpha\alpha}$ is the surface area connecting the sphere within the cell to its neighbours, or the surface area shown as the

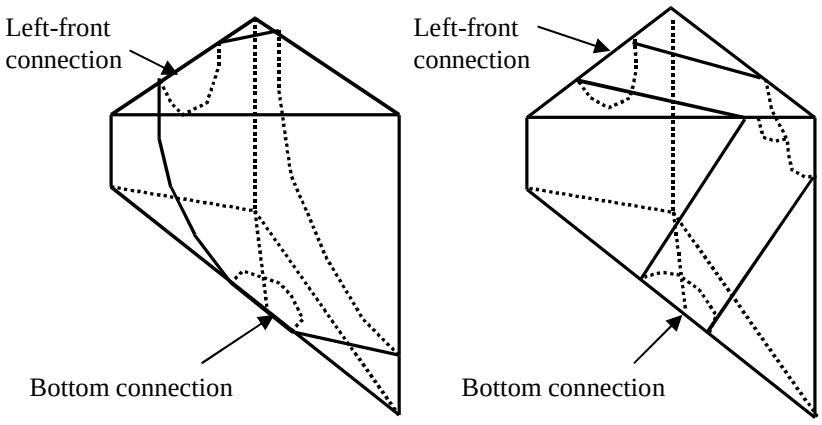

Figure 4.7. Unit cells showing connections to neighbouring particles

semicircles on the bottom and left-front faces. The interfacial surface area between phases ($S_v^{\alpha\beta}$) is then the area between phases interior to the unit cell. If the entire sphere is considered, the amount that is in the half prism unit cell is only one-twelfth of the total. This means that $S_v^{\alpha\alpha}$ and $S_v^{\alpha\beta}$ should be twelve times greater, but since contiguity is the ratio of these values, it would remain unchanged. Contiguity can therefore be determined by considering only the material within the half prism unit cell.

Gurland's definition for the surface areas becomes somewhat more problematic for the cylindrical model, as the proper place to designate individual cylinder particles is not easily determined. Using the same procedure with the cylindrical half prism unit cell as was used with the spherical half prism unit cell should, however, provide a consistent definition. In this case, $S_v^{\alpha\alpha}$ is the semicircular areas connecting cylinders in adjacent unit cells (see Fig. 4.7) and $S_v^{\alpha\beta}$ is again the surface area between the phases interior to the unit cell. The detailed calculations used to determine the contiguities for each model are provided in Appendix H.

The contiguity for both models at each of their different volume fractions can be calculated to produce Figure 4.8. The contiguity of the stiffer phase is plotted against the volume fraction of the stiffer phase. Along with curves for the spherical and cylindrical models, dashed lines have been added to extrapolate the data to the extremes. Figure 4.8 may be used to determine the influence of shape on the relationship between contiguity and volume fraction. First, this influence near the extreme of 100% contiguity indicates that none of the more flexible phase exists, so the volume fraction of the stiffer phase is 100% for both models at this point. When 0% contiguity exists for the cylindrical model, none of the stiffer phase exists so the volume fraction in this case is 0% (detailed reasons for this were discussed in Sec. 3.2). For the spherical model, 0% contiguity marks the lower percolation point where the spheres are no longer in contact. This was calculated in Section 3.1 to be at a volume fraction of 74.05% of the stiffer phase.

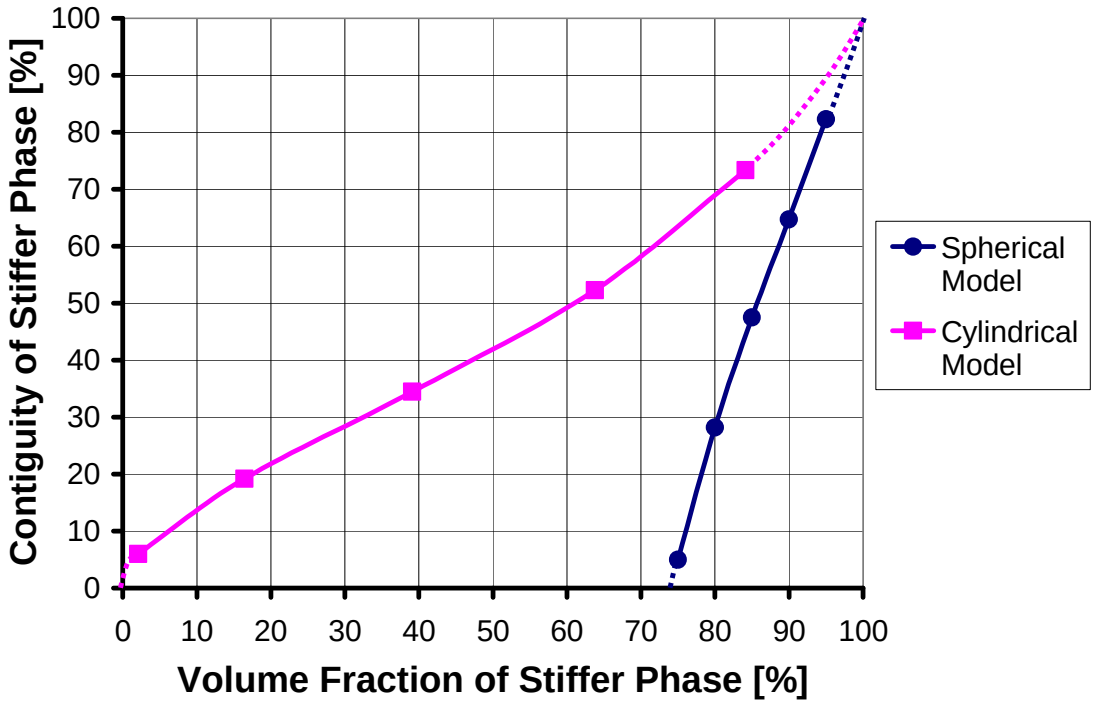

Figure 4.8. Relationship between contiguity and volume fraction

A second influence of phase shape is the curvature of each models' relationship on Figure 4.8. Careful study of each curve shows that near the low end the contiguity grows with volume fraction at a decreasing rate, evidenced by concavity towards the right (this is more obvious with the cylindrical model than the spherical model, but it does exist for both). There is then a region approximating a linear relationship, followed by an increasing contiguity growth rate. The region with an increasing rate of contiguity growth is shown by the concavity at the upper end towards the left.

This behaviour is related to the relative growth rates of the stiffer phase interconnection area ($S_v^{\alpha\alpha}$) and the interfacial surface area ($S_v^{\alpha\beta}$) with volume fraction, which controls the growth of contiguity (see Equation 4.1). In the cylindrical model, where the behaviour is more obvious, $S_v^{\alpha\alpha}$ and $S_v^{\alpha\beta}$ both begin to grow as the radius of the interconnection between adjacent cylinders increases from very small values, but the value $S_v^{\alpha\beta}$ grows more quickly, thus reducing the possible contiguity growth (consider Fig. 4.9(a), (b) and Fig. 4.10). With further increase of the radius of interconnection (between volume fractions

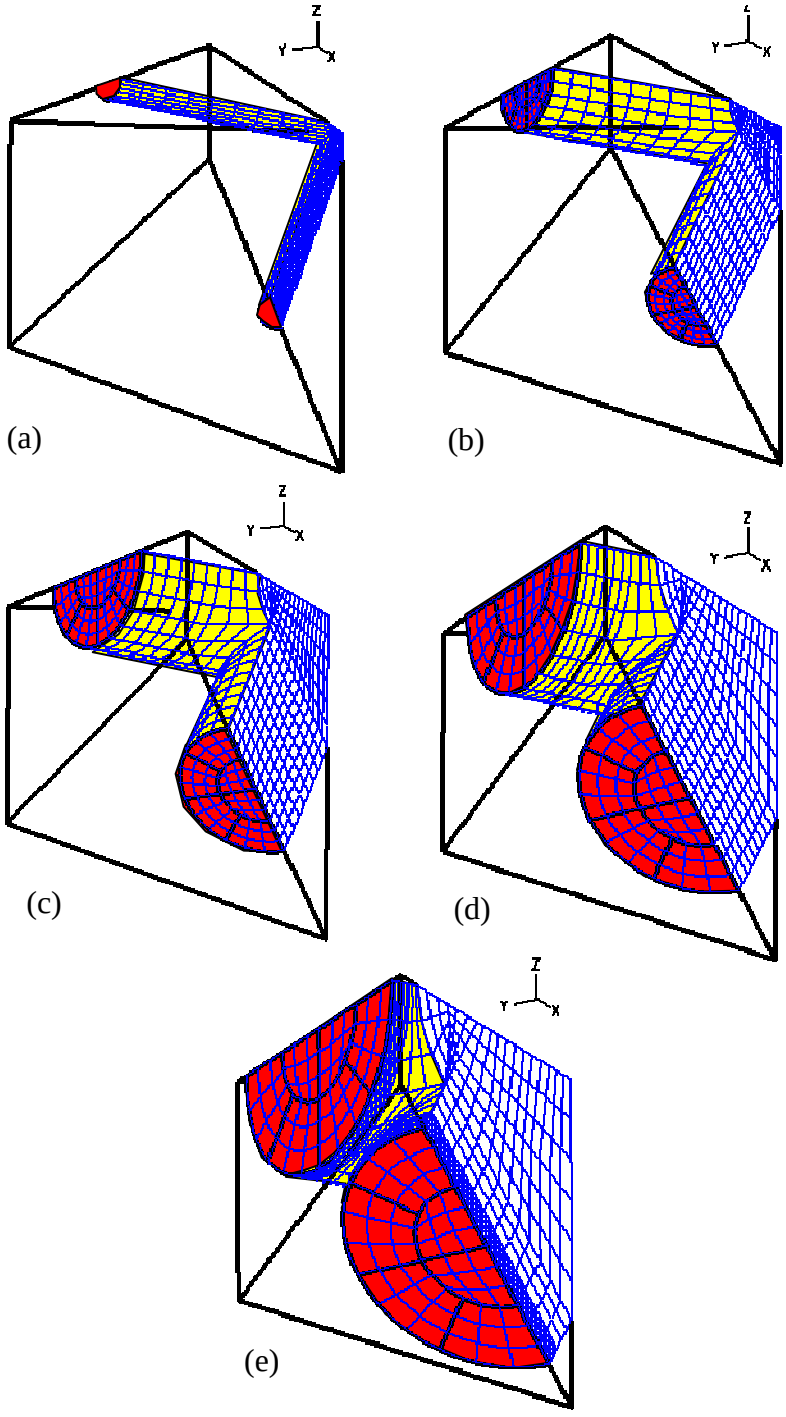

Figure 4.9. Surface areas for the cylindrical model ($S_v^{\alpha\alpha}$ shown as red semicircles and $S_v^{\alpha\beta}$ shown as yellow area internal to cell)

(a) Volume fraction = 2%, contiguity = 6%
(b) Volume fraction = 16%, contiguity = 19%
(c) Volume fraction = 39%, contiguity = 34%
(d) Volume fraction = 64%, contiguity = 52%
(e) Volume fraction = 84%, contiguity = 73%

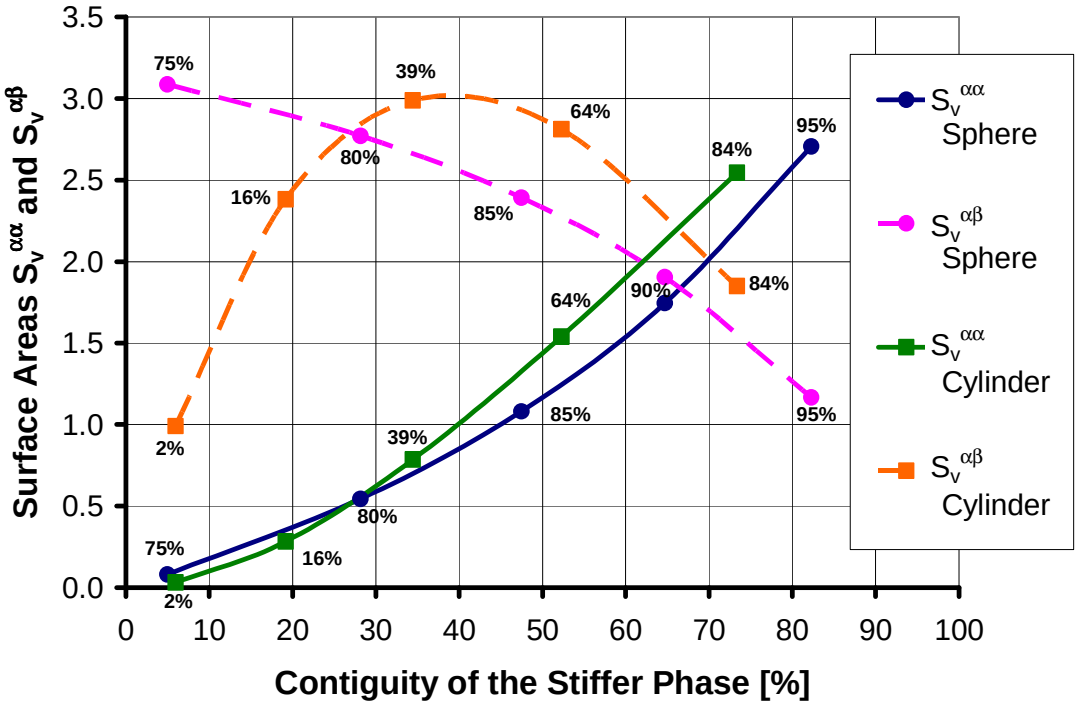

Figure 4.10. Relationship between surface areas and contiguity
- The percentages on the figure indicate the volume fractions of the adjacent data points

of 16% and 64%) the value of $S_v^{\alpha\alpha}$ continues to grow and $S_v^{\alpha\beta}$ shows slowly increasing and then slowly decreasing growth (Fig. 4.9(b), (c), (d) and Fig. 4.10). The changing behaviour of $S_v^{\alpha\beta}$ is due to limitations enforced by the unit cell boundaries and the intersection of the cylinders, resulting in a flattening of its curve. Thus contiguity growth follows the nearly linear behaviour of $S_v^{\alpha\alpha}$ in this region. Finally, at higher volume fractions, while $S_v^{\alpha\alpha}$ grows at a more rapid pace, $S_v^{\alpha\beta}$ becomes increasingly limited such that it rapidly decreases in value, leading to the upper zone of Figure 4.8 where both these surface area parameters contribute to an increasing growth rate for contiguity.

In the spherical model, $S_v^{\alpha\alpha}$ shows nearly identical behaviour to that of the cylindrical model, but the $S_v^{\alpha\beta}$ curve differs since it has only a decreasing behaviour (see Fig. 4.10 and Fig. 4.11). The nature of the contiguity – volume fraction curves (Fig. 4.8) is, however, very similar for both models. This is due to the initial slow increase of $S_v^{\alpha\alpha}$ and slow decrease of $S_v^{\alpha\beta}$, becoming a rapid increase and decrease, respectively, as volume fraction increases. This

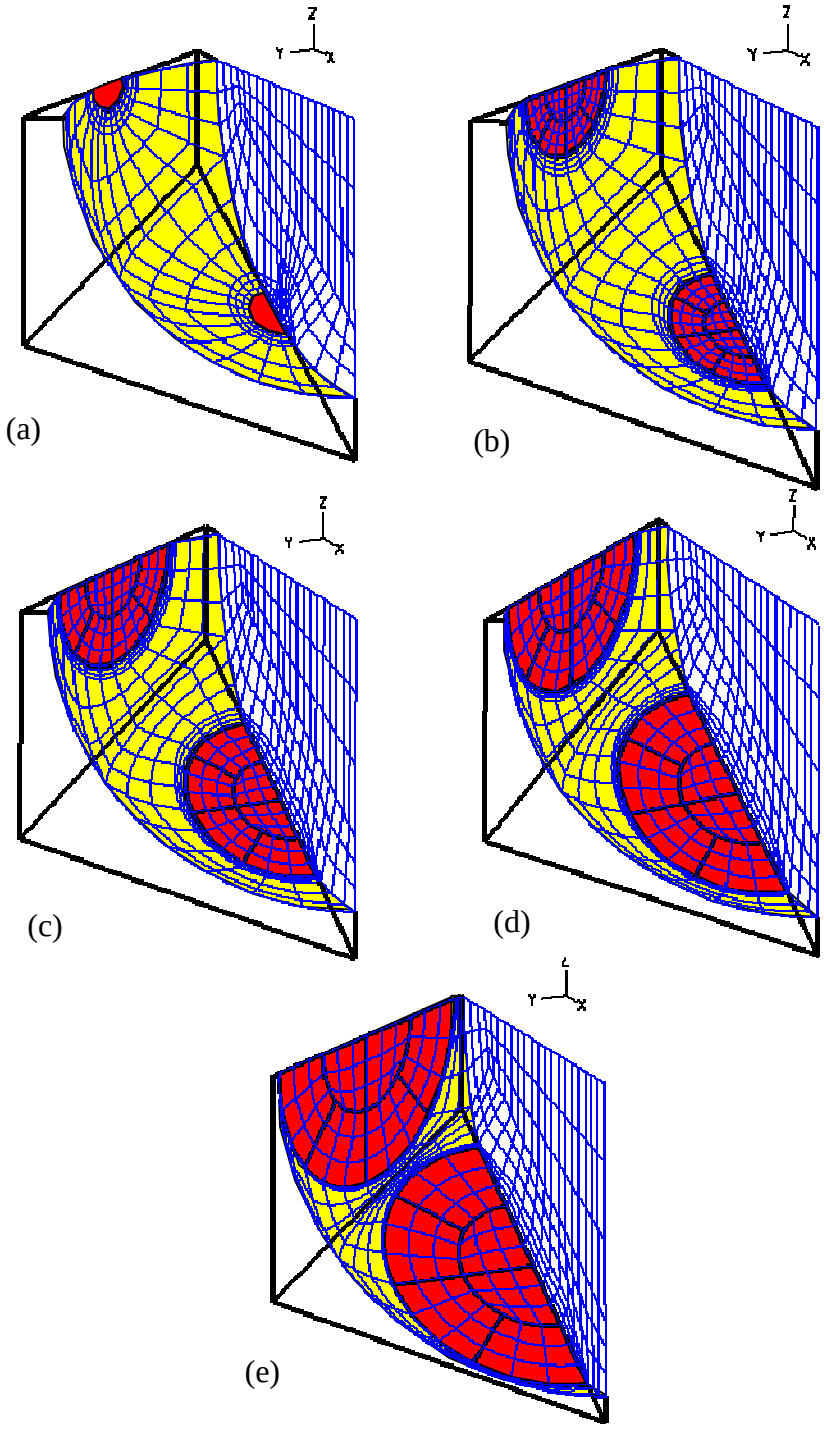

Figure 4.11. Surface areas for the spherical model ($S_v^{\alpha\alpha}$ shown as red semicircles and $S_v^{\alpha\beta}$ shown as yellow area internal to cell)

(a) Volume fraction = 75%, contiguity = 5%
(b) Volume fraction = 80%, contiguity = 28%
(c) Volume fraction = 85%, contiguity = 47%
(d) Volume fraction = 90%, contiguity = 65%
(e) Volume fraction = 95%, contiguity = 82%

changing behaviour again results from the limitations set by the boundaries of the unit cell, and produces contiguity growth that increases with volume fraction

The third point of interest from Figure 4.8 is that the curve for the cylindrical model always lies above the curve for the spherical model, indicating that it is more efficient at creating contiguity since less volume fraction of the stiffer phase is always needed. This efficiency difference is greatest at the percolation point of the spherical model (the volume fraction equals 74.05%) where the curves have the greatest vertical difference. As volume fraction increases above the spherical model's percolation point, its contiguity grows much more rapidly than that of the cylindrical model. As an example, at the volume fraction of 75% the contiguities of the spherical and cylindrical models differ by approximately 0.59, while at a volume fraction of 90% they differ by only about 0.18. This is a reduction in contiguity difference of 0.41 over a volume fraction change of only 0.15.

The discussion of the contiguity – volume fraction relationship should be kept in mind as the influence of contiguity on the effective Young's moduli of the models is studied using Figure 4.12. Only the results for an elastic modular ratio of 10 are shown, since it was thought to be a reasonable intermediate case between the ratios of 2 and 100, and the general trends were similar for these other two cases. The spherical model plots above the cylindrical model and labels indicating the volume fraction of the stiffer phase have been placed beside each of the calculated data points. Also plotted are dashed lines indicating the extrapolated behaviour for contiguity near 0% and 100%. An examination of the behaviour near the extremes shows results that could be predicted from the previous discussion. A contiguity of 100% again indicates that none of the more flexible phase exists, so the effective Young's modulus corresponds to that of the stiffer phase. Contiguity of 0% for the cylinder indicates that none of the stiffer phase exists and the effective Young's modulus becomes that of the more flexible phase, and contiguity of 0% for the spherical model again notes the lower percolation point where the spheres are no longer in contact.

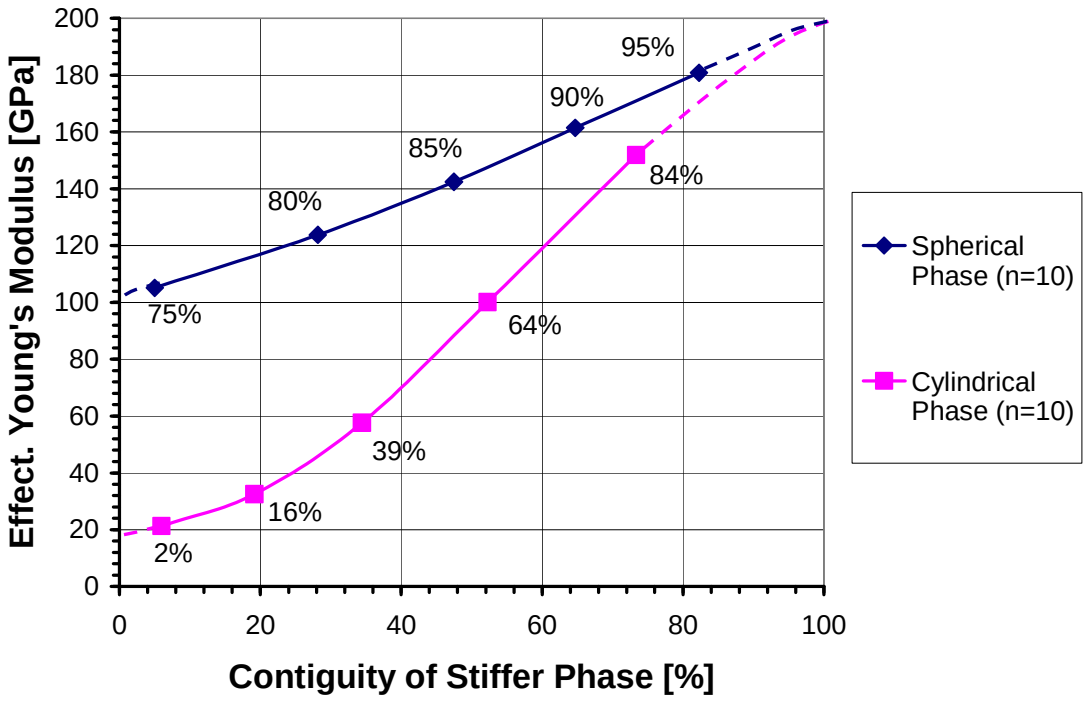

Figure 4.12. Effective Young's modulus versus contiguity of the stiffer phase
The percentages on the figure indicate the volume fractions of the adjacent data points

From the graph in Figure 4.12, a few more observations about the effect of phase shape on IPCs can be made. First, it is interesting to note that despite tremendously different amounts of the stiffer phase, the 75% volume fraction sphere model has a nearly identical contiguity to the 2% volume fraction cylinder model (the contiguities for these sphere and cylinder models are approximately 5% and 6%, respectively). The fact that the effective Young's moduli for these two models are so different shows that contiguity is not the only geometric parameter of the microstructure that affects composite elastic behaviour; otherwise they should be equal. Second, as in Figure 4.8 the greatest difference between each of the models' curves is at the percolation point of the sphere model. Above this point, the results for the spherical model rapidly converge towards those of the cylindrical model. This point is considered in more detail in the following discussion.

To properly understand what Figure 4.12 reveals about the influence of phase shape on contiguity for macroscopic elastic behaviour, a value for the

effective Young's modulus needs to be examined. As an example, consider 105 GPa, which corresponds to the sphere model at the 75% volume fraction and the cylinder model at the 66% volume fraction. The contiguities for these sphere and cylinder models are 5% and 54%, respectively. To achieve a similar effective Young's modulus by using the cylinder phase shape in place of the sphere phase shape, a 9% reduction in the necessary volume fraction of the stiffer phase is possible due to the 49% increase in the contiguity. Essentially, the cylinder shape provides a more advantageous positioning of the stiffer phase than the sphere shape (this was determined previously using Fig. 4.8). This allows the stiffer phase a greater area for interconnection through which stress can be directly transferred. The greater efficiency in stress transfer possible with the cylinder shape therefore allows a reduction in the required amount of stiffer phase to reach the same effective Young's modulus as the sphere shape.

Table 4.3 lists further comparisons of the volume fraction and contiguity for each model as the effective Young's modulus increases. It can be seen that the amount that the volume fraction of stiffer phase can be reduced when using the cylinder instead of the sphere shape decreases as the model results converge at higher volume fractions. Simultaneously, the difference in contiguity between the two shapes also decreases.

From the previous discussions in this section, it should now be apparent that phase shape influences the elastic properties of an IPC through both volume fraction and contiguity, and that the effect of these parameters is

Table 4.3. Comparison of the effective Young's modulus to the topological parameters

Effective Young's Modulus [GPa]	Vol. Frac. of Spheres [%]	Vol. Frac. of Cylinders [%]	Difference between Vol. Frac.	Contiguity of Spheres [%]	Contiguity of Cylinders [%]	Difference between Contiguity
105	75	65.70	-9.30	5	54.27	49.27
124	80	73.17	-6.83	28	62.00	34.00
142	85	80.24	-4.76	47	69.32	22.32

coupled. Despite the coupled nature of these parameters' influence, it is obvious that they affect the effective Young's modulus to different degrees, as shown by the plots with elastic modulus equal to 10 (see Fig. 4.6(a) and Fig. 4.12). In the case of the effective Young's modulus versus volume fraction, the data for both models plot quite closely together, suggesting that volume fraction has a strong effect and only a minor influence keeps them from aligning completely (Fig. 4.6(a)). When the effective Young's modulus is plotted against the contiguity, the models are far apart relative to the volume fraction figure, suggesting that contiguity is a minor influence and more significant parameters exist.

A more direct way to determine the relative influence of each topological parameter on the effective Young's modulus is to derive a new parameter that is a function of the original parameters, such that when the effective Young's modulus is plotted against this new parameter, data for the two models are perfectly aligned. The corrections needed to align the data would then provide the proportional influences of volume fraction and contiguity. This can be better understood by considering the form of the alignment function,

$$CI_{sp} = (A)\phi_{sp} + (B)C_{sp}, \tag{4.2}$$

where CI_{sp} is the parameter denoting the coupled influence of the volume fraction and contiguity on the stiffer phase, ϕ_{sp} and C_{sp} are the volume fraction and contiguity of the stiffer phase, respectively, and A and B are constants. The constants are used to correct the alignment of each models' data such that they become co-linear. It is a requirement of the function that the sum of A and B equals 1.0, so that the coupled influence parameter varies from 0% to 100% just like volume fraction and contiguity. The aligned data is seen in Figure 4.13 with the effective Young's modulus plotted against the coupled influence parameter.

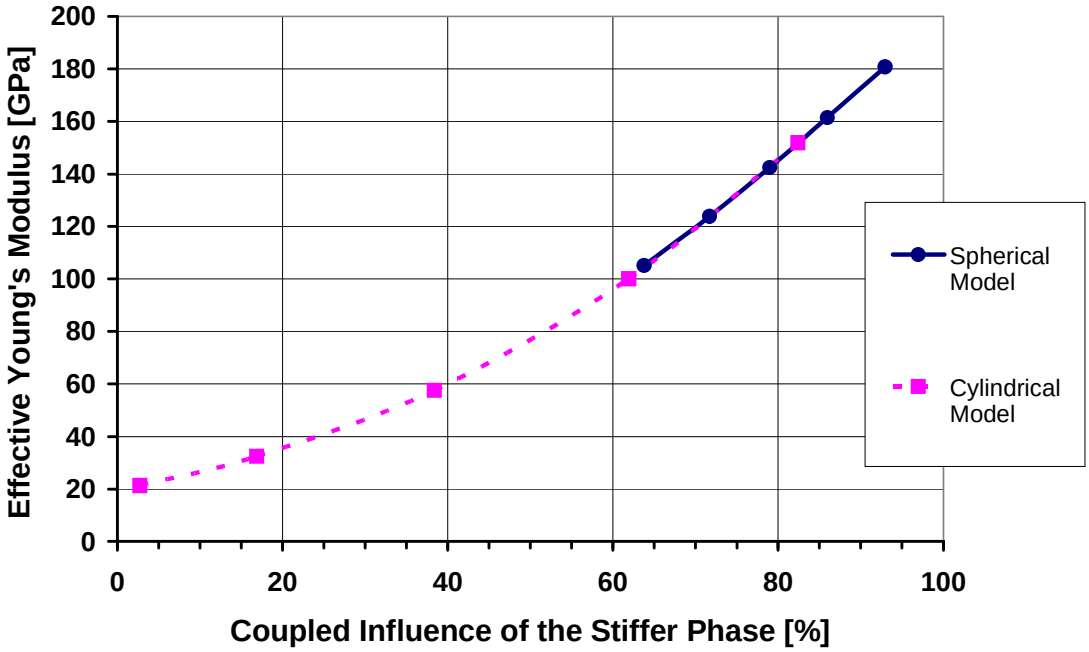

Figure 4.13. Aligned model data for the elastic macroscopic analysis
Coupled influence is a function of volume fraction and contiguity (see Eq. 4.2)

The correction constants provide a measure of the importance of each topological parameter. The constant for volume fraction, A, was found to equal to 0.84, and the constant for contiguity, B, was 0.16. The value correcting the influence of volume fraction is 5.25 times greater than the value correcting contiguity. Since a larger value denotes a more important effect, this shows that volume fraction is the dominant part of the coupled influence. Therefore, the amount of a phase, rather than its level of contiguity is of greater importance for the elastic properties of an IPC.

The newly derived coupled influence parameter is of limited value at this point, since it was derived using data from only two microstructural geometries. However, if it can be shown to be valid for other interpenetrating morphologies, this would imply that the effective Young's modulus of an IPC depends only upon the topological parameters of volume fraction and contiguity (in addition to constituent properties) and therefore that the effective Young's modulus can be reliably predicted if these two variables can be quantified for a given IPC geometry. This would make the parameter highly useful for predicting the

effective Young's modulus for different IPCs and optimizing their microstructural geometries.

4.2.2 Microstructural Stress Mechanisms

In the previous section on the macroscopic behaviour of the different IPC models, references were made to two geometric parameters of the microstructure: the phase volume fraction and shape. These parameters are important because the macroscopic behaviour of composites is dependent on the average statistical response of its components at the microstructural level. To complete the study on the elastic behaviour of IPCs, the results of the previous section should be explained through an investigation of microscopic behaviour, with specific attention paid to the role of phase volume fraction and shape. It should be noted that the microstructural investigation discussed in this section was performed more to explain general trends rather than any specific local behaviour.

The microstructural analysis consisted of two parts, the first providing qualitative descriptions of the microstructural behaviour and the second providing an attempt to quantify those descriptions into more definitive results. Both of these analyses relied on ADINA's post-processing functions which provide many possible plots of various stress distributions for each of the models.

The qualitative analysis consisted of studying stress distribution plots of each of the phases within both IPCs to gain an understanding of their deformation behaviour. Each of these plots was a three-dimensional view of one of the model's phases, showing contours of the relative stress levels in different regions. A discussion based on this qualitative data was then used to analyse how the spherical and cylindrical models were able to resist the applied strain. To understand this analysis, it is important to understand the referencing system used for the two IPC models. This system is shown in Figure 4.14 and should be recalled by the reader during the discussions of the microstructural mechanisms for the IPCs' behaviour. Due to time limitations, only the results for

the intermediate phase property ratio were considered (i.e. for an elastic modular ratio of 10). The stress distribution plots which form the raw data for the qualitative analysis are collected in Appendix I.

The stress component chosen to represent each model's response to the applied strain was the first principal stress. Since the first principal stress at a point is the maximum normal tensile stress at that point, it provides the preferred direction for stress transfer. Plots of this stress therefore indicate the direction and location of the preferred stress path for the qualitative analysis. The absolute values of the first principal stress have little meaning, so it was useful to compare them to a base situation. Base values were obtained by considering the first principal stress that would have developed had an identical uniaxial strain been applied to pure samples of each phase. In pure samples of each phase, the maximum stress would have developed in the direction of the

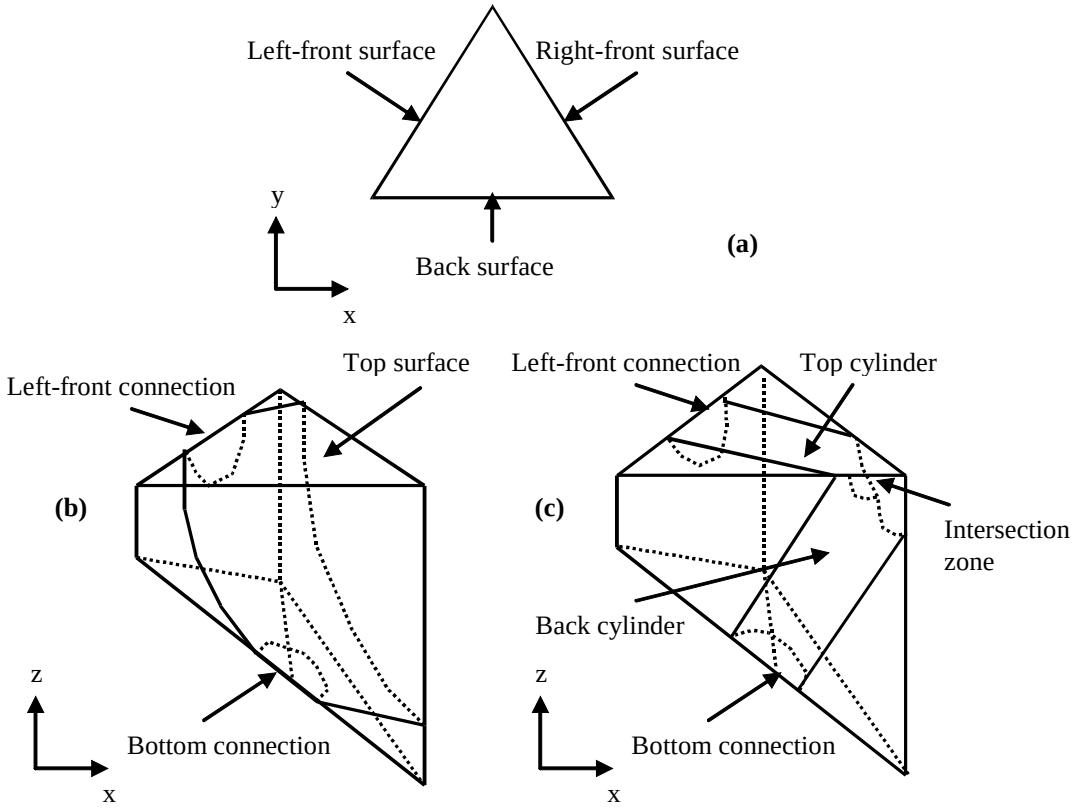

Figure 4.14. Reference system for spherical and cylindrical models
(a) Two-dimensional view of either model from top
(b) Three-dimensional view of spherical model from back
(c) Three-dimensional view of cylindrical model from back

applied strain, since no external lateral load was applied. The first principal stress in a pure sample of the more flexible phase was therefore

$$\sigma_{P1(mf)} = E_{mf} \cdot \varepsilon_a \,, \tag{4.3}$$

where $\sigma_{P1(mf)}$ is the first principal stress in the more flexible phase when there is no stiffer phase, ε_a is the applied strain equal to 0.001, and E_{mf} is the elastic modulus of the more flexible phase (this was 20 GPa for an elastic modular ratio of 10). Similarly, the first principal stress in a sample of the stiffer phase is

$$\sigma_{P1(sp)} = E_{sp} \cdot \varepsilon_a \,, \tag{4.4}$$

where $\sigma_{P1(sp)}$ is the stress in the stiffer phase when there is no flexible phase, ε_a is the same as above, and E_{sp} is the elastic modulus for the stiffer phase (200 GPa for an elastic modular ratio of 10). The first principal stresses calculated by ADINA were normalised by the values from Equations 4.3 and 4.4 for the more flexible phase and stiffer phase, respectively, to depict the relative stress difference for an IPC compared to a pure sample of each phase. This comparison should provide help in understanding how each composite's behaviour differs from that of the constituent phases.

The mechanisms affecting the behaviour of each of the two different microstructures can be determined by considering the qualitative results from the various plots of stress distributions in Appendix I. An example of the phases' responses for the spherical model is shown in Figure 4.15. In the stiffer phase, the plot of the first principal stress shows the preferred stress path to be from the top surface, down the back surface, towards the interconnection point on the bottom surface (highlighted as Region 1). Away from this region, stresses are lower and are shown as Region 2. In the more flexible phase, high first principal stresses radiate out from the bottom connection and are highlighted as Region 3. Parts of the more flexible phase away from the bottom connection carry significantly less stress (Regions 4 and 5).

The reasons for the stress distributions in the spherical model are linked to the difference in stiffness between the two phases. In Region 1, stress is

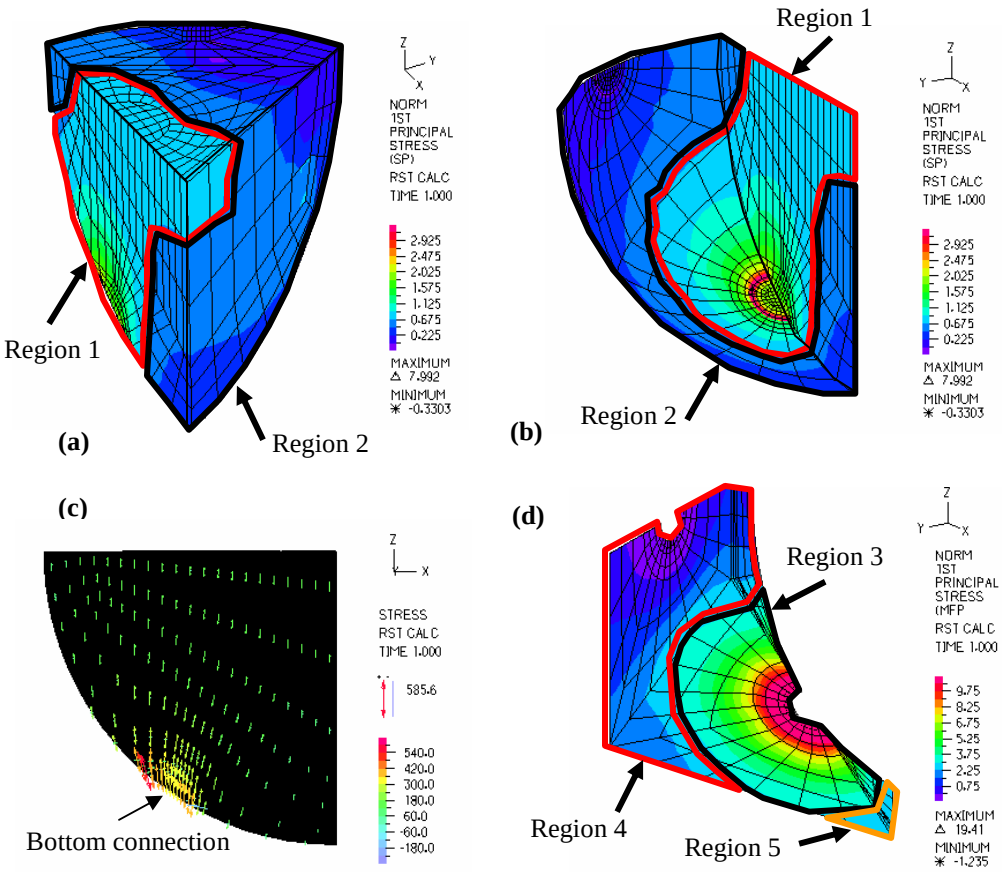

Figure 4.15. Normalised first principal stress distributions in the spherical model (ϕ = 75%)
(a) Stiffer phase showing back, top and right-front surfaces
(b) Stiffer phase showing left-front, bottom and back surfaces
(c) Stiffer phase vector plot showing stress concentration at bottom connection
(d) More flexible phase showing left-front, bottom and back surfaces

transferred vertically in the stiffer phase from the top surface to the bottom surface, but this transfer is not distributed equally in all directions as stresses are also laterally transferred through shear away from zones with underlying more flexible phase (Region 2). This is what causes the concentration of stress at the bottom connection. The vector plot in Figure 4.15(c) also shows that the direction of first principal stresses is predominately vertical with convergence towards the bottom connection. Although the sharply delineated colours of the contour plots over-emphasise the difference between nearby stresses, for simplicity it is still useful to view Region 1 as the preferred stress path.

Consider now both Regions 1 and 3 at the phase interface near the bottom connection. The stiffer phase in Region 1, just above Region 3, has experienced higher stresses, and therefore larger strains, towards the bottom

connection. Due to strain compatibility along the phase interface (both phases are assumed perfectly bonded) the nearby more flexible phase is forced to stretch to a similar amount. Thus, the high strains in Region 1 transfer stress to the more flexible phase, causing Region 3 to have increased first principal stresses. Region 4 of the more flexible phase is also near the phase interface, but in a zone of low stress. In Region 5, the more flexible phase is bypassed as a stress transfer path. The presence of this more flexible region between spheres was the reason for lower stresses along the back surface of the stiffer phase in Region 2. Stress was more easily transferred through Region 1, the path of least compliance, leaving Regions 2 and 5 with low first principal stresses.

Mechanisms affecting the microstructural behaviour of the cylindrical model are also attributable to the difference in stiffness between the two phases and may be determined from an examination of the first principal stress distribution plots (see Fig. 4.16). For the stiffer phase, the preferred stress path goes from the top surface in the cylinder intersection zone down the back cylinder (Region 1). Significantly less stress is found in the top cylinder (Region 2) and along the “heel” of the back cylinder (Region 3), suggesting that these regions lie outside the preferred path for stress transfer. In the more flexible phase, higher first principal stresses are created in Regions 4, 5 and 6, which are between vertically adjacent cylinders. Vertical adjacency refers to cylinders that are nearest neighbours but do not lie on the same horizontal plane (x-y plane). The use of this definition will become clearer in the following discussions. In zones away from these cylinders, stresses are reduced.

Two mechanisms account for the stress development in the stiffer cylindrical phase: axial tension and bending. Axial tension enhances first principal stresses in Region 1 as a result of the back cylinder and cylinder intersection zone forming the most direct, low compliance path for load to be carried through the IPC. The same levels of axial induced stresses do not occur in Region 2, where the top cylinder is underlain by the more flexible phase, thus

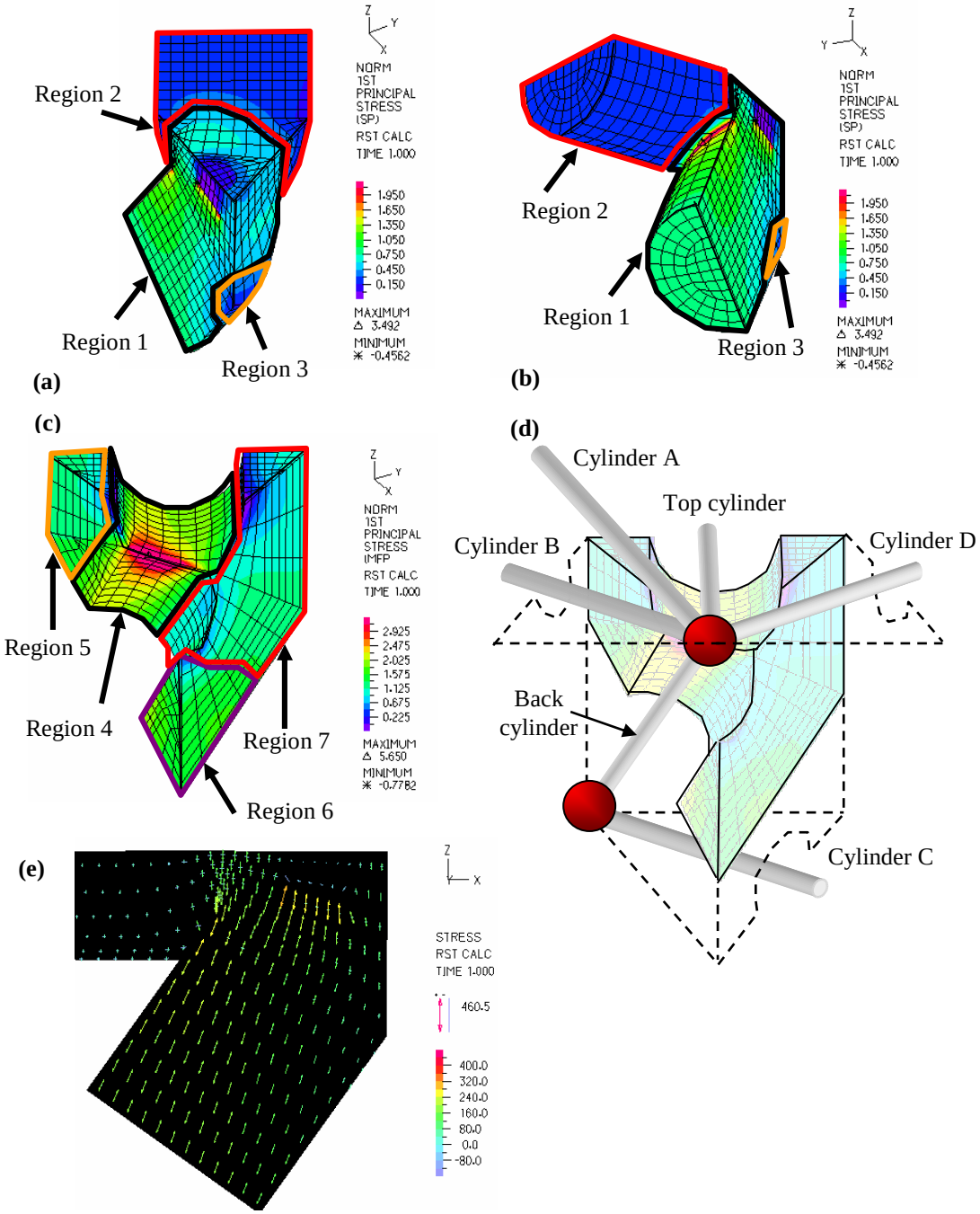

Figure 4.16. Normalised first principal stress distributions in the cylindrical model (ϕ = 39%)
(a) Stiffer phase showing back, top and right-front surfaces
(b) Stiffer phase showing left-front, bottom and back surfaces
(c) More flexible phase showing back, top and right-front surfaces
(d) More flexible phase showing adjacent cylinders
(e) Stiffer phase vector plot showing first principal stress direction in the back cylinder

interrupting a vertical stress path. Similarly, stress passing vertically through Region 3 also needs to pass through the more flexible phase, making it a poor zone for axial stress transfer. Bending stresses in the back cylinder are also

responsible for its stress response. Since the uniaxial strain applied to the model is in the z-direction, the back cylinder is displaced towards a more vertical position. In order for this to occur, extension is required along the side of the back cylinder with an acute angle to the top cylinder, and contraction along the opposite side. This provides a reason for the higher tensile stresses on the left side of Region 1 and the lower tensile stresses on the right side, including Region 3 (see Fig. 4.16(b)). In Region 2, bending should produce little stress response, since only minor vertical strains are applied. Without a more significant displacement of the top cylinder, both axial and bending related stresses in Region 2 should be negligible.

Although simple in appearance, the first principal stress distribution for the more flexible phase is a result of a series of interactions between it and the complex geometry of the stiffer phase. To understand these interactions, it is necessary to know the positions of several adjacent cylinders whose existence is imposed by the boundary conditions of the model (the position of several of these adjacent cylinders is indicated in Figure 4.16(d) by their centrelines; those unimportant to the following discussion have been omitted). Region 4 forms a relatively effective pathway for stress transfer due to its constricted position between the top and back cylinders (which are vertically adjacent). Stress passes into this region from the top cylinder (Region 2 of the stiffer phase) more easily than it is able to transfer towards the back cylinder. The stress from Region 2 is therefore passed down into Region 4, from which it is transferred into the back cylinder.

The first principal stress in Region 5 is a result of constraint placed on the more flexible phase by a network of several vertically adjacent cylinders, specifically Cylinder A, the top cylinder, Cylinder B and the back cylinder. Although the optimum path for the stress transfer is through Cylinder B to the cylinder intersection zone and onwards through the back cylinder (this is the path completely through the stiffer phase as shown in Region 1), the constraint in Region 5 also makes it a reasonably effective pathway. By limiting the ease with which the more flexible phase is able to distort, higher stresses are

supportable in Region 5. This situation also exists in Region 6, between the vertically adjacent back cylinder and Cylinder C. Cylinder C is enforced by the anti-symmetric boundary condition and holds the position of the top cylinder when the half prism unit cell is rotated about its axis of anti-symmetry (see Fig. 3.7; the counterparts for Cylinders A and B have been omitted for clarity). Region 6 is therefore an extension of the stress response found in Regions 4 and 5, though the majority of this region is closer to the latter.

For Regions 4, 5 and 6, higher first principal stresses arise from constraint provided by vertically adjacent cylinders. Lower stresses arise in Region 7 due to the lower constraint imposed on it without these vertically adjacent neighbours. The top cylinder and Cylinder D are adjacent to each other and Region 7; however, because they are horizontally adjacent, or adjacent on a plane perpendicular to the direction of applied strain, they have a significantly reduced ability to constrain the distortion of Region 7.

Although it was not described here, it should be expected that the previously explained mechanisms would show slightly different results for different elastic modular ratios. With an elastic modular ratio of 2, the more flexible phase is much more similar to that of the stiffer phase and could therefore be expected to sustain much higher loads. This would make the axial tension mechanism of stress transfer more dominant in the stiffer phase as an increased amount of the load could be passed effectively through the more flexible phase. This would then also increase the stress levels in the more flexible phase. Alternatively, with an elastic modular ratio of 100, the stress transfer bending mechanism in the stiffer phase should become dominant because of the poor ability to transfer load through the more flexible phase.

A more quantitative analysis of results is now undertaken. The data for the quantitative analysis were taken from ADINA's post-processing results calculated at the integration points of each element. As mentioned previously, the results of interest for the elastic analysis were the first principal stresses, which were then normalised by Equations 4.3 or 4.4 (depending on the phase

considered) so that the values used were ratios of the stresses within the IPCs to those that would occur in pure samples of each phase. The normalised first principal stresses were then separated by incremental limits dividing them into sub-domains of the total stress domain. This allowed the number of integration points within each of these sub-domains to be counted so that the stress distributions could be determined for each phase of both models. The distributions were found to be highly dependent upon the increment used to provide the limits for each sub-domain. A high level of accuracy was obtainable because the majority of the stresses were distributed within a relatively small domain (0 to 2 for the stiffer phase data and -1 to 5 for the more flexible phase data), and it was possible to choose a very small increment for the sub-domains without creating unmanageably large amounts of data (the increment chosen was 0.05).

Unfortunately this method provides only an approximation of the quantified stress distribution because it does not take into account the volumes of individual elements. In regions of likely stress concentrations, more elements were placed than in regions of lower stresses to provide a greater degree of solution accuracy (see the bottom connection in Fig. 4.15 and the intersection of the cylinders in Fig. 4.16). It is therefore likely that the following data is biased towards the stress levels found in regions of small elements. Despite this limitation, the analysis does provide some useful insights into how stress is transferred through the different microstructures.

The normalised first principal stress distributions for both phases of each model are shown in Figure 4.17. All the figures contain results for the spherical and cylindrical models at their lowest, medium and highest stiffer phase volume fractions (the other two intermediate volume fractions were not considered so that the figures would not become overly crowded).

Use of the normalised first principal stress distributions should be done with care taken to properly understand what the figures are indicating. As an example, consider the stiffer phase of the spherical model at each of its volume

fractions (see Fig. 4.17(a)). At its 85% volume fraction, normalised stresses in each of the sub-domains between 0.15 and 1.25 are sustained in 1% or more of the stiffer phase, while those between 0.75 and 1.0 are sustained in 5% or more, and only one stress sub-domain takes up as much as 10% of the stiffer phase. This indicates that there is a gradual variation of stress from the minimum stress of -0.290 to the maximum stress concentration of 5.48 (the maximum and minimum stresses are shown in Table 4.4). No stress sub-domain takes up a significant amount of the stiffer phase and the majority of the stiffer phase sustains a normalised stress of less than 1.0. It can therefore be said that the stiffer phase in the spherical model at a volume fraction of 85% has a non-uniform stress distribution and is not as effective as its base situation in transferring stress (remember the base situation is that of a pure sample of

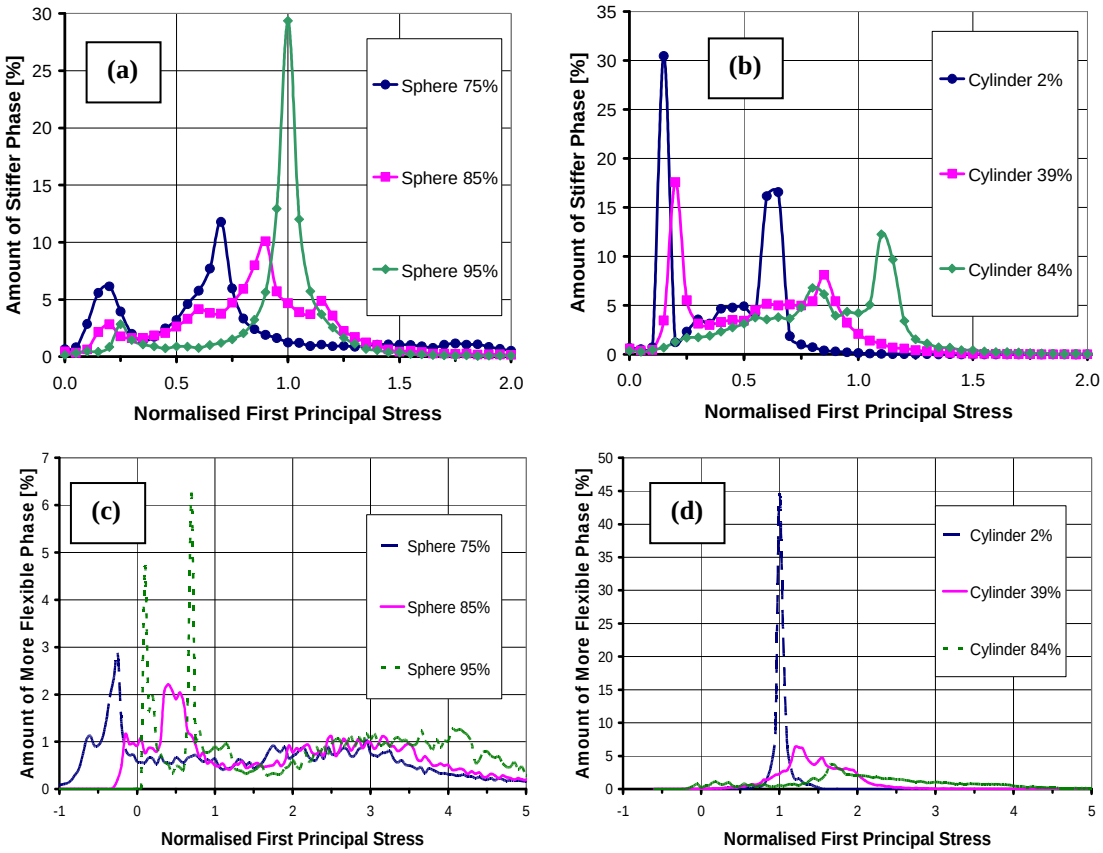

Figure 4.17. Quantitative normalised first principal stress distribution for both models
(a) Stiffer phase of spherical model
(b) Stiffer phase of cylindrical model
(c) More flexible phase of spherical model
(d) More flexible phase of cylindrical model

the stiffer phase, and although the spheres in the IPC should not be expected carry a similar level of stress as a pure sample, comparison to a pure sample provides a means to judge the effectiveness of the phase in transferring stress). In the case of the stiffer phase of the spherical model at 75%, the stress distribution appears to be as non-uniform as the 85% model, but in this case an even larger amount of the stiffer phase carries normalised stresses below 1.0. The behaviour of the stiffer phase for the 95% spherical model is in stark contrast to these previous cases. Here 1% or more of the stiffer phase sustains stresses in each of the sub-domains in the narrow band between 0.75 and 1.25, and nearly 30% of the stiffer phase sustains normalised stresses in the single sub-domain centred at 1.0. The stiffer phase in this case has a much more uniform stress distribution and much more of it appears to be near its base effectiveness. This is to be expected; since 95% of the sample is made up of the stiffer phase, it therefore behaves much like the base case of a pure sample of the stiff material.

An easier way exists to judge the effectiveness and uniformity of stresses in the phases in each model as compared with the observations made thus far. Statistically, how effective a phase is compared to its base situation is represented by the mean normalised first principal stress (the closer the mean value is to one, the closer it is to the base situation), and the uniformity of the of the stress distribution is represented by the standard deviation (the closer the standard deviation is to zero, the more uniform the stress distribution). These values are listed for each phase of both models in Table 4.4. The use of the mean and standard deviation is sufficient for the further discussion of the microstructural mechanisms as long as the physical meaning of these numbers is kept in mind. It is also important to remember at this point that these values do not represent a volumetric distribution, but distributions based strictly on a number count of integration points which represent different volumes.

As just shown in the example for the stiffer phase of the spherical model, the volume fractions of the phases change the microstructural response. This situation is, however, more complicated since this change in response could

Table 4.4. Statistical data for normalised first principal stresses from the elastic microstructual analysis

(a) Data for the stiffer phase of both models

(b) Data for the more flexible phase of both models

(a)

Model	Stiffer Phase		Mean Stress	Standard Deviation	Maximum Stress	Minimum Stress
	Volume Fraction [%]	Contiguity [%]				
Sphere	75	5	0.77	0.56	5.86	-0.216
	85	47	0.85	0.42	5.48	-0.290
	95	82	0.95	0.33	4.14	-0.361
Cylinder	2	6	0.41	0.23	1.85	-0.435
	39	34	0.56	0.32	2.78	-0.527
	84	73	0.85	0.35	3.37	-0.630

(b)

Model	More Flexible Phase		Standard Deviation	Maximum Stress	Minimum Stress
	Volume Fraction [%]	Mean Stress			
Sphere	25	3.66	4.17	18.52	-1.152
	15	3.07	2.54	11.02	-0.301
	5	2.90	2.12	10.03	0.016
Cylinder	98	1.02	0.11	1.78	0.073
	61	1.46	0.46	5.04	-0.587
	16	2.21	1.24	20.96	-0.202

have been equally well attributed to change in the contiguity of the stiffer phase. Both of these topological parameters increase in the example; the volume fraction of the stiffer phase increased from 75% to 85% and then to 95%, and simultaneously the contiguity of this phase increased from 5% to 48% and then to 82% (a comparison of these parameters to each other was made in Sec. 4.2.1). The influence of these parameters is therefore coupled and the following discussion considers their combined effect.

If the stiffer phase of the spherical model is now studied using the mean first principal stress and the standard deviation values of Table 4.4, rather than the plots of Figure 4.17, it can be seen that the mean stress increases and standard deviation decreases with increasing volume fraction and contiguity. This shows exactly what the previous discussion had found: that the effectiveness of the stiffer phase increases and the stress distribution becomes more uniform as volume fraction and contiguity increase. For the stiffer phase of the cylindrical model, increasing mean stresses point to a growth in the

effectiveness of the phase and increasing standard deviation indicates a decrease in its uniformity with increasing volume fraction and contiguity. It is likely in both models that the increased effectiveness is due to a greater proportion of the applied load being transferred directly into and then through the larger, more connected stiffer phase. This mechanism is attributable to increases in both topological parameters.

The difference in the influence of volume fraction and contiguity on the uniformity of stresses in each model requires more careful inspection. In the spherical model, increasing uniformity requires less stress concentration towards the bottom interconnection, which is directly related to the phase contiguity. This is shown by the expanded size of the preferred stress path in Figure 4.18 as volume fraction and contiguity increase (Region 1 is the preferred stress path).

In the cylindrical model, careful examination of Figure 4.17(b) shows each volume fraction of the stiffer phase has two sub-domains possessing large amounts of the stiffer phase (seen as spikes in the figure). The lower stress sub-domain likely represents Regions 2 and 3, including the top cylinder and back cylinder heel (see Fig. 4.16), and the higher stress sub-domain represents Region 1, which includes the back cylinder. For the 2% volume fraction, the cylindrical model can almost be broken into two uniform zones, with Regions 2 and 3 having stresses in the lower sub-domain, Region 1 having stresses in the higher sub-domain, and a small series of sub-domains between these representing the cylinder intersection between these zones. With the increase in stiffer phase volume fraction to 39%, the distribution shifts towards the right, with more of the material in Region 2 having stresses between the spikes (due to an increased ability to transfer stress from the top cylinder to the back cylinder through direct transfer or indirectly through the more constrained flexible phase), and the back cylinder able to sustain higher stresses (though the back cylinder decreases as a proportion of the total phase). When the stiffer phase is increased to a volume fraction of 84%, the stress distribution is again shifted to the right, but with a notable difference. Region 1 is the higher stress

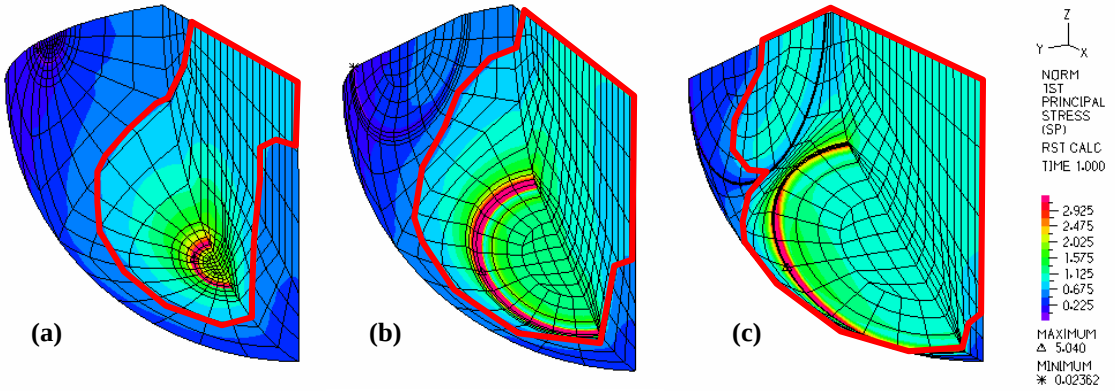

Figure 4.18. Change of bottom connection area and preferred stress path for spherical model
(a) Volume fraction = 75%, contiguity = 5%
(b) Volume fraction = 85%, contiguity = 47%
(c) Volume fraction = 95%, contiguity = 82%
Note: The area bounded by the red line is the preferred stress path (Region 1 of Fig. 4.14).

sub-domain and much of Regions 2 and 3 fall either within the lower stress sub-domain or the intermediate zone, but significant amounts of Regions 2 and 3 still exist within the broad lower stress region between 0.25 and 0.70. It is this region of lower stress sub-domains that makes the stress distribution of the cylindrical model non-uniform even when similar parameters have resulted in uniformity for the spherical model.

Two reasons suggest themselves for the difference in the models' uniformity. First, the difference in the spherical and cylindrical models' behaviours may be due to the difference in the scale of the volume fraction change between them. A smaller volume fraction change in the cylindrical model, for example 70% to 90%, might result in its behaviour more closely matching that of the spherical model. Second, if the stress transfer in the cylindrical model were due in part to bending, it should be expected that its distribution would have greater non-uniformity than the spherical model (bending requires stresses to vary between high and low values in order to reach force equilibrium). This is suggested by the 2% and 39% cylindrical models whose means lie approximately midway between the high and low spikes (see Fig. 4.17(b)).

Before beginning to study the influence of volume fraction and contiguity on the microstructural behaviour of the more flexible phase for each model, a

few important points should be made. First, because each successive volume fraction considered reduces the volume fraction of the more flexible phase (from 25% to 5% for the spherical model and 98% to 16% for the cylindrical model), it is a certainty that the absolute influence of the phase is decreasing. Second, the contiguity of the more flexible phase will not be considered. It should be expected that this phase's contiguity has some effect; however, high stresses in the more flexible phase are believed to be a result of stress transferring between regions of the stiffer phase through an intervening layer of the more flexible phase. Therefore, without the significance of direct stress transfer through the more flexible phase, its contiguity appears less important. Finally, the actual sub-domains used are not shown for this phase, for clarity of the figures (they are the same as those used for the stiffer phase).

The more flexible phase in the spherical model has a decreasing effectiveness with increasing volume fraction of the stiffer phase, and an increasing uniformity (see Table 4.4). This phase for the cylindrical model shows the opposite trend, with increasing effectiveness and decreasing uniformity. These differences are related to the dissimilar volume fraction ranges over which the more flexible phase changed for each model. The volume fraction change with the spherical model is, relative to that of the cylindrical model, quite small, and a simple inspection of the stress distributions (see Fig. 4.17 (c) and (d)) shows the different responses of the spherical model to be small compared to that of the cylindrical model.

Considering first the spherical model, it can be seen that two zones of the stress distribution have higher amounts of the more flexible phase (see Fig. 4.17(c)). The notable lower stress sub-domains, between -1 and 1 for all three volume fractions, contain the phase material closer to the top surface of the model and away from the high stress transfer region on the bottom surface (see Fig. 4.15(d)). Alternatively, the series of sub-domains between 1.75 and 4.15 contain the phase material near the bottom surface that experiences high stress transfer between adjacent stiffer phase spheres. Also important to this model are the large maximum stress concentrations (see Table 4.4), which

substantially decrease with the increase in stiffer phase volume fraction. The combination of these mechanisms causes a reduction of the mean stress (the effectiveness). Although constraint of the more flexible phase increases stresses in the top and bottom surface sub-domains, the reduced maximum stress concentration is the more drastic change. When the reduced maximum stress concentration is combined with the increase of the top surface stress sub-domain, it should be expected that the uniformity of the stress distribution increases. Despite these changes with volume fraction, it should still be noted that the mean stresses remain high in a more flexible phase with a very non-uniform stress distribution.

If the cylindrical model stress distribution for the more flexible phase is now examined, vastly different conditions are found. At the 2% volume fraction, a highly uniform distribution near the base normalised stress of 1.0 exists, indicating that the more flexible phase appears to behave as if the stiffer phase were not there (this situation is similar to the stress distribution that would be expected for a pure sample of the more flexible phase). This significantly changes as volume fraction is increased to 39% and then 84%, showing increasing effectiveness and greater non-uniformity. Both of these phenomena are due to the increasing deformation constraint on the more flexible phase provided by the stiffer phase as its volume fraction increases. Increasing constraint allows a greater amount of stress to be transferred through the more flexible phase, but this constraint is not equal everywhere. Pieces of the more flexible phase in more constricted locations and between vertically adjacent cylinders have the most enhanced normalised first principal stresses (for the definition of vertically adjacent cylinders see Fig. 4.16(d)). This creates the conditions for both increasing effectiveness, as sustainable stresses are raised, and increasing non-uniformity, as variable constraint makes the sustainable stresses location dependent.

The effect of phase shape on the microstructural mechanisms for stress transfer through the IPC models occurs through the coupled influence of volume fraction and contiguity. Although it is not possible to consider the effect

of either topological parameter completely independently of the other, it is possible to test the relative importance of each parameter in the composite response. This was done through the creation of a function that aligns the mean normalised first principal stress data for the stiffer phase of each model. The aligned condition of the models' data may be viewed as a datum, from which the corrections necessary to create alignment provide the relative importance of each parameter. The form and use of the aligning function are the same as was described in Sec. 4.2.1 (see Equation 4.2; alignment was achieved by solving for the coefficients A and B). The aligned data is plotted for both models in Figure 4.19 with the coupled influence of volume fraction and contiguity along the abscissa and the mean normalised first principal stress on the ordinate.

The relative effect of volume fraction and contiguity can now be determined by an examination of the values for the correction constants used to enforce alignment of the models' data. The value of A, the correction constant for the volume fraction, was 0.95, and the value for B, the correction constant for the contiguity, was 0.05. Alignment of data was therefore achieved by reducing the influence of volume fraction by 5% and the contiguity by 95% in

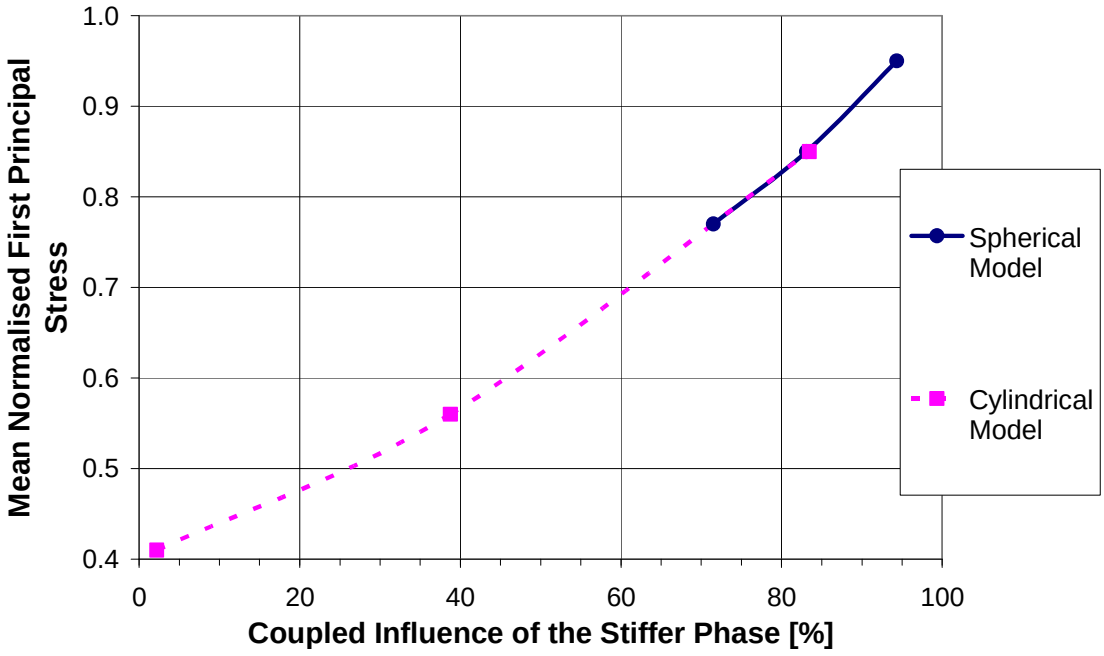

Figure 4.19. Aligned model data for the elastic microstructural analysis
Coupled influence is a function of volume fraction and contiguity (see Eq. 4.2)

each model. Essentially, this means that the data for both models is much more greatly affected by the volume fraction parameter of the coupled influence and only to a much smaller extent affected by the contiguity. Therefore, although the effect of phase shape on the microstructural stress transfer mechanisms is linked to the coupled influence of both topological parameters, it is the volume fraction parameter that is dominant for elastic behaviour.

4.2.3 Summary of Elastic Behaviour for Interpenetrating Microstructures

The previous two sections presented and attempted to explain how the elastic behaviour of an IPC is affected by the elastic modular ratio of the constituent phases and two topological parameters of the microstructure: the phase volume fraction and contiguity. The focus of these sections was on linking composite behaviour to the three variables without necessarily explicitly noting any unique characteristics due to the interpenetration of the microstructure. In this section, the results of the studies on macroscopic behaviour and microstructural mechanisms are summarised, and note is made of their importance to IPCs.

In the study of elastic macroscopic behaviour, the easiest result to find was the connection between behaviour and the volume fraction of the phases. In all the simulations, the effective Young's modulus of the composite increased with the volume fraction of the stiffer phase (see Fig. 4.6). This result is, in general, similar for all composites and simply states that the effect of a phase on composite behaviour is related to the amount of the phase in the composite. Despite the simplicity of this result, there are interactions between several variables making the behaviour significantly more complex. The influence of the elastic modular ratio was to increase the range of potential composite behaviour as the difference between the Young's moduli of the phases increased. This influence was found to be dependent on the volume fraction, with the highest divergence in the Hashin-Shtrikman bounds between the volume fractions of 50% to 75%.

Simple comparison of the response of different phase shape models showed the cylindrical model to produce a higher effective Young's modulus relative to that of the spherical model. The topological parameter of contiguity was introduced to explain the reason for this property difference, and it was noted that the shape of the phases links the contiguity and volume fraction. The ability of the cylindrical shape to create greater contiguity at the same volume fraction as the spherical shape allowed the improvement in the effective Young's modulus. The coupled nature of the topological parameters makes quantifying their individual effects impossible, but their relative significance could still be studied by plotting them as a linear combination of volume fraction and contiguity. This study showed that the volume fraction was over five times more important than contiguity in determining IPC elastic behaviour.

The use of these results is of particular importance to the development of IPCs since it is likely that nearly equal amounts of both phases are desirable in order to obtain beneficial properties from both phases. Knowing that divergence of the elastic bounds is optimum near the middle range of volume fractions and that contiguity can improve behaviour within the bounds, the materials engineer must now consider phase shape as well as the amount of the phases in the creation of IPCs for specific applications.

The study of microstructural behaviour linked the mechanisms for stress development to the difference in phase stiffness. In the spherical model, stresses were low near the top surface where the area connecting the stiffer phase upwards was large. This was not the case near the bottom surface, where stresses concentrate towards the small stiffer phase connection. These stress concentrations are a direct result of the increased stress transfer in regions of low compliance, or away from paths that must transfer stress through the more flexible phase (see Fig. 4.15). In the cylindrical model, the orientation of the stiffer phase increases the complexity. The top cylinder, because it is oriented perpendicular to the direction of the applied strain, requires transfer of stress through the more flexible phase. This makes it a poor stress path and it therefore has low stresses. In contrast, the back cylinder is the most direct low

compliance path in the direction of applied strain, causing it to develop high stresses through a combination of axial tension and bending (see Fig. 4.16).

These basic microstructural mechanisms remain consistent for each of the volume fraction variations considered in each model, but both the volume fraction and contiguity have an effect on the location and level of stress that develops. For the spherical model, increasing volume fraction and contiguity increases the stresses in the stiffer phase and its uniformity. This also results in a reduction of the stress being transferred through the more flexible phase between vertically adjacent spheres. These changes are due to a broadening of the preferred stress path, allowing smoother vertical stress transfer and therefore reducing the creation of stress concentrations. In the cylindrical model, stresses increase in both phases as the volume fraction of the stiffer phase increases, and greater non-uniformity of the stresses suggests an increase in local stress concentrations. This is due to the much greater interaction between the phases with the large increases in the amount of the stiffer phase. With more of the stiffer phase in the IPC, more stress is able to be transferred through it as the path of least compliance, but it also places more constraint on the more flexible phase, increasing its ability to carry stress.

The coupled influence of volume fraction and contiguity was studied for the microstructural analysis through alignment of the mean normalised first principal stresses in the stiffer phase. The relative influence of the volume fraction on the microstructural response was much greater than that of the contiguity. Although the magnitudes of the relative influences differ, this result agrees with the macroscopic study that volume fraction is of greater importance than the contiguity. It is therefore reasonable to state that the elastic behaviour of an IPC is related to the phase shape by the coupled influence of volume fraction and contiguity, and of these two parameters the volume fraction has a much more dominant effect.

4.3 NON-LINEAR PLASTIC BEHAVIOUR OF INTERPENETRATING MICROSTRUCTURES

4.3.1 Macroscopic Behaviour

After an initial completely elastic response, further increases in tension to a two phase ductile composite begin to initiate plastic deformation in regions sustaining the highest stresses with lower stress regions remaining elastic. This partially elastic, partially plastic behaviour continues until all portions of both phases reach a sufficient stress to cause completely plastic behaviour to occur. It is this non-linear elasto-plastic behaviour that is the focus of this section. The effective yield strength of each IPC is used to provide the basis for a simplified quantitative macroscopic analysis. The variables whose influences are studied include the yield strengths of the constituent phases, the amounts of the phases and the phase shapes.

A non-linear solution to the plastic behaviour of the spherical and cylindrical IPCs required use of the iterative full Newton method in the FEM. In the simulations performed, this involved applying a set strain increment, calculating the stress by an iterative procedure and then applying the next higher strain level (discussed previously in Section 3.6). This process was continued until either the model failed (i.e. convergence was not achieved) or a final set strain level was reached. The strain increments were experimented with so that each simulation was able to reach its maximum possible strain (either the final set strain or a strain at which the model would not converge to a solution). The most successful increments are listed in Appendix J. Such simulations were completed for the spherical model with stronger phase volume fractions of 75%, 80%, 85%, 90% and 95%, and for the cylindrical model with stronger phase volume fractions of 2%, 16%, 39%, 64% and 84%. The tests were replicated for yield strength ratios of 2 and 10 for the constituents (the weaker phase was given a yield strength of 110 MPa and the stronger phase that of 220 MPa or 1100 MPa, depending on the ratio considered). Other

information about the material properties for the plastic analysis models was provided in Section 3.5.

The value used to quantify the initial plastic behaviour of IPCs is more debatable than the use of the effective Young's modulus for a uniaxial test of elastic behaviour. Both the proportional limit and the yield strength of IPCs could be useful measures. The effective yield strength of the models was defined to be the stress at the standard 0.2% strain offset. The value for yield strength derived from this definition is generally significantly greater than the proportional limit. For the case of a two ductile phase composite, the proportional limit coincides with the initial yielding, most likely of the weaker phase. Since the purpose of this section is to evaluate the overall macroscopic plastic behaviour of the IPCs, the use of the proportional limit is a poor measure as it is too dependent on locally high stresses and the performance of only one phase. The effective yield strength is therefore used as the quantifiable measure of plastic behaviour.

General elasto-plastic behaviour with a low strain hardening modulus was found for most models. This is characterised on the stress-strain graphs by an initial linear section that denotes a fully elastic response followed by a curvilinear transition section where initial plastic deformation begins, and finally a low slope linear section where nearly complete plastic behaviour exists. This type of behaviour may be seen in Figure 4.20 for each model and yield strength ratio. The 2% strain offsets used to determine the effective yield strengths are shown in Appendix J, with the values for the effective yield strengths listed in Table 4.5.

Unfortunately, several of the models, especially those with a spherical shape, failed prior to reaching their yield strengths (convergence was not achieved at strains below the 0.2% strain offset). In these cases, the maximum value they reached before failure was used as the effective yield strength, though it should be noted that use of these values results in some error (asterisks are used to indicate the failed simulations in Fig. 4.20). This error is

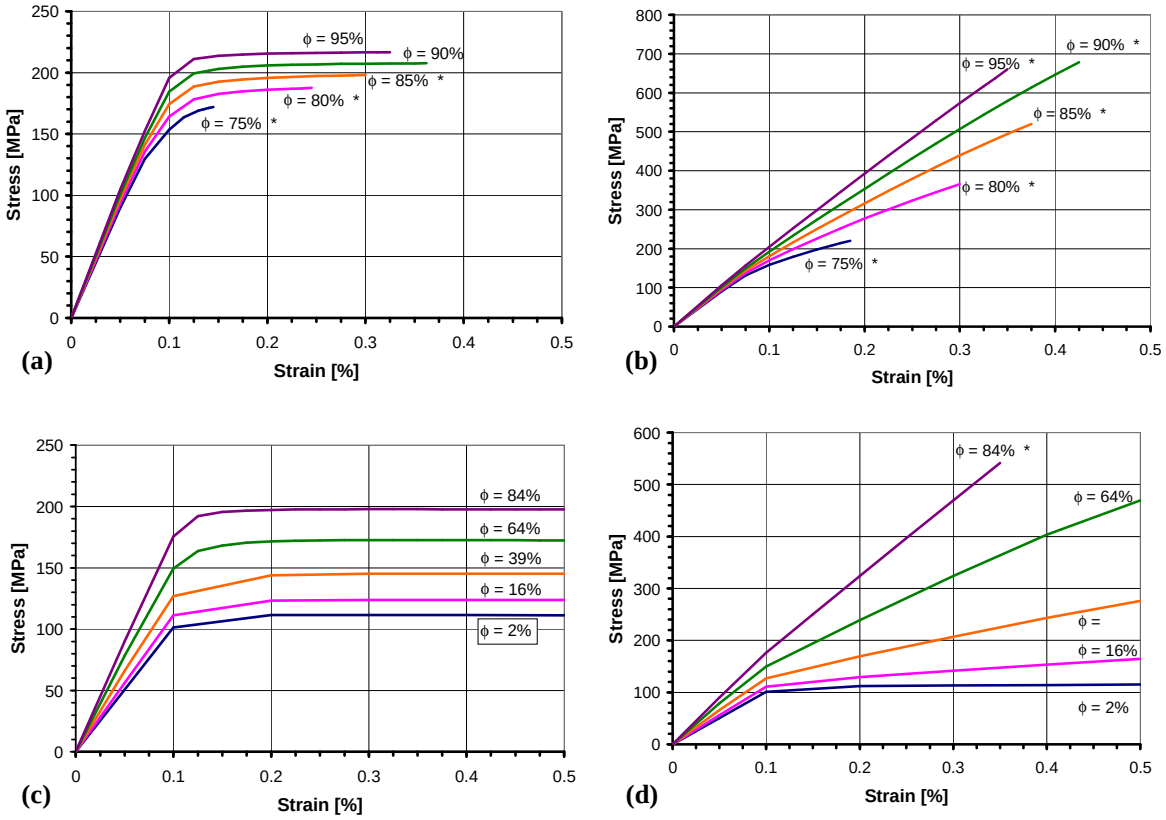

Figure 4.20. Stress-strain behaviour for both models at each simulated volume fraction of the phases

(a) Spherical model with the yield strength ratio = 2
(b) Spherical model with the yield strength ratio = 10
(c) Cylindrical model with the yield strength ratio = 2
(d) Cylindrical model with the yield strength ratio = 10

relatively small for results from models with a yield strength ratio of 2, since their stresses had already reached a plateau and would not be expected to change significantly if higher levels of strain had been reached. However, the error is large for results from models with a yield strength ratio of 10, where stress increases were still expected between the failure strength and the stress at the 0.2% strain offset.

The failure of several of the simulations to converge was likely produced by numerical instability. Elements in regions of high stress, particularly in the weaker phase, became highly distorted as the applied strain increased. A small number of these elements reached the rupture condition set through the maximum allowable effective plastic strain as 0.2. ADINA reacted to this situation by setting the stiffness contributions of the ruptured elements to zero as they were now considered unable to sustain any load (for the calculations,

Table 4.5. Effective yield strength of both models for all volume fractions

Model	Volume Fraction [%]	Effective Yield Strength [MPa] with the Yield Strength Ratio of 2	with the Yield Strength Ratio of 10
Spherical	75	172	220
	80	188	365
	85	198	520
	90	208	678
	95	216	660
Cylindrical	2	111	114
	16	123	146
	39	144	235
	64	172	465
	84	198	541

setting the stiffness values equal to zero is the same as removing the ruptured elements, see ADINA R&D, Inc. 2000b). The most likely result of these actions was to cause the already large distortions in neighbouring elements to become excessive, producing a poorly conditioned stiffness matrix that was unable to achieve numerical convergence. It cannot, however, be completely ruled out that material failure may have occurred. The rupture of a few elements could have initiated a chain reaction of such ruptures in the surrounding elements as the maximum allowable effective plastic strain was reached in each due to the extra load that they must sustain. This scenario is less likely than that of numerical instability since it would require elements of the stronger phase to also rupture. As shown in Table 4.6, the maximum effective plastic strain in any element of the stronger phase at the last strain increment was much lower than those in the weaker phase, making overall failure of the IPC unlikely.

The effective yield strength is plotted against volume fraction of the stronger phase in Figure 4.21. The stronger phase in all cases was always either the sphere or cylinder shape, never the surrounding material. Results for the simulations that failed to converge prior to reaching the 0.2% offset yield strength are indicated by an asterisk on these figures. The first important thing to note is the large number of early failures for the models with a yield strength ratio of 10. Given the previously mentioned large error that is present with these results, a significant amount of uncertainty exists in using them, especially

Table 4.6. Maximum effective plastic strains in the stronger phase of models that failed prematurely

Model	Volume Fraction of Stonger Phase [%]	Maximum Effective Plastic Strain	Percentage of Maximum Allowable Effective Plastic Strain [%]
Spherical (YSR = 2)	75	0.07355	36.78
	80	0.12351	61.76
	85	0.12780	63.90
Spherical (YSR = 10)	75	0.06357	31.79
	80	0.10811	54.05
	85	0.13140	65.70
	90	0.14421	72.10
	95	0.04203	21.02
Cylindrical (YSR = 10)	84	0.01291	6.46

Note: The maximum allowable effective plastic strain was set at 0.2

those of the spherical model where no actual yield strength was achieved. Fortunately, a similar spherical model with identical phase properties was created by Wegner and Gibson (2000a) and tested by the same method, so their results are directly comparable to those in this study. Wegner and Gibson's results are shown in Figure 4.21 by the open circles. Since they plot above those from the spherical model of this study, it is certain that they are superior, and all further references to results for the spherical model with a yield strength ratio of 10 will use Wegner and Gibson's data.

Also plotted on Figure 4.21 are the tightest reasonable bounds that can be drawn around the model data. No analytical method has been derived for plastic properties such as that of Hashin and Shtrikman (1963) for elastic properties, so the bounds drawn based on the data from this study represent only a useful guess. It is expected that if other parameters of the microstructural geometry were studied, the bounds could be improved. However, they are sufficient for the purposes of further discussion.

The effect of constituent phase properties on the behaviour of the IPCs can be seen by comparing the responses at different yield strength ratios (i.e. compare Fig. 4.21(a) and (b)). For both the ratios studied, the reasonable

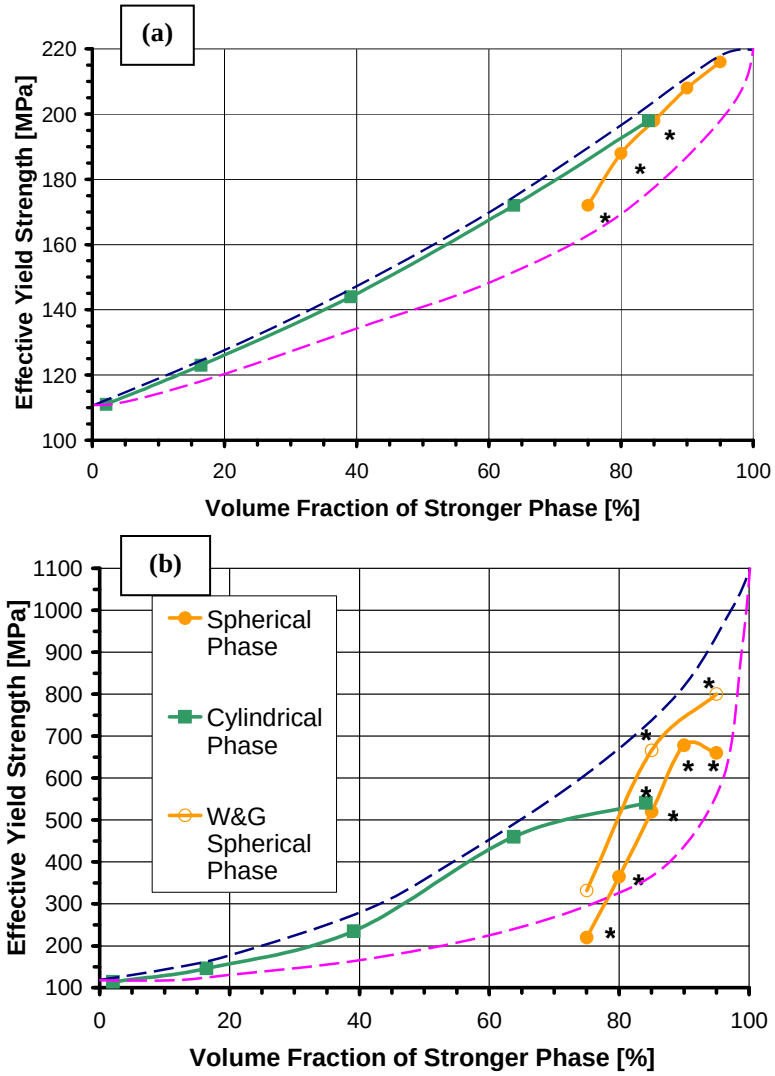

Figure 4.21. Effective yield strength versus the volume fraction of the stronger phase
(a) for a yield strength ratio of 2, and
(b) for a yield strength ratio of 10

bounds are divergent between the two volume fraction extremes. However, the divergence is far greater for the higher yield strength ratio. The bounds indicate the range of potential effective yield strengths, so this observation shows that the difference in constituent phase properties affects the range of response for the derived composite. It is also interesting to compare these bounds for plastic behaviour to the Hashin-Shtrikman bounds for elastic behaviour. If the comparison is made between the bounds having the same phase property ratios (compare the elastic modular ratio of 2 in Fig. 4.6 to the yield strength ratio of 2, etc.) it is noticeable that those for the plastic behaviour are much

looser. This suggests that parameters of the microstructural geometry have a greater effect on the plastic properties of an IPC than on their elastic properties.

The influence of the amount of each phase on the behaviour of the IPCs was determined by considering the effect of phase volume fraction changes. It is easily seen from Figure 4.21 that the effective yield strength increases with increases in the amount of the stronger phase in the composite. This influence is based on the greater ability for the stronger phase to dominate composite behaviour when more of it exists in the composite. Although the position of the bounds is only a reasonable guess, it can be seen that they follow the same pattern as those of Hashin and Shtrikman. Convergence occurs at either volume fraction extreme, denoting a pure sample of one of the constituent phases, and divergence is greatest through an intermediate range of about 50% to 85% of the stronger phase, depending on the yield strength ratio. This is significant, since it is within this range that IPCs are likely to find their greatest applicability (see brief discussion of this in Sec. 4.2.3).

The shape of the phases has an influence on the plastic behaviour of IPC's, as shown in Figure 4.21 by the difference in performance of the spherical and cylindrical models over their common volume fraction range (75% to 84% of the stronger phase). With the lower yield strength ratio of 2, the cylindrical shape is slightly more efficient than that of the sphere. This allows it to produce a higher effective yield strength for the same volume fraction. A similar situation should likely exist for the higher yield strength ratio of 10, but these results are skewed by the premature failure of the 84% volume fraction cylinder model below the strength obtained by Wegner and Gibson for the sphere model.

A better understanding of the effect of phase shape on the plastic behaviour of IPCs can be obtained by again considering the contiguity associated with each geometry. Contiguity is a property of the microstructural geometry and the values for both models at each of their volume fractions are the same as those calculated for the previous elastic analysis of Section 4.2.1. The effective yield strength is plotted against the contiguity of the stronger

phase in Figure 4.22, with results provided for both yield strength ratios. An analysis of the effect of contiguity at a yield strength ratio of 10 is desired, since it can be compared to the similar analysis for the elastic study in Section 4.2.1,

which used an elastic modular ratio of 10; however, the poor performance of the sphere model from this study makes it unsuitable for the microstructural analysis of the next section. The microstructural analysis therefore uses results for a yield strength ratio of 2, which may be compared to the results of the

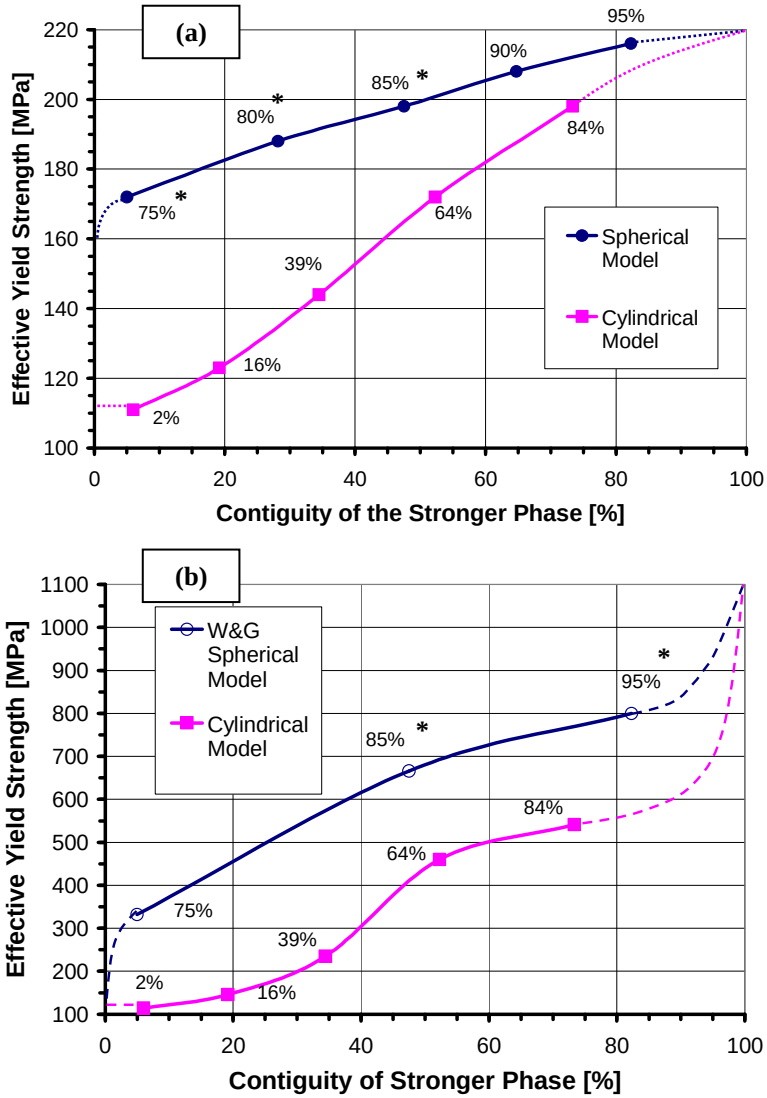

Figure 4.22. Effective yield strength versus the contiguity of the stronger phase

(a) for the yield strength ratio of 2, and
(b) for the yield strength ratio of 10
Note: The percentages on the figure are the volume fractions for the adjacent data points

macroscopic analysis with a yield strength ratio of 2. The labels on the figures indicate the corresponding volume fractions for the data points and the dashed lines represent the extrapolated behaviour at the extreme contiguities of 0% and 100% (the extreme contiguities have the same meanings as discussed in Section 4.2.1). It is important to note that the spherical model results for the yield strength ratio of 10 are the superior values taken from Wegner and Gibson (2000a).

An understanding of the effect of phase shape on the macroscopic plastic behaviour of IPCs may be determined from an examination of Figure 4.22. The contiguities for the 75% volume fraction sphere model and 2% volume fraction cylinder model are almost the same (5% and 6%, respectively) but their results are quite different, implying that contiguity is not the only factor affecting plastic behaviour. However, contiguity does have a definite influence, which is best seen by consideration of single values for the effective yield strength. As an example, consider the yield strength ratio of 10 (see Fig. 4.22(b)), and focus on an effective yield strength of 332 MPa. This corresponds to a spherical model volume fraction of stronger phase equal to 75% and a contiguity of 5%. For the cylindrical model, the same effective yield strength is created with a volume fraction of 50% (again see Fig. 4.22(b)) and a contiguity of 42%. In using the cylinder instead of the sphere shape, there is a reduction in the necessary volume fraction of stronger phase of 25% due to the 37% greater contiguity between pieces of the stronger phase. As with the elastic behaviour, the greater efficiency of the cylindrical model in plastic behaviour is due to the increased path for direct stress transfer through the stronger phase.

Table 4.7 lists other similar comparisons of the models for different effective yield strengths and for both yield strength ratios. It can be seen that the effect of contiguity is reduced as the models converge towards a pure specimen of the stronger phase. (Results for the yield strength ratio of 10 are incomplete because less data was obtained at the higher volume fractions due to the premature failure of the models at these volume fractions).

Table 4.7. Comparison of effective yield strength to the topological parameters
(a) for a yield strength ratio of 2, and
(b) for a yield strength ratio of 10

(a)

Effective Yield Strength [MPa]	Vol. Frac. of Spheres [%]	Vol. Frac. of Cylinders [%]	Difference between Vol. Frac.	Contiguity of Spheres [%]	Contiguity of Cylinders [%]	Difference between Contiguity
172	75	63.77	-11.23	5	52.27	47.27
188	80	76.31	-3.69	28	65.24	37.24
198	85	84.14	-0.86	47	73.35	26.35

(b)

Effective Yield Strength [MPa]	Vol. Frac. of Spheres [%]	Vol. Frac. of Cylinders [%]	Difference between Vol. Frac.	Contiguity of Spheres [%]	Contiguity of Cylinders [%]	Difference between Contiguity
332	75	49.74	-25.26	5	42.13	37.13
375	76	54.45	-21.55	10	45.54	35.54
425	78	59.93	-18.07	17	49.50	32.50

If the result just found in the previous example is compared to the example result from Section 4.2.1, it can be seen that contiguity has a far greater influence on the plastic behaviour of IPCs than it does on their elastic behaviour (see Table 4.3, page 82). Both results are based on phase property ratios equal to 10, but an increase of contiguity equal to 49% was required to reduce the volume fraction by 9% when replacing spheres with cylinders in the elastic case while only a 37% increase in contiguity was necessary to reduce the volume fraction by 25% in the plastic case. While the influence of contiguity on elastic behaviour is relatively minor, its influence on plastic behaviour appears to be highly important.

The effect of phase shape on IPC plastic behaviour is related to the coupled influence of both the volume fraction and contiguity of the phases. As detailed in the macroscopic elastic analysis in Section 4.2.1, the relative importance of the volume fraction and contiguity may be found by aligning the effective property data for both models using a linear function of these parameters. The coefficients A and B of the linear function (see Equation 4.2, page 83) provide a simple quantitative measure of each parameter's influence. The aligned data for the macroscopic plastic behaviour of the models is seen in

Figure 4.23. For the models with a yield strength ratio of 2, a rough alignment is achieved when A, the coefficient for the volume fraction equals 0.87, and B, the coefficient for the contiguity equals 0.13. When the yield strength ratio is 10 the linear function is unable to achieve a good alignment over the entire common domain of the models. While a non-linear function of volume fraction and contiguity could produce a more exact alignment, for the purposes of providing a simple relation between the two parameters the best fit given by the linear

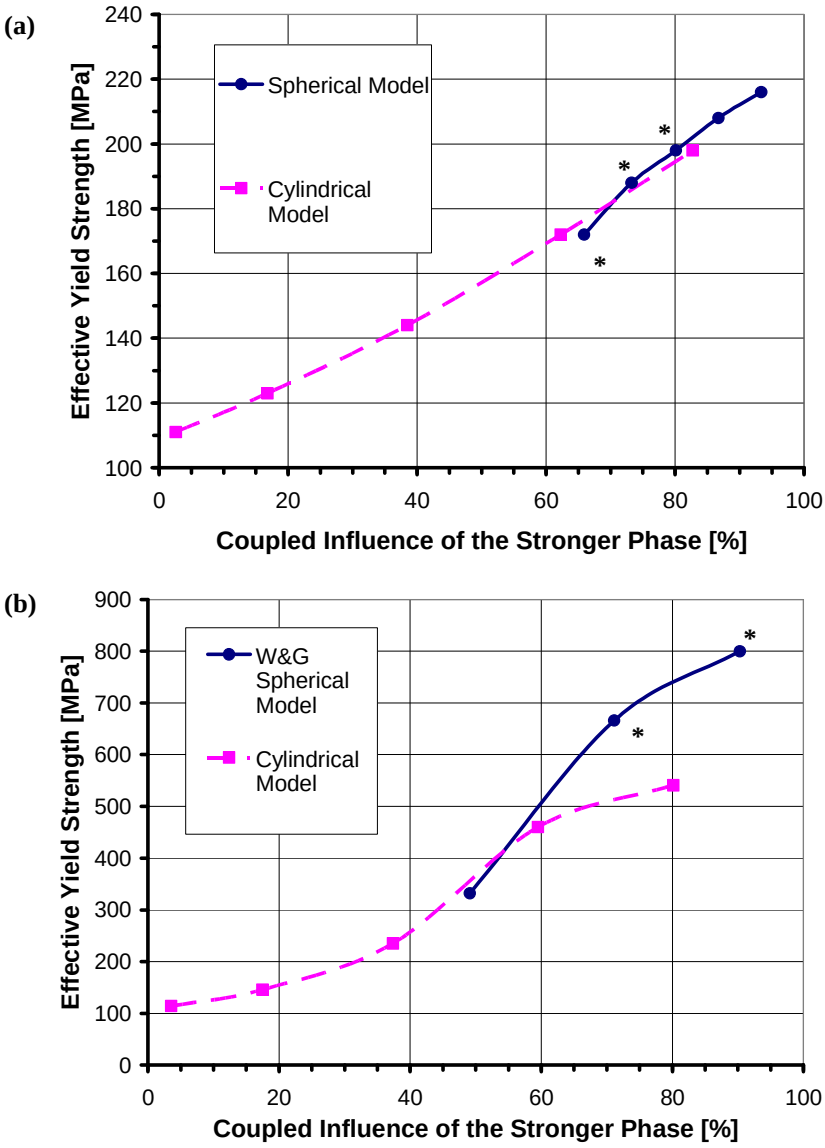

Figure 4.23. Aligned model data for the plastic macroscopic analysis
(a) for the yield strength ratio of 2, and
(b) for the yield strength ratio of 10
Coupled influence is a function of volume fraction and contiguity (see Eq. 4.2)

function is considered sufficient. For the best fit alignment the value of A is 0.63 and the value for B is 0.37.

A simple comparison of the coefficient values shows that volume fraction has a more significant influence than contiguity for both yield strength ratios. In the case of the yield strength ratio of 2, the volume fraction is much more important than contiguity since it accounts for 87% of the coupled response. A comparison of this value to the one found in the macroscopic elastic analysis shows them to be quite similar (the A coefficient in Sec. 4.2.1 was 0.84), but it is important to note that the elastic modular ratio in that case was 10. Although results for the yield strength ratio of 10 are less accurate, they have the same phase property ratio, making them more valuable for comparison between behaviours. For the plastic situation, the contiguity has a significantly greater influence than that for the elastic behaviour (the B coefficient for the plastic and elastic analyses were 0.37 and 0.16, respectively).

This increase in the importance of the contiguity parameter after yielding of the composite agrees with the previous discussion regarding the use of the effective yield strength versus contiguity graphs of Figure 4.21. Given the importance of plastic behaviour to ductile phase IPCs under higher loads, it appears that microstructural geometry has increasing significance as the failure of the composite is approached. This influence is not simple, however, since it is affected by the phase property ratio and the volume fractions and contiguities of the phases.

4.3.2 Microstructural Stress Mechanisms

After completion of the macroscopic analysis, a study looking into plastic behaviour at the microstructural level was undertaken. The purpose of this study was to find the underlying mechanisms responsible for the observed overall plastic behaviour of the IPCs. As described in more detail previously in Section 4.2.2, a qualitative and quantitative investigation of the stress distributions within the model microstructures was performed. Both model shapes were studied at three volume fractions of the stronger phase (low,

intermediate and high). The stress distribution of interest was the effective stresses, since ADINA uses the von Mises effective stress criterion to determine yielding of the phases (ADINA R&D, Inc., 2002b). When the effective stress distribution in each phase is divided by its yield strength, these normalised values provide the relative distribution of yielding within each phase. The normalising equation is

$$\sigma_{eff\,(norm)} = \frac{\sigma_{eff}}{\sigma_y}, \tag{4.5}$$

where $\sigma_{eff(norm)}$ is the normalised effective stress, σ_{eff} the effective stresses calculated by ADINA, and σ_y the yield strength of the phase being examined.

Only the models having a yield strength ratio of 2 were considered, since results for a yield strength ratio of 10 were incomplete due to several premature failures of the simulations. The stress distributions investigated for all three of the cylindrical models were at an applied strain of 0.005. None of the spherical models considered were able to converge at strain levels as high as 0.005, so the last strain level at which they did converge was used (these were 0.00145, 0.003 and 0.00325 for the 75%, 85% and 95% volume fractions, respectively). It is also important to note that the spherical models at stronger phase volume fractions of 75% and 85% did not reach their 0.2% offset yield strength prior to failure. All the normalised effective stress distribution plots for each phase of both models are provided in Appendix K.

The qualitative descriptions of the stress distributions during the plastic behaviour will focus only on the previously stated strain state. Since only a single state of each model is considered during its strain history, it was not possible to determine how each model changes as it was loaded. This would have required examination of the models at many strain increments, which was beyond the objective of determining the effectiveness of each microstructure. Instead of focussing on when and by what means the microstructures yield, this study looked simply at where yielding occurred and the overall distribution of

yielding within the models. This task was possible at a single strain state and provided a means to judge the effectiveness of each microstructure.

The normalised effective stress distribution for the spherical model at a stronger phase volume fraction of 75% is shown in Figure 4.24 (see Fig. 4.14 for the referencing systems for the unit cells). A simple examination of the stronger phase in the model allows it to be separated into two distinct regions. Region 1 lies on the path of preferred stress transfer through the bottom connection, which was seen previously in Section 4.2.2. The material in this region has all yielded. Region 2 does not lie on the preferred path since any

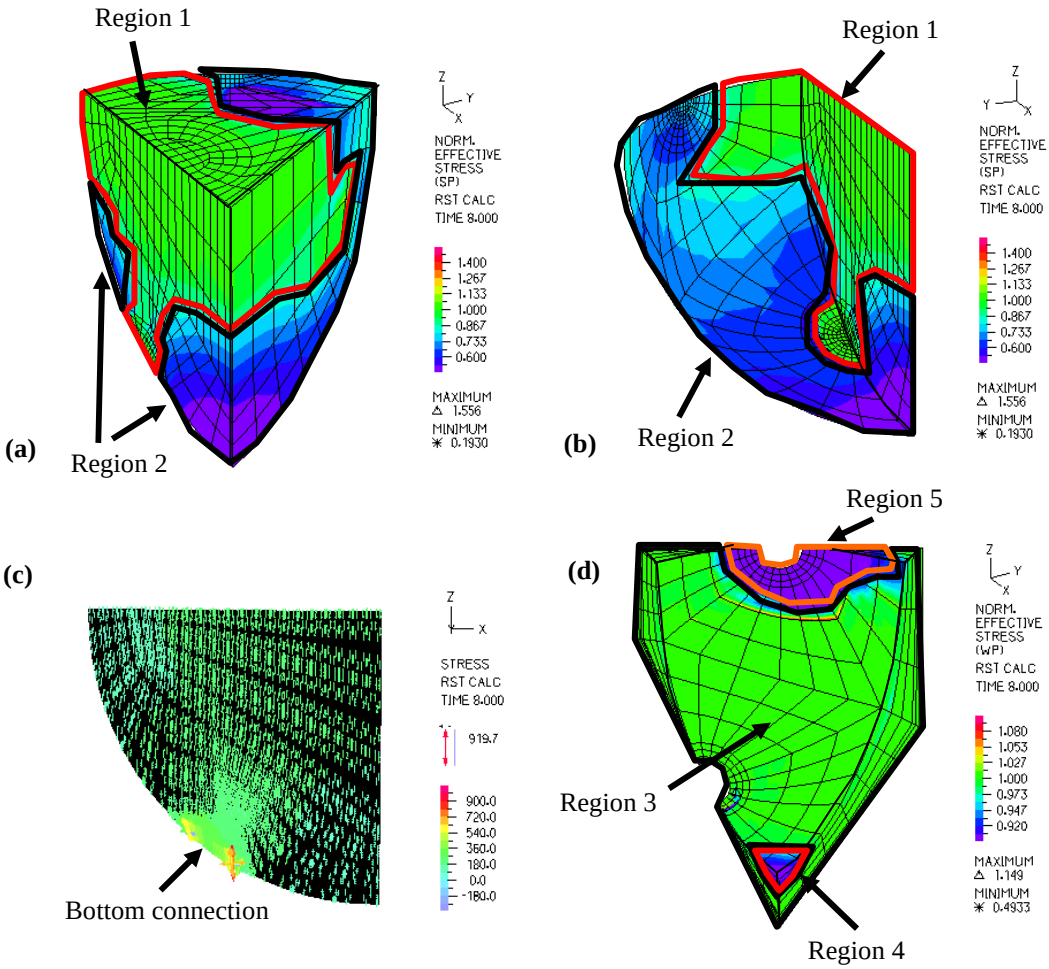

Figure 4.24. Normalised effective stress distribution in the spherical model (ϕ = 75%) at an overall applied strain of 0.00145
(a) Stronger phase showing back, top and right-front surfaces
(b) Stronger phase showing left-front, bottom and back surfaces
(c) Stronger phase vector plot showing stress concentration at bottom connection
(d) Weaker phase showing top, right-front and back surfaces

stress passing through it must also pass through the underlying weaker phase. With stress concentrating away from this region, it remains below its yield strength.

It should be expected that the majority of the weaker phase has yielded, since the macroscopic stress at the final converged strain was 172 MPa, well above the yield strength of the phase (which was 110 MPa). This expected response is found in Region 3. However, small Regions 4 and 5 remain below the yielded condition. In the case of Region 4, it is important to note that it lies below Region 2 in the stronger phase, and since Region 2 has a reduced amount of stress transferring through it, it passes on less stress to Region 4, allowing it to remain below yield. Region 5 lies off a path of preferred stress transfer in the upper half of the model. In the upper half of the model, most of the stress passing through the weaker phase is from direct transfer within the phase, not transfer between phases. However, the left-front surface connection of the stronger phase breaks this path and forms a stiffer alternate path. Stress passing through the weaker phase near this connection prefers to pass into the surrounding stronger phase, leaving the weaker phase at a lower stress below the yield point.

These responses to the applied strain suggest an important role for contiguity in the plastic behaviour of IPCs. The concentration of stress towards the direct connections of the stronger phase should be expected to increase as the weaker phase yields; that is, stress should continue to transfer along paths of least compliance (the weaker phase's stiffness reducing to zero after it yields). Zones of the stronger phase which lie along the path of a direct connection will be effectively used for stress transfer (such as Region 1), while those that do not will be much less effective (such as Region 2).

For the cylindrical model, the normalised effective stress distribution is shown for the stronger phase volume fraction of 39% in Figure 4.25. A brief examination of the weaker phase shows that it has completely yielded. As with the spherical model, this should be expected since the yield strength of the

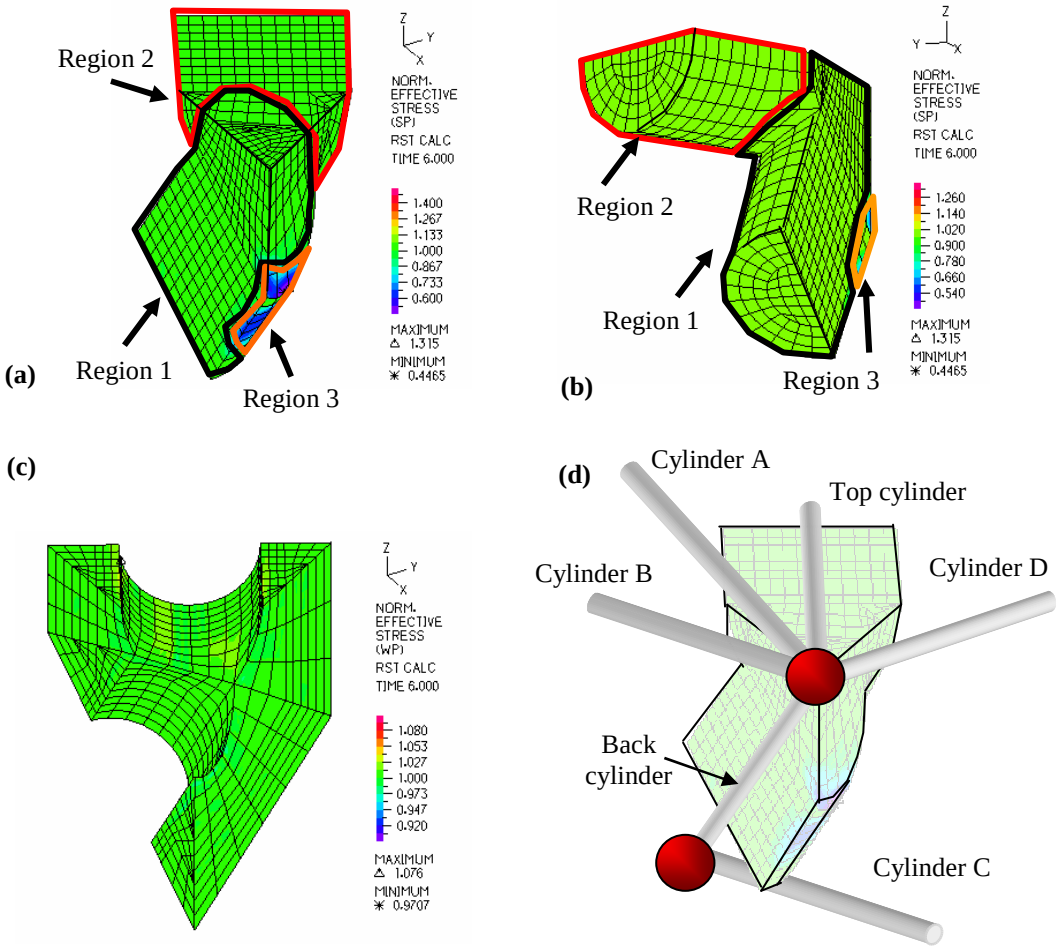

Figure 4.25. Normalised effective stress distribution in the cylindrical model (ϕ = 39%) at an overall applied strain of 0.005
(a) Stronger phase showing back, top and right-front surfaces
(b) Stronger phase showing left-front, bottom and back surfaces
(c) Weaker phase showing back, top and right-front surfaces
(d) Stronger phase showing adjacent cylinders

weaker phase is 110 MPa and the approximate stress at the strain of 0.005 is 144 MPa. The stronger phase for the cylindrical model appears to have almost completely yielded, with the exception of Region 3, at the heel of the cylinder intersection. This confirms that nearly complete yielding has occurred after the offset yield strength has been exceeded. The reasons for the lower stress in Region 3 of the cylindrical model are, in part, the same as those for Region 2 of the spherical model: neither region lies on the path of preferred stress transfer. In both cases, the region was underlain by the weaker phase causing stress to concentrate away from it towards paths with greater stiffness. Region 3 is also a zone of contraction for bending of the back cylinder, as was previously

discussed for elastic conditions in Sec. 4.2.2. The bending mechanism reduces the tensile stresses in Region 3, which leaves it non-yielded even when the rest of the stronger phase has yielded.

The non-yielded state of Region 3 raises the question as to why Region 2 of the cylindrical model does not have a lower stress similar to Region 3, since it is also underlain by the weaker phase. In this case, the back cylinder in Region 1 lies quite close to Region 2, making stress transfer through the intervening weaker phase more effective than below Region 3 (which must transfer stress through the weaker phase to Cylinder C). This allows Region 2 to sustain higher stresses at lower strains than Region 3, causing it to yield earlier. It could be expected that at slightly lower strains, both Regions 2 and 3 would be below the stronger phase yield strength, and at slightly higher strains, Region 3 would also yield (though no analysis to substantiate this claim will be considered here).

The fundamental qualitative plastic behaviour described above for examples of the spherical and the cylindrical models was seen for all the volume fractions of each model (though there were minor variations). To determine how each model changed with the volume fraction and contiguity of the phases, it was more instructive to consider the quantitative normalised effective stress distribution data provided in Figure 4.26 and Table 4.8. The data in this quantitative analysis were determined using the same means described in Sec. 4.2.2, and are therefore only a rough approximation of the volumetric stress distribution. However, due to the uniform stress state of each simulation, it is likely that the true volumetric stress distribution would be similar.

Investigation of either the figure or the table quickly reveals that both phases of each model had uniform stress distributions, with normalised mean effective stresses near 1.0. This signifies that both of the phases in each model have almost entirely yielded. Given the fact that the weaker phase was essentially completely yielded for both models, for all the volume fractions of the

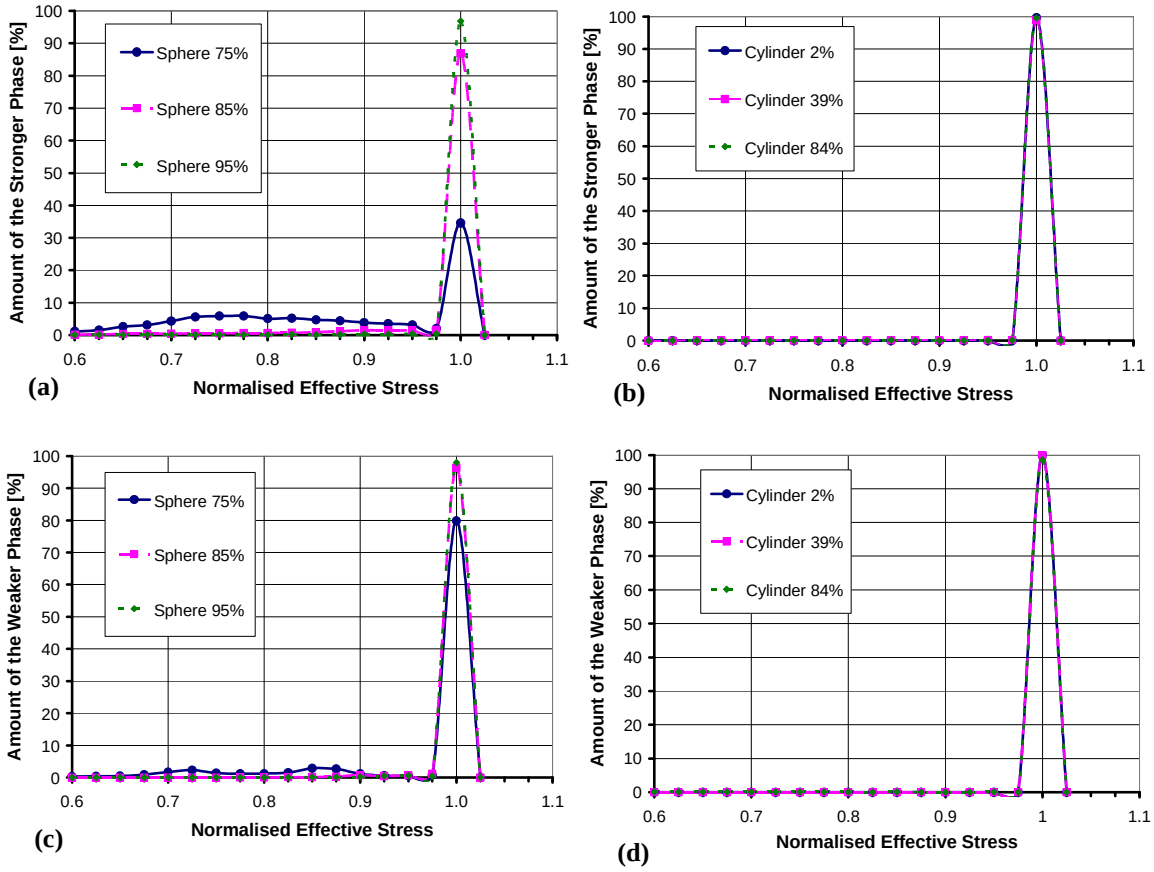

Figure 4.26. Quantitative normalised effective stress distribution for both models
(all cylindrical models were analysed at a strain of 0.005, strains for the spherical models were: 0.00145 for ϕ = 75%, 0.003 for ϕ = 85% and 0.00325 for ϕ = 95%)
(a) Stronger phase of spherical model
(b) Stronger phase of cylindrical model
(c) Weaker phase of spherical model
(d) Weaker phase of cylindrical model

phases, the rest of this analysis will consider only the stronger phase in each model.

The stronger phase in the spherical model does show some definite change in its effective stress distribution as the volume fraction and contiguity increase. Consideration of Figure 4.26(a) shows a significant increase in the uniformity of the stress distribution towards a normalised stress of 1.0 as the topological parameters increase. There are two likely reasons for this behaviour. The first is the different strains at which each of these simulations is being analysed. The 75% stronger phase volume fraction failed to converge past a strain of 0.00145, while the 85% and 95% volume fractions made it to

0.003 and 0.00325, respectively, before failing (see Fig. 4.20). To some extent, the smaller degree of uniformity in the 75% volume fraction simulation is due to the lower level of strain it is subjected to in this analysis. Higher levels of strain should cause a greater amount of yielding. However, it is important not to neglect that the increase in contiguity with the three volume fractions also increases the preferred stress path and the effectiveness of the phases to sustain load. This is the second reason for increasingly uniform behaviour around the phase's yield strength. As previously noted in the qualitative discussion, the effectiveness of the stronger phase to sustain load is based on its ability to lie within the preferred stress path to the bottom surface connection. With increasing volume fraction, the contiguity increases (see Fig. 4.8), allowing more of the stronger phase to transfer its stress directly within the phase through the bottom connection rather than through the weaker phase. By doing so, contiguity is able to increase the amount of the phase which is effective, thus increasing the uniformity about the yield strength of the stronger phase

Table 4.8. Statistical data for normalised effective stresses from the plastic microstructual analysis

(a) Data for the stronger phase of both models

(b) Data for the weaker phase of both models

(a)

Model	Stronger Phase					
	Volume Fraction [%]	Contiguity [%]	Mean Stress	Standard Deviation	Maximum Stress	Minimum Stress
Sphere	75	5	0.855	0.144	1	0.148
	85	47	0.978	0.077	1	0.226
	95	82	0.993	0.053	1	0.266
Cylinder	2	6	1.000	0.011	1	0.490
	39	34	0.998	0.018	1	0.521
	84	73	0.999	0.013	1	0.570

(b)

Model	Weaker Phase				
	Volume Fraction [%]	Mean Stress	Standard Deviation	Maximum Stress	Minimum Stress
Sphere	75	0.960	0.090	1	0.550
	85	0.997	0.016	1	0.740
	95	0.999	0.011	1	0.795
Cylinder	2	1.000	0.000	1	1.000
	39	1.000	0.000	1	1.000
	84	0.996	0.038	1	0.431

(the normalised effective stress of 1.0).

The cylindrical model results probably have a similar response to that of the spherical model, but it is too subtle to be noticeable. Examination of either Figure 4.26 or Table 4.8 shows little difference between the results and no obvious pattern. This similar state for all three volume fractions is likely due to the much higher strain level analysed for the cylindrical model compared to the spherical model (all cylindrical models were tested at a strain of 0.005, the highest spherical model only at 0.00325). As mentioned in the previous paragraph, increasing the applied strain tends to increase the uniformity of the stress distribution, so these responses should be expected.

It is also interesting to note the pattern of behaviour seen in the combined results for the stronger phase for both models when compared to the level of applied strain. Altogether the results were analysed around three different strains: the 75% spherical model at 0.00145, the 85% and 95% spherical models around 0.003, and the cylindrical models all at 0.005. Comparing the response of these three different groups, it is possible to see the general behaviour of the models, irrespective of volume fraction or phase shape, to increases in strain. As strain increases beyond the proportional limit, an increasing amount of the composite will yield, but major portions will remain below yielding, this is shown in the effective stress distribution of the spherical model at 75% volume fraction (see Fig. 4.26(a)). Further increases in strain expand the amount of stronger phase that has yielded such that it is nearly all behaving plastically by the 0.2% offset yield strength (see the effective stress distributions for the 85% and 95% spherical models in Fig. 4.26 and the stress-strain responses in Fig. J.1). While further strain increases slowly remove the final non-yielded portions of the stronger phase, almost all this strain should be resulting in plastic flow within previously yielded regions (see the effective stress distributions of the cylindrical models). This general response to slowly applied strain is considered likely by the author for all low yield strength ratio IPCs; however, since it has not been analysed using a single model at a single volume fraction it should not be deemed as conclusive.

The effect of phase shape, as previously mentioned, is not a simple factor to determine. It is related to the coupled influence of both the volume fractions and contiguities of the phases, and is best discussed in terms of the relative influences of these two topological parameters. Using the method of a linear aligning function of the coupled influence, described in Section 4.2.1, the coefficient on each parameter may be used to determine each parameter's relative effect. To simplify the analysis, the microstructural response of the stronger phase is investigated. The closest alignment of the mean normalised effective stress for each model is seen in Figure 4.27.

The coefficient for the volume fraction and contiguity of the stronger phase are zero and one, respectively. However, this alignment is so poor as to be completely without value. The reason for this poor alignment is likely due to the different strain levels at which each of the spherical model simulations was analysed. As has been noted several previous times, the low strain state to which the spherical model volume fractions reached (especially the 75% volume fraction) caused them to have significantly less uniform distributions of

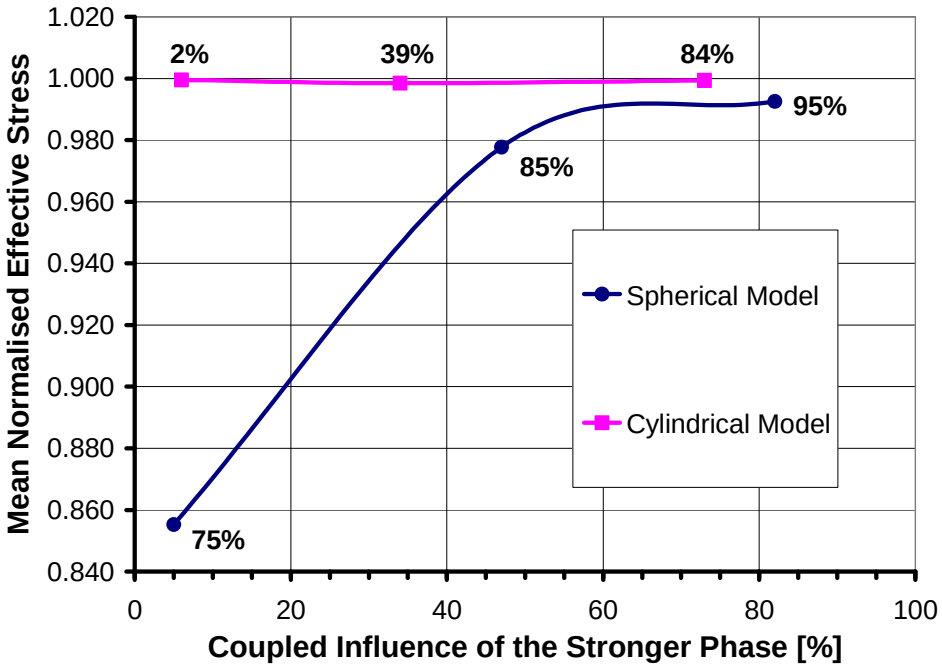

Figure 4.27. Aligned model data for the plastic microstructural analysis
Coupled influence is a function of volume fraction and contiguity (see Eq. 4.2).
The percentages on the figure are the volume fractions for the adjacent data points.

effective stress compared to those in the cylindrical models. Less uniform stress distributions produce lower mean normalised effective stresses and account for the much more curved behaviour seen for spherical model results in Figure 4.27. Even without being able to use these results, the previous analyses suggest that contiguity has a more significant effect for plastic behaviour than for elastic behaviour. This is due to the increased requirement of stress to transfer through the stronger phase after the weaker phase has yielded.

4.3.3 Summary of Plastic Behaviour for Interpenetrating Microstructures

The purpose of Section 4.3 was to investigate the plastic behaviour of two differently shaped IPCs. Numerical tests were performed to study the influences of the amounts of the phases, the shapes of the phases and the constituent properties of the phases on this behaviour. In order to ensure the discussion came to appropriate conclusions, two different methods were used to analyse the data. The first involved a study of the macroscopic behaviour produced by the models, and the second an examination of the microstructural mechanisms that led to the macroscopic behaviour. The results from the plastic behaviour were also compared to those from the elastic behaviour to distinguish how the composites responded differently after yielding.

The constituent phase properties affected the models through the yield strength ratio. The effect of the yield strength ratio was most easily seen by the divergence of the approximate bounds placed around the models' data. Since the bounds indicate potential plastic behaviour, the greater divergence for the yield strength ratio of 10, rather than 2, shows that the potential behaviour becomes more variable as the ratio grows. Comparing these bounds to the Hashin-Shtrikman bounds on elastic behaviour, it can be seen that the range of divergence is much greater for a yield strength ratio of 2 than for an elastic modular ratio of 2 (compare Figures 4.21(a) and 4.6(a)). This suggests that IPC plastic behaviour has greater possible variation than elastic behaviour, so parameters of the microstructural geometry are more important.

The bounds are also dependent on the volume fractions of the phases. The effective yield strength for both types of IPC increased with increasing amounts of the stronger phase, but of more interest was the changing divergence of the bounds from exceptionally tight at the extremes to highly divergent through intermediate volume fractions. For a yield strength ratio of 2, the greatest divergence was at a stronger phase volume fraction of 50%, and at a ratio of 10 at a volume fraction of 85%.

It could be seen in Figure 4.21 that the cylindrical model produced higher results than the spherical model. This improvement in the effective yield strength was explained through the different contiguities of the stronger phase in each model. The cylindrical model was able to have the same effective yield strength as the spherical model with less of the stronger phase because of a greater connection between distinct pieces of the stronger phase. The effect of shape on the plastic behaviour of an IPC was therefore linked to both the amount of the phases in the composite (represented by volume fraction) and the continuity of the stronger phase (represented by the contiguity).

Comparison of the relative influence of volume fraction and contiguity using a linear function of the two parameters determined that volume fraction had an effect approximately 1.7 times greater than the contiguity. When this result for the plastic analysis is compared to that for the elastic analysis, an important determination about IPC behaviour was found. Although volume fraction was the dominant parameter in both cases, contiguity clearly becomes more significant with yielding of the composite. When this is linked to the greater potential range of IPCs for plastic behaviour, the level of contiguity becomes a strong determinant of whether effective behaviour is near the upper or lower bound. Since the level of contiguity obtainable with a certain volume fraction of material is related to microstructural shape, the materials engineer needs to consider it in his or her designs.

The microstructural study was used to investigate the mechanisms that caused the behaviour found in the macroscopic study. The typical response of

both microstructural geometries was related to regional differences in stiffness. Stress was transferred preferentially along paths of least compliance connecting the stronger phase from the top surface to the bottom surface. This mechanism was studied against strain history in an approximate manner, to determine the influence of yielding. In general, it was found that increased strain produced early widespread yielding of the weaker phase with only more minor amounts of yielding in the stronger phase. At such strains, contiguity between pieces of the stronger phase is highly significant in providing a low compliance path for stress transfer since the stiffness of the weaker phase had reduced to zero. There was also a correlation between increasing uniformity of yielding in the stronger phase and increasing contiguity and volume fraction in the spherical model. Since increasing these parameters increases the size of the preferred stress path, it also improves in the effectiveness of the microstructure to sustain load. This directly contributes to higher effective yield strengths at the macroscopic level.

CHAPTER FIVE

CONCLUSION

5.1 SUMMARY

In recent years the increased ease with which composites can be manufactured has encouraged an interest in the behaviour of special composites that were not previously practical. One such type of composite is the interpenetrating phase composite (IPC), in which both phases are three-dimensionally continuous. The complexity of IPC microstructures makes it difficult to predict their mechanical behaviour based on traditional methods, so more research is required in order to obtain an accurate prediction for these materials. The focus of this study was the effect that microstructural phase shape has on the elastic and plastic behaviour of IPCs, though some other significant variables were also considered. As part of this study, an initial review of previous research into methods of investigating IPCs, and results regarding their elastic and plastic behaviours, was completed. After this, a numerical modelling program was undertaken to determine the effect of phase shape on the mechanical properties.

The first two sections of the literature review considered the possible methods for characterising the microstructure and studying the mechanical properties of IPCs. The most obvious method is to create an IPC for use in an experimental study. While this has the advantage of providing actual data about an IPC's performance, it is extremely difficult to examine the microstructure and isolate the influence of any specific variable. However, the topological parameters often developed from experimental work can be highly useful in characterising these materials for analytical or numerical studies.

A more simplified approach is to use general bounds or analogy models to estimate the behaviour of IPCs. Unfortunately, general bound methods are limited to studying elastic behaviour and analogy methods can often only determine trends. IPCs containing random microstructures have been modelled

using self-consistent methods that produce reasonably good approximations of the material behaviour. However, they cannot be used for directly studying the influence of microstructural parameters, since they consider the structure of the composite to be some statistical average of the actual structure. The microstructural geometry remains unimportant to this approach, so the effect of phase shape cannot be examined. Unit cell numerical models offer the best method for studying the response of different microstructures since they allow a simplified representation of the material. However, their periodic nature means they likely predict responses that are higher to those of more common random IPCs.

In the third section of the literature review, the results of previous studies on the elastic and plastic behaviour of IPCs were investigated. Although not considered as part of this study, thermal residual stresses have been shown to have an influence on the elastic and plastic behaviour of IPCs. Their effect is connected to the relative properties of the constituent phases, notably thermal expansion, stiffness and yield strength. In general, researchers have noted that thermal residual stresses significantly reduce the effective stiffness of an IPC but have a negligible effect on the effective yield strength. Considerable work has been completed in the elastic range of behaviour such that IPCs can be generally said to be well understood at service loads; work within the plastic range of behaviour is notably less extensive. For both types of behaviour, the constituent phase properties affect the range of the potential properties at a given volume fraction. The range can be calculated accurately for elastic behaviour using the Hashin-Shtrikman bounds (1963), but is less definite for plastic behaviour. There is also an improvement in both behaviours with an increase in the amount or volume fraction of the stiffer phase. The influence of continuity is much smaller for elastic behaviour as compared to plastic behaviour. While there is an increase in the effective stiffness of IPCs relative to non-IPC materials, it is minor compared to the increase in effective yield strength for IPC materials. Continuity is a property of the microstructure which is affected by parameters such as phase shape and spatial distribution. Shen

(1994b, 1995) studied the influence of shape and spatial distribution on two-phase composites (non-IPCs), but no research has yet determined the effect of these parameters on the properties of IPCs.

The unit cell method was chosen for the numerical modelling program because it allowed a simplified representation of the actual IPC and an explicitly defined microstructure. Two different unit cell models, one with a spherical phase and the other with a cylindrical phase, were created to determine the influence of shape differences. Both models could be used to investigate a variety of phase volume fractions and constituent properties. The spatial distribution of the phases in each model was based on the hexagonal close-packed (HCP) system. This system behaves isotropically, removing the need to consider direction dependence for the results. The boundary conditions applied to the models required that the unit cell consist of half a triangular prism in order to represent the periodic microstructure of the IPCs. The models were then used to simulate uniaxial tension tests for linear elastic and non-linear plastic conditions and solved using the finite element method (FEM). Results of these simulations provided the effective Young's modulus and effective yield strength of the IPCs for an analysis of the macroscopic behaviour. In addition, stress distributions of the elastic and plastic responses were used to develop an understanding of the microstructural behaviour mechanisms.

5.2 CONCLUSIONS

The results of both the macroscopic and microstructural components of this study lead to three basic conclusions. First, the shape of the phases affects their volume fraction and contiguity, both of which were linked to changes in macroscopic behaviour. Volume fraction influences behaviour through the amount of each phase in the IPC, and contiguity by improving the interconnection of the phases. Comparative analyses of the relative influence of these two factors showed that volume fraction was always more dominant, though contiguity was highly significant for plastic behaviour.

The second conclusion notes that the level of contiguity affects the path of least compliance. Microstructural stress analysis showed that differences in stiffness between the phases resulted in a preferred stress transfer path through local regions of high stiffness, the path of least compliance. The path of least compliance was influenced by the volume fraction of the phases and the relative difference in their stiffnesses, but the contiguous nature of the IPC geometry allowed the path to exist completely within the stiffer phase. Since contiguity is a measure of the interconnectedness of the stiffer phase, its value influences the size of the path of least compliance.

Finally, the path of least compliance affects how stress is transferred through the stiffer phase. The path of least compliance is the preferred stress path so how it transfers stress and the magnitude of stress it transfers influence macroscopic behaviour. An interesting result of the microstructural stress analysis was that the spherical model transferred stress in direct tension while the cylindrical model had direct tension and flexural mechanisms.

These basic conclusions lead to two improvements in understanding the phase shape – mechanical behaviour relationship for IPCs. For elastic behaviour it was found that phase shape's influence was minor. This was due to the relatively small stiffness differences between the constituent phases during elastic deformation. Without a great difference in phase stiffness, the path of least compliance is only slightly preferred as a stress transfer path. Therefore the path of least compliance is only of minor importance to overall stress transfer, and the contiguity that creates it is also of only slight importance. Since phase shape's influence has been linked to contiguity's influence, the effect of phase shape on the elastic behaviour of IPCs is minor.

In the case of plastic behaviour, however, the influence of phase shape is significant for IPCs. In contrast to the elastic behaviour, there is a great difference in stiffness between the constituent materials when one has yielded and the other is still experiencing elastic deformation. With a large stiffness difference, high magnitudes of stress are transferred through the path of least

compliance because its deformation is low relative to its surroundings. This makes the contiguity that creates the path of least compliance an important factor, and consequently the phase shape producing the contiguity highly significant.

5.3 RECOMMENDATIONS FOR FUTURE RESEARCH

The ultimate purpose of research such as that described in this thesis is an improvement in the understanding of a material's behaviour. Where this research ends is therefore somewhat arbitrary, since a perfect understanding of the behaviour would require an infinite amount of studying, not including any research that might be focussed on possible applications for the material. However, in the reasonably short term a number of goals can be defined.

The first set of research goals involves perfecting and completing the models already developed. The simulations investigated in this thesis only considered the sphere and cylindrical shapes as the stiffer or stronger phase, never as the surrounding material. Without much difficulty, simulations could be completed so that the more flexible or weaker phase was the sphere or cylinder shape. For some IPCs currently being developed, data such as these would be more representative than those produced as part of this study. The IPCs were also always modelled as two ductile phases, but there is a growing use of brittle phases in such groups as metal matrix composites (MMCs) and ceramic matrix composites (CMCs). Many of the composites within these groups either have interpenetrating microstructures or could have them, making it useful to provide data on the behaviour of a brittle/ductile IPC. This could be done by changing the non-linear portion of the models so that one phase behaved completely elastically (similar to a brittle constituent) while the other continued to have a ductile elasto-plastic response.

If the complete elastic behaviour of the IPCs studied here is particularly important, it would be valuable to define all the elastic constitutive properties. For an isotropic material, this requires finding only one additional elastic constant, since the effective Young's modulus has already been found as part

of the current study. It is possible that the effective Poisson's ratio could be calculated from the current uniaxial tension simulations or the effective bulk modulus could be found by simulating a state of hydrostatic pressure.

Finally, the geometry of each model should be improved or a more flexible discretisation algorithm found to ensure that numerical failure of the FEM simulations does not occur prior to failure of the material. This problem is likely to be more difficult, but if it is solved it would allow much more extensive study of plastic behaviour. This could include the definition of more basic properties such as the ultimate strength and toughness, and further modifications might produce results regarding fracture and fatigue.

Within the short term, but beyond the models already developed, would be the development of simple mechanistically based analytical relationships for IPC elastic and plastic behaviours. Such relationships would require additional understanding of how microstructural parameters affect behaviour. Besides the amount and shape of the phases, the influence of the spatial distribution and size distribution needs to be established. The size distribution could be studied by varying the size of the two cylinders in the cylindrical model. Geometry problems may occur, requiring a new discretisation, but the model should otherwise work relatively easily. The spatial distribution needs a different periodic microstructure to compare to the hexagonal close-packed (HCP) system already studied. An isotropic microstructure could be created using the diamond crystal lattice with its carbon tetrahedrons as a basis, although it will likely also be desirable to study anisotropic periodic microstructures in order to obtain more generalised data. This step is more difficult than the size distribution analysis since a completely new unit cell will need to be developed and perfected.

It is important to note that the size and spatial distribution parameters, as well as the phase shape and amount, affect the topological parameters of volume fraction and contiguity that are likely to appear as variables within a behaviour equation. It is therefore necessary to determine a generalised

definition for contiguity that may be applied universally. This means that besides being applicable to numerical models, it should be a useful, relatively easy measurement for experimental IPCs so that it does not remain confined to theoretical research. Taking into account the thermal residual stresses and other effects of processing, an approximate equation for the prediction of IPC behaviour should be possible. Although the equation would be based on data from ordered periodic microstructures, it is probable that the behaviour of IPCs with random microstructures would be similar to those with periodic microstructures on average. This would make the equation completely applicable to any general IPC and valuable for the prediction of both elastic and plastic behaviour.

REFERENCES

ADINA R&D, Inc. 2002a. ADINA – Automatic Dynamic Incremental Nonlinear Analysis, Version 8.0. Watertown, MA.

ADINA R&D, Inc. 2002b. *ADINA Theory and Modeling Guide, Volume I: ADINA*, Watertown, MA: 251-255, 475-480, 600-602.

Agrawal, P., Conlon, K., Bowman, K.J., Sun, C.T., Cichocki JR, F.R. and Trumble, K.P. 2003. Thermal residual stresses in co-continuous composites, *Acta Materialia*, 51: 1143-1156.

Aldrich, D.E. and Fan, Z. 2001. Microstructural characterisation of interpenetrating nickel/alumina composites, *Materials Characterization*, 47: 167-173.

Bathe, K.-J. 1996. *Finite Element Procedures*, Upper Saddle River, NJ: 148-225, 485-566.

Bowen, C.R., Perry, A., Kara, H. and Mahon, S.W. 2001. Analytical modelling of 3-3 piezoelectric composites, *Journal of the European Ceramic Society*, 21: 1463-1467.

Camus, P.P., Soffa, W.A., Brenner, S.S. and Miller, M.K. 1984. Quantification of interconnected microstructures by FIM, *Journal de Physique*, 45(12): C9 265-268.

Christensen, R.M. 1979. *Mechanics of Composite Materials*, John Wiley & Sons, Toronto: 52-61.

Clarke, D.R. 1992. Interpenetrating phase composites, *Journal of the American Ceramic Society*, 75(4): 739-758.

Coker, D.A., Torquato, S. and Dunsmuir, J.H. 1996. Morphology and physical properties of Fontainebleau sandstone via a tomographic analysis, *Journal of Geophysical Research*, 101(B8): 17497-17506.

Daehn, G.S., Starck, B., Xu, L., Elfishawy, K.F., Ringnalda, J. and Fraser, H.L. 1995. Elastic and plastic behavior of a co-continuous alumina/aluminum composite, *Acta Materialia*, 44(1): 249-261.

Dong, M, Leβle, P., Weber, U. and Schmauder, S. 1999. Mesomechanical modelling of composites containing FGM related interpenetrating microstructures based on micromechanical matricity models, *Materials Science Forum*, 308-311: 1000-1005.

Dong, M. and Schmauder, S. 1996. Modeling of metal matrix composites by a self-consistent embedded cell model, *Acta Materialia*, 44(6): 2465-2478.

Fan, Z. and Miodownik, A.P. 1993a. The deformation behaviour of alloys comprising two ductile phases – I. deformation theory, *Acta Metallurgica et Materialia*, 41(8): 2403-2413.

Fan, Z. and Miodownik, A.P. 1993b. The deformation behaviour of alloys comprising two ductile phases – 2. applications of the theory, *Acta Metallurgica et Materialia,* 41(8): 2415-2423.

Fan, Z., Tsakiropoulos, P. and Miodownik, A.P. 1992. Prediction of Young's modulus of particulate two-phase composites, *Materials Science and Technology*, 8: 922-929.

Feng, X.-Q., Mai, Y.-W. and Qin, Q.-H. 2003. A micromechanical model for interpenetrating multiphase composites, *Computational Materials Science*, 28: 486-493.

Flannery, B.P., Deckman, H.W., Roberge, W.G. and D'Amico, K.L. 1987. Three-dimensional x-ray microtomography, *Science*, 237: 1439-1444.

Fredrich, J.T., Menendez, B. and Wong, T.-F. 1995. Imaging the pore structure of geomaterials, *Science*, 268: 276-279.

Gurland, J. 1958. The measurement of grain contiguity in two-phase alloys, *Transactions of the American Institute of Mining, Metallurgical and Petroleum Engineers*, 212:452-455.

Hashin, Z. 1962. The elastic moduli of heterogeneous materials, *Journal of Applied Mechanics*, 29(1): 143-150.

Hashin, Z. and Shtrikman, S. 1963. A variational approach to the theory of the elastic behaviour of multiphase materials, *Journal of the Mechanics and Physics of Solids*, 11(2): 127-140.

Hoffman, M., Skirl, S., Pompe, W. and Rödel, J. 1999. Thermal residual strains and stresses in Al_20_3/Al composites with interpenetrating networks, *Acta Materialia*, 47(2): 565-577.

Lee, H.C. and Gurland, J. 1978. Hardness and deformation of cemented tungsten carbide, *Materials Science and Engineering*, 33: 125-133.

Lee, N.-S. and Bathe, K.-L. 1993. Effects of element distortions on the performance of isoparametric elements, *International Journal for Numerical Methods in Engineering*, 36: 3553-3576.

Leβle, P., Dong, M., Soppa, E. and Schmauder, S. 1998. Simulation of interpenetrating microstructures by self consistent matricity models, *Scripta Materialia*, 38(9): 1327-1332.

Leβle, P., Dong, M. and Schmauder, S. 1999. Self-consistent matricity model to simulate the mechanical behaviour of interpenetrating microstructures, *Computational Materials Science*, 15: 455-465.

Liu, W. and Köster, U. 1996. Microstructures and properties of interpenetrating alumina/aluminium composites made by reaction of SiO_2 glass performs with molten aluminium, *Materials Science and Engineering A*, 210(1): 1-7.

Microsoft Corporation. 2003. Microsoft Visual C++ .NET, Version 1.1.

Moore, R.E. 1979. *Methods and Applications of Interval Analysis*, Society for Industrial and Applied Mathematics, Philadelphia: 75-85.

Moukarzel, C. and Duxbury, P.M. 1994. Failure of three-dimensional random composites, *Journal of Applied Physics*, 76(7): 4086-4094.

Peng, H.X., Fan, Z. and Evans, J.R.G. 2001. Bi-continuous metal matrix composites, *Materials Science and Engineering A*, 303: 37-45.

Peng, H.X., Fan, Z., Evans, J.R.G. and Busfield J.J.C. 2000. Microstructure of ceramic foams, *Journal of the European Ceramic Society*, 20: 807-813.

Pezzotti, G. and Sbaizero, O. 2001. Residual and bridging microstress fields in Al_2O_3/Al interpenetrating network composite evaluated by fluorescence spectroscopy, *Materials Science and Engineering A*, 303: 267-272.

Ravichandran, K.S. 1994. Deformation behaviour of interpenetrating phase composites, *Composites Science and Technology*, 52(4): 541-549.

San Marchi, C., Kouzeli, M., Rao, R., Lewis, J.A. and Dunand, D.C. 2003. Alumina-aluminum interpenetrating-phase composites with three-dimensional periodic architecture, *Scripta Materialia*, 49: 861-866.

Shen, Y.-L. 1998. Thermal expansion of metal-ceramic composites: a three-dimensional analysis, *Materials Science and Engineering A*, 252: 269-275.

Shen, Y.-L., Needleman, A. and Suresh, S. 1994a. Coefficients of thermal expansion of metal-matrix composites of electronic packaging, *Metallurgical and Materials Transactions A*, 25A: 839-850.

Shen, Y.-L., Finot, M., Needleman, A. and Suresh, S. 1994b. Effective elastic response of two-phase composites, *Acta Metallurgica et Materialia*, 42(1): 77-97.

Shen, Y.-L., Finot, M., Needleman, A. and Suresh, S. 1995. Effective plastic response of two-phase composites, *Acta Metallurgica et Materialia*, 43(4):1701-1722.

Skirl, S., Hoffman, M., Bowman, K., Wiederhorn, S. and Rödel, J. 1998. Thermal expansion behaviour and macrostrain of Al_2O_3/Al composites with interpenetrating networks, *Acta Materialia*, 46(7): 2493-2499.

Torquato, S. 1991. Random heterogeneous media: microstructure and improved bounds on effective properties, *Applied Mechanics Review*, 44(2): 37-76.

Torquato, S. 2002. *Random Heterogeneous Materials: Microstructure and Macroscopic Properties*, Springer-Verlag, Inc. New York: 289.

Wegner, L.D. 1997. *PhD Thesis – Mechanical Behavior of Cellular Solid Composites: Microsandwich Foams and Interpenetrating Phase Composites*, Massachusetts Institute of Technology, Cambridge, MA: 76-86, 104-110, 135-145, 250-256.

Wegner, L.D. and Gibson, L.J. 2000a. The mechanical behaviour of interpenetrating phase composites – I: modelling, *International Journal of Mechanical Sciences*, 42: 925-942.

Wegner, L.D. and Gibson, L.J. 2000b. The mechanical behaviour of interpenetrating phase composites – II: a case study of a three-dimensionally printed material, *International Journal of Mechanical Sciences*, 42: 943-964.

APPENDIX A

VOLUME FRACTION OF SPHERE MATERIAL WITHIN THE HALF PRISM UNIT CELL

The following calculations illustrate how Equation 3.1, describing the volume fraction of sphere material within the half prism unit cell, was derived. It was desirable to consider a range of volume fractions based on changing the size of the spheres within the unit cell. These requirements were accommodated by solving for the volume fraction in terms of the spheres' radii and the centre-to-centre distance between spheres. The derivation is actually solved by considering the geometry of the prism unit cell (see Fig. A.1); however, since the ratio of sphere volume to unit cell volume is the same between the prism and half prisms their volume fractions are also the same.

- Volume of sphere material in the prism unit cell (see Fig. A.2):

$$V_s = V_{s(total)} - V_{s(lost)} \tag{A.1}$$

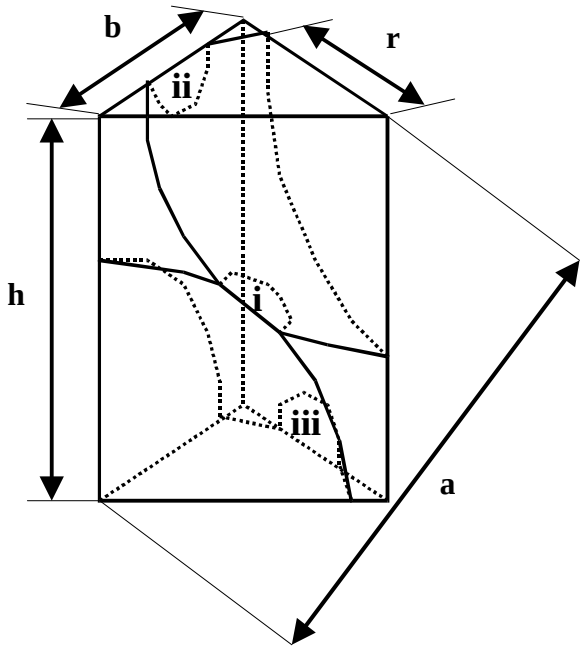

Figure A.1: Prism unit cell of spherical HCP system

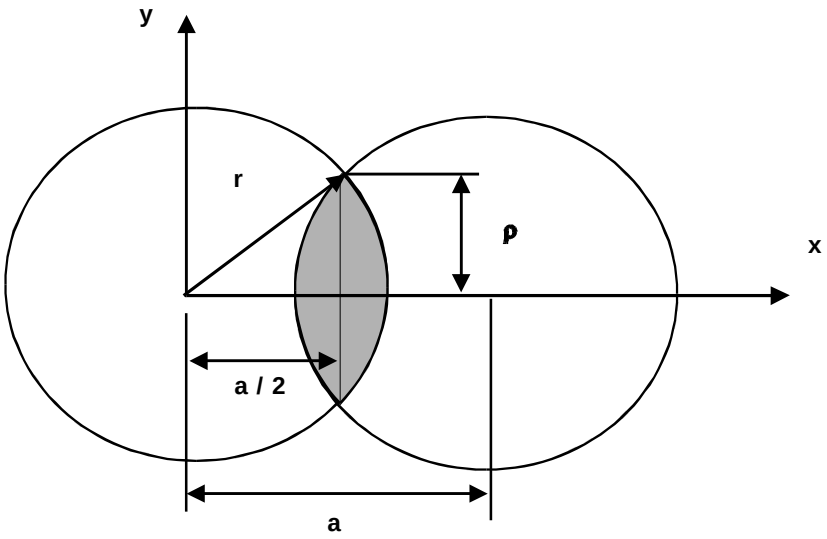

Figure A.2: Two spheres showing the volume lost due to intersection in grey

$V_{s(total)}$: *volume of sphere in unit cell ignoring the intersection*

$$= \frac{1}{6} V_{sphere}$$

$$= \frac{1}{6}\left(\frac{4}{3}\pi \cdot r^3\right)$$

$$= \frac{2}{9} r^3 \cdot \pi \qquad \text{(A.2)}$$

$V_{s(lost)}$: *volume of sphere lost due to the intersections (of the total volume lost half is from region i and a quarter from each of regions ii and iii, see Fig. A.1)*

$$= 2 \int_{\left(\frac{a}{2}\right)}^{r} \pi \cdot \left(r^2 - x^2\right) \cdot dx$$

$$= 2\pi\left[\left(\frac{2}{3} r^3\right) - \left(\frac{1}{2} r^2 a\right) + \left(\frac{1}{24} a^3\right)\right]$$

$$= \frac{4}{3} r^3 \pi\left[1 - \frac{3}{4}\left(\frac{a}{r}\right) + \frac{1}{16}\left(\frac{a}{r}\right)^3\right] \qquad \text{(A.3)}$$

$$V_s = \left(\frac{2}{9}r^3\pi\right) - \frac{4}{3}r^3\pi\left[1 - \frac{3}{4}\left(\frac{a}{r}\right) + \frac{1}{16}\left(\frac{a}{r}\right)^3\right]$$

$$= \left(\frac{2}{9}r^3\pi\right) - \left(\frac{4}{3}r^3\pi\right) + \left(r^2 a\pi\right) - \left(\frac{1}{12}a^3\pi\right)$$

$$= -\left(\frac{10}{9}r^3\pi\right) + \left(r^2 a\pi\right) - \left(\frac{1}{12}a^3\pi\right)$$

$$V_s = \frac{4}{3}r^3\pi\left[-\frac{5}{6} + \frac{3}{4}\left(\frac{a}{r}\right) - \frac{1}{16}\left(\frac{a}{r}\right)^3\right] \quad \text{(A.4)}$$

- Volume of prism unit cell (see Fig. A.1 and A.3):

$$V_p = h \cdot A_{triangle} \quad \text{(A.5)}$$

$A_{triangle}$: area of the top or bottom sides of the prism unit cell

$$= \frac{1}{2}(b)\left(\frac{a}{2}\right)$$

$$= \frac{1}{2}\left(\frac{a}{\sqrt{3}}\right)\left(\frac{a}{2}\right)$$

$$= \frac{a^2}{4\sqrt{3}} \quad \text{(A.6)}$$

h: height of prism unit cell

$$= \sqrt{a^2 - b^2}$$

$$= \sqrt{a^2 - \frac{a^2}{3}}$$

$$= \sqrt{\frac{2}{3}}a \quad \text{(A.7)}$$

$$V_p = \left(\sqrt{\frac{2}{3}}a\right)\left(\frac{a^2}{4\sqrt{3}}\right)$$

$$= \frac{a^3\sqrt{2}}{12}$$

$$= \frac{a^3}{6}\left(\frac{\sqrt{2}}{2}\right)$$

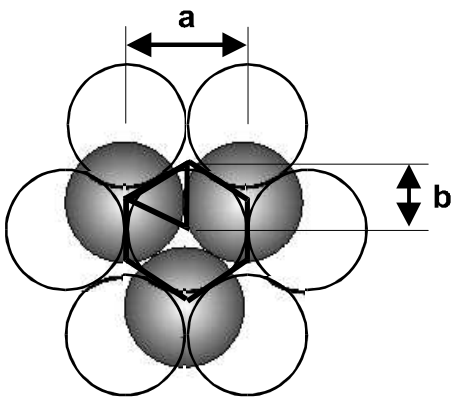

Figure A.3: Plan view of spherical HCP system

$$V_p = \frac{a^3}{6\sqrt{2}} \tag{A.8}$$

- Volume fraction of sphere material in the prism or half prism unit cells:

$$\phi_s = \frac{V_s}{V_p}$$

$$= \frac{\frac{4}{3}r^3\pi\left[-\frac{5}{6}+\frac{3}{4}\left(\frac{a}{r}\right)-\frac{1}{16}\left(\frac{a}{r}\right)^3\right]}{\left(\frac{a^3}{6\sqrt{2}}\right)}$$

$$= \frac{4}{3}r^3\pi\left[-\frac{5}{6}+\frac{3}{4}\left(\frac{a}{r}\right)-\frac{1}{16}\left(\frac{a}{r}\right)^3\right]\cdot\left(\frac{6\sqrt{2}}{a^3}\right)$$

$$\phi_s = 8\sqrt{2}\pi\left(\frac{r}{a}\right)^3\left[-\frac{5}{6}+\frac{3}{4}\left(\frac{a}{r}\right)-\frac{1}{16}\left(\frac{a}{r}\right)^3\right] \tag{3.1}$$

APPENDIX B

VOLUME FRACTION OF CYLINDER MATERIAL WITHIN THE HALF PRISM UNIT CELL

The volume fraction of the cylinder material within the half prism unit cell was determined through the use of a Monte Carlo simulation (also known as a single point probability function). This appendix includes the development of this Monte Carlo simulation, as well as the C++ program that was created to run it.

B.1 DEVELOPMENT OF THE MONTE CARLO SIMULATION

B.1.1 Surface Conditions for the Half Prism Unit Cell

The simulation generates groups of three random numbers that are used to define the coordinates of points within a space represented by the box shown in Figure B.1. The box dimensions are set such that the half prism unit cell lies completely within it, see Figure 3.8 for the coordinates of points 1 to 6. The relationship between points a, b and h are shown in Figures B.2 and B.3. All the generated random points must fall within the box but their coordinates must be tested against the following five surface criteria to determine if they are also within the half prism unit cell:

Top surface: $z \le h$ (B.1)

Back surface: $y \ge 0$ (B.2)

Left-front surface: $y \le \sqrt{3}x$ (B.3)

Right-front surface: $y \le \sqrt{3}(b - x)$ (B.4)

Bottom surface: $z \ge \frac{3b}{2\sqrt{2}} - \frac{x}{\sqrt{2}}$ (B.5)

x, y, z: *coordinates of the random points to be tested*

h: *height of the prism unit cell as defined in Figure B.2 or B.3*

b: *base edge length of prism unit cell as defined in Figure B.2 or B.3*

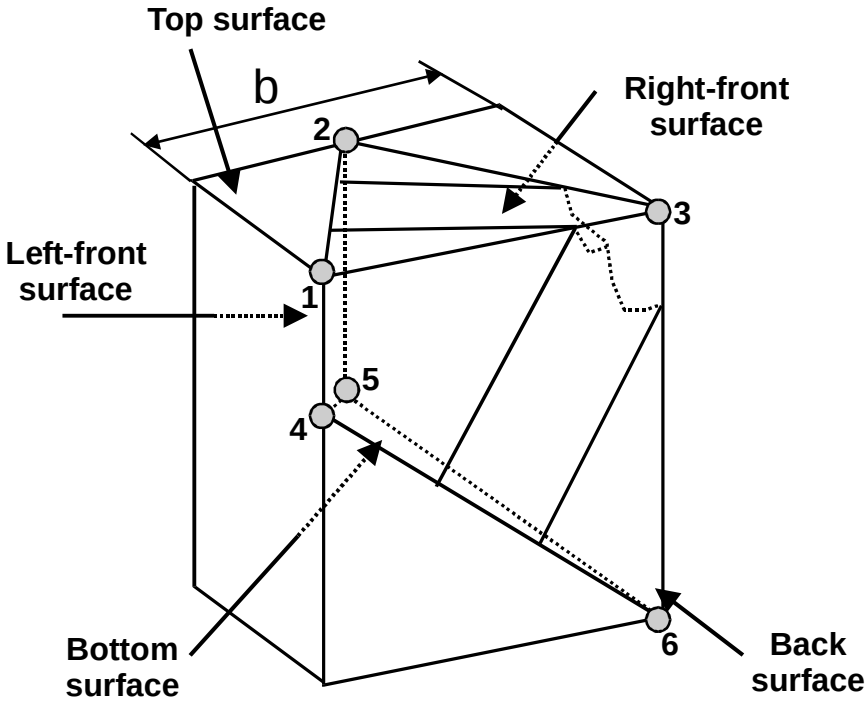

Figure B.1: Box for Monte Carlo simulation with half prism unit cell inside

The first two conditions (Equations B.1 and B.2) are ensured because of the dimensions of the box; however, the other three conditions may or may not be met so only a certain percentage of the random points fall within the unit cell.

B.1.2 Surface Conditions for the Back Cylinder

If a point falls within the half prism unit cell it then needs to be determined if it also falls within one of the cylinders. The conditions that define the surfaces of the cylinders are more complex than those of the half prism unit cell, so a detailed derivation is provided below. To start with, it is important to remember that if a coordinate system is such that one axis lines up with the longitudinal axis of the cylinder then the equation of the cylinder is simply that of a circle. For the back cylinder, consider Figure B.2, where the local z-axis coincides with the axis of the cylinder. The equation for the back cylinder is then simply:

$$(x')^2 + (y')^2 = \rho^2 \tag{B.6}$$

x', y': coordinates in terms of the local axes defined in Figure B.2

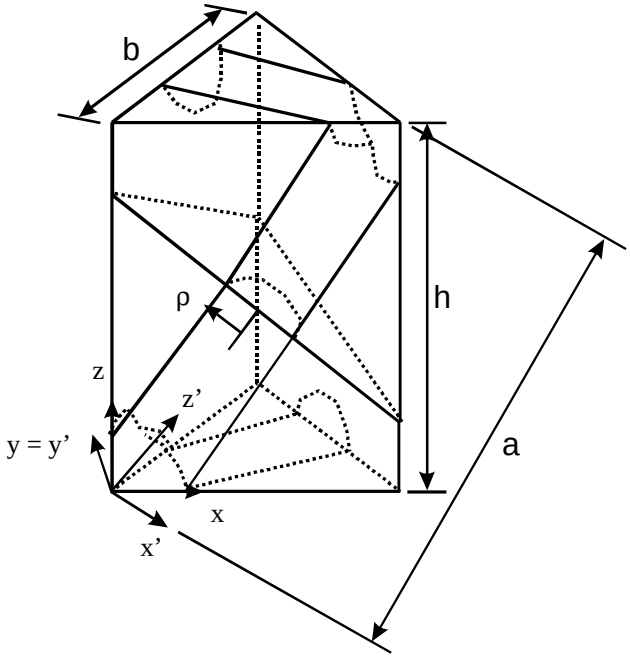

Figure B.2: Unit cell showing global axes and local axes for back cylinder

ρ: radius of cylinders as defined in Figure B.2

In order to use Equation B.6 in the Monte Carlo simulation it is necessary to relate it to the random points which reference the global coordinate system. This may be done by applying the normal laws for coordinate transformation to determine the local coordinates in the global system. The relationship between the local x and y-axes to the global axes in Figure B.2 is:

$$y' = y \tag{B.7}$$

$$x' = \left(\frac{h}{a}\right)x - \left(\frac{b}{a}\right)z \tag{B.8}$$

Substituting Equations B.7 and B.8 into Equation B.6, the following transformation of the equation for the back cylinder is found:

$$\left[\left(\frac{h}{a}\right)x - \left(\frac{b}{a}\right)z\right]^2 + [y]^2 = \rho^2$$

$$\left(\frac{h}{a}\right)^2 x^2 - 2\left(\frac{h \cdot b}{a^2}\right)x \cdot z + \left(\frac{b}{a}\right)^2 z^2 + y^2 = \rho^2$$

$$y \le \sqrt{\rho^2 - \left[\left(\frac{h}{a}\right)^2 x^2 - 2\left(\frac{h \cdot b}{a^2}\right) x \cdot z + \left(\frac{b}{a}\right)^2 z^2\right]} \tag{B.9}$$

In the Monte Carlo simulation the x and z-coordinates for each random point are inserted into Equation B.9 and a maximum y-coordinate calculated. If the actual y-coordinate for a tested point is less than the limiting value it is within the back cylinder and if it is greater than the limiting value it is not.

B.1.3 Surface Conditions for the Top Cylinder

The procedure for finding the condition for a point to lie within the top cylinder is similar to that just given for finding a point within the back cylinder. Consider Figure B.3 where the x' axis is aligned with the longitudinal axis of the top cylinder so that the equation for the top cylinder becomes:

$$(y')^2 + (z')^2 = \rho^2 \tag{B.10}$$

y', z': coordinates in terms of the local axes defined in Figure B.3

The transformation equations from Figure B.3 between the local to the global axes in this case are:

$$z' = z - h \tag{B.11}$$

$$y' = \left(\frac{1}{2}\right) x + \left(\frac{\sqrt{3}}{2}\right) y - \left(\frac{1}{2} b\right) \tag{B.12}$$

Substituting Equations B.11 and B.12 into Equation B.10, the equation for the top cylinder can be determined:

$$\left[\left(\frac{1}{2}\right) x + \left(\frac{\sqrt{3}}{2}\right) y - \left(\frac{1}{2} b\right)\right]^2 + (z - h)^2 = \rho^2$$

$$\left(\frac{1}{4}\right) x^2 + \left(\frac{3}{4}\right) y^2 + z^2 + \left(\frac{\sqrt{3}}{2}\right) x \cdot y - \left(\frac{1}{2} b\right) x - \left(\frac{\sqrt{3}}{2} b\right) y - (2h) z + \left(\frac{1}{4} b^2\right) + h^2 = \rho^2$$

$$z \ge h - \frac{1}{2}\sqrt{-x^2 - 3y^2 - \left(2\sqrt{3}\right) x \cdot y + (2b) x + \left(2\sqrt{3} b\right) y - b^2 + 4\rho^2} \tag{B.13}$$

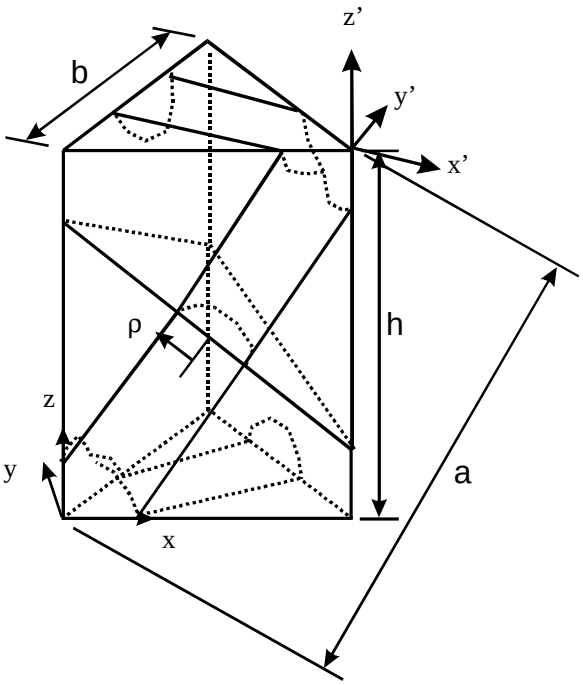

Figure B.3: Unit cell showing global axes and local axes for the top cylinder

Equation B.13 is therefore the condition determining if a random point is within the top cylinder or not. It is also important to note that for a point to fall within the intersection region of the top cylinder and back cylinder it must meet the conditions of Equations B.9 and B.13.

B.1.4 Volume Fraction of Cylinder Material

Calculation of the volume fraction of the cylinders within the half prism unit cell is based on the direct relationship between the volume fraction and the number fraction of the random points. The solution can be found by counting the number of random points that passed the cylinder test criteria and dividing this number by the total number of points that passed the half prism unit cell criteria. Note that it is necessary to subtract from the number of random points within the cylinders the number of points at the cylinders' intersection, since these points are counted once in the top cylinder and once in the back cylinder. The volume fraction of cylinders in the half prism unit cell is then:

$$\phi_c = \left(\frac{n_c}{n_{hp}} \right) \cdot 100 \qquad (3.27)$$

$$n_c = n_{bc} + n_{tc} - n_i \tag{3.28}$$

ϕ_c: *volume fraction of cylinders in half prism unit cell*

n_{hp}: *number of points in half prism unit cell*

n_c: *number of points in cylinders*

n_{bc}: *number of points in back cylinder (Eq. B.9)*

n_{tc}: *number of points in top cylinder (Eq.B.13)*

n_i: *number of points in the intersection (Eq. B.9 and B.13)*

B.2 C++ PROGRAM TO RUN THE MONTE CARLO SIMULATION

```
//CHCP_VF 1.1: Volume Fraction of Cylindrical HCP Model using Single
//Point Probability
//
//   Last Modified: Apr.8, 2004

//Step 1: Preprocessor Directives
#include <iostream>
#include <fstream>
#include <stdlib.h>
#include <math.h>
#include <iomanip>
#include <time.h>

using namespace std;

int main()
{
      //Step 2: Initial Information
          //Step 2.1: Variable Declarations
            int i;
            int nhp, nbc, ntc, ncr, nmat, max;
            double rho1, rho2;
            double x, y, z;
            double zmin, zmax;
            double yf, zbot;
            double x1, x2, y1, y2;
            double ybc1, ybc2, ztc1, ztc2;
            double vfhp, vfcyl, vftb, vfcr, vfmat;

            //Step 2.2: Initialize Variables
            i = 0;
            x = y = z = 0;
            zmin = 1.0/sqrt(2.0);
            zmax = 2.0 * sqrt(2.0);

            nhp = nbc = ntc = ncr = nmat = 0;

            x1 = x2 = y1 = y2 = 3.0;
```

```
        yf = 0.0;
        zbot = 3.0;
        ybc1 = ybc2 = -0.1;
        ztc1 = ztc2 = 3.0;

        //Step 2.3: Input from User
        cout << "CHCP_VF 1.1: Volume Fraction of"<< endl
             << " Cylindrical HCP Model using " << endl
             << " Single Point Probability";
             << endl << endl;

        cout << "(a) Provide the number of values" << endl
             << "    pseudo-random that should be generated:  ";
        cin >> max;
        cout << "(b) Provide the radius of the back" << endl
             << " cylinder" << endl
             << "(value between 0 and 1.0):  ";
        cin >> rho1;
        cout << "(c) Provide the radius of the top << endl
             << " surface cylinder" << endl
             << " (value between 0 and 1.0):  ";
        cin >> rho2;


//Step 3: Generate Random Numbers and Locate their Positions
srand(time(NULL));
for (i = 1; i <= max; i++)
{
        x = double(rand())/RAND_MAX * 2.0;
        y = double(rand())/RAND_MAX * sqrt(3.0);
        z = zmin + double(rand())/RAND_MAX * (zmax - zmin);

        //Step 3.1: Find Points within Half Prism Unit Cell
        if (x <= 1.0)
              yf = sqrt(3.0) * x;
        else
              yf = sqrt(3.0) * (2.0 - x);

        zbot = (1.0/sqrt(2.0)) * (3.0 - x);

        if (y <= yf && z >= zbot)
        {
              nhp = nhp + 1;

              //Step 3.2: Find Points within Back Cylinder
              x1 = (1.0/sqrt(2.0)) * z;
              x2 = x - x1;

              ybc1 = (rho1 * rho1) - (2.0/3.0) * (x2 * x2);

              if (ybc1 < 0.0)
                    ybc2 = ybc1;
              else
                    ybc2 = sqrt(ybc1);

              if (y <= ybc2)
              {
```

```
                        nbc = nbc + 1;
                }

                //Step 3.3: Find Points within Top Cylinder
                y1 = (sqrt(3.0)/3.0) * (2.0 - x);
                y2 = y - y1;

                ztc1 = (rho2 * rho2) - (3.0/4.0) * (y2 * y2);

                if (ztc1 < 0.0)
                        ztc2 = 3.0;
                else
                        ztc2 = (2.0 * sqrt(2.0)) - sqrt(ztc1);

                if (z >= ztc2)
                {
                        ntc = ntc + 1;

                        //Step 3.4: Find Points within Intersection of
                                    Cylinders
                        if (y <= ybc2)
                        {
                                ncr = ncr + 1;
                        }
                }

                if (z < ztc2 && y > ybc2)
                        nmat = nmat + 1;
        }

    //Step 4: Calculations and Output
    vfhp = ((double)nhp/(double)max) * 100;
    vfcyl = (((double)nbc + (double)ntc - (double)ncr)/(double)nhp)
             * 100;

    cout << "Volume Fraction of Box that is the Half Prism" << endl
         << "   Unit Cell:  ";
    cout << vfhp << endl;

    cout << "Volume Fraction of Half Prism Unit Cell that" << endl
         << " is Cylinder:  ";
    cout << vfcyl << endl;

    return 0;
}
```

APPENDIX C

BOUNDARY CONDITIONS FOR A HEXAGONAL CLOSED-PACKED UNIT CELL

The boundary conditions for both the spherical and cylindrical models were the same since they were based on the constant spatial distribution of the phases. In this thesis, the spatial distribution chosen was the hexagonal closed-packed system. The material in this appendix provides the C++ computer program used to create a text file that applies the boundary conditions to the non-linear plastic models in ADINA. A similar program was used for producing a text file for the conditions of the linear elastic models. In order to change the following program so that it produces linear elastic text files, it is necessary to delete the lines that are italicised in Steps 2.1, 2.5 and 6.1. Greater detail about the use of these boundary conditions may be found in Section 3.3.

C.1 C++ PROGRAM TO APPLY BOUNDARY CONDITIONS

```
//HCPP_BC_1.0: Boundary Conditions for Hexagonal-Closed-Packed Model
//
//   Last Modified: Jul.23,2003

//Step 1: Preprocessor Directives
#include <iostream>
#include <fstream>
#include <stdlib.h>
#include <math.h>
#include <iomanip>

using namespace std;

int main()
{
      //Step 2: Initial Information
          //Step 2.1: Variable Declarations
           const int MAX1 = 35000;
           const int MAX2 = 2000;
           const int MAX3 = 7000;
           const int MAXNAME = 80;
           char date[MAXNAME];
           char gmd[MAXNAME];
           char nodefile[MAXNAME];
           char model[MAXNAME];
           int nstep;
           double factor;
```

```
  //(3: Read Node Coordinates)
  static double x[MAX1], y[MAX1], z[MAX1];
  int n[MAX1];
  int check, ntot;
  ifstream infile;
  //(4: Find Positions of Nodes)
  int i, k;
  double toler;
      //(Count Variables)
      int ALcnt, Tcnt, LFcnt, RFcnt;
      int Bcnt, LBcnt, RBcnt;
      int Fcnt, BLFcnt, BRFcnt;
      int APcnt, TLBcnt;
      int OTcnt, OLFcnt, ORFcnt;
      //(Flag Variables)
      int ALflag[MAX3], Tflag[MAX3];
      int LFflag[MAX3], RFflag[MAX3];
      int LBflag[MAX3], RBflag[MAX3];
      int BLFflag[MAX3];
      int TLBflag[MAX3];
      //(List Variables)
      int AL[MAX2], T[MAX2], LF[MAX2], RF[MAX2];
      int B[MAX2], LB[MAX2], RB[MAX2];
      int F[MAX2], BLF[MAX2], BRF[MAX2];
      int AP[MAX2], TLB[MAX2];
      int OT[MAX2], OLF[MAX2], ORF[MAX2];
      //(Difference Variables)
      double dx1, dy1, dz1, dz2;
  //(5: Pair Nodes on Bottom Surface)
  int j, paircnt;
  int pair[MAX2];
  //(6: Apply Boundary Conditions)
  int constraintname;
  double betacoeff1, betacoeff2;

//Step 2.2: Initialize Variables
  //(3: Read Nodal Coordinates)
  factor = nstep = ntot = 0;
  k = 0;
  //(4: Find Nodal Positions)
  toler = 0.0001;
        ALcnt = Tcnt = 0;
        LFcnt = RFcnt = 0;
        Bcnt = LBcnt = RBcnt = 0;
        Fcnt = BLFcnt = BRFcnt =0;
        APcnt = TLBcnt = 0;
        OTcnt = OLFcnt = ORFcnt = 0;
  //(5: Pair Nodes on Bottom Surface)
  paircnt = 0;
  for (i = 1; i <= MAX3; i++)
  {
        ALflag[i] = 0;
        Tflag[i] = 0;
        LFflag[i] = 0;
        RFflag[i] = 0;
        LBflag[i] = 0;
        RBflag[i] = 0;
```

```
      BLFflag[i] = 0;
      TLBflag[i] = 0;
 }

//Step 2.3: Open Output File
 cout << "HCPP_BC_1.0: Boundary Conditions for”
      << “ Hexagonal Closed-Packed Model"
      << endl << endl;

 cout << "  (a) Provide the date (M.D,Y):  ";
 cin >> date;
 cout << endl;
 cout << "  (b) Provide the model output"  << endl
      << "      file name:  ";
 cin >> model;
 cout << endl;

 ofstream outfile;
 outfile.open(model);

 if (outfile.fail())
 {
      cout << "WARNING: The file in Step 2.3 was not”
           << “ opened." << endl;
      exit(1);
 }

 outfile << setiosflags(ios::fixed)
         << setiosflags(ios::showpoint)
         << setprecision(7);

 //Step 2.4: Initial Formatting
 outfile << "*"                                    << endl
 << "*   Hexagonal-Closed-Packed Plastic Model"  << endl
 << "*"                                          << endl
 << "*   Created on:  "
 << date                                         << endl
 << "*"                                          << endl
 << "Database New   Save = No   Prompt = No"     << endl
 << "FEProgram ADINA"                            << endl
 << "Control Fileversion = v75"                  << endl
 << "FEProgram   Program = ADINA"                << endl
 << "Master   Analysis = Static,"                << endl
 << "         IDOF = 000111,"                    << endl
 << "         Reactions = Yes,"                  << endl
 << "         Solver = Iterative"                << endl;

 //Step 2.5: Non-Linear Solution Data
 outfile << "*"                                  << endl
 << "*   Non-Linear Solution Data"               << endl
 << "Kinematics Displacements = Large Strains = Large"
 << endl
 << "Iteration   Method = Full-Newton"           << endl
 << "Tolerances Iteration  ETOL = 0.001"         << endl;

 cout << "  (c) Number of Solution Steps: ";
 cin >> nstep;
```

```
        cout << endl;

        outfile << "Timestep      Name = 1"             << endl
                << setw(5) << nstep << setw(5) << 1     << endl
                << "Timefunction Name = 1"        << endl;

        cout << "  (d) Multiplication Factor for Displacement: "
             << endl;
        outfile << setw(5) << 0 << setw(15) << 0 << endl;
        for (i = 1; i <= nstep; i++)
        {
              outfile << setw(5) << i;
              cout << "      Factor for Step " << i << ": ";
              cin >> factor;
              outfile << setw(15) << factor << endl;
        }
        cout << endl;

        //Step 2.6: Read Geometry - Material - Discretization Data
        cout << "  (e) Provide geometry-material-discretization"
             << endl
             << "      file name:  ";
        cin >> gmd;
        cout << endl;

        outfile << "*"
                << endl
                << "*    Read Geometry-Material-Discretization”
                << “ File" << endl
                << "Read File = "
                << gmd                                  << endl;

//Step 3: Read Node Coordinates
cout << "  (f) Provide the node coordinate"
     << endl
     << "      file name:  ";
cin >> nodefile;
cout << endl;

infile.open(nodefile);

if (infile.fail())
{
      cout << "WARNING: The file was not successfully opened."
           << endl
           << " Please check that the file currently exists."
           << endl;
      exit(1);
}

while ((check = infile.peek()) != EOF)
{
      k = k + 1;
      infile >> n[k];
      infile >> x[n[k]] >> y[n[k]] >> z[n[k]];

      ntot = ntot + 1;
```

```
}

      cout << "Input Model Information to ADINA:"        << endl
           << "Total Nodes:                  " << ntot  << endl;

infile.close();

//Step 4: Find Positions of Nodes
for (i = 1; i <= ntot; i++)
{
      //Step 4.1: Axis of Anti-symmetry
      dx1 = fabs(x[n[i]] - 1.0);
      dz1 = fabs(z[n[i]] - sqrt(2.0));

      if (dx1 <= toler && dz1 <= toler)
      {
            ALflag[i] = 1;
            ALcnt = ALcnt + 1;
            AL[ALcnt] = n[i];
      }

      //Step 4.2: Top Surface
      dz1 = fabs(z[n[i]] - (2 * sqrt(2.0)));

      if (dz1 <= toler)
      {
            Tflag[i] = 1;
            Tcnt = Tcnt + 1;
            T[Tcnt] = n[i];
      }

      //Step 4.3: Left-Front Surface
      dy1 = fabs(y[n[i]] - (sqrt(3.0) * x[n[i]]));

      if (dy1 <= toler)
      {
            LFflag[i] = 1;
            LFcnt = LFcnt + 1;
            LF[LFcnt] = n[i];
      }

      //Step 4.4: Right-Front Surface
      dy1 = fabs(y[n[i]] - (sqrt(3.0) * (2.0 - x[n[i]])));

      if (dy1 <= toler)
      {
            RFflag[i] = 1;
            RFcnt = RFcnt + 1;
            RF[RFcnt] = n[i];
      }

      //Step 4.5: Back Surface
      if (y[n[i]] <= toler)
      {
            Bcnt = Bcnt + 1;
            B[Bcnt] = n[i];
      }
```

```
	//Step 4.6: Bottom Surface
dz1 = fabs(z[n[i]] - ((3.0/sqrt(2.0)) - (x[n[i]]/sqrt(2.0))));

	if (dz1 <= toler && ALflag[i] == 0)
	{
		dz2 = (z[n[i]] - sqrt(2.0));

		if (dz2 > toler)
		{
			LBflag[i] = 1;
			LBcnt = LBcnt + 1;
			LB[LBcnt] = n[i];
		}

		if (dz2 < toler)
		{
			RBflag[i] = 1;
			RBcnt = RBcnt + 1;
			RB[RBcnt] = n[i];
		}
	}

	//Step 4.7: Front Line
	dy1 = fabs(y[n[i]] - sqrt(3.0));

	if (dy1 <= toler)
	{
		Fcnt = Fcnt + 1;
		F[Fcnt] = n[i];
	}

	//Step 4.8: Bottom Left-Front Line
	if (LFflag[i] == 1 && LBflag[i] == 1)
	{
		BLFflag[i] = 1;
		BLFcnt = BLFcnt + 1;
		BLF[BLFcnt] = n[i];
	}

	//Step 4.9: Bottom Right-Front Line
	if (RFflag[i] == 1 && RBflag[i] == 1)
	{
		BRFcnt = BRFcnt + 1;
		BRF[BRFcnt] = n[i];
	}

	//Step 4.10: Axis Point
	if (ALflag[i] == 1 && y[n[i]] <= toler)
	{
		APcnt = APcnt + 1;
		AP[APcnt] = n[i];
	}

	//Step 4.11: Top Left Back Corner (Master Node)
	if (x[n[i]] <= toler && y[n[i]] <= toler && Tflag[i] == 1)
	{
```

```
                TLBflag[i] = 1;
                TLBcnt = TLBcnt + 1;
                TLB[TLBcnt] = n[i];
        }

        //Step 4.12: Other Top Surface
        if (Tflag[i] == 1 && TLBflag[i] == 0)
        {
                OTcnt = OTcnt + 1;
                OT[OTcnt] = n[i];
        }

        //Step 4.13: Other Left-Front Surface
        if (LFflag[i] == 1 && TLBflag[i] == 0 && dy1 > toler)
        {
                OLFcnt = OLFcnt + 1;
                OLF[OLFcnt] = n[i];
        }

        //Step 4.14: Other Right-Front Surface
        if (RFflag[i] == 1 && dy1 > toler && RBflag[i] == 0)
        {
                ORFcnt = ORFcnt + 1;
                ORF[ORFcnt] = n[i];
        }
}

//Step 5: Pair Nodes on Bottom Surface
        //Step 5.1: Check if Equal Number of Nodes on Upper and
        //          Lower Parts
        if (LBcnt == 0 && RBcnt == 0)
        {
                cout << "WARNING: Step 5.1 Check: No nodes on”
                     << “ anti-symmetric plane." << endl
                     << "         DISCRETIZATION ERROR" << endl;
                exit(1);
        }

        if (LBcnt != RBcnt)
        {
                cout << "WARNING: Step 5.1 Check: Number of nodes”
                     << “ on upper part of plane does not "
                     << "equal number on lower." << endl
                     << "         DISCRETIZATION ERROR" << endl;
                exit(1);
        }

        //Step 5.2: Pair Nodes for Anti-symmetric Boundary
        //          Condition
        for (i = 1; i <= RBcnt; i++)
        {
                for (j = 1; j <= LBcnt; j++)
                {
                  dz1 = fabs((z[RB[i]] + z[LB[j]])/2.0 - sqrt(2.0));
                  dy1 = fabs(y[RB[i]] - y[LB[j]]);

                      if (dz1 <= toler && dy1 <= toler)
```

```
                {
                        paircnt = paircnt + 1;
                        pair[i] = LB[j];
                }
        }
}

if (paircnt != RBcnt)
{
        cout << "WARNING: Step 5.2 Check: Insufficient"
             << " node pairs." << endl
             << "         DISCRETIZATION ERROR" << endl;
        exit(1);
}

cout << "Masters for Slaves on Bottom (paircnt):"
     << paircnt << endl
     << endl;

//Step 6: Apply Boundary Conditions
outfile << "*"                                  << endl
        << "*   Boundary Conditions"            << endl;

//Step 6.1: Top Left Back Corner (Master Node)
outfile << "*"                                        << endl
        << "*   Top Left Back Corner (Master Node)"<< endl
        << "Apply Displacement   Substructure = 0"
        << " Reuse = 1" << endl
        << "*Node     Direction    Factor    Ncur"<< endl;

outfile << setw(5)  << TLB[1]
        << setw(10) << 3
        << setw(16) << 0.0014142
        << setw(5) << 1 << endl;

//Step 6.2: Back Surface
outfile << "*"                                  << endl
        << "*   Back Surface"                   << endl
        << "Boundaries   Substructure = 0"      << endl
        << "*Node     ux     uy     uz"         << endl;

for (i = 1; i <= Bcnt; i++)
{
        outfile << setw(5) << B[i]
                << setw(9) << "free"
                << setw(8) << "fixed"
                << setw(6) << "free" << endl;
}

//Step 6.3: Front Line
outfile << "*"                                  << endl
        << "*   Front Line"                     << endl
        << "Boundaries   Substructure = 0"      << endl
        << "*Node     ux     uy     uz"         << endl;

for (i = 1; i <= Fcnt; i++)
{
```

```
      outfile << setw(5) << F[i]
              << setw(9) << "fixed"
              << setw(7) << "free"
              << setw(7) << "free" << endl;
}

//Step 6.4: Axis of Anti-symmetry
outfile << "*"                                    << endl
        << "*   Axis of Antisymmetry"             << endl
        << "Boundaries   Substructure = 0"        << endl
        << "*Node     ux     uy     uz"           << endl;

for (i = 1; i <= ALcnt; i++)
{
      outfile << setw(5)  << AL[i]
              << setw(10) << "fixed"
              << setw(8)  << "free"
              << setw(8)  << "fixed" << endl;
}

//Step 6.5: Axis Point
outfile << "*"                                    << endl
        << "*   Axis Point"                       << endl
        << "Boundaries   Substructure = 0"        << endl
        << "*Node     ux     uy     uz"           << endl;

outfile << setw(5)  << AP[1]
        << setw(10) << "fixed"
        << setw(8)  << "fixed"
        << setw(8)  << "fixed" << endl;

//Step 6.6: Top Surface
betacoeff1 = 1.0;
constraintname = 1;

outfile << "*"                                     << endl
        << "*   Top Surface"                      << endl
        << "Constraint-Node"
        << "   Name = " << constraintname
        << "   SlaveNode = " << OT[1]
        << "   SlaveDOF = " << "'Z-Translation'" << endl;

for (i = 1; i <= OTcnt; i++)
{
      outfile << setw(5) << TLB[1] << " 'Z-Translation' "
              << betacoeff1 << " "
              << setw(5) << OT[i]  << " 'Z-Translation' "
              << endl;
}

//Step 6.7: Bottom Surface
betacoeff1 = -1.0;
betacoeff2 = -1/sqrt(3.0);
constraintname = 2;

outfile << "*"                                    << endl
        << "*   Bottom Surface"                   << endl
```

```
        << "Constraint-Node"
        << "   Name = " << constraintname
        << "   SlaveNode = " << RB[1]
        << "   SlaveDOF = " << "'X-Translation'" << endl;

for (i = 1; i <= paircnt; i++)
{
dy1 = fabs(y[RB[i]] - (sqrt(3.0) * (2.0 - x[RB[i]])));

      if (dy1 <= toler)
      {
        outfile << setw(5) << TLB[1]
            << " 'X-Translation' " << betacoeff1 << " "
            << setw(5) << RB[i]   << " 'X-Translation' "
            << endl
            << setw(5) << pair[i] << " 'Y-Translation' "
            << betacoeff2 << " "
            << setw(5) << RB[i]   << " 'X-Translation' "
            << endl;
      }

      if (dy1 > toler)
      {
        outfile << setw(5) << pair[i]
            << " 'X-Translation' " << betacoeff1 << " "
            << setw(5) << RB[i]   << " 'X-Translation' "
            << endl;
      }
}

betacoeff1 = 1.0;
constraintname = 3;

outfile << "*"                                    << endl
        << "Constraint-Node"
        << "   Name = " << constraintname
        << "   SlaveNode = " << RB[1]
        << "   SlaveDOF = " << "'Y-Translation'" << endl;

for (i = 1; i <= paircnt; i++)
{
  outfile << setw(5) << pair[i]
          << " 'Y-Translation' " << betacoeff1 << " "
          << setw(5) << RB[i]   << " 'Y-Translation' "
          << endl;
}

betacoeff1 = -1.0;
constraintname = 4;

outfile << "*"                                    << endl
        << "Constraint-Node"
        << "   Name = " << constraintname
        << "   SlaveNode = " << RB[1]
        << "   SlaveDOF = " << "'Z-Translation'" << endl;

for (i = 1; i <= paircnt; i++)
```

```
{
  outfile << setw(5) << pair[i]
          << " 'Z-Translation' " << betacoeff1 << " "
          << setw(5) << RB[i]   << " 'Z-Translation' "
          << endl;
}

//Step 6.8: Left-Front Surface
betacoeff1 = 1.0;
betacoeff2 = 1/sqrt(3.0);
constraintname = 5;

outfile << "*"                                    << endl
        << "*   Left Front Surface"               << endl
        << "Constraint-Node"
        << "   Name = " << constraintname
        << "   SlaveNode = " << OLF[1]
        << "   SlaveDOF = " << "'X-Translation'" << endl;

for (i = 1; i <= OLFcnt; i++)
{
  outfile << setw(5) << TLB[1]
          << " 'X-Translation' " << betacoeff1 << " "
          << setw(5) << OLF[i] << " 'X-Translation' "
          << endl
          << setw(5) << OLF[i]
          << " 'Y-Translation' " << betacoeff2 << " "
          << setw(5) << OLF[i] << " 'X-Translation' "
          << endl;
}

//Step 6.9: Right-Front Surface
betacoeff1 = -1.0;
betacoeff2 = -1.0/sqrt(3.0);
constraintname = 6;

outfile << "*"                                    << endl
        << "*   Right Front Surface"              << endl
        << "Constraint-Node"
        << "   Name = " << constraintname
        << "   SlaveNode = " << ORF[1]
        << "   SlaveDOF = " << "'X-Translation'" << endl;

for (i = 1; i <= ORFcnt; i++)
{
  outfile << setw(5) << TLB[1]
          << " 'X-Translation' " << betacoeff1 << " "
          << setw(5) << ORF[i] << " 'X-Translation' "
          << endl
          << setw(5) << ORF[i]
          << " 'Y-Translation' " << betacoeff2 << " "
          << setw(5) << ORF[i] << " 'X-Translation' "
          << endl;
}

//Step 6.10: Front Line
betacoeff1 = -sqrt(3.0);
```

```
            constraintname = 7;

            outfile << "*"                                        << endl
                    << "*   Front Line"                          << endl
                    << "Constraint-Node"
                    << "   Name = "      << constraintname
                    << "   SlaveNode = " << F[2]
                    << "   SlaveDOF = "  << "'X-Translation'" << endl;

            for (i = 1; i <= Fcnt; i++)
            {
                  outfile << setw(5) << TLB[1]
                          << " 'X-Translation' " << betacoeff1 << " "
                          << setw(5) << F[i]   << " 'Y-Translation' "
                          << endl;
            }

      outfile.close();

      return 0;
}
```

APPENDIX D

DISCRETISATION OF UNIT CELL GEOMETRY FOR THE SPHERICAL MODEL

To use the finite element method (FEM) it is necessary to break models of continuous objects into a number of smaller pieces, or to discretise them. For the spherical model, the initial discretisation of the unit cell geometry was carefully completed in order to prevent the creation of elements with boundaries that overlap. This is done for points in Steps 3 and 4 of the program listed below for the surrounding (matrix) phase and the sphere phase, respectively. Arc lines to provide the base for curved surfaces are defined in Step 5 and the volumes supplying the initial elements in Step 6. The constituent material properties data is defined in Step 7. The programming for the elastic case is shown in this appendix with the spherical model and the programming for the plastic case is shown with the cylindrical model in Appendix E. Both cases are, however, applicable to both models and the parts that need to be changed to switch between the two are shown in italics (in Steps 2.1, 2.3 and 7). Steps 8, 9 and 10 are then used to define the elements to be used, the number of subdivisions into which the initial volumes may be broken and the generation of these elements. The final step then simply provides a listing of all the nodes created by the program. The overall purpose of this program and the source of its development are discussed in Sections 3.1 and 3.4.

D.1 C++ PROGRAM FOR DISCRETISATION OF SPHERICAL MODEL

```
//SHCPE_GMD_1.2: Geometry-Material-Discretisation for Spherical
//               Hexagonal-Closed-Packed Model
//
//     Last Modified: Aug. 10, 2004

//Step 1: Preprocessor Directives
#include <iostream>
#include <fstream>
#include <stdlib.h>
#include <math.h>
#include <iomanip>
```

```
using namespace std;

int main()
{
	//Step 2: Initial Information
		//Step 2.1: Variable Declarations
			//(Constants)
			const double PI = 3.14159265359;
			const int MAX = 500;
			const int MAXNAME = 80;
			//(Basic Variables)
			int i, k;
			char date[MAXNAME];
			char gmd[MAXNAME];
			char node[MAXNAME];
			//(3&4: Geometry Point Variables)
			double x[MAX], y[MAX], z[MAX];
			double r, rho, rhop, rhopp;
			double alpha1p, alpha1, alpha2, alpha3, alpha4p;
			double beta1, beta2, beta3;
			double gamma1, gamma2;
			double delta;
			double a, b, c, s;
			//(5: Line Arc Variables)
			int p1[MAX], p2[MAX], p3[MAX];
			//(6: Volume Variables)
			int v1[MAX], v2[MAX], v3[MAX], v4[MAX], v5[MAX];
			int v6[MAX], v7[MAX], v8[MAX];
			//(7: Material Property Variables)
			double E1, E2, nu1, nu2;
			//(9&10: Discretisation Variables)
			int ndiv1, ndiv2, ndiv3, elemnodes;

		//Step 2.2: Open Output File
		cout << "SHCPE_GMD_1.2: Geometry-Material-Discretisation”
			<< “ for Spherical Hexagonal Closed-Packed Model"
			<< endl << endl;

		cout << "STEP 1: Initial Information" << endl
		     << "    (a) Provide the date (M.D,Y):  ";
		cin >> date;
		cout << "    (b) Provide the geometry-material-“
		     << “discretisation:" << endl
		     << "        file name:  ";
		cin >> gmd;
		cout << "    (c) Provide the node coordinate" << endl
		     << "        file name:  ";
		cin >> node;
		cout << endl;

		ofstream outfile;
		outfile.open(gmd);

		if (outfile.fail())
		{
			cout << "WARNING: The file in Step 2.2 was not”
```

```
            << " opened." << endl;
      exit(1);
}

outfile << setiosflags(ios::fixed)
        << setiosflags(ios::showpoint)
        << setprecision(7);

outfile << "*"                                    << endl
        << "* GMD File created on: "
        << date                                   << endl;

//Step 2.3: Input from User
cout << "STEP 2: Volume Fraction Information from Radii"
     << " of Spheres"   << endl
     << "    Input the radii of the spheres:  ";
cin >> r;
cout << endl;

cout << "STEP 3: Material Properties"           << endl
     << "    (a) The Matrix Material"           << endl
     << "        (i) Input the Young's Modulus:  ";
cin >> E1;
cout << "        (ii) Input the Poisson's Ratio: ";
cin >> nu1;
cout << "    (b) The Sphere Material"           << endl
     << "        (i) Input the Young's Modulus:  ";
cin >> E2;
cout << "        (ii) Input the Poisson's Ratio: ";
cin >> nu2;
cout << endl;

cout << "STEP 4: Discretisation of the Model"   << endl
     << "    (a) Subdivision Data"              << endl
     << "        (i) Input for direction 1:         ";
cin >> ndiv1;
cout << "        (ii) Input for direction 2:        ";
cin >> ndiv2;
cout << "        (iii) Input for direction 3:       ";
cin >> ndiv3;
cout << "    (b) Input number of nodes per element: ";
cin >> elemnodes;
cout << endl;

//Step 2.4: Initialize Variables
i = k = 0;

alpha1p = atan(sqrt(2.0)/2);
alpha1 = (PI/2) + alpha1p;
alpha2 = (PI/2) - alpha1p;
alpha3 = atan(2 / (sqrt(2.0)/2));
alpha4p = atan((sqrt(2.0)/2) / 2);
a = b = c = 0;
s = 0;

rho = sqrt(pow(r,2.0) - 3);
```

```
        beta1 = 60 * (PI/180);
        beta2 = 30 * (PI/180);
        beta3 = 75 * (PI/180);
        gamma1 = (PI/2) - atan((3/(2 * sqrt(2.0)))/sqrt(3.0));
        gamma2 = (PI/2) - atan(((5/sqrt(2.0))/2)/(2/2));

    //Step 3: Surrounding Phase (Matrix) Points
        //Step 3.1: Outer Layer
        x[1] = 0;
        y[1] = 0;
        z[1] = 2 * sqrt(2.0);

        x[2] = 0;
        y[2] = 0;
        z[2] = 3/sqrt(2.0);

        x[3] = 1;
        y[3] = sqrt(3.0);
        z[3] = 2 * sqrt(2.0);

        x[4] = 1;
        y[4] = sqrt(3.0);
        z[4] = sqrt(2.0);

        x[5] = 2;
        y[5] = 0;
        z[5] = 1/sqrt(2.0);

        x[6] = 3.0/2.0;
        y[6] = sqrt(3.0)/2;
        z[6] = (3/sqrt(2.0))/2;

        x[7] = 1.0/2.0;
        y[7] = sqrt(3.0)/2;
        z[7] = (5/sqrt(2.0))/2;

        //Step 3.2: Sphere Layer
        x[8] = 2 - r;
        y[8] = 0;
        z[8] = 2 * sqrt(2.0);

        x[9] = 2 - r * cos(beta1);
        y[9] = r * sin(beta1);
        z[9] = 2 * sqrt(2.0);

        x[10] = 2;
        y[10] = 0;
        z[10] = (2 * sqrt(2.0)) - r;

        x[11] = 2 - (r * sin(alpha2) * cos(beta1));
        y[11] = r * sin(alpha2) * sin(beta1);
        z[11] = (2 * sqrt(2.0)) - (r * cos(alpha2));

        x[12] = 2 - (r * sin(gamma2) * cos(beta1));
        y[12] = r * sin(gamma2) * sin(beta1);
        z[12] = (2 * sqrt(2.0)) - (r * cos(gamma2));
```

```
x[13] = 2 - (r * sin(alpha3));
y[13] = 0;
z[13] = (2 * sqrt(2.0)) - (r * cos(alpha3));

x[14] = 2 - (r * sin(gamma1) * cos(beta2));
y[14] = r * sin(gamma1) * sin(beta2);
z[14] = (2 * sqrt(2.0)) - (r * cos(gamma1));

//Step 3.3: Centre of Sphere
x[15] = 2;
y[15] = 0;
z[15] = 2 * sqrt(2.0);

//Step 3.4: Bottom Intersecting Circle
x[16] = 1;
y[16] = 0;
z[16] = sqrt(2.0);

for (i = 17; i <= 21; i++)
{
            delta = (i - 17) * (PI/4);
   x[i] = 1 - (rho * cos(delta) * cos(alpha1p));
   y[i] = rho * sin(delta);
   z[i] = sqrt(2.0) + (rho * cos(delta) * sin(alpha1p));
}

//Step 3.5: Bottom (Lower-Outer) Intersecting Circle
s = asin(sin(1/cos(alpha1p))*(sin(beta1)/sin(beta3)))-rho;
rhop = rho + (s)/3;

for (i = 22; i <= 26; i++)
{
            delta = (i - 22) * (PI/4);
   x[i] = 1 - (rhop * cos(delta) * cos(alpha1p));
   y[i] = rhop * sin(delta);
   z[i] = sqrt(2.0) + (rhop * cos(delta) * sin(alpha1p));
}

//Step 3.6: Bottom (Upper-Outer) Intersecting Circle
rhopp = rho + (s)/6;
a = 1;
b = -(4 * sqrt(2.0));

for (i = 27; i <= 31; i++)
{
     delta = (i - 27) * (PI/4);
   x[i] = 1 - (rhopp * cos(delta) * cos(alpha1p));
   y[i] = rhopp * sin(delta);
     c = (pow((x[i] - 2),2) + pow(y[i],2) - pow(r,2) + 8);
   z[i] = (-b - sqrt(pow(b,2.0) - 4 * a * c))/(2 * a);
}

//Step 3.7: Left Intersecting Circle
x[32] = (x[1] + x[3])/2;
y[32] = (y[1] + y[3])/2;
z[32] = 2 * sqrt(2.0);
```

```
for (i = 33; i <= 37; i++)
{
            delta = (i - 33) * (PI/4);
      x[i] = (1 + rho * cos(delta)) * cos(beta1);
      y[i] = (1 + rho * cos(delta)) * sin(beta1);
      z[i] = (2 * sqrt(2.0)) - (rho * sin(delta));
}

//Step 3.8: Left (Lower-Outer) Intersecting Circle
s = 1 - rho;
rhop = rho + (s)/3;

for (i = 38; i <= 42; i++)
{
            delta = (i - 38) * (PI/4);
      x[i] = (1 + rhop * cos(delta)) * cos(beta1);
      y[i] = (1 + rhop * cos(delta)) * sin(beta1);
      z[i] = (2 * sqrt(2.0)) - (rhop * sin(delta));
}

//Step 3.9: Left (Upper-Outer) Intersecting Circle
rhopp = rho + (s)/6;
a = 1;
b = -4;

for (i = 43; i <= 47; i++)
{
     delta = (i - 43) * (PI/4);
   y[i] = (1 + rhopp * cos(delta)) * sin(beta1);
   z[i] = (2 * sqrt(2.0)) - (rhopp * sin(delta));
c = (pow(y[i],2)+pow((z[i]-(2*sqrt(2.0))),2)-pow(r,2)+4);
   x[i] = (-b - sqrt(pow(b,2.0) - 4 * a *c))/(2 * a);
}

//Step 3.10: Intermediate Points
x[48] = x[1] + ((x[8] - x[1]) * (1.0/4.0));
y[48] = y[1];
z[48] = z[1];

x[49] = x[2] + ((x[13] - x[2]) * (1.0/4.0));
y[49] = y[2];
z[49] = z[2] + ((z[13] - z[2]) * (1.0/4.0));

x[50] = x[3] + ((x[9] - x[3]) * (1.0/4.0));
y[50] = y[3] - ((y[3] - y[9]) * (1.0/4.0));
z[50] = z[3];

x[51] = x[4] + ((x[11] - x[4]) * (1.0/4.0));
y[51] = y[4] - ((y[4] - y[11]) * (1.0/4.0));
z[51] = z[4] + ((z[11] - z[4]) * (1.0/4.0));

x[52] = x[6] + ((x[12] - x[6]) * (1.0/4.0));
y[52] = y[6] - ((y[6] - y[12]) * (1.0/4.0));
z[52] = z[6] + ((z[12] - z[6]) * (1.0/4.0));

x[53] = x[5];
y[53] = y[5];
```

```
        z[53] = z[5] + ((z[10] - z[5]) * (1.0/4.0));

        x[54] = x[7] + ((x[14] - x[7]) * (1.0/4.0));
        y[54] = y[7] - ((y[7] - y[14]) * (1.0/4.0));
        z[54] = z[7] + ((z[14] - z[7]) * (1.0/4.0));

        //Step 3.11: Output for Matrix Geometry Points
        outfile << "*"                                    << endl
                << "*   Geometry Points"                  << endl
                << "Coordinates Point System = 0" << endl
                << "* Point"
                << setw(10)  << "X"
                << setw(13) << "Y"
                << setw(15) << "Z"                        << endl
                << "*      Matrix Points"                 << endl;

        for (i = 1; i <= 54; i++)
        {
              outfile << setw(5)  << i
                      << setw(15) << x[i]
                      << setw(15) << y[i]
                      << setw(15) << z[i]   << endl;
        }

    //Step 4: Interior Sphere Points
          //Step 4.1: Bottom Inner Intersecting Circle
          for (i = 55; i <=59; i++)
          {
                     delta = (i - 55) * (PI/4);
             x[i] = 1 - ((rho/2) * cos(delta) * cos(alpha1p));
             y[i] = (rho/2) * sin(delta);
             z[i] = sqrt(2.0)+((rho/2)*cos(delta)*sin(alpha1p));
          }

          //Step 4.2: Bottom (Upper-Inner) Intersecting Circle
          x[60] = 1 + ((r/10) * cos(alpha2));
          y[60] = 0;
          z[60] = sqrt(2.0) + ((r/10) * sin(alpha2));

          for (i = 61; i <= 65; i++)
          {
                     delta = (i - 61) * (PI/4);
             x[i] = x[60] - ((rho/2) * cos(delta) * cos(alpha1p));
             y[i] = (rho/2) * sin(delta);
             z[i] = z[60] + ((rho/2) * cos(delta) * sin(alpha1p));
          }

          //Step 4.3: Left Inner Intersecting Circle
          for (i = 66; i <= 70; i++)
          {
                     delta = (i - 66) * (PI/4);
               x[i] = (1 + (rho/2) * cos(delta)) * cos(beta1);
               y[i] = (1 + (rho/2) * cos(delta)) * sin(beta1);
               z[i] = (2 * sqrt(2.0)) - ((rho/2) * sin(delta));
          }

          //Step 4.4: Left (Upper-Inner) Intersecting Circle
```

```
x[71] = cos(beta1) + ((r/10) * cos(beta2));
y[71] = sin(beta1) - ((r/10) * sin(beta2));
z[71] = 2 * sqrt(2.0);

for (i = 72; i <= 76; i++)
{
            delta = (i - 72) * (PI/4);
   x[i] = ((1+(rho/2)*cos(delta))*cos(beta1))+((r/10)*
          cos(beta2));
   y[i] = ((1+(rho/2)*cos(delta))*sin(beta1))-((r/10)*
          sin(beta2));
   z[i] = (2 * sqrt(2.0)) - ((rho/2) * sin(delta));
}

//Step 4.5: Top Back Row
k = 0;

for (i = 77; i <= 82; i++)
{
            k = k + 1;
      x[i] = 2 - (k * (r/7));
      y[i] = 0;
      z[i] = 2 * sqrt(2.0);
}

//Step 4.6: Top Right Row
x[83] = 2 - ((6.0/7.0) * r) * cos(beta1);
y[83] = ((6.0/7.0) * r) * sin(beta1);
z[83] = 2 * sqrt(2.0);

x[84] = (x[15] + x[83])/2.0;
y[84] = (y[15] + y[83])/2.0;
z[84] = 2 * sqrt(2.0);

//Step 4.7: Intermediate Back Row
x[85] = 2;
y[85] = 0;
z[85] = (2 * sqrt(2.0)) - ((3.0/4.0) * r);

for (i = 86; i <= 90; i++)
{
      x[i] = x[i - 9];
      y[i] = 0;
      z[i] = z[i - 1] + ((1.0/7.0) * r) * tan(alpha1p);
}

x[91] = x[82] + ((x[81] - x[82])/4);
y[91] = 0;
z[91] = z[90] + (x[81] - x[91]) * tan(alpha1p);

//Step 4.8: Intermediate Right Row
x[92] = x[84];
y[92] = y[84];
z[92] = z[85] + ((y[84]/sin(beta1)) * tan(alpha4p));

x[93] = x[83] + ((x[84] - x[83])/4);
y[93] = sqrt(3.0) * (2.0 - x[93]);
```

```
z[93] = z[85] + ((y[93]/sin(beta1)) * tan(alpha4p));

//Step 4.9: Intermediate Inner Circle
for (i = 94; i <= 96; i++)
{
            delta = (i - 93) * (PI/4);
   x[i] = x[88] - ((1.0/7.0) * r) * cos(delta);
   y[i] = (((1.0/7.0) * r)/cos(alpha1p)) * sin(delta);
   z[i] = z[88]+((1.0/7.0)*r)*cos(delta)*tan(alpha1p);
}

//Step 4.10: Intermediate Circle
for (i = 97; i <= 99; i++)
{
            delta = (i - 96) * (PI/4);
   x[i] = x[88] - (2 * (1.0/7.0) * r) * cos(delta);
   y[i] = ((2 * (1.0/7.0) * r)/cos(alpha1p)) * sin(delta);
   z[i] = z[88]+(2*(1.0/7.0)*r)*cos(delta)*tan(alpha1p);
}

//Step 4.11: Top Inner Circle
for (i = 100; i <= 102; i++)
{
            delta = (i - 99) * (PI/4);
      x[i] = x[79] - ((1.0/7.0) * r) * cos(delta);
      y[i] = ((1.0/7.0) * r) * sin(delta);
      z[i] = 2 * sqrt(2.0);
}

//Step 4.12: Top Circle
for (i = 103; i <= 105; i++)
{
            delta = (i - 102) * (PI/4);
      x[i] = x[79] - (2 * (1.0/7.0) * r) * cos(delta);
      y[i] = (2 * (1.0/7.0) * r) * sin(delta);
      z[i] = 2 * sqrt(2.0);
}

//Step 4.13: Intermediates of Circles
x[106] = (x[82] + x[83])/2;
y[106] = (y[82] + y[83])/2;
z[106] = 2 * sqrt(2.0);

x[107] = (x[91] + x[93])/2;
y[107] = (y[91] + y[93])/2;
z[107] = (z[91] + z[93])/2;

//Step 4.14: Output for Interior Sphere Geometry Points
outfile << "*      Interior Sphere Points" << endl;

for (i = 55; i <= 107; i++)
{
      outfile << setw(5)  << i
              << setw(15) << x[i]
              << setw(15) << y[i]
              << setw(15) << z[i] << endl;
}
```

```
//Step 5: Line Arcs
      //Step 5.1: Line Arcs in Matrix
      for (i = 1; i <= 5; i++)
      {
                  k = i - 1;
            p1[i] = 47 - k;
            p2[i] = 37 - k;
            p3[i] = 15;

            p1[i + 25] = 31 - k;
            p2[i + 25] = 21 - k;
            p3[i + 25] = 15;
      }

      for (i = 6; i <= 9; i++)
      {
                  k = i - 6;
            p1[i] = 42 - k;
            p2[i] = 41 - k;
            p3[i] = 32;

            p1[i + 4] = 47 - k;
            p2[i + 4] = 46 - k;
            p3[i + 4] = 32;

            p1[i + 8] = 37 - k;
            p2[i + 8] = 36 - k;
            p3[i + 8] = 32;

            p1[i + 12] = 31 - k;
            p2[i + 12] = 30 - k;
            p3[i + 12] = 16;

            p1[i + 16] = 26 - k;
            p2[i + 16] = 25 - k;
            p3[i + 16] = 16;

            p1[i + 25] = 21 - k;
            p2[i + 25] = 20 - k;
            p3[i + 25] = 16;
      }

      for (i = 35; i <= 36; i++)
      {
                  k = i - 35;
            p1[i] = 46 - k;
            p2[i] = 13 + k;

            p1[i + 2] = 44 - k;
            p2[i + 2] = 11 - (2 * k);

            p1[i + 5] = 14 - (3 * k);
            p2[i + 5] = 11 - (2 * k);

            p1[i + 7] = 14 - k;
            p2[i + 7] = 13 - (5 * k);
```

```
        p1[i + 9] = 28 - k;
        p2[i + 9] = 14 - k;

        p1[i + 11] = 30 - k;
        p2[i + 11] = 12 - k;

        p1[i + 13] = 12;
        p2[i + 13] = 11 - k;
}

p1[39] = 47;
p2[39] = 8;

p1[50] = 31;
p2[50] = 10;

for (i = 35; i <= 50; i++)
        p3[i] = 15;

//Step 5.2: Line Arcs in Interior Sphere
for (i = 51; i <= 54; i++)
{
                k = i - 51;
        p1[i] = 76 - k;
        p2[i] = 75 - k;
        p3[i] = 71;

        p1[i + 4] = 70 - k;
        p2[i + 4] = 69 - k;
        p3[i + 4] = 32;

        p1[i + 8] = 65 - k;
        p2[i + 8] = 64 - k;
        p3[i + 8] = 60;

        p1[i + 12] = 59 - k;
        p2[i + 12] = 58 - k;
        p3[i + 12] = 16;
}

for (i = 67; i <= 68; i++)
{
                k = i - 67;
        p1[i] = 99 - k;
        p2[i] = 98 - k;

        p1[i + 2] = 96 - k;
        p2[i + 2] = 95 - k;

        p1[i + 4] = 99 - (2 * k);
        p2[i + 4] = 86 + (4 * k);

        p1[i + 6] = 96 - (2 * k);
        p2[i + 6] = 87 + (2 * k);

        p1[i + 8] = 105 - k;
```

```
            p2[i + 8] = 104 - k;

            p1[i + 10] = 102 - k;
            p2[i + 10] = 101 - k;

            p1[i + 12] = 105 - (2 * k);
            p2[i + 12] = 77 + (4 * k);

            p1[i + 14] = 102 - (2 * k);
            p2[i + 14] = 78 + (2 * k);
      }

      for (i = 67; i <= 74; i++)
            p3[i] = 88;

      for (i = 75; i <= 82; i++)
            p3[i] = 79;

      //Step 5.3: Output for Line Arcs
      for (i = 1; i <= 82; i++)
      {
            outfile << "Line Arc"
                    << "   Name = "    << i
                    << "   P1 = "      << p1[i]
                    << "   P2 = "      << p2[i]
                    << "   Centre = "  << p3[i]
                    << endl;
      }

//Step 6: Volumes
      //Step 6.1: Bottom Layer of Matrix Volumes
      for (i = 1; i <= 4; i++)
      {
                  k = i - 1;
            v2[i] = 42 - k;
            v3[i] = 41 - k;
            v1[i + 4] = 22 + k;
            v4[i + 4] = 23 + k;
      }

      for (i = 1; i <= 2; i++)
      {
                  k = i - 1;
            v4[i] = v2[i + 4] = 2 + (5 * k);
            v1[i + 2] = v3[i + 4] = 7 - (3 * k);
            v6[i] = v5[i + 4] = 49 + (5 * k);
            v5[i + 2] = v6[i + 4] = 54 - (3 * k);

            v1[i] = 1 + k;
            v5[i] = 48 + k;
            v4[i + 2] = 4 - k;
            v6[i + 2] = 51 - k;
            v2[i + 6] = 4 + (2 * k);
            v3[i + 6] = 6 - k;
            v5[i + 6] = 51 + k;
            v6[i + 6] = 52 + k;
      }
```

```
//Step 6.2: Top Layer of Matrix Volumes
for (i = 9; i <= 12; i++)
{
            k = i - 9;
      v1[i] = 42 - k;
      v2[i] = 37 - k;
      v3[i] = 36 - k;
      v4[i] = 41 - k;
      v5[i] = 47 - k;
      v6[i] = 46 - k;
      v2[i + 4] = 42 - k;
      v3[i + 4] = 41 - k;
      v6[i + 4] = 47 - k;
      v7[i + 4] = 46 - k;
      v1[i + 8] = 22 + k;
      v4[i + 8] = 23 + k;
      v8[i + 8] = 28 + k;
      v5[i + 8] = 27 + k;
      v1[i + 12] = 17 + k;
      v2[i + 12] = 22 + k;
      v3[i + 12] = 23 + k;
      v4[i + 12] = 18 + k;
      v5[i + 12] = 27 + k;
      v6[i + 12] = 28 + k;
}

for (i = 13; i <= 14; i++)
{
            k = i - 13;
      v4[i] = v2[i + 4] = 49 + (5 * k);
      v1[i + 2] = v3[i + 4] = 54 - (3 * k);
      v8[i] = v6[i + 4] = 13 + k;
      v5[i + 2] = v7[i + 4] = 14 - (3 * k);

      v1[i] = 48 + k;
      v5[i] = 8 + (5 * k);
      v4[i + 2] = 51 - k;
      v8[i + 2] = 11 - (2 * k);
      v2[i + 6] = 51 + k;
      v3[i + 6] = 52 + k;
      v6[i + 6] = 11 + k;
      v7[i + 6] = 12 - (2 * k);
}

//Step 6.3: Intersecting Circle Layer of Sphere Volumes
for (i = 25; i <= 26; i++)
{
            k = i - 25;
      v1[i] = 70 - (38 * k);
      v2[i] = 32 + (34 * k);
      v3[i] = 68 - k;
      v4[i] = 69 - k;
      v5[i] = 76 - (5 * k);
      v6[i] = 71 + k;
      v7[i] = 74 - k;
      v8[i] = 75 - k;
```

```
        v1[i + 6] = 16 + (43 * k);
        v2[i + 6] = 55 - (39 * k);
        v3[i + 6] = 56 + k;
        v4[i + 6] = 57 + k;
        v5[i + 6] = 60 + (5 * k);
        v6[i + 6] = 61 - k;
        v7[i + 6] = 62 + k;
        v8[i + 6] = 63 + k;
}

for (i = 27; i <= 30; i++)
{
              k = i - 27;
        v1[i] = 37 - k;
        v2[i] = 70 - k;
        v3[i] = 69 - k;
        v4[i] = 36 - k;
        v5[i] = 47 - k;
        v6[i] = 76 - k;
        v7[i] = 75 - k;
        v8[i] = 46 - k;
        v1[i + 6] = 55 + k;
        v2[i + 6] = 17 + k;
        v3[i + 6] = 18 + k;
        v4[i + 6] = 56 + k;
        v5[i + 6] = 61 + k;
        v6[i + 6] = 27 + k;
        v7[i + 6] = 28 + k;
        v8[i + 6] = 62 + k;
}

//Step 6.4: Surface Layer of Interior Sphere Volumes
for (i = 37; i <= 40; i++)
{
              k = i - 37;
        v2[i] = 47 - k;
        v3[i] = 46 - k;
        v6[i] = 76 - k;
        v7[i] = 75 - k;
        v1[i + 6] = 27 + k;
        v4[i + 6] = 28 + k;
        v1[i + 10] = 61 + k;
        v2[i + 10] = 27 + k;
        v3[i + 10] = 28 + k;
        v4[i + 10] = 62 + k;
}

for (i = 37; i <= 38; i++)
{
              k = i - 37;
        v8[i] = v1[i + 4] = v6[i + 6] = 91 + (16 * k);
        v5[i + 2] = v4[i + 4] = v7[i + 6] = 107 - (14 * k);
        v4[i] = v2[i + 6] = 13 + k;
        v1[i + 2] = v3[i + 6] = 14 - (3 * k);

        v1[i] = 8 + (5 * k);
        v5[i] = 82 + (9 * k);
```

```
      v4[i + 2] = 11 - (2 * k);
      v8[i + 2] = 93 - (10 * k);
      v2[i + 4] = 75 - k;
      v3[i + 4] = 74 - k;
      v5[i + 4] = 82 + (24 * k);
      v6[i + 4] = 76 - (5 * k);
      v7[i + 4] = 71 + k;
      v8[i + 4] = 106 - (23 * k);
      v2[i + 8] = 11 + k;
      v3[i + 8] = 12 - (2 * k);
      v6[i + 8] = 93 - k;
      v7[i + 8] = 92 - (7 * k);
      v1[i + 14] = 61 - k;
      v2[i + 14] = 62 + k;
      v3[i + 14] = 63 + k;
      v4[i + 14] = 60 + (5 * k);
      v5[i + 14] = 89 - k;
      v6[i + 14] = 94 + k;
      v7[i + 14] = 95 + k;
      v8[i + 14] = 88 - k;
}

for (i = 37; i <= 39; i++)
{
            k = i - 37;
 v5[i + 7] = v8[i + 6] = v6[i + 11] = v7[i + 10] = 97 + k;
 v5[i + 11] = v8[i + 10] = 94 + k;
}

v5[43] = 90;
v8[46] = v7[50] = 86;
v5[47] = 89;
v6[47] = 90;
v8[50] = 87;

//Step 6.5: Core Layer of Interior Sphere Volumes
for (i = 53; i <= 55; i++)
{
            k = i - 53;
      v1[i + 1] = v4[i] = v3[i + 4] = 97 + k;
      v5[i + 1] = v8[i] = v6[i + 5] = v7[i + 4] = 103 + k;
      v1[i + 5] = v4[i + 4] = 94 + k;
      v2[i + 5] = 97 + k;
      v5[i + 5] = v8[i + 4] = 100 + k;
}

for (i = 53; i <= 54; i++)
{
            k = i -53;
      v2[i] = 91 + (16 * k);
      v3[i] = 107 - (14 * k);
      v6[i] = 82 + (24 * k);
      v7[i] = 106 - (23 * k);
      v2[i + 2] = 93 - k;
      v3[i + 2] = 92 - (7 * k);
      v6[i + 2] = 83 + k;
      v7[i + 2] = 84 - (69 * k);
```

```
        v1[i + 8] = 89 - k;
        v2[i + 8] = 94 + k;
        v3[i + 8] = 95 + k;
        v4[i + 8] = 88 - k;
        v5[i + 8] = 80 - k;
        v6[i + 8] = 100 + k;
        v7[i + 8] = 101 + k;
        v8[i + 8] = 79 - k;
}

v1[53] = 90;
v4[56] = v3[60] = 86;
v5[53] = v6[57] = 81;
v8[56] = v7[60] = 77;
v1[57] = 89;
v2[57] = 90;
v4[60] = 87;
v5[57] = 80;
v8[60] = 78;

//Step 6.6: Output for Volumes
for (i = 1; i <= 12; i++)
{
        outfile << "Volume" << " Vertex" << " Shape = Prism"
                << "   Name = " << i << "," << endl
                << "         vertex1 = " << v1[i]
                << "   vertex2 = " << v2[i]
                << "   vertex3 = " << v3[i]
                << "   vertex4 = " << v4[i] << "," << endl
                << "         vertex5 = " << v5[i]
                << "   vertex6 = " << v6[i]
                << endl;
}

for (i = 13; i <= 20; i++)
{
        outfile << "Volume" << " Vertex" << " Shape = Hex"
                << "   Name = " << i << "," << endl
                << "         vertex1 = " << v1[i]
                << "   vertex2 = " << v2[i]
                << "   vertex3 = " << v3[i]
                << "   vertex4 = " << v4[i] << "," << endl
                << "         vertex5 = " << v5[i]
                << "   vertex6 = " << v6[i]
                << "   vertex7 = " << v7[i]
                << "   vertex8 = " << v8[i]
                << endl;
}

for (i = 21; i <= 24; i++)
{
        outfile << "Volume" << " Vertex" << " Shape = Prism"
                << "   Name = " << i << "," << endl
                << "         vertex1 = " << v1[i]
                << "   vertex2 = " << v2[i]
                << "   vertex3 = " << v3[i]
                << "   vertex4 = " << v4[i] << "," << endl
```

```
                        << "         vertex5 = " << v5[i]
                        << "   vertex6 = " << v6[i]
                        << endl;
        }

        for (i = 25; i <= 62; i++)
        {
                outfile << "Volume" << " Vertex" << " Shape = Hex"
                        << "   Name = " << i << "," << endl
                        << "         vertex1 = " << v1[i]
                        << "   vertex2 = " << v2[i]
                        << "   vertex3 = " << v3[i]
                        << "   vertex4 = " << v4[i] << "," << endl
                        << "         vertex5 = " << v5[i]
                        << "   vertex6 = " << v6[i]
                        << "   vertex7 = " << v7[i]
                        << "   vertex8 = " << v8[i]
                        << endl;
        }

//Step 7: Material Properties
        outfile << "Material Elastic"
                << "    Name = " << 1
                << "    E = "    << E1
                << "    Nu = "   << nu1
                << endl;

outfile << "Material Elastic"
                << "    Name = " << 2
                << "    E = "    << E2
                << "    Nu = "   << nu2
                << endl;

//Step 8: Element Groups
for (i = 1; i <= 2; i++)
{
        outfile << "EGroup ThreeDSolid"
                << "    Name = "     << i
                << "    Material = " << i
                << endl;
}

//Step 9: Subdivision Data
outfile << "Subdivide Volume"
          << "    Name = "  << 1
          << "    NDiv1 = " << ndiv1
          << "    NDiv2 = " << ndiv2
          << "    NDiv3 = " << ndiv3
          << endl;

for (i = 2; i <= 62; i++)
{
        outfile << "    " << i
                << endl;
}

//Step 10: Generate Elements
```

```
            //Step 10.1: Surrounding Material (Matrix)
            outfile << "GVolume"
                    << "    Name = "  << 1
                    << "    Nodes = " << elemnodes
                    << "    Group = " << 1
                    << "    PrefShape = Hexahedral"
                    << endl;

            for (i = 2; i <= 24; i++)
            {
                  outfile << "    " << i
                          << endl;
            }

            //Step 10.2: Interior Sphere
            outfile << "GVolume"
                    << "    Name = "  << 25
                    << "    Nodes = " << elemnodes
                    << "    Group = " << 2
                    << "    PrefShape = Hexahedral"
                    << endl;

            for (i = 26; i <= 62; i++)
            {
                  outfile << "    " << i
                          << endl;
            }

      //Step 11: List Node Coordinates
      outfile << "FileList   Option = File,"          << endl
              << "           File = "
              << node                                 << endl;

      outfile << "List Coordinates Node   First = 1   Last = All,"
              << endl
              << "                        System = 0  Global = Yes"
              << endl;

      return 0;
}
```

APPENDIX E

DISCRETISATION OF UNIT CELL GEOMETRY FOR THE CYLINDRICAL MODEL

The procedure used to discretise the geometry of the cylindrical model is the same as that used to discretise the spherical model. Steps 3 and 4 define a number of initially mapped points. Step 5 describes complex lines such as arcs and splines, and Step 6 defines the initial volumes. The constituent material properties are listed in Step 7, just as they are with the spherical model. In this appendix, however, plastic conditions are considered, while elastic conditions were studied in Appendix D. The commands that need to be changed in order to switch between plastic and elastic conditions are shown in italics (Sec. 2.1, 2.3, 7). Finally, Steps 7, 8 and 9 describe the creation and generation of elements. It should be noted that this program does not produce a list of nodes useful for applying the boundary conditions of Appendix C to the final text file for ADINA. These commands may be found in Step 11 of Appendix D.

E.1 C++ PROGRAM FOR DISCRETISATION OF CYLINDRICAL MODEL

```
//CHCPP_GMD_1.1: Geometry-Material-Discretisation for Cylindrical
//               Hexagonal-Closed-Packed Model
//
//     Last Modified: Aug. 10, 2003

//Step 1: Preprocessor Directives
#include <iostream>
#include <fstream>
#include <stdlib.h>
#include <math.h>
#include <iomanip>

using namespace std;

int main()
{
   //Step 2: Initial Information
      //Step 2.1: Variable Declarations
         //(Constants)
         const double PI = 3.14159265359;
         const int MAX = 500;
         const int MAXNAME = 80;
```

```
   //(Basic Variables)
   int i, k;
   char date[MAXNAME];
   char gmd[MAXNAME];
   //(3&4: Geometry Point Variables)
   double x[MAX], y[MAX], z[MAX];
   double rho, rhop;
   double alpha1p, alpha1, alpha2, alpha3, alpha4p;
   double beta1, beta2, beta3;
   double gamma1, gamma2, gamma3, gamma4, gamma5, gamma6;
   double delta;
   double a, b, c, s, c1, c2, c3;
   double x1, x2, z1, z2;
   double zmin, ymin, xmin, amin, bmin, cmin;
   //(5: Line Arc Variables)
   int p1[MAX], p2[MAX], p3[MAX];
   //(6: Volume Variables)
   int v1[MAX], v2[MAX], v3[MAX], v4[MAX];
   int v5[MAX], v6[MAX], v7[MAX], v8[MAX];
   //(7: Material Property Variables)
   double E1, E2, nu1, nu2, Y1, Y2;
   double ET1, ET2, EPA1, EPA2;
   //(9&10: Discretisation Variables)
   int ndiv1, ndiv2, ndiv3, elemnodes;

//Step 2.2: Open Output File
cout << "CHCPP_GMD_1.1: Geometry-Material-Discretisation"
     << " for Cylindrical Hexagonal-Closed-Packed Model"
     << endl << endl;

cout << "STEP 1: Initial Information" << endl
     << "    (a) Provide the date (M.D,Y):  ";
cin >> date;
cout << "    (b) Provide the geometry-material-
     << "discretisation file name:  ";
cin >> gmd;
cout << endl;
cout << "    NOTE: This file does not ask for a listing"
     << " of  nodes." <<endl;
cout << endl;

ofstream outfile;
outfile.open(gmd);

if (outfile.fail())
{
   cout << "WARNING: The file in Step 2.2 was not"
        << " opened." << endl;
        exit(1);
}

outfile << setiosflags(ios::fixed)
        << setiosflags(ios::showpoint)
        << setprecision(7);

outfile << "*"                                    << endl
        << "* GMD File created on: "
```

```
        << date                                    << endl;

//Step 2.3: Input from User
cout << "STEP 2: Volume Fraction Information from Radii”
     << “ of Cylinders" << endl
     << "    Input the radii of the cylinders:  ";
cin >> rho;
cout << endl;

cout << "STEP 3: Material Properties"           << endl
     << "    (a) The Matrix Material"           << endl
     << "        (i) Input the Young's Modulus [MPa]:  ";
cin >> E1;
cout << "        (ii) Input the Poisson's Ratio:       ";
cin >> nu1;
cout << "        (iii) Input the Yield Strength [MPa]: ";
cin >> Y1;
cout << "    (b) The Cylinder Material"         << endl
     << "        (i) Input the Young's Modulus [MPa]:  ";
cin >> E2;
cout << "        (ii) Input the Poisson's Ratio:       ";
cin >> nu2;
cout << "        (iii) Input the Yield Strength [MPa]: ";
cin >> Y2;
cout << endl;

cout << "STEP 4: Discretization of the Model"   << endl
     << "    (a) Subdivision Data"              << endl
     << "        (i) Input for direction 1:             ";
cin >> ndiv1;
cout << "        (ii) Input for direction 2:            ";
cin >> ndiv2;
cout << "        (iii) Input for direction 3:           ";
cin >> ndiv3;
cout << "    (b) Input number of nodes per element:    ";
cin >> elemnodes;
cout << endl;

//Step 2.4: Initialize Variables
i = k = 0;
a = b = c = c1 = c2 = c3 = s = 0;
ymin = xmin = amin = bmin = cmin = 0;
x1 = x2 = 2.0;
z1 = z2 = 0;
zmin = 2 * sqrt(2.0);

alpha1p = atan(sqrt(2.0)/2);
alpha1 = (PI/2) + alpha1p;
alpha2 = (PI/2) - alpha1p;
alpha3 = atan(2 / (sqrt(2.0)/2));
alpha4p = atan((sqrt(2.0)/2) / 2);

beta1 = 60 * (PI/180);
beta2 = 30 * (PI/180);
beta3 = 75 * (PI/180);
//gamma1: Defined in Step 4.12
gamma2 = atan(sqrt(3.0)/(1.0/cos(alpha1p)));
```

```
   //gamma3: Defined in Step 4.20, gamma4: Defined in Step 4.20
   //gamma5: Defined in Step 3.9, gamma6: Defined in Step 3.9

//Step 3: Surrounding Phase (Matrix) Points
   //Step 3.1: Outer Points
   x[1] = 0;
   y[1] = 0;
   z[1] = 2 * sqrt(2.0);

   x[2] = 0;
   y[2] = 0;
   z[2] = 3/sqrt(2.0);

   x[3] = 1;
   y[3] = sqrt(3.0);
   z[3] = 2 * sqrt(2.0);

   x[4] = 1;
   y[4] = sqrt(3.0);
   z[4] = sqrt(2.0);

   x[5] = 2;
   y[5] = 0;
   z[5] = 1/sqrt(2.0);

   x[6] = 3.0/2.0;
   y[6] = sqrt(3.0)/2;
   z[6] = (3/sqrt(2.0))/2;

   x[7] = 1.0/2.0;
   y[7] = sqrt(3.0)/2;
   z[7] = (5/sqrt(2.0))/2;

   x[8] = 2;
   y[8] = 0;
   z[8] = 2 * sqrt(2.0);

   //Step 3.2: Outer Circle of Top Cylinder on Left-Front Surface
   x[101] = (x[1] + x[3])/2;
   y[101] = (y[1] + y[3])/2;
   z[101] = 2 * sqrt(2.0);

   s = 1 - rho;
   rhop = rho + (s/3);

   for (i = 9; i <= 13; i++)
   {
         delta = (i - 9) * (PI/4);
      x[i] = (1 + rhop * cos(delta)) * cos(beta1);
      y[i] = (1 + rhop * cos(delta)) * sin(beta1);
      z[i] = (2 * sqrt(2.0)) - (rhop * sin(delta));
   }

   //Step 3.3: Points at Two-Thirds between Left-Front &
   //          Intersection
   x[129] = (3.0/2.0) - rho;
   y[129] = (sqrt(3.0)/6.0) * (1.0 + 2 * rho);
```

```
z[129] = 2 * sqrt(2.0);

x[14] = x[15] = (4.0/3.0) * (1.0 - rho);
x[16] = x[17] = (1.0/3.0) * (5.0 - 2 * rho);
x[18] = x[129];

y[14] = y[15] = 0;
y[16] = y[17] = (sqrt(3.0)/3.0) * (1.0 + 2 * rho);
y[18] = y[129];

z[14] = z[16] = 2 * sqrt(2.0);
z[15] = (1.0/(2 * sqrt(2.0))) * x[15] + (3.0/sqrt(2.0));
z[17] = sqrt(2.0) * x[17];
z[18] = (z[15] + z[17])/2.0;

//Step 3.4: Outer Circle at One-Third between Left-Front &
//          Intersection
x[118] = (1.0/2.0) * (2.0 - rho);
y[118] = (sqrt(3.0)/6.0) * (2.0 + rho);
z[118] = 2 * sqrt(2.0);

for (i = 19; i <= 23; i++)
{
      delta = (i - 19) * (PI/4);
   x[i] = x[118] + (rhop * cos(delta) * cos(beta1));
   y[i] = y[118] + (rhop * cos(delta) * sin(beta1));
   z[i] = (2 * sqrt(2.0)) - (rhop * sin(delta));
}

//Step 3.5: Points at One-Third between Left-Front Surface &
//          Intersection
x[24] = x[25] = (2.0/3.0) * (1.0 - rho);
x[26] = x[27] = (1.0/3.0) * (4.0 - rho);
x[28] = x[118];

y[24] = y[25] = 0;
y[26] = y[27] = (sqrt(3.0)/3.0) * (2.0 + rho);
y[28] = y[118];

z[24] = z[26] = 2 * sqrt(2.0);
z[25] = ((1.0/(2 * sqrt(2.0))) * x[25]) + (3.0/sqrt(2.0));
z[27] = sqrt(2.0) * x[27];
z[28] = (z[25] + z[27])/2.0;

//Step 3.6: Points at One-Third between Bottom & Intersection
x[160] = 2.0;
y[160] = 0;
z[160] = (2 * sqrt(2.0)) - (sqrt(3.0) * rho);

x[144] = (2.0 * sqrt(3.0) - rho)/sqrt(3.0);
y[144] = rho;
z[144] = sqrt(2.0) * x[144];

a = (1.0/3.0);
zmin = 2 * sqrt(2.0);
z1 = 0;
x1 = 2.0;
```

```
while (z1 < zmin)
{
   x2 = x1;
   x1 = x1 - 0.01;

   b = -(((2 * sqrt(2.0))/3.0) * x1);
   c = ((11.0/3.0) * pow(x1,2)) - (12.0 * x1) + 12 - pow(rho,2);
   z1 = (-b - sqrt(pow(b,2.0) - 4 * a *c))/(2 * a);

   if (z1 < zmin)
   {
      zmin = z1;
      z1 = 0;
   }
}
//The minimum point values are zmin and:
xmin = x2;
ymin = sqrt(3.0) * (2.0 - x2);

z[161] = zmin + (z[144] - zmin)/10.0;
a = (11.0/3.0);
b = -(((2 * sqrt(2.0))/3.0) * z[161] + 12);
c = (1.0/3.0) * pow(z[161],2) + 12 - pow(rho,2);
x[161] = (-b - sqrt(pow(b,2.0) - 4 * a *c))/(2 * a);
y[161] = sqrt(3.0) * (2.0 - x[161]);

x[29] = 2.0;
y[29] = 0;
z[29] = z[5] + (7.0/24.0) * (z[160] - z[5]);

x[30] = (7.0/24.0) * (x[161] - x[6]) + x[6];
y[30] = sqrt(3.0) * (2.0 - x[30]);
z[30] = (7.0/24.0) * (z[161] - z[6]) + z[6];

//Step 3.7: Points at Two-Thirds between Bottom & Intersection
x[31] = 2.0;
y[31] = 0;
z[31] = z[5] + (7.0/12.0) * (z[160] - z[5]);

x[32] = (7.0/12.0) * (x[161] - x[6]) + x[6];
y[32] = sqrt(3.0) * (2.0 - x[32]);
z[32] = (7.0/12.0) * (z[161] - z[6]) + z[6];

//Step 3.8: Outer Circle of Back Cylinder on Bottom Surface
x[149] = 1.0;
y[149] = 0;
z[149] = sqrt(2.0);

s = (sin(gamma2)/cos(alpha1p)) - rho;
rhop = rho + (s)/3;

for (i = 33; i <= 37; i++)
{
      delta = (i - 33) * (PI/4);
   x[i] = x[149] + (rhop * cos(delta) * cos(alpha1p));
   y[i] = y[149] + (rhop * sin(delta));
```

```
   z[i] = z[149] - (rhop * cos(delta) * sin(alpha1p));
}

//Step 3.9: Outer Circle of Back Cylinder at One-Third between
//          Bottom & Intersection
a = 9.0/4.0;
b = -(9 - 2 * sqrt(6.0) * rho);
c = (2 * pow(rho,2)) - (4 * sqrt(6.0) * rho) + 9.0;
x[141] = (-b - sqrt(pow(b,2.0) - 4 * a *c))/(2 * a);
z[141] = (sqrt(2.0) * x[141]) + (sqrt(3.0) * rho);
y[141] = 0;

x[164] = (x[141] + x[160])/2.0;
y[164] = 0;
z[164] = (z[141] + z[160])/2.0;

amin = sqrt(pow((2.0 - xmin),2.0) + pow(ymin,2.0));
gamma5 = atan(amin/(zmin - z[5]));
gamma6 = alpha3 - gamma5;
bmin = (1/sqrt(2.0)) * tan(gamma6);
cmin = (bmin * sin(gamma6 + alpha4p))/sin(alpha2);

x1 = x[149] + (1.0/3.0) * cmin * cos(alpha2);
z1 = z[149] + (1.0/3.0) * cmin * sin(alpha2);

x2 = x[149] + (1.0/3.0) * (x[164] - x[149]);
z2 = z[149] + (1.0/3.0) * (z[164] - z[149]);

if (x1 <= x2)
{
   x[170] = x1;
   z[170] = z1;
}
else
{
   x[170] = x2;
   z[170] = z2;
}
y[170] = 0;

for (i = 38; i <= 42; i++)
{
      delta = (i - 38) * (PI/4);
   x[i] = x[170] + (rhop * cos(delta) * cos(alpha1p));
   y[i] = y[170] + (rhop * sin(delta));
   z[i] = z[170] - (rhop * cos(delta) * sin(alpha1p));
}

//Step 3.10: Output for Matrix Geometry Points
outfile << "*"                                          << endl
        << "*   Geometry Points"                        << endl
        << "Coordinates Point System = 0" << endl
        << "* Point"
        << setw(10)  << "X"
        << setw(13)  << "Y"
        << setw(15)  << "Z"                             << endl
        << "*      Matrix Points"                       << endl;
```

```
   for (i = 1; i <= 42; i++)
   {
         outfile << setw(5)  << i
                 << setw(15) << x[i]
                 << setw(15) << y[i]
                 << setw(15) << z[i]                    << endl;
   }

//Step 4: Cylinder Points
   //Step 4.1: Circle of Top Cylinder on Left-Front Surface
      //Note: Point 101 was input in Step 3.2
      for (i = 102; i <= 106; i++)
      {
            delta = (i - 102) * (PI/4);
         x[i] = (1 + rho * cos(delta)) * cos(beta1);
         y[i] = (1 + rho * cos(delta)) * sin(beta1);
         z[i] = (2 * sqrt(2.0)) - (rho * sin(delta));
      }

   //Step 4.2: Inner Circle of Top Cylinder on Left-Front Surface
   for (i = 107; i <= 111; i++)
   {
         delta = (i - 107) * (PI/4);
      x[i] = (1 + (rho/2.0) * cos(delta)) * cos(beta1);
      y[i] = (1 + (rho/2.0) * cos(delta)) * sin(beta1);
      z[i] = (2 * sqrt(2.0)) - ((rho/2.0) * sin(delta));
   }

   //Step 4.3: Inner Circle of Top Cylinder at Intersection
   x[112] = 2.0 - (3.0/2.0) * rho;
   y[112] = (sqrt(3.0)/2.0) * rho;
   z[112] = 2 * sqrt(2.0);

   for (i = 113; i <= 117; i++)
   {
         delta = (i - 113) * (PI/4);
      x[i] = x[112] + ((rho/2.0) * cos(delta) * cos(beta1));
      y[i] = y[112] + ((rho/2.0) * cos(delta) * sin(beta1));
      z[i] = (2 * sqrt(2.0)) - ((rho/2.0) * sin(delta));
   }

   //Step 4.4: Circle of Top Cylinder at One-Third between Left-
   //          Front & Intersection
   //Note: Point 118 was input in Step 3.4
   for (i = 119; i <= 123; i++)
   {
         delta = (i - 119) * (PI/4);
      x[i] = x[118] + (rho * cos(delta) * cos(beta1));
      y[i] = y[118] + (rho * cos(delta) * sin(beta1));
      z[i] = (2 * sqrt(2.0)) - (rho * sin(delta));
   }

   //Step 4.5: Inner Circle of Top Cylinder at One-Third between
   //          Left-Front & Intersection
   for (i = 124; i <= 128; i++)
   {
```

```
      delta = (i - 124) * (PI/4);
   x[i] = x[118] + ((rho/2.0) * cos(delta) * cos(beta1));
   y[i] = y[118] + ((rho/2.0) * cos(delta) * sin(beta1));
   z[i] = (2 * sqrt(2.0)) - ((rho/2.0) * sin(delta));
}

//Step 4.6: Circle of Top Cylinder at Two-Thirds between Left-
//          Front & Intersection
//Note: Point 129 was input in Step 3.3
for (i = 130; i <= 134; i++)
{
      delta = (i - 130) * (PI/4);
   x[i] = x[129] + (rho * cos(delta) * cos(beta1));
   y[i] = y[129] + (rho * cos(delta) * sin(beta1));
   z[i] = (2 * sqrt(2.0)) - (rho * sin(delta));
}

//Step 4.7: Inner Circle of Top Cylinder at Two-Thirds between
//          Left-Front & Intersection
for (i = 135; i <= 139; i++)
{
      delta = (i - 135) * (PI/4);
   x[i] = x[129] + ((rho/2.0) * cos(delta) * cos(beta1));
   y[i] = y[129] + ((rho/2.0) * cos(delta) * sin(beta1));
   z[i] = (2 * sqrt(2.0)) - ((rho/2.0) * sin(delta));
}

//Step 4.8: Pseudo-Circle of Top Cylinder at Intersection
//Note: Point 144 was input in Step 3.6 & Point 141 was input in
//      Step 3.9
x[140] = 2 * (1 - rho);
y[140] = y[142] = 0;
z[140] = z[143] = 2 * sqrt(2.0);

a = 1.0/4.0;
b = -1.0;
z[142] = (z[140] + z[141])/2.0;
c = pow(z[142],2) - (4 * sqrt(2.0) * z[142]) + 9.0 - pow(rho,2);
x[142] = (-b - sqrt(pow(b,2.0) - 4 * a *c))/(2 * a);

x[143] = 2.0 - rho;
y[143] = sqrt(3.0) * rho;

a = 1.0;
b = -4.0;
z[145] = (z[143] + z[144])/2.0;
c = pow(z[145],2)-(4 * sqrt(2.0) * z[145]) + 12.0 - pow(rho,2);
x[145] = (-b - sqrt(pow(b,2.0) - 4 * a *c))/(2 * a);
y[145] = sqrt(3.0) * (2.0 - x[145]);

y[146] = 0.82 * rho;
y[147] = 0.41 * rho;
y[148] = 0.94 * rho;

for (i = 146; i <= 148; i++)
{
   a = 2 - (sqrt(3.0)/9.0) * y[i];
```

```
   c1 = -3 * pow(y[i],2);
   c2 = 2*pow((c1+3*pow(rho,2)),0.5)*sqrt(2.0)*sqrt(3.0)*y[i];
   c3 = 6 * pow(rho,2);
   b = -(4.0/9.0) * pow((c1 + 3 * pow(rho,2)),0.5) * sqrt(2.0);
   c = -(2.0/9.0) * pow((c1 + c2 + c3),0.5);

   x[i] = a + b + c;
   z[i] = sqrt(2.0) * x[i] + pow((c1 + 3 * pow(rho,2)),0.5);
}
//Step 4.9: Circle of Back Cylinder on Bottom Surface
//Note: Point 149 was input in Step 3.8
for (i = 150; i <= 154; i++)
{
      delta = (i - 150) * (PI/4);
   x[i] = x[149] + (rho * cos(delta) * cos(alpha1p));
   y[i] = y[149] + (rho * sin(delta));
   z[i] = z[149] - (rho * cos(delta) * sin(alpha1p));
}

//Step 4.10: Inner Circle of Back Cylinder on Bottom Surface
for (i = 155; i <= 159; i++)
{
      delta = (i - 155) * (PI/4);
   x[i] = x[149] + ((rho/2.0) * cos(delta) * cos(alpha1p));
   y[i] = y[149] + ((rho/2.0) * sin(delta));
   z[i] = z[149] - ((rho/2.0) * cos(delta) * sin(alpha1p));
}

//Step 4.11: Pseudo-Circle of Back Cylinder at Intersection
//Note: Points 160 & 161 were input in Step 3.6
x[162] = (x[160] + xmin)/2.0;
a = (1.0/3.0);
b = -(((2 * sqrt(2.0))/3.0) * x[162]);
c = ((11.0/3.0)*pow(x[162],2))-(12.0*x[162])+12-pow(rho,2);
z[162] = (-b - sqrt(pow(b,2.0) - 4 * a *c))/(2 * a);

z[163] = (z[144] + zmin)/2.0;
a = (11.0/3.0);
b = -(((2 * sqrt(2.0))/3.0) * z[163] + 12);
c = (1.0/3.0) * pow(z[163],2) + 12 - pow(rho,2);
x[163] = (-b - sqrt(pow(b,2.0) - 4 * a *c))/(2 * a);

for (i = 162; i <= 163; i++)
      y[i] = sqrt(3.0) * (2.0 - x[i]);

//Step 4.12: Inner Circle of Back Cylinder at Intersection
//Note: Point 164 was input in Step 3.9
gamma1 = atan((z[141] - z[160])/(x[160] - x[141]));

for (i = 165; i <= 169; i++)
{
      delta = (i - 165) * (PI/4);
   x[i] = x[164] + ((rho/2.0) * cos(delta) * cos(gamma1));
   y[i] = y[164] + ((rho/2.0) * sin(delta));
   z[i] = z[164] - ((rho/2.0) * cos(delta) * sin(gamma1));
}
```

```
//Step 4.13: Circle of Back Cylinder at One-Third between Bottom
//           & Intersection
//Note: Point 170 was input in Step 3.9
for (i = 171; i <= 175; i++)
{
      delta = (i - 171) * (PI/4);
   x[i] = x[170] + (rho * cos(delta) * cos(alpha1p));
   y[i] = y[170] + (rho * sin(delta));
   z[i] = z[170] - (rho * cos(delta) * sin(alpha1p));
}

//Step 4.14: Inner Circle of Back Cylinder at One-Third between
//           Bottom & Intersection
for (i = 176; i <= 180; i++)
{
      delta = (i - 176) * (PI/4);
   x[i] = x[170] + ((rho/2.0) * cos(delta) * cos(alpha1p));
   y[i] = y[170] + ((rho/2.0) * sin(delta));
   z[i] = z[170] - ((rho/2.0) * cos(delta) * sin(alpha1p));
}

//Step 4.15: Circle of Back Cylinder at Two-Thirds between
//           Bottom & Intersection
x1 = x[149] + (2.0/3.0) * cmin * cos(alpha2);
z1 = z[149] + (2.0/3.0) * cmin * sin(alpha2);

x2 = x[149] + (2.0/3.0) * (x[164] - x[149]);
z2 = z[149] + (2.0/3.0) * (z[164] - z[149]);

if (x1 <= x2)
{
      x[181] = x1;
      z[181] = z1;
}
else
{
      x[181] = x2;
      z[181] = z2;
}
y[181] = 0;

for (i = 182; i <= 186; i++)
{
      delta = (i - 182) * (PI/4);
   x[i] = x[181] + (rho * cos(delta) * cos(alpha1p));
   y[i] = y[181] + (rho * sin(delta));
   z[i] = z[181] - (rho * cos(delta) * sin(alpha1p));
}

//Step 4.16: Inner Circle of Back Cylinder at Two-Thirds between
//           Bottom & Intersection
for (i = 187; i <= 191; i++)
{
      delta = (i - 187) * (PI/4);
   x[i] = x[181] + ((rho/2.0) * cos(delta) * cos(alpha1p));
   y[i] = y[181] + ((rho/2.0) * sin(delta));
   z[i] = z[181] - ((rho/2.0) * cos(delta) * sin(alpha1p));
```

```
}

//Step 4.17: First Layer of Cylinder Intersection
x[192] = 2.0 - (rho/2.0) * (2.0 + sqrt(3.0/2.0));
y[192] = 0;
z[192] = 2 * sqrt(2.0);

x1 = (rho/2.0) * (2.0 + sqrt(3.0/2.0));
a = 9.0;
b = -(36.0 - (8 * sqrt(6.0) * rho));
c = ((12*pow(rho,2))-(16*sqrt(6.0)*rho)+36.0-pow(x1,2));
x[193] = (-b - sqrt(pow(b,2.0) - 4 * a *c))/(2 * a);
y[193] = 0;
z[193] = (sqrt(2.0) * x[193]) + (sqrt(3.0) * rho);

z[194] = (z[192] + z[193])/2.0;
a = 1.0;
b = -4.0;
c = ((4*pow(z[194],2))-(16*sqrt(2.0)*z[194])+36.0-pow(x1,2));
x[194] = (-b - sqrt(pow(b,2.0) - 4 * a * c))/(2 * a);
y[194] = 0;

x[195] = 2.0 - (rho/2.0) * (1.0 + sqrt(3.0/11.0));
y[195] = (sqrt(3.0)/2.0) * rho * (1.0 + sqrt(3.0/11.0));
z[195] = 2 * sqrt(2.0);

x[196] = 2.0 - (sqrt(3.0/11.0) * rho);
y[196] = 3.0/sqrt(11.0) * rho;
z[196] = ((2 * sqrt(2.0)) + z[144])/2.0;

z[197] = z[196] + (z[195] - z[196])/4.0;
x1 = rho * (1.0 + sqrt(3.0/11.0));
a = 1.0;
b = -4.0;
c = (pow(z[197],2)-(4.0*sqrt(2.0)*z[197])+12.0-pow((x1/2.0),2));
x[197] = (-b - sqrt(pow(b,2.0) - 4 * a * c))/(2 * a);
y[197] = sqrt(3.0) * (2.0 - x[197]);

x[198] = (x[193] + x[196])/2.0;
y[198] = (y[193] + y[196])/2.0;
z[198] = (z[193] + z[196])/2.0;

//Step 4.18: Third Layer of Cylinder Intersection
x[199] = 2.0 - sqrt(3.0/2.0) * rho;
y[199] = 0;
z[199] = z[200] = z[201] = 2 * sqrt(2.0);

x[200] = 2.0*(1.0-(sqrt(3.0)/sqrt(11.0))*rho*cos(beta1));
y[200] = 2.0 * (sqrt(3.0)/sqrt(11.0)) * rho * sin(beta1);

x[201] = (x[199] + x[200])/2.0;
y[201] = (y[199] + y[200])/2.0;

//Step 4.19: Fourth Layer of Cylinder Intersection
x[202] = 2.0 - (sqrt(3.0)/sqrt(11.0)) * rho * cos(beta1);
y[202] = (sqrt(3.0)/sqrt(11.0)) * rho * sin(beta1);
z[202] = z[203] = 2 * sqrt(2.0);
```

```
   x[203] = 2.0 - sqrt(3.0/2.0) * (rho/2.0);
   y[203] = 0;

   for (i = 204; i <= 208; i++)
   {
         delta = (i - 204) * (PI/4);
      x[i] = x[203] + (rho/3.0) * cos(delta);
      y[i] = y[203] + (rho/3.0) * sin(delta);
      z[i] = z[203];
   }

   //Step 4.20: Second Layer of Cylinder Intersection
   x[209] = 2.0;
   y[209] = 0;
   z[209] = (z[8] + z[160])/2.0;

   x[210] = (x[196] + x[209])/2.0;
   y[210] = (y[196] + y[209])/2.0;
   z[210] = (z[196] + z[209])/2.0;

   x[211] = (x[193] + x[209])/2.0;
   y[211] = 0;
   z[211] = (z[193] + z[209])/2.0;

   gamma3 = atan((z[193] - z[209])/(x[209] - x[193]));
   c = sqrt(pow((y[144]-y[209]),2.0)+pow((x[209]-x[144]),2.0));
   gamma4 = atan((z[196] - z[209])/c);

   for (i = 212; i <= 216; i++)
   {
         delta = (i - 212) * (PI/4);
      x[i] = x[211] + ((rho/3.0) * cos(delta) * cos(gamma3));
      y[i] = y[211] + ((rho/3.0) * sin(delta) * cos(gamma4));
      c1 = (rho/3.0) * cos(delta) * sin(gamma3);
      c2 = (rho/3.0) * sin(delta) * sin(gamma4);
      z[i] = z[211] - (c1) + (c2);
   }

   //Step 4.21: Output for Cylinder Geometry Points
   outfile << "*      Cylinder Points" << endl;

   for (i = 101; i <= 216; i++)
   {
         outfile << setw(5)  << i
                 << setw(15) << x[i]
                 << setw(15) << y[i]
                 << setw(15) << z[i] << endl;
   }

//Step 5: Arc Lines and Splines
   //Step 5.1: Block Layers along Top Surface
   for (i = 1; i <= 4; i++)
   {
         k = i - 1;
      p1[i] = 102 + k;
      p2[i] = 103 + k;
```

```
   p3[i] = 101;

   p1[i + 4] = 107 + k;
   p2[i + 4] = 108 + k;
   p3[i + 4] = 101;

   p1[i + 8] = 113 + k;
   p2[i + 8] = 114 + k;
   p3[i + 8] = 112;

   p1[i + 12] = 119 + k;
   p2[i + 12] = 120 + k;
   p3[i + 12] = 118;

   p1[i + 16] = 124 + k;
   p2[i + 16] = 125 + k;
   p3[i + 16] = 118;

   p1[i + 20] = 130 + k;
   p2[i + 20] = 131 + k;
   p3[i + 20] = 129;

   p1[i + 24] = 135 + k;
   p2[i + 24] = 136 + k;
   p3[i + 24] = 129;
}

p1[29] = p1[31] = 141;
p1[30] = p3[32] = 144;
p1[32] = p3[31] = 146;

p2[29] = 142;
p2[30] = 145;
p2[31] = 147;
p2[32] = 148;

p3[29] = 140;
p3[30] = 143;

//Step 5.2: Block Layers along Back Surface
for (i = 33; i <= 36; i++)
{
      k = i - 33;
   p1[i] = 150 + k;
   p2[i] = 151 + k;
   p3[i] = 149;

   p1[i + 4] = 155 + k;
   p2[i + 4] = 156 + k;
   p3[i + 4] = 149;

   p1[i + 10] = 165 + k;
   p2[i + 10] = 166 + k;
   p3[i + 10] = 164;

   p1[i + 14] = 171 + k;
   p2[i + 14] = 172 + k;
```

```
   p3[i + 14] = 170;

   p1[i + 18] = 176 + k;
   p2[i + 18] = 177 + k;
   p3[i + 18] = 170;

   p1[i + 22] = 182 + k;
   p2[i + 22] = 183 + k;
   p3[i + 22] = 181;

   p1[i + 26] = 187 + k;
   p2[i + 26] = 188 + k;
   p3[i + 26] = 181;
}

for (i = 41; i <= 42; i++)
{
      k = i - 41;
   p1[i] = 160 + k;
   p2[i] = 162 + k;
   p3[i] = 161 - (17 * k);
}

//Step 5.3: Block Layers at Cylinder Intersection
for (i = 63; i <= 66; i++)
{
      k = i - 63;
   p1[i] = 212 + k;
   p2[i] = 213 + k;
   p3[i] = 211;

   p1[i + 4] = 204 + k;
   p2[i + 4] = 205 + k;
   p3[i + 4] = 203;
}

//Step 5.4: Extra Arcs to Solve a Problem
for (i = 71; i <= 74; i++)
{
      k = i - 71;
   p1[i] = 9 + k;
   p2[i] = 10 + k;
   p3[i] = 101;

   p1[i + 4] = 19 + k;
   p2[i + 4] = 20 + k;
   p3[i + 4] = 118;

   p1[i + 8] = 33 + k;
   p2[i + 8] = 34 + k;
   p3[i + 8] = 149;

   p1[i + 12] = 38 + k;
   p2[i + 12] = 39 + k;
   p3[i + 12] = 170;
}
```

```
   //Step 5.5: Output for Arc Lines & Splines
   for (i = 1; i <= 28; i++)
   {
         outfile << "Line Arc"
                 << "   Name = "    << i
                 << "   P1 = "      << p1[i]
                 << "   P2 = "      << p2[i]
                 << "   Centre = "  << p3[i]
                 << endl;
   }

   for (i = 29; i <= 32; i++)
   {
         outfile << "Line Polyline"
                 << "   Name = "              << i
                 << "   Type = Spline"        << endl
                 << p1[i]                     << endl
                 << p2[i]                     << endl
                 << p3[i]                     << endl;
   }

   for (i = 33; i <= 40; i++)
   {
         outfile << "Line Arc"
                 << "   Name = "    << i
                 << "   P1 = "      << p1[i]
                 << "   P2 = "      << p2[i]
                 << "   Centre = "  << p3[i]
                 << endl;
   }

   for (i = 41; i <= 42; i++)
   {
         outfile << "Line Polyline"
                 << "   Name = "              << i
                 << "   Type = Spline"        << endl
                 << p1[i]                     << endl
                 << p2[i]                     << endl
                 << p3[i]                     << endl;
   }

   for (i = 43; i <= 86; i++)
   {
         outfile << "Line Arc"
                 << "   Name = "    << i
                 << "   P1 = "      << p1[i]
                 << "   P2 = "      << p2[i]
                 << "   Centre = "  << p3[i]
                 << endl;
   }

//Step 6: Volumes
   //Step 6.1: First Matrix Block Layer along Top Surface
   for (i = 1; i <= 4; i++)
   {
         k = i - 1;
      v1[i] = v5[i + 4] = 9 + k;
```

```
   v2[i] = v6[i + 4] = 10 + k;
   v3[i] = v7[i + 4] = 20 + k;
   v4[i] = v8[i + 4] = 19 + k;
}

for (i = 1; i <= 2; i++)
{
      k = i - 1;
   v5[i] = 3 + k;
   v6[i] = 4 + (3 * k);
   v7[i] = 27 + k;
   v8[i] = 26 + k;
   v5[i + 2] = 7 - (5 * k);
   v6[i + 2] = 2 - k;
   v7[i + 2] = 25 - k;
   v8[i + 2] = 28 - (3 * k);
}

for (i = 5; i <= 8; i++)
{
      k = i - 5;
   v1[i] = 102 + k;
   v2[i] = 103 + k;
   v3[i] = 120 + k;
   v4[i] = 119 + k;
}

//Step 6.2: First Cylinder Block Layer along Top Surface
for (i = 9; i <= 12; i++)
{
      k = i - 9;
   v1[i] = 107 + k;
   v2[i] = 108 + k;
   v3[i] = 125 + k;
   v4[i] = 124 + k;
   v5[i] = 102 + k;
   v6[i] = 103 + k;
   v7[i] = 120 + k;
   v8[i] = 119 + k;
}

for (i = 13; i <= 14; i++)
{
      k = i - 13;
   v1[i] = 101 + (10 * k);
   v2[i] = 109 + k;
   v3[i] = 126 + k;
   v4[i] = 118 + (10 * k);
   v5[i] = 107 - (6 * k);
   v6[i] = 108 + k;
   v7[i] = 125 + k;
   v8[i] = 124 - (6 * k);
}

//Step 6.3: Second Matrix Block Layer along Top Surface
for (i = 15; i <= 18; i++)
{
```

```
      k = i - 15;
   v2[i] = 19 + k;
   v3[i] = 20 + k;
}

for (i = 15; i <= 16; i++)
{
      k = i - 15;
   v1[i] = 16 + k;
   v4[i] = 17 + k;
   v5[i] = 26 + k;
   v6[i] = 27 + k;
   v1[i + 2] = 18 - (3 * k);
   v4[i + 2] = 15 - k;
   v5[i + 2] = 28 - (3 * k);
   v6[i + 2] = 25 - k;
   v7[i + 4] = 17 + k;
   v8[i + 4] = 16 + k;
   v7[i + 6] = 15 - k;
   v8[i + 6] = 18 - (3 * k);
}

for (i = 19; i <= 22; i++)
{
      k = i - 19;
   v1[i] = 119 + k;
   v2[i] = 120 + k;
   v3[i] = 131 + k;
   v4[i] = 130 + k;
   v5[i] = 19 + k;
   v6[i] = 20 + k;
}

//Step 6.4: Second Cylinder Block Layer along Top Surface
for (i = 23; i <= 26; i++)
{
      k = i - 23;
   v1[i] = 124 + k;
   v2[i] = 125 + k;
   v3[i] = 136 + k;
   v4[i] = 135 + k;
   v5[i] = 119 + k;
   v6[i] = 120 + k;
   v7[i] = 131 + k;
   v8[i] = 130 + k;
}

for (i = 27; i <= 28; i++)
{
      k = i - 27;
   v1[i] = 118 + (10 * k);
   v2[i] = 126 + k;
   v3[i] = 137 + k;
   v4[i] = 129 + (10 * k);
   v5[i] = 124 - (6 * k);
   v6[i] = 125 + k;
   v7[i] = 136 + k;
```

```
   v8[i] = 135 - (6 * k);
}

//Step 6.5: Third Matrix Block Layer along Top Surface
for (i = 29; i <= 30; i++)
{
      k = i - 29;
   v1[i] = 143 + k;
   v2[i] = 130 + k;
   v3[i] = 131 + k;
   v4[i] = 144 + (2 * k);
   v5[i] = 16 + k;
   v6[i] = 17 + k;
   v1[i + 2] = 146 - (5 * k);
   v2[i + 2] = 132 + k;
   v3[i + 2] = 133 + k;
   v4[i + 2] = 141 - k;
   v5[i + 2] = 18 - (3 * k);
   v6[i + 2] = 15 - k;
}

//Step 6.6: Third Cylinder Block Layer along Top Surface
for (i = 33; i <= 36; i++)
{
      k = i - 33;
   v1[i] = 135 + k;
   v2[i] = 136 + k;
   v3[i] = 114 + k;
   v4[i] = 113 + k;
   v5[i] = 130 + k;
   v6[i] = 131 + k;
}

for (i = 33; i <= 34; i++)
{
      k = i - 33;
   v7[i] = 144 + (2 * k);
   v8[i] = 143 + k;
   v7[i + 2] = 141 - k;
   v8[i + 2] = 146 - (5 * k);
   v1[i + 4] = 129 + (10 * k);
   v2[i + 4] = 137 + k;
   v3[i + 4] = 115 + k;
   v4[i + 4] = 112 + (5 * k);
   v5[i + 4] = 135 - (6 * k);
   v6[i + 4] = 136 + k;
   v7[i + 4] = 114 + k;
   v8[i + 4] = 113 - k;
}

//Step 6.7: First Matrix Block Layer along Back Surface
for (i = 39; i <= 42; i++)
{
      k = i - 39;
   v1[i] = v5[i + 4] = 42 - k;
   v2[i] = v6[i + 4] = 37 - k;
   v3[i] = v7[i + 4] = 36 - k;
```

```
   v4[i] = v8[i + 4] = 41 - k;
}

for (i = 39; i <= 40; i++)
{
      k = i - 39;
   v5[i] = 25 + (3 * k);
   v6[i] = 2 + (5 * k);
   v7[i] = 7 - (3 * k);
   v8[i] = 28 - k;
   v5[i + 2] = 27 + (3 * k);
   v6[i + 2] = 4 + (2 * k);
   v7[i + 2] = 6 - k;
   v8[i + 2] = 30 - k;
}

for (i = 43; i <= 46; i++)
{
      k = i - 43;
   v1[i] = 175 - k;
   v2[i] = 154 - k;
   v3[i] = 153 - k;
   v4[i] = 174 - k;
}

//Step 6.8: First Cylinder Block Layer along Back Surface
for (i = 47; i <= 50; i++)
{
      k = i - 47;
   v1[i] = 180 - k;
   v2[i] = 159 - k;
   v3[i] = 158 - k;
   v4[i] = 179 - k;
   v5[i] = 175 - k;
   v6[i] = 154 - k;
   v7[i] = 153 - k;
   v8[i] = 174 - k;
}

for (i = 51; i <= 52; i++)
{
      k = i - 51;
   v1[i] = 170 + (6 * k);
   v2[i] = 149 + (6 * k);
   v3[i] = 157 - k;
   v4[i] = 178 - k;
   v5[i] = 180 - (10 * k);
   v6[i] = 159 - (10 * k);
   v7[i] = 158 - k;
   v8[i] = 179 - k;
}

//Step 6.9: Second Matrix Block Layer along Back Surface
for (i = 53; i <= 56; i++)
{
      k = i - 53;
   v2[i] = v6[i + 4] = 42 - k;
```

```
   v3[i] = v7[i + 4] = 41 - k;
   v1[i + 4] = 186 - k;
   v2[i + 4] = 175 - k;
   v3[i + 4] = 174 - k;
   v4[i + 4] = 185 - k;
}

for (i = 53; i <= 54; i++)
{
      k = i - 53;
   v1[i] = v5[i + 4] = 15 + (3 * k);
   v4[i] = v8[i + 4] = 18 - k;
   v5[i] = 25 + (3 * k);
   v6[i] = 28 - k;
   v1[i + 2] = v5[i + 6] = 17 + (15 * k);
   v4[i + 2] = v8[i + 6] = 32 - k;
   v5[i + 2] = 27 + (3 * k);
   v6[i + 2] = 30 - k;
}

//Step 6.10: Second Cylinder Block Layer along Back Surface
for (i = 61; i <= 64; i++)
{
      k = i - 61;
   v1[i] = 191 - k;
   v2[i] = 180 - k;
   v3[i] = 179 - k;
   v4[i] = 190 - k;
   v5[i] = 186 - k;
   v6[i] = 175 - k;
   v7[i] = 174 - k;
   v8[i] = 185 - k;
}

for (i = 65; i <= 66; i++)
{
      k = i - 65;
   v1[i] = 181 + (6 * k);
   v2[i] = 170 + (6 * k);
   v3[i] = 178 - k;
   v4[i] = 189 - k;
   v5[i] = 191 - (10 * k);
   v6[i] = 180 - (10 * k);
   v7[i] = 179 - k;
   v8[i] = 190 - k;
}

//Step 6.11: Third Matrix Block Layer along Back Surface
for (i = 67; i <= 70; i++)
{
      k = i - 67;
   v2[i] = 186 - k;
   v3[i] = 185 - k;
}

for (i = 67; i <= 68; i++)
{
```

```
      k = i - 67;
   v1[i] = 141 + (5 * k);
   v4[i] = 146 - (2 * k);
   v5[i] = 15 + (3 * k);
   v6[i] = 18 - k;
   v1[i + 2] = 144 + (17 * k);
   v4[i + 2] = 161 - k;
   v5[i + 2] = 17 + (15 * k);
   v6[i + 2] = 32 - k;
}

//Step 6.12: Third Cylinder Block Layer along Back Surface
for (i = 71; i <= 74; i++)
{
      k = i - 71;
   v1[i] = 169 - k;
   v2[i] = 191 - k;
   v3[i] = 190 - k;
   v4[i] = 168 - k;
   v6[i] = 186 - k;
   v7[i] = 185 - k;
}

for (i = 71; i <= 72; i++)
{
      k = i -71;
   v5[i] = 141 + (5 * k);
   v8[i] = 146 - (2 * k);
   v5[i + 2] = 144 + (17 * k);
   v8[i + 2] = 161 - k;
   v1[i + 4] = 164 + k;
   v2[i + 4] = 181 + (6 * k);
   v3[i + 4] = 189 - k;
   v4[i + 4] = 167 - k;
   v5[i + 4] = 169 - (5 * k);
   v6[i + 4] = 191 - (10 * k);
   v7[i + 4] = 190 - k;
   v8[i + 4] = 168 - k;
}

//Step 6.13: First Layer of Cylinder Intersection
for (i = 77; i <= 80; i++)
{
      k = i - 77;
   v2[i] = 113 + k;
   v3[i] = 114 + k;
}

for (i = 77; i <= 78; i++)
{
      k = i - 77;
   v1[i] = 195 + k;
   v4[i] = 197 + k;
   v5[i] = 143 + k;
   v6[i] = 144 + (2 * k);

   v1[i + 2] = 198 - (4 * k);
```

```
   v4[i + 2] = 193 - k;
   v5[i + 2] = 146 - (5 * k);
   v6[i + 2] = 141 - k;
}

v1[81] = 197;
v2[81] = 114;
v3[81] = 196;
v4[81] = 144;
v1[82] = 193;
v2[82] = 194;
v3[82] = 116;
v4[82] = 141;

//Step 6.14: Second Layer of Cylinder Intersection
for (i = 83; i <= 86; i++)
{
      k = i - 83;
   v1[i] = 216 - k;
   v2[i] = 169 - k;
   v3[i] = 168 - k;
   v4[i] = 215 - k;
}

for (i = 83; i <= 84; i++)
{
      k = i - 83;
   v5[i] = 193 + (5 * k);
   v6[i] = 141 + (5 * k);
   v7[i] = 146 - (2 * k);
   v8[i] = 198 - (2 * k);
   v5[i + 2] = 196 + (14 * k);
   v6[i + 2] = 144 + (17 * k);
   v7[i + 2] = 161 - k;
   v8[i + 2] = 210 - k;
   v1[i + 4] = 211 + k;
   v2[i + 4] = 164 + k;
   v3[i + 4] = 167 - k;
   v4[i + 4] = 214 - k;
   v5[i + 4] = 216 - (5 * k);
   v6[i + 4] = 169 - (5 * k);
   v7[i + 4] = 168 - k;
   v8[i + 4] = 215 - k;
}

//Step 6.15: Third Layer of Cylinder Intersection
for (i = 89; i <= 90; i++)
{
      k = i - 89;
   v1[i] = 112 + (5 * k);
   v2[i] = 115 + k;
   v3[i] = 198 - (5 * k);
   v4[i] = 201 - (2 * k);
   v5[i] = 113 - k;
   v6[i] = 114 + k;
   v7[i] = 196 + (2 * k);
   v8[i] = 200 + k;
```

```
   v1[i + 2] = 200 - k;
   v2[i + 2] = 113 + (4 * k);
   v3[i + 2] = 114 + (2 * k);
   v4[i + 2] = 196 - (3 * k);
   v5[i + 2] = 195 - (3 * k);
   v6[i + 2] = 197 - (3 * k);
}

//Step 6.16: Fourth Layer of Cylinder Intersection
for (i = 93; i <= 96; i++)
{
      k = i - 93;
   v1[i] = 208 - k;
   v2[i] = 216 - k;
   v3[i] = 215 - k;
   v4[i] = 207 - k;
}

for (i = 93; i <= 94; i++)
{
      k = i - 93;
   v5[i] = 199 + (2 * k);
   v6[i] = 193 + (5 * k);
   v7[i] = 198 - (2 * k);
   v8[i] = 201 - k;
   v5[i + 2] = 200 + (2 * k);
   v6[i + 2] = 196 + (14 * k);
   v7[i + 2] = 210 - k;
   v8[i + 2] = 202 - (194 * k);
   v1[i + 4] = 203 + k;
   v2[i + 4] = 211 + k;
   v3[i + 4] = 214 - k;
   v4[i + 4] = 206 - k;
   v5[i + 4] = 208 - (5 * k);
   v6[i + 4] = 216 - (5 * k);
   v7[i + 4] = 215 - k;
   v8[i + 4] = 207 - k;
}

//Step 6.17: Output for Volumes
for (i = 1; i <= 14; i++)
{
      outfile << "Volume" << "   Vertex" << "   Shape = Hex"
              << "   Name = " << i << "," << endl
              << "         vertex1 = " << v1[i]
              << "   vertex2 = " << v2[i]
              << "   vertex3 = " << v3[i]
              << "   vertex4 = " << v4[i] << "," << endl
              << "         vertex5 = " << v5[i]
              << "   vertex6 = " << v6[i]
              << "   vertex7 = " << v7[i]
              << "   vertex8 = " << v8[i]
              << endl;
}

for (i = 15; i <= 18; i++)
```

```
{
      outfile << "Volume" << "   Vertex" << "   Shape = Prism"
              << "   Name = " << i << "," << endl
              << "         vertex1 = " << v1[i]
              << "   vertex2 = " << v2[i]
              << "   vertex3 = " << v3[i]
              << "   vertex4 = " << v4[i] << "," << endl
              << "         vertex5 = " << v5[i]
              << "   vertex6 = " << v6[i]
              << endl;
}

for (i = 19; i <= 28; i++)
{
      outfile << "Volume" << "   Vertex" << "   Shape = Hex"
              << "   Name = " << i << "," << endl
              << "         vertex1 = " << v1[i]
              << "   vertex2 = " << v2[i]
              << "   vertex3 = " << v3[i]
              << "   vertex4 = " << v4[i] << "," << endl
              << "         vertex5 = " << v5[i]
              << "   vertex6 = " << v6[i]
              << "   vertex7 = " << v7[i]
              << "   vertex8 = " << v8[i]
              << endl;
}

for (i = 29; i <= 32; i++)
{
      outfile << "Volume" << "   Vertex" << "   Shape = Prism"
              << "   Name = " << i << "," << endl
              << "         vertex1 = " << v1[i]
              << "   vertex2 = " << v2[i]
              << "   vertex3 = " << v3[i]
              << "   vertex4 = " << v4[i] << "," << endl
              << "         vertex5 = " << v5[i]
              << "   vertex6 = " << v6[i]
              << endl;
}

for (i = 33; i <= 52; i++)
{
      outfile << "Volume" << "   Vertex" << "   Shape = Hex"
              << "   Name = " << i << "," << endl
              << "         vertex1 = " << v1[i]
              << "   vertex2 = " << v2[i]
              << "   vertex3 = " << v3[i]
              << "   vertex4 = " << v4[i] << "," << endl
              << "         vertex5 = " << v5[i]
              << "   vertex6 = " << v6[i]
              << "   vertex7 = " << v7[i]
              << "   vertex8 = " << v8[i]
              << endl;
}

for (i = 53; i <= 56; i++)
{
```

```
      outfile << "Volume" << "   Vertex" << "   Shape = Prism"
              << "   Name = " << i << "," << endl
              << "         vertex1 = " << v1[i]
              << "   vertex2 = " << v2[i]
              << "   vertex3 = " << v3[i]
              << "   vertex4 = " << v4[i] << "," << endl
              << "         vertex5 = " << v5[i]
              << "   vertex6 = " << v6[i]
              << endl;
}

for (i = 57; i <= 66; i++)
{
      outfile << "Volume" << "   Vertex" << "   Shape = Hex"
              << "   Name = " << i << "," << endl
              << "         vertex1 = " << v1[i]
              << "   vertex2 = " << v2[i]
              << "   vertex3 = " << v3[i]
              << "   vertex4 = " << v4[i] << "," << endl
              << "         vertex5 = " << v5[i]
              << "   vertex6 = " << v6[i]
              << "   vertex7 = " << v7[i]
              << "   vertex8 = " << v8[i]
              << endl;
}

for (i = 67; i <= 70; i++)
{
      outfile << "Volume" << "   Vertex" << "   Shape = Prism"
              << "   Name = " << i << "," << endl
              << "         vertex1 = " << v1[i]
              << "   vertex2 = " << v2[i]
              << "   vertex3 = " << v3[i]
              << "   vertex4 = " << v4[i] << "," << endl
              << "         vertex5 = " << v5[i]
              << "   vertex6 = " << v6[i]
              << endl;
}

for (i = 71; i <= 76; i++)
{
      outfile << "Volume" << "   Vertex" << "   Shape = Hex"
              << "   Name = " << i << "," << endl
              << "         vertex1 = " << v1[i]
              << "   vertex2 = " << v2[i]
              << "   vertex3 = " << v3[i]
              << "   vertex4 = " << v4[i] << "," << endl
              << "         vertex5 = " << v5[i]
              << "   vertex6 = " << v6[i]
              << "   vertex7 = " << v7[i]
              << "   vertex8 = " << v8[i]
              << endl;
}

for (i = 77; i <= 80; i++)
{
      outfile << "Volume" << "   Vertex" << "   Shape = Prism"
```

```
                << "   Name = " << i << "," << endl
                << "         vertex1 = " << v1[i]
                << "   vertex2 = " << v2[i]
                << "   vertex3 = " << v3[i]
                << "   vertex4 = " << v4[i] << "," << endl
                << "         vertex5 = " << v5[i]
                << "   vertex6 = " << v6[i]
                << endl;
}

for (i = 81; i <= 82; i++)
{
      outfile << "Volume" << "   Vertex" << "   Shape = Tetra"
                << "   Name = " << i << "," << endl
                << "         vertex1 = " << v1[i]
                << "   vertex2 = " << v2[i]
                << "   vertex3 = " << v3[i]
                << "   vertex4 = " << v4[i]
                << endl;
}

for (i = 83; i <= 90; i++)
{
      outfile << "Volume" << "   Vertex" << "   Shape = Hex"
                << "   Name = " << i << "," << endl
                << "         vertex1 = " << v1[i]
                << "   vertex2 = " << v2[i]
                << "   vertex3 = " << v3[i]
                << "   vertex4 = " << v4[i] << "," << endl
                << "         vertex5 = " << v5[i]
                << "   vertex6 = " << v6[i]
                << "   vertex7 = " << v7[i]
                << "   vertex8 = " << v8[i]
                << endl;
}

for (i = 91; i <= 92; i++)
{
      outfile << "Volume" << "   Vertex" << "   Shape = Prism"
                << "   Name = " << i << "," << endl
                << "         vertex1 = " << v1[i]
                << "   vertex2 = " << v2[i]
                << "   vertex3 = " << v3[i]
                << "   vertex4 = " << v4[i] << "," << endl
                << "         vertex5 = " << v5[i]
                << "   vertex6 = " << v6[i]
                << endl;
}

for (i = 93; i <= 98; i++)
{
      outfile << "Volume" << "   Vertex" << "   Shape = Hex"
                << "   Name = " << i << "," << endl
                << "         vertex1 = " << v1[i]
                << "   vertex2 = " << v2[i]
                << "   vertex3 = " << v3[i]
                << "   vertex4 = " << v4[i] << "," << endl
```

```
                << "         vertex5 = " << v5[i]
                << "   vertex6 = " << v6[i]
                << "   vertex7 = " << v7[i]
                << "   vertex8 = " << v8[i]
                << endl;
   }


//Step 7: Material Properties
ET1 = ET2 = 0.001;
EPA1 = EPA2 = 0.2;

outfile << "Material Plastic-Bilinear"
        << "    Name = " << 1
        << "    E = "    << E1
        << "    Nu = "   << nu1
        << "    Y = "    << Y1
        << "    ET = "   << ET1
        << "    EPA = "  << EPA1
        << endl;

outfile << "Material Plastic-Bilinear"
        << "    Name = " << 2
        << "    E = "    << E2
        << "    Nu = "   << nu2
        << "    Y = "    << Y2
        << "    ET = "   << ET2
        << "    EPA = "  << EPA2
        << endl;

//Step 8: Element Groups
for (i = 1; i <= 2; i++)
{
   outfile << "EGroup ThreeDSolid"
           << "    Name = "     << i
           << "    Material = " << i
           << endl;
}

//Step 9: Subdivision Data
outfile << "Subdivide Volume"
        << "    Name = "  << 1
        << "    NDiv1 = " << ndiv1
        << "    NDiv2 = " << ndiv2
        << "    NDiv3 = " << ndiv3
        << endl;

for (i = 2; i <= 98; i++)
{
   outfile << "    " << i
           << endl;
}

//Step 10: Generate Elements
   //Step 10.1: Surrounding Material (Matrix)
   outfile << "GVolume"
           << "    Name = "  << 1
```

```
        << "    Nodes = " << elemnodes
        << "    Group = " << 1
        << "    PrefShape = Hexahedral"
        << endl;

for (i = 2; i <= 8; i++)
{
      outfile << "    " << i
              << endl;
}

for (i = 15; i <= 22; i++)
{
      outfile << "    " << i
              << endl;
}

for (i = 29; i <= 32; i++)
{
      outfile << "    " << i
              << endl;
}

for (i = 39; i <= 46; i++)
{
      outfile << "    " << i
              << endl;
}

for (i = 53; i <= 60; i++)
{
      outfile << "    " << i
              << endl;
}

for (i = 67; i <= 70; i++)
{
      outfile << "    " << i
              << endl;
}


//Step 10.2: Cylinder
outfile << "GVolume"
        << "    Name = "  << 9
        << "    Nodes = " << elemnodes
        << "    Group = " << 2
        << "    PrefShape = Hexahedral"
        << endl;

for (i = 10; i <= 14; i++)
{
      outfile << "    " << i
              << endl;
}

for (i = 23; i <= 28; i++)
```

```
        {
              outfile << "    " << i
                      << endl;
        }

        for (i = 33; i <= 38; i++)
        {
              outfile << "    " << i
                      << endl;
        }

        for (i = 47; i <= 52; i++)
        {
              outfile << "    " << i
                      << endl;
        }

        for (i = 61; i <= 66; i++)
        {
              outfile << "    " << i
                      << endl;
        }

        for (i = 71; i <= 98; i++)
        {
              outfile << "    " << i
                      << endl;
        }

    return 0;
}
```

APPENDIX F

RAW DATA FOR THE MACROSCOPIC BEHAVIOUR DISCRETISATION VALIDATION

The data provided in this appendix shows how increasing the level of discretisation refinement leads to the convergence of the macroscopic behaviour to the exact solution. This validation was completed for both the spherical and cylindrical models simulating linear elastic conditions. It was assumed that results for non-linear plastic conditions would follow a similar trend. Table F.1 presents the results for the spherical model and Table F.2 presents the results for the cylindrical model. For a discussion of these results see Section 4.1.2. Note that the effective Young's modulus of each model was calculated using Equations 3.16 and 3.17 with the top surface area of 1.732 mm^2 and the applied strain of 0.001.

Table F.1: Raw Data for the Validation of the Spherical Model
(elastic modular ratio = 1.9)

Volume Fraction of Spheres [%]	Level of Refinement	Reaction at Master Node [N]	Effective Young's Modulus [GPa]	Difference [%]
75	1-1-1	311.080	179.602	n/a
	2-2-2	311.018	179.566	0.0199
	3-3-3	311.011	179.562	0.0023
80	1-1-1	320.971	185.313	n/a
	2-2-2	320.933	185.291	0.0118
	3-3-3	320.928	185.288	0.0016
83.2	1-1-1	327.515	189.091	n/a
	2-2-2	327.479	189.070	0.0110
	3-3-3	327.473	189.067	0.0018
85	1-1-1	331.255	191.250	n/a
	2-2-2	331.218	191.229	0.0112
	3-3-3	331.211	191.225	0.0021
90	1-1-1	341.812	197.345	n/a
	2-2-2	341.774	197.323	0.0111
	3-3-3	341.763	197.317	0.0032
95	1-1-1	352.641	203.597	n/a
	2-2-2	352.607	203.578	0.0096
	3-3-3	352.598	203.573	0.0026

Table F.2: Raw Data for the Validation of the Cylindrical Model
(elastic modular ratio = 2)

Volume Fraction of Cylinders [%]	Level of Refinement	Reaction at Master Node [N]	Effective Young's Modulus [GPa]	Difference [%]
2.09	1-1-1	175.830	101.515	n/a
	2-2-2	175.800	101.498	0.0171
	3-3-3	175.792	101.494	0.0046
16.45	1-1-1	194.905	112.528	n/a
	2-2-2	194.814	112.476	0.0467
	3-3-3	194.806	112.471	0.0041
39.11	1-1-1	229.124	132.285	n/a
	2-2-2	228.981	132.202	0.0624
	3-3-3	228.973	132.198	0.0035
63.77	1-1-1	272.271	157.196	n/a
	2-2-2	272.081	157.086	0.0698
	3-3-3	272.069	157.079	0.0044
84.14	1-1-1	312.507	180.426	n/a
	2-2-2	312.224	180.263	0.0906
	3-3-3	312.199	180.248	0.0080

APPENDIX G

RAW DATA FOR THE LINEAR ELASTIC MACROSCOPIC BEHAVIOUR

The linear elastic macroscopic behaviour analysis in Section 4.2.1 is based on the effective Young's moduli of the composites. This data was obtained from the simulation of the two unit cell models to a uniaxial tension test in the finite element program ADINA (ADINA R&D, Inc., 2002a). ADINA provided the reactions of each simulation at the master node from which the effective Young's moduli could be calculated (see Section 3.6). The data for the spherical model is listed in Table G.1 and the data for the cylindrical model in Table G.2.

Table G.1: Raw Data for the Linear Elastic Macroscopic Analysis of the Spherical Model

Modular Ratio	Volume Fraction of Spheres [%]	Contiguity of Spheres [%]	Reaction at Master Node [N]	Effective Young's Modulus [GPa]
2	75	5.00	292.127	168.660
	80	28.17	302.303	174.535
	85	47.48	312.875	180.638
	90	64.70	323.749	186.917
	95	82.27	334.928	193.371
10	75	5.00	182.056	105.110
	80	28.17	214.401	123.784
	85	47.48	246.722	142.445
	90	64.70	279.684	161.476
	95	82.27	313.161	180.804
100	75	5.000	79.092	45.663
	80	28.174	147.272	85.028
	85	47.484	201.591	116.389
	90	64.702	252.570	145.821
	95	82.27	301.121	173.852

Table G.2: Raw Data for the Linear Elastic Macroscopic Analysis of the Cylindrical Model

Modular Ratio	Volume Fraction of Cylinders [%]	Contiguity of Cylinders [%]	Reaction at Master Node [N]	Effective Young's Modulus [GPa]
2	2.09	5.97	175.792	101.494
	16.45	19.19	194.806	112.471
	39.11	34.45	228.973	132.198
	63.77	52.27	272.069	157.079
	84.14	73.35	312.199	180.248
10	2.09	5.97	36.954	21.335
	16.45	19.19	56.310	32.511
	39.11	34.45	99.800	57.619
	63.77	52.27	173.365	100.092
	84.14	73.35	263.119	151.912
100	2.09	5.97	5.198	3.001
	16.45	19.19	20.572	11.877
	39.11	34.45	59.150	34.150
	63.77	52.27	134.346	77.565
	84.14	73.35	242.527	140.023

APPENDIX H

CONTIGUITIES OF SPHERICAL AND CYLINDRICAL MODELS

The methodology for calculating the contiguities of the spherical and cylindrical models using Equation 4.1 was described in Section 4.2.1. While this information was sufficient to allow the reader to understand the physical meaning of contiguity, it was much too simplified to describe how the contiguities were actually calculated. The geometry of the spherical model makes the calculation of its contiguity relatively simple so that it is possible to determine an exact solution. This is not the case for the cylindrical model where determining the surface areas of the cylinders within the half prism unit cell and within the intersection is particularly difficult. An approximate solution was therefore derived for the cylindrical model. The calculations for each model are described in the following two sections: Section H.1 for the spherical model and Section H.2 for the cylindrical model.

H.1 CONTIGUITY OF THE SPHERICAL MODEL

- Parameters of the geometry (see Fig. H.1):

$$c = \sqrt{2^2 + 1^2} = \sqrt{3}$$

$$\rho = \sqrt{r^2 - 3}$$

$$h = r - c$$

r: radius of sphere

c: distance from centre of sphere to edge of section

ρ: radius of contact area

h: height of sphere section

- Surface area between adjacent spheres ($S_v^{\alpha\alpha}$):

$$S_v^{\alpha\alpha} = \pi \cdot \rho^2 \qquad \text{(H.1)}$$

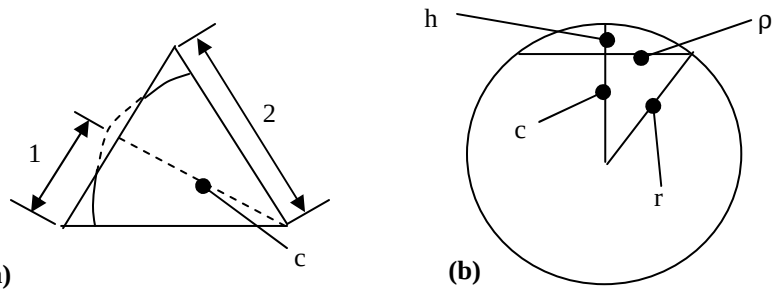

Figure H.1: Spherical Model
(a) Top view of the unit cell showing the piece of sphere
(b) Circle showing the variables used in the calculations

- Surface area between phases ($S_v^{\alpha\beta}$):

$$A_{sphere} = \frac{1}{12}\left(4 \cdot \pi \cdot r^2\right)$$

$$A_{section} = 2 \cdot \pi \cdot r \cdot h$$

A_{sphere}: surface area of sphere within unit cell assuming none is outside

$A_{section}$: surface area of sphere that is outside unit cell

$$S_v^{\alpha\beta} = A_{sphere} - A_{section} \tag{H.2}$$

Equations H.1 and H.2 may now be inserted into Equation 4.1 to determine the contiguity of the spherical model for any interpenetrating volume fraction.

H.2 CONTIGUITY OF THE CYLINDRICAL MODEL

For the cylindrical model it is necessary to integrate the surface area of a cylinder. Given the function of a cylinder;

$$z = f(x, y), \tag{H.3}$$

the surface area is;

$$S = \int\int \sqrt{1 + \left(\frac{\partial z}{\partial x}\right)^2 + \left(\frac{\partial z}{\partial y}\right)^2}\, \partial x \partial y\,. \tag{H.4}$$

- Parameters of the geometry (see Fig. H.2):

$$l = \sqrt{2^2 + 1^2} = \sqrt{3}$$

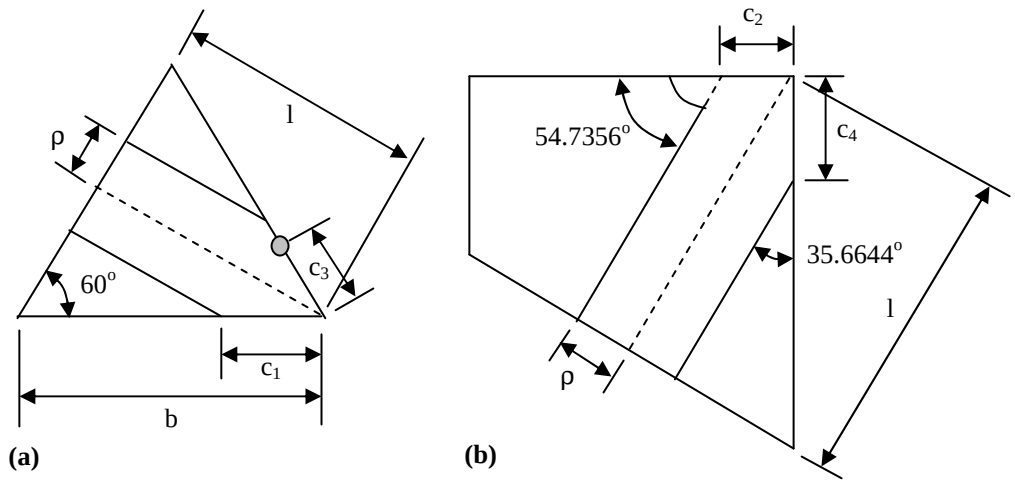

Figure H.2: Cylindrical Model
(a) Top view of the unit cell showing the top cylinder
(b) Back view of the unit cell showing the back cylinder

ρ: *radius of a cylinder*

l: *length of a cylinder on its centreline* $\left[l = \sqrt{3}\right]$

b: *length of each horizontal edge for the unit cell* $\left[b = 2\right]$

h: *height of full prism unit cell (see Fig. H.4)* $\left[h = 2\sqrt{2}\right]$

c_1: *distance from top-right-back corner to where top cylinder intercepts the top-back edge and the top-right edge* $\left[c_1 = 2\rho\right]$

c_2: *distance from top-right-back corner to where back cylinder intercepts the top-back edge* $\left[c_2 = \sqrt{\frac{3}{2}}\rho\right]$

c_3: *distance from top-right-back corner to where back cylinder intercepts the top-right edge* $\left[c_3 = \frac{2\sqrt{3}}{\sqrt{11}}\rho\right]$

c_4: *distance from top-right-back corner to where back cylinder intercepts the right-back edge* $\left[c_4 = \sqrt{3}\rho\right]$

- Surface area between cylinders inside and outside of unit cell ($S_v^{\alpha\alpha}$):

$$S_v^{\alpha\alpha} = \pi \cdot \rho^2 \tag{H.5}$$

- Surface area between phases ($S_v^{\alpha\beta}$):
  - Surface area of a cylinder if its entire length was within the unit cell:

$$A_{total} = \frac{1}{2}(2 \cdot \pi \cdot \rho \cdot l)$$

o Surface area of top cylinder:

a) Remove surface area that is beyond back surface and right front surface (see Fig. H.3):

- Equation of top cylinder: $z = \sqrt{\rho^2 - x^2}$

$$\left(\frac{\partial z}{\partial x}\right)^2 = \left[\frac{\partial}{\partial x}\left(\sqrt{\rho^2 - x^2}\right)\right]^2 = \frac{x^2}{\left(\rho^2 - x^2\right)}$$

$$\left(\frac{\partial z}{\partial y}\right)^2 = \left[\frac{\partial}{\partial y}\left(\sqrt{\rho^2 - x^2}\right)\right]^2 = 0$$

- Equation of back surface: $y = \sqrt{3}x$

- The surface area goes between 0 and ρ in the x-direction, and 0 and $\sqrt{3}x$ in the y-direction.

$$A_{top(a)} = \int_0^{\rho}\int_0^{\sqrt{3}x} \sqrt{1 + \left[\frac{x^2}{\left(\rho^2 - x^2\right)}\right] + (0)}\,\partial y \partial x$$

b) Remove approximate surface area that enters the cylinder intersection (see Fig. H.3):

- Location of point 141 based on global axes (see Fig. H.4):

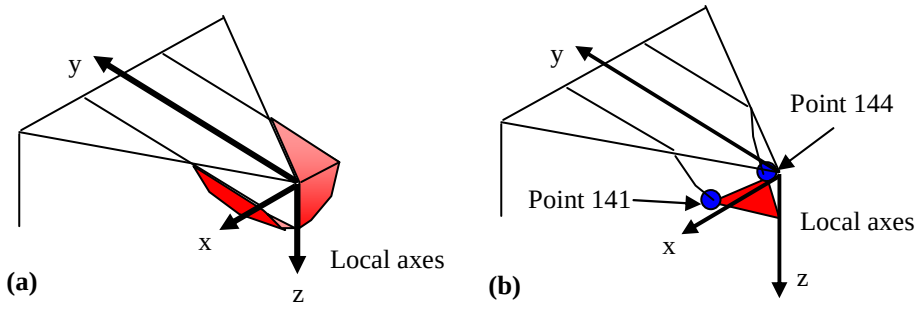

Figure H.3: Top part of unit cell showing the top cylinder
(a) Surface areas of top cylinder removed in step (a) shown in red
(b) Surface area of top cylinder removed in step (b) shown in red, important geometry points shown in blue

$$\left(\frac{9}{4}\right)x'^2-\left(9-2\sqrt{6}\rho\right)x'+\left(2\rho^2-4\sqrt{6}\rho+9\right)=0$$

$$x'_{141}=2-\frac{2}{3}\sqrt{6}\rho$$

- Location of point 141 based on local axes (see Fig. H.3):

$$d=b-x'_{141}$$

$$x_{141}=d\cdot\cos(60) \qquad y_{141}=d\cdot\sin(60)$$

- Location of point 144 based on global axes (see Fig. H.4):

$$x'_{144}=\frac{2\sqrt{3}-\rho}{\sqrt{3}} \qquad y'_{144}=\sqrt{3}\left(b-x'_{144}\right)$$

- Location of point 144 based on local axes (see Fig. H.3):

$$d=\sqrt{\left(2-x'_{144}\right)^2+\left(y'_{144}\right)^2}$$

$$x_{144}=-d\cdot\cos(60) \qquad y_{144}=d\cdot\sin(60)$$

- Upper bound in y-direction:

$$m_{(top\,b)}=\frac{\left(y_{141}-y_{144}\right)}{\left(x_{141}-x_{144}\right)} \qquad n_{(top\,b)}=y_{141}-m_{(top\,b)}\left(x_{141}-0\right)$$

$$y_{up(top\,b)}=\left(m_{(top\,b)}\right)x+n_{(top\,b)}$$

- The surface area goes between x_{144} and x_{141} in the x-direction, and 0 and $y_{up(top\,b)}$ in the y-direction.

$$A_{top(b)}=\int_{x_{144}}^{x_{141}}\int_{0}^{y_{up(top\,b)}}\sqrt{1+\left[\frac{x^2}{\left(\rho^2-x^2\right)}\right]+(0)}\,\partial y\,\partial x$$

Therefore the surface area of the top cylinder is:

$$A_{top}=A_{total}-(2A_{top(a)}+A_{top(b)}) \qquad \text{(H.6)}$$

o Surface area of back cylinder:

a) Remove surface area that is beyond the top surface (see Fig. H.4):

- The equation for the back cylinder is the same as it was for the top cylinder based on the change in the local axes. The derivatives are also the same.

- Equation for top surface: $y = \frac{1}{\sqrt{2}} x$

- The surface area goes between -ρ and 0 in the x-direction, and 0

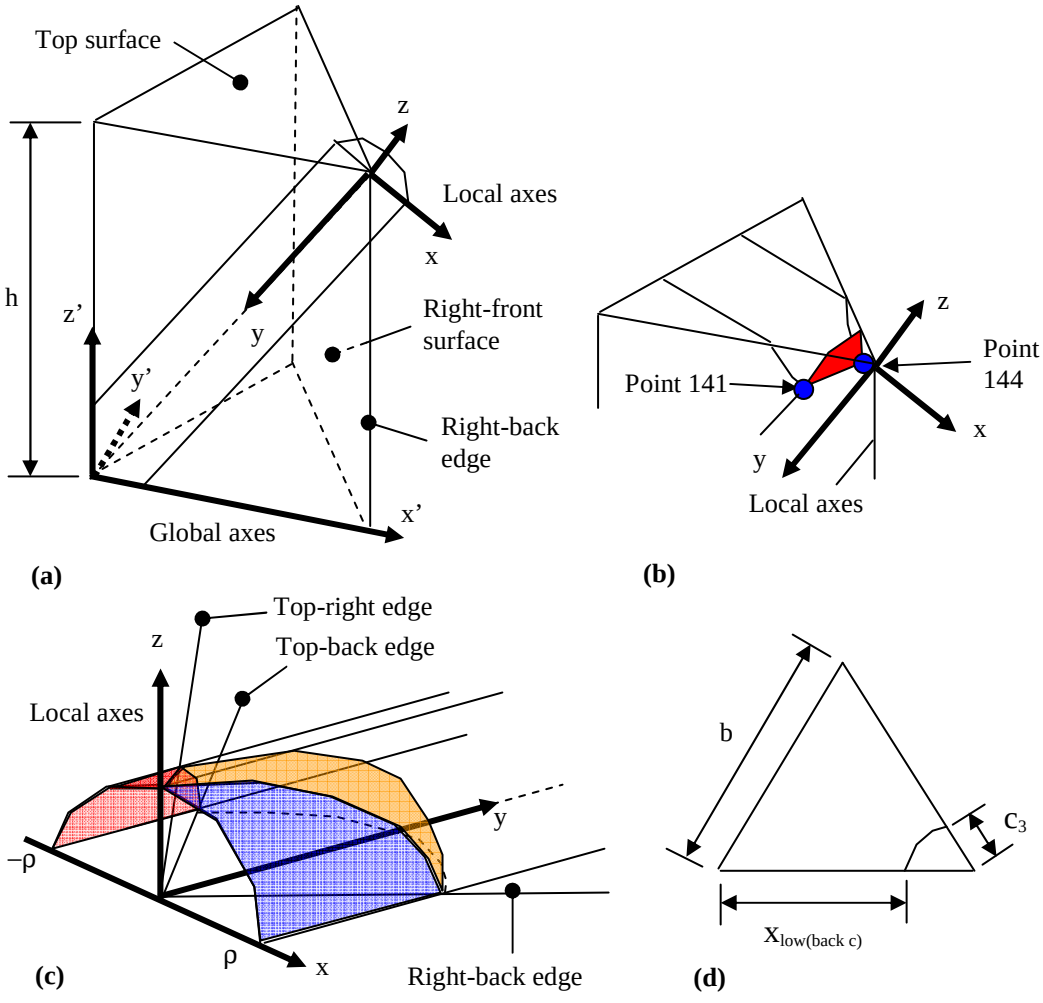

Figure H.4: Unit cell showing the back cylinder

(a) Prism unit cell showing axes and back cylinder
(b) Piece of unit cell showing the surface area removed in step (d) in red with important geometry points shown in blue
(c) Back cylinder showing surface areas removed in step (a) in red, step (b) in blue, and step (c) in orange
(d) Top view showing intersection with back cylinder and lower bound for x-direction used in step (c)

and $\frac{1}{\sqrt{2}}x$ in the y-direction.

$$A_{back(a)} = \int_{-\rho}^{0}\int_{0}^{-\frac{1}{\sqrt{2}}x}\sqrt{1+\left[\frac{x^2}{\left(\rho^2-x^2\right)}\right]+(0)}\partial y\partial x$$

b) Remove surface area that is beyond the right-back edge (see Fig. H.4):

- Equation for right-back edge: $y=\sqrt{2}x$
- The surface area goes between 0 and ρ in the x-direction, and 0 and $\sqrt{2}x$ in the y-direction.

$$A_{back(b)} = \int_{0}^{\rho}\int_{0}^{\sqrt{2}x}\sqrt{1+\left[\frac{x^2}{\left(\rho^2-x^2\right)}\right]+(0)}\partial y\partial x$$

c) Remove surface area that is beyond the right-front surface (see Fig. H.4):

- Equation for right-front surface based on global axes:

  $y'=\sqrt{3}\left(2-x'\right)$

- Equation for back cylinder based on global axes:

  $$\frac{2}{3}x'^2-\frac{2\sqrt{2}}{3}x'z'+\frac{1}{3}z'^2+y'^2=\rho^2$$

  $$z'=\sqrt{2}x'-\sqrt{-3y'^2+3\rho^2}$$

  $$\left(\frac{\partial z'}{\partial x'}\right)^2=\left[\frac{\partial}{\partial x'}\left(\sqrt{2}x'-\sqrt{-3y'^2+3\rho^2}\right)\right]^2=2$$

  $$\left(\frac{\partial z'}{\partial y'}\right)^2=\left[\frac{\partial}{\partial y'}\left(\sqrt{2}x'-\sqrt{-3y'^2+3\rho^2}\right)\right]^2=\frac{9y'^2}{\left(-3y'^2+3\rho^2\right)}$$

- Lower bound in x-direction:

$$x_{low(back\,c)} = b - c_3\cos(60)$$

- The surface area goes between $x_{low(back\ c)}$ and 0 in the x-direction, and 0 and $\sqrt{3}(2-x')$ in the y-direction.

$$A_{back(c)} = \int_{x_{low(back\,c)}}^{0}\int_{0}^{\sqrt{3}(2-x')}\sqrt{1+\left[\frac{9y'^2}{\left(-3y'^2+3\rho^2\right)}\right]+(2)}\,\partial y'\partial x'$$

d) Remove approximate surface area that enters the cylinder intersection (see Fig. H.4):

- Location of point 141 based on global axes:

$$x'_{141} = 2-\frac{2}{3}\sqrt{6}\rho \qquad z'_{141} = \sqrt{2}x'_{141}+\sqrt{3}\rho$$

- Location of point 141 based on local axes:

$$d = \sqrt{\left(b-x'_{141}\right)^2+\left(h-z'_{141}\right)^2}$$

$$x_{141} = -\rho \qquad y_{141} = \sqrt{d^2-x_{141}{}^2} \qquad z_{141} = 0$$

- Location of point 144 based on global axes:

$$x'_{144} = \frac{2\sqrt{3}-\rho}{\sqrt{3}} \qquad z'_{144} = \sqrt{2}x'_{144}$$

- Location of point 144 based on local axes:

$$d' = \frac{\left(b-x'_{144}\right)}{\cos(60)} \qquad d = \sqrt{d'^2+\left(h-z'_{144}\right)}$$

$$x_{144} = 0 \qquad y_{144} = \sqrt{d^2-z_{144}{}^2} \qquad z_{144} = \rho$$

- Upper bound in y-direction:

$$m_{(back\,d)} = \frac{\left(y_{141}-y_{144}\right)}{\left(x_{144}-x_{141}\right)} \qquad n_{(back\,d)} = y_{144}$$

$$y_{up(back\,d)} = \left(m_{(back\,d)}\right)x + n_{(back\,d)}$$

- The surface area goes between x_{141} and x_{144} in the x-direction, and $\frac{1}{\sqrt{2}}x$ (the equation of the top surface) and $y_{up(back\,d)}$ in the y-direction.

$$A_{back(d)} = \int_{x_{141}}^{x_{144}} \int_{\frac{1}{\sqrt{2}}x}^{y_{up(back\,d)}} \sqrt{1+\left[\frac{x^2}{\left(\rho^2 - x^2\right)}\right] + (0)}\,\partial y \partial x$$

Therefore the surface area of the back cylinder is:

$$A_{back} = A_{total} - \left(A_{back(a)} + A_{back(b)} + A_{back(c)} + A_{back(d)}\right) \tag{H.7}$$

Therefore the approximate surface area between the phases for the cylinder model is:

$$S_v^{\alpha\beta} = A_{top} + A_{back} \tag{H.8}$$

Note that the approximations for the surface areas that needed to be removed from the intersection region for both cylinders are both slightly low. Had more exact surfaces been calculated the areas removed this region would have been higher. This means that the surface areas between the phases for the top and back cylinders (A_{top} and A_{back}) would have been lower. The total surface area between phases would then also be lower ($S_v^{\alpha\beta}$), and this would cause the contiguities calculated to be slightly greater than they are with this approximate method.

APPENDIX I

STRESS DISTRIBUTION PLOTS FOR THE LINEAR ELASTIC MICROSTRUCTURAL ANALYSIS

In the linear elastic investigation for microstructural mechanisms in Section 4.2.2, qualitative and quantitative analyses of the stress distributions in both models were undertaken. The qualitative analysis was based on contour and vector plots of the first principal stresses at three different volume fractions, and the quantitative analysis on these stresses at each element integration point (from which the plots were derived). The volume fractions based on the stiffer phase were the 75%, 85% and 95% for the spherical model, and for the cylindrical model were the 2%, 39% and 84%. All of this information came from simulations performed using ADINA (ADINA R&D, Inc., 2000a), a computer software application of the finite element method. The contour and vector plots of the first principal stresses in each model are shown below.

I.1 FIRST PRINCIPAL STRESS DISTRIBUTION FOR THE SPHERICAL MODEL

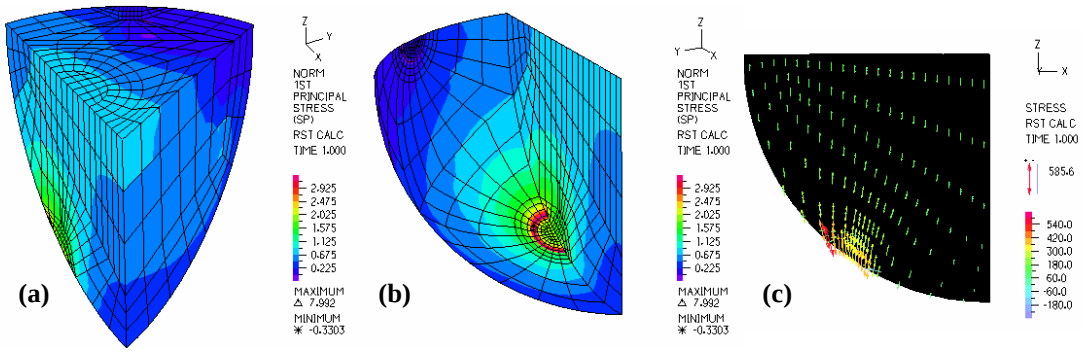

Figure I.1: Stiffer phase (ϕ = 75%)
(a) Contour plot with view from top-right-back corner
(b) Contour plot with view from bottom-left-back corner
(c) Vector plot with view from back

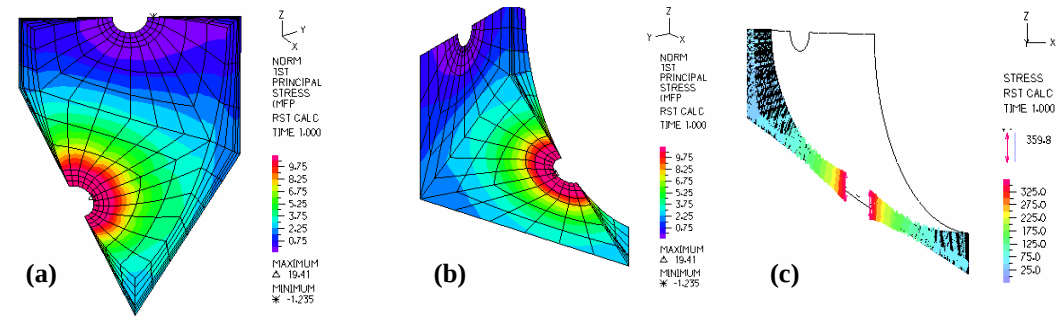

Figure I.2: More flexible phase (ϕ = 75%)
(a) Contour plot with view from top-right-back corner
(b) Contour plot with view from bottom-left-back corner
(c) Vector plot with view from back

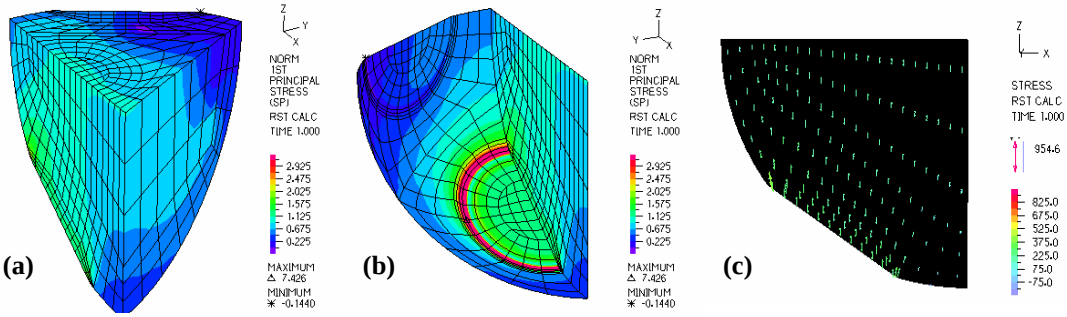

Figure I.3: Stiffer phase (ϕ = 85%)
(a) Contour plot with view from top-right-back corner
(b) Contour plot with view from bottom-left-back corner
(c) Vector plot with view from back

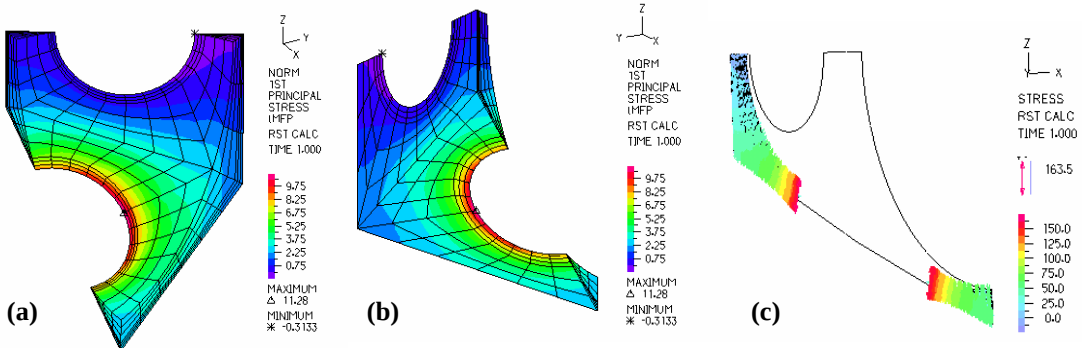

Figure I.4: More flexible phase (ϕ = 85%)
(a) Contour plot with view from top-right-back corner
(b) Contour plot with view from bottom-left-back corner
(c) Vector plot with view from back

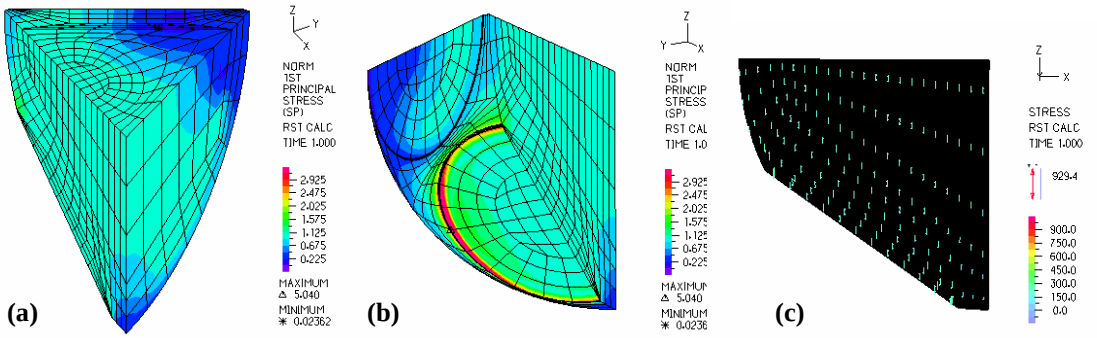

Figure I.5: Stiffer phase (ϕ = 95%)
(a) Contour plot with view from top-right-back corner
(b) Contour plot with view from bottom-left-back corner
(c) Vector plot with view from back

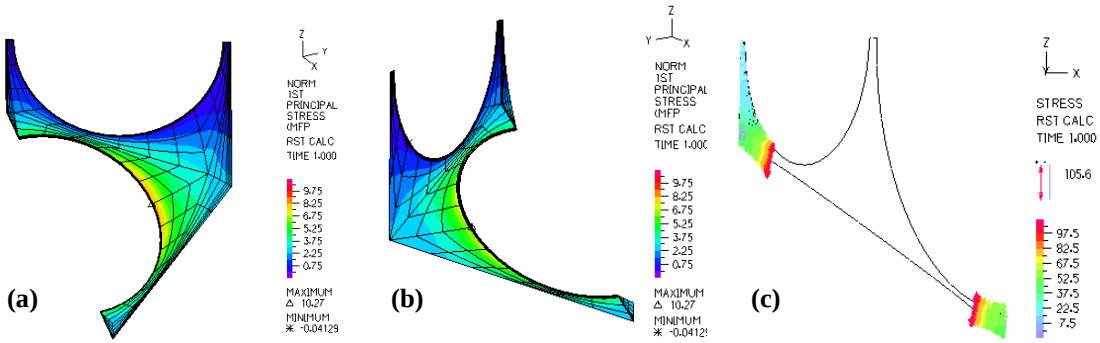

Figure I.6: More flexible phase (ϕ = 95%)
(a) Contour plot with view from top-right-back corner
(b) Contour plot with view from bottom-left-back corner
(c) Vector plot with view from back

I.2 FIRST PRINCIPAL STRESS DISTRIBUTION FOR THE CYLINDRICAL MODEL

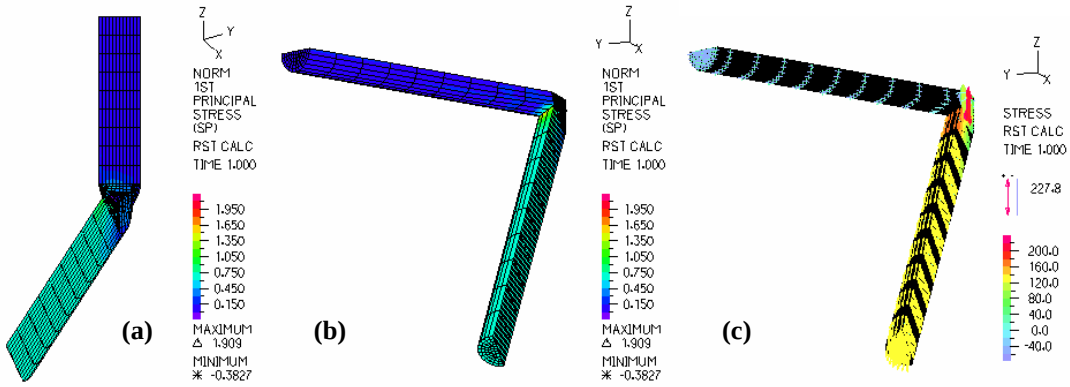

Figure I.7: Stiffer phase (ϕ = 2%)
(a) Contour plot with view from top-right-back corner
(b) Contour plot with view from bottom-left-back corner
(c) Vector plot with view from bottom-left-back corner

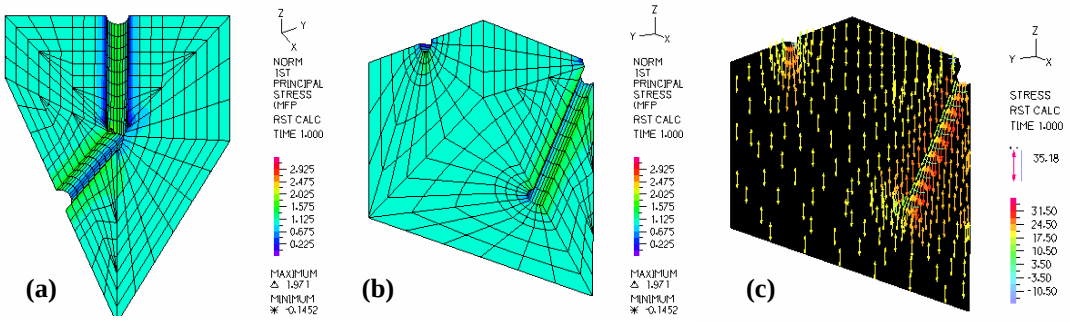

Figure I.8: More flexible phase (ϕ = 2%)
(a) Contour plot with view from top-right-back corner
(b) Contour plot with view from bottom-left-back corner
(c) Vector plot with view from bottom-left-back corner

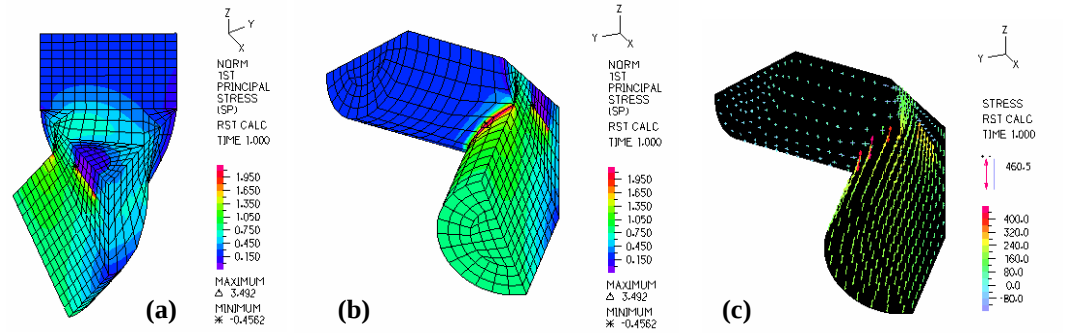

Figure I.9: Stiffer phase (ϕ = 39%)
(a) Contour plot with view from top-right-back corner
(b) Contour plot with view from bottom-left-back corner
(c) Vector plot with view from bottom-left-back corner

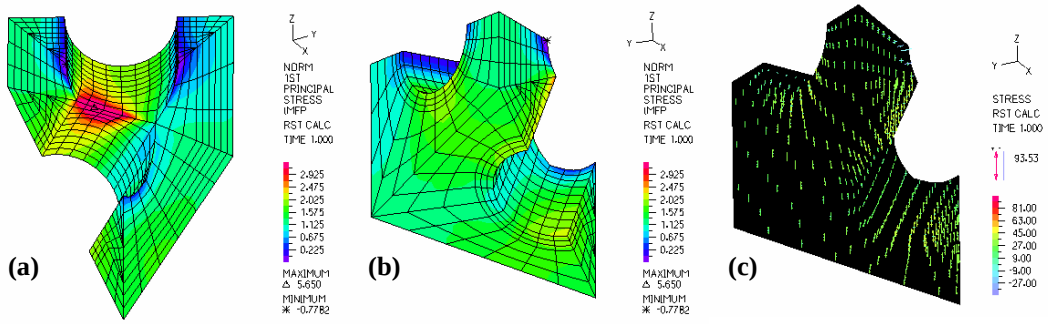

Figure I.10: More flexible phase (ϕ = 39%)

(a) Contour plot with view from top-right-back corner
(b) Contour plot with view from bottom-left-back corner
(c) Vector plot with view from bottom-left-back corner

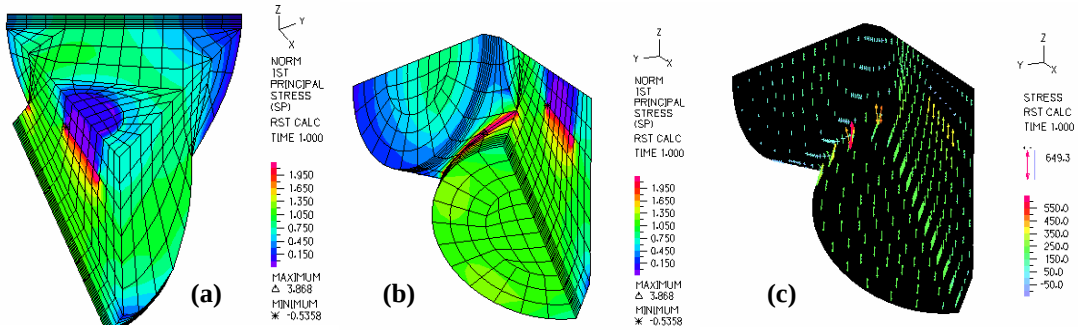

Figure I.11: Stiffer Phase (ϕ = 84%)

(a) Contour plot with view from top-right-back corner
(b) Contour plot with view from bottom-left-back corner
(c) Vector plot with view from bottom-left-back corner

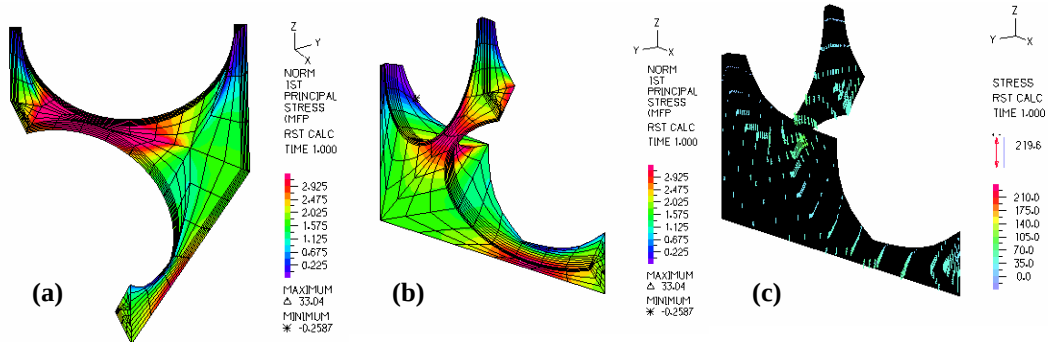

Figure I.12: More flexible phase (ϕ = 84%)

(a) Contour plot with view from top-right-back corner
(b) Contour plot with view from bottom-left-back corner
(c) Vector plot with view from bottom-left-back corner

APPENDIX J

RAW DATA FOR THE NON-LINEAR PLASTIC MACROSCOPIC BEHAVIOUR

This appendix contains the raw data taken from the finite element method program ADINA used to determine the non-linear plastic macroscopic behaviour of the interpenetrating phase composites (IPCs). The IPCs were tested in a simulated uniaxial tension test in which the strain increment was slowly increased and the resulting stress calculated. From this data the figures for the stress-strain behaviour of each IPC were determined. The yield strengths for these IPCs were then determined using the standard definition of the 0.2% strain offset or the highest stress the model reached if it failed prior to the offset. The simulated tension test strain increments and strain offsets for the stress-strain behaviour are provided here with the effective yield strengths listed in Table 4.5.

Table J.1: Simulated tension test strain increments for the spherical model with a yield strength ratio of 2

Volume Fraction of Stronger Phase [%]	75	80	85	90	95
Applied Strain for Uniaxial Tension Test [%]	0	0	0	0	0
	0.0500	0.0500	0.0500	0.0500	0.0500
	0.0750	0.0750	0.0750	0.0750	0.0750
	0.1000	0.1000	0.1000	0.1000	0.1000
	0.1150	0.1250	0.1250	0.1250	0.1250
	0.1300	0.1500	0.1500	0.1500	0.1500
	0.1350	0.1750	0.1750	0.1750	0.1750
	0.1400	0.2000	0.2000	0.2000	0.2000
	0.1450	0.2250	0.2250	0.2250	0.2250
		0.2350	0.2500	0.2500	0.2500
		0.2450	0.2750	0.2750	0.2750
			0.2870	0.3000	0.3000
			0.3000	0.3250	0.3120
				0.3370	0.3250
				0.3500	
				0.3620	

Table J.2: Simulated tension test strain increments for the spherical model with a yield strength ratio of 10

Volume Fraction of Stronger Phase [%]	75	80	85	90	95
Applied Strain for Uniaxial Tension Test [%]	0	0	0	0	0
	0.0500	0.0500	0.0500	0.0500	0.0500
	0.0750	0.0750	0.0750	0.0750	0.0750
	0.1000	0.1000	0.1000	0.1000	0.1000
	0.1250	0.1250	0.1250	0.1250	0.1250
	0.1500	0.1500	0.1500	0.1500	0.1500
	0.1650	0.1750	0.1750	0.1750	0.1750
	0.1750	0.2000	0.2000	0.2000	0.2000
	0.1850	0.2250	0.2250	0.2250	0.2250
		0.2500	0.2500	0.2500	0.2500
		0.2750	0.2750	0.2750	0.2750
		0.3000	0.3000	0.3000	0.3000
			0.3250	0.3250	0.3250
			0.3500	0.3500	0.3370
			0.3620	0.3750	0.3500
			0.3750	0.4000	
				0.4250	

Table J.3: Simulated tension test strain increments for the cylindrical model with a yield strength ratio of 2

Volume Fraction of Stronger Phase [%]	2.09	16.45	39.11	63.77	84.14
Applied Strain for Uniaxial Tension Test [%]	0	0	0	0	0
	0.0500	0.0500	0.0500	0.0500	0.0500
	0.1000	0.1000	0.1000	0.1000	0.1000
	0.2000	0.2000	0.2000	0.1250	0.1250
	0.3000	0.3000	0.3000	0.1500	0.1500
	0.4000	0.4000	0.4000	0.1750	0.1750
	0.5000	0.5000	0.5000	0.2000	0.2000
				0.2250	0.2250
				0.2500	0.2500
				0.2750	0.2750
				0.3000	0.3000
				0.3250	0.3250
				0.3500	0.3500
				0.3750	0.3750
				0.4000	0.4000
				0.4250	0.4250
				0.4500	0.4500
				0.4750	0.4750
				0.5000	0.5000

Table J.4: Simulated tension test strain increments for the cylindrical model with a yield strength ratio of 10

Volume Fraction of Stronger Phase [%]	2.09	16.45	39.11	63.77	84.14
Applied Strain for Uniaxial Tension Test [%]	0	0	0	0	0
	0.0500	0.0500	0.0500	0.0500	0.0500
	0.1000	0.1000	0.1000	0.1000	0.1000
	0.2000	0.2000	0.2000	0.2000	0.1500
	0.3000	0.3000	0.3000	0.3000	0.2000
	0.4000	0.4000	0.4000	0.4000	0.2500
	0.5000	0.5000	0.5000	0.5000	0.3000
					0.3500

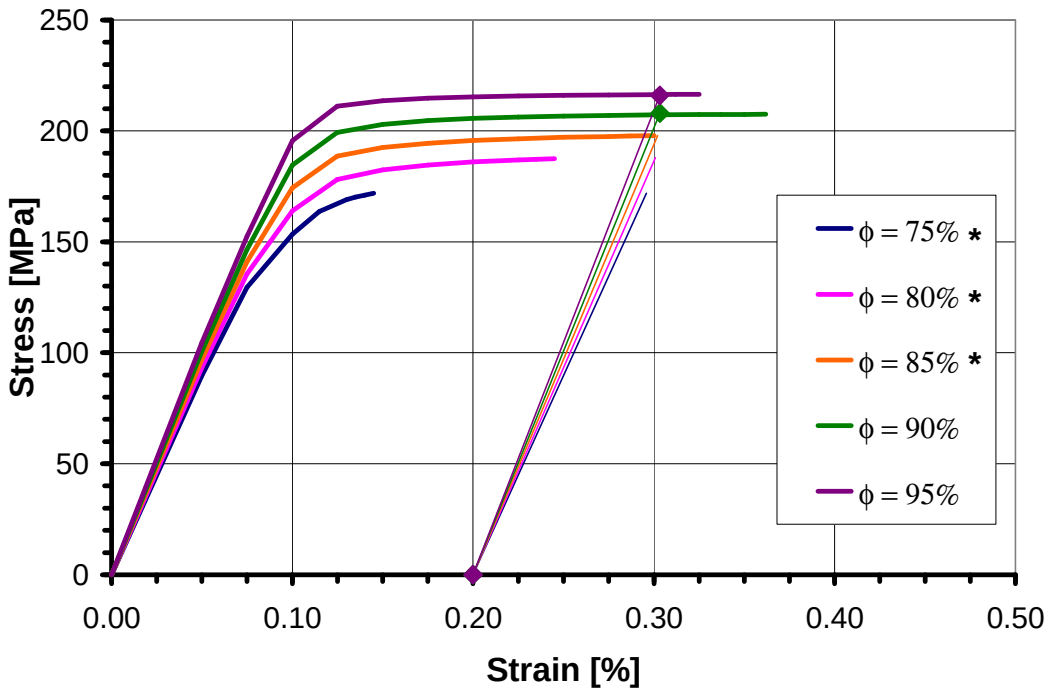

Figure J.1: Stress-strain behaviour of spherical models for a yield strength ratio of 2
Note: - Asterisks indicate failure to converge prior to reaching yield strength.
- 0.2% strain offsets shown in colour of their simulation.

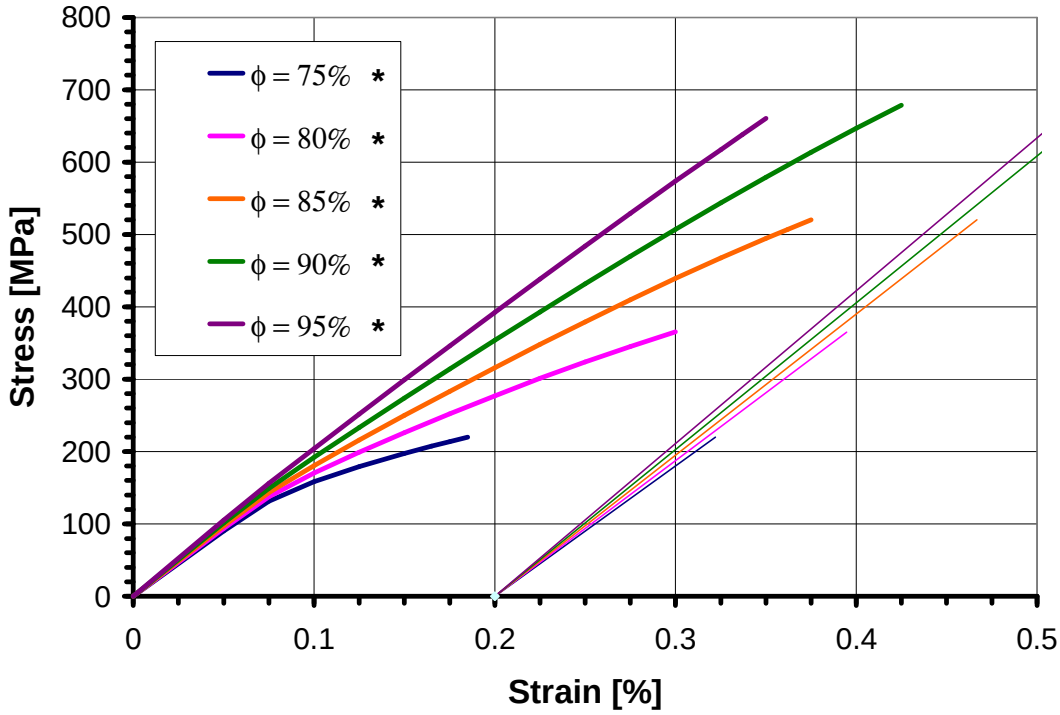

Figure J.2: Stress-strain behaviour of spherical models for a yield strength ratio of 10
Note: - Asterisks indicate failure to converge prior to reaching yield strength.
- 0.2% strain offsets shown in colour of their simulation.

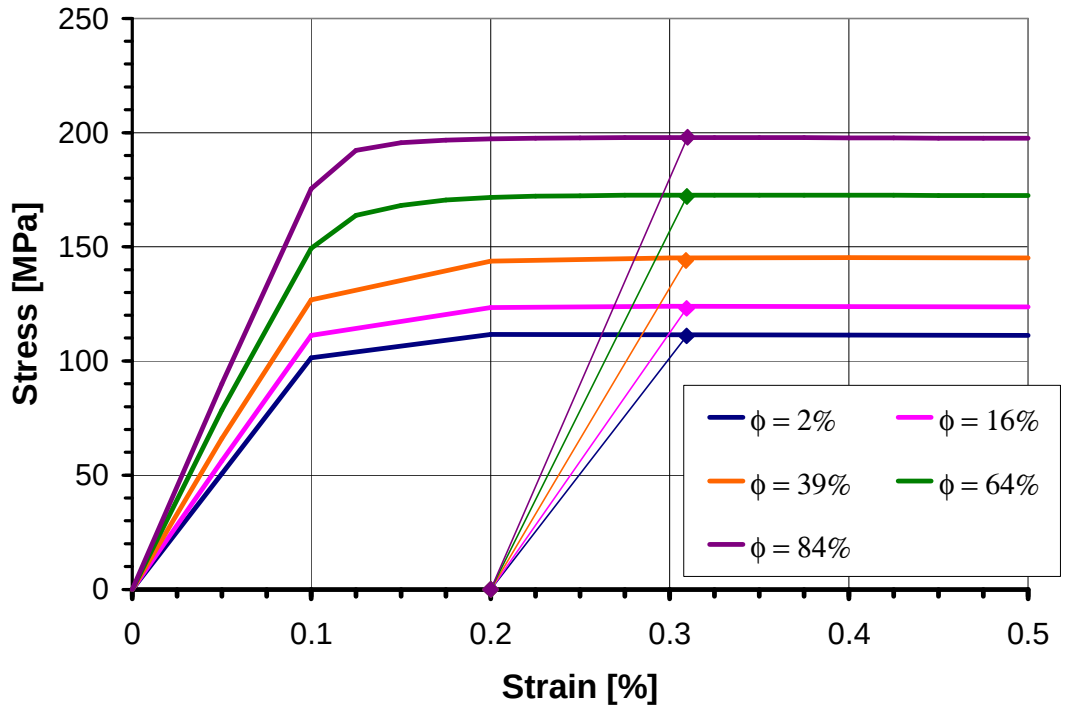

Figure J.3: Stress-strain behaviour of cylindrical models for a yield strength ratio of 2
Note: - Asterisks indicate failure to converge prior to reaching yield strength.
- 0.2% strain offsets shown in colour of their simulation.

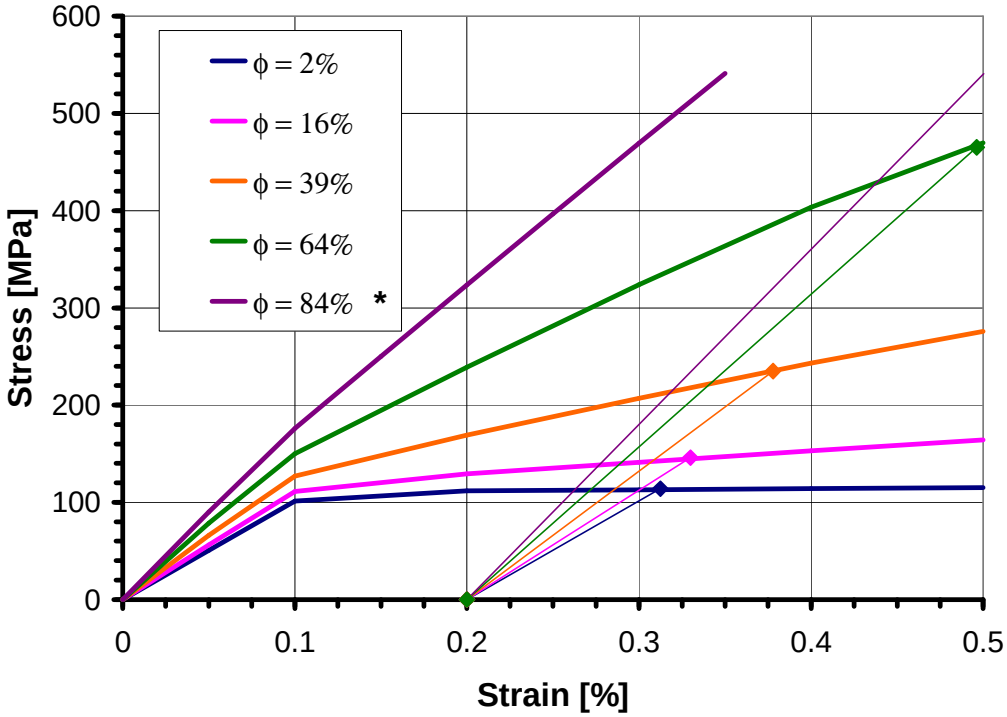

Figure J.4: Stress-strain behaviour of cylindrical models for a yield strength ratio of 10
Note: - Asterisks indicate failure to converge prior to reaching yield strength.
- 0.2% strain offsets shown in colour of their simulation.

APPENDIX K

STRESS DISTRIBUTION PLOTS FOR THE NON-LINEAR PLASTIC MICROSTRUCTURAL ANALYSIS

The study into the microstructural mechanisms affecting non-linear plastic behaviour quantified the stress distributions of the spherical and cylindrical models through a similar procedure as described for the linear elastic investigation. The effective stress distribution plots shown in this appendix are for the stronger phase volume fractions of 75%, 85% and 95% with the spherical model, and 2%, 39% and 84% with the cylindrical model. All the contour and vector plots were taken from the final strain increment which each of the models reached. To determine the final strain increment of any one model, see the tables in Appendix J.

K.1 EFFECTIVE STRESS DISTRIBUTION FOR THE SPHERICAL MODEL

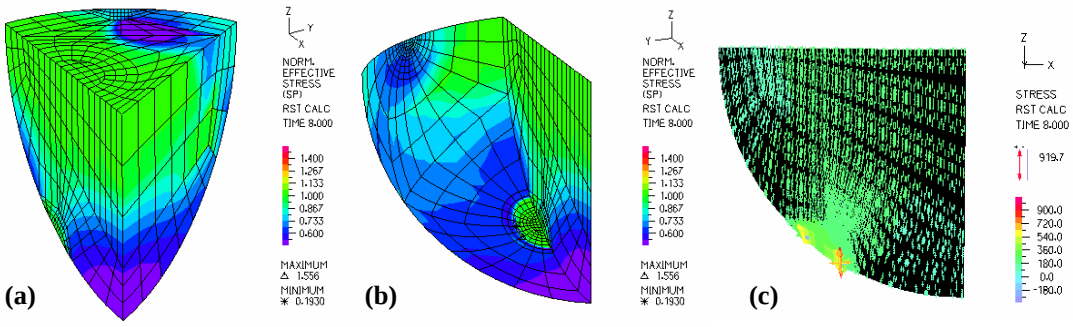

Figure K.1: Stronger phase (ϕ = 75%)
(a) Contour plot with view from top-right-back corner
(b) Contour plot with view from bottom-left-back corner
(c) Vector plot with view from back

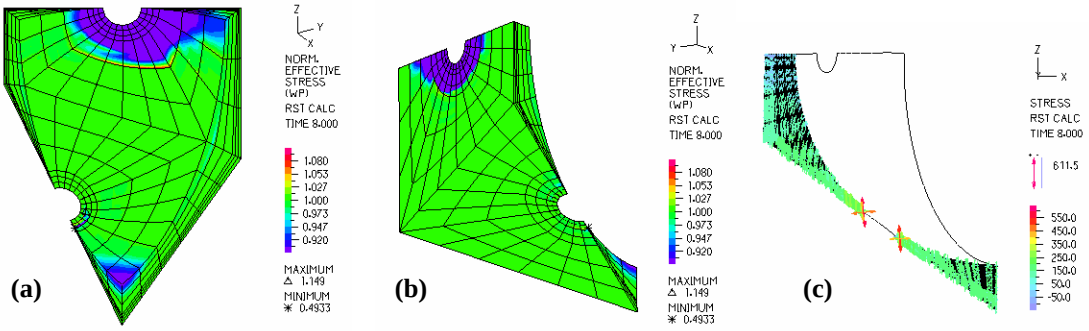

Figure K.2: Weaker phase (ϕ = 75%)
(a) Contour plot with view from top-right-back corner
(b) Contour plot with view from bottom-left-back corner
(c) Vector plot with view from back

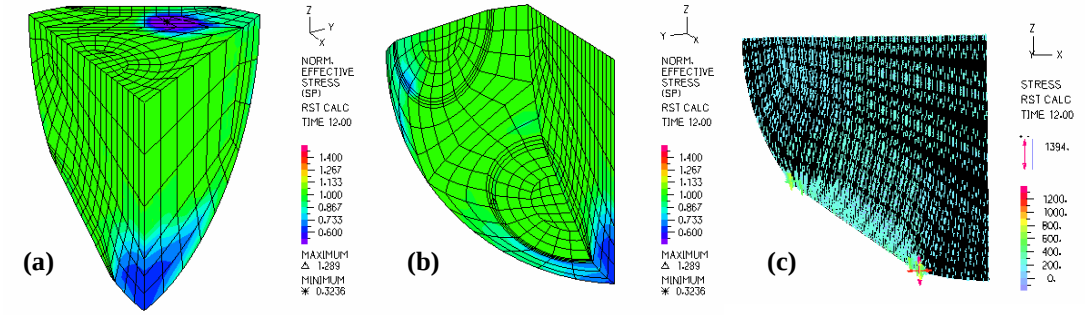

Figure K.3: Stronger phase (ϕ = 85%)
(a) Contour plot with view from top-right-back corner
(b) Contour plot with view from bottom-left-back corner
(c) Vector plot with view from back

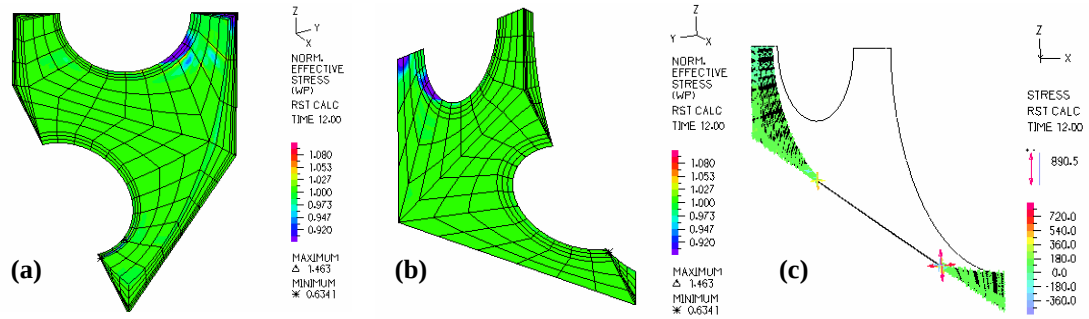

Figure K.4: Weaker phase (ϕ = 85%)
(a) Contour plot with view from top-right-back corner
(b) Contour plot with view from bottom-left-back corner
(c) Vector plot with view from back

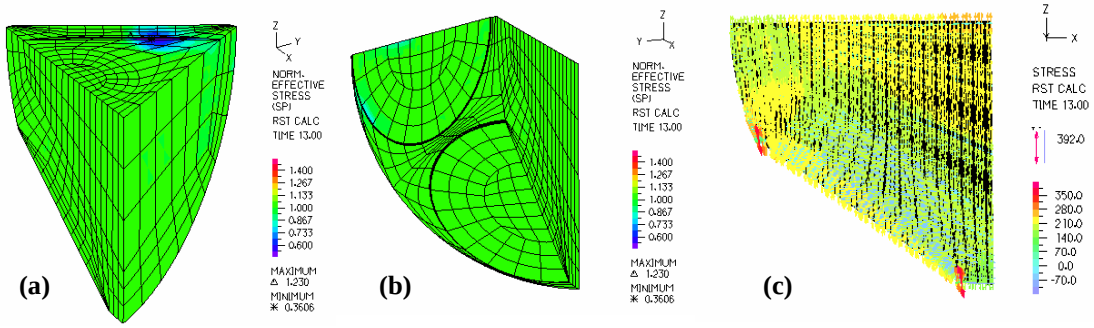

Figure K.5: Stronger phase (ϕ = 95%)
(a) Contour plot with view from top-right-back corner
(b) Contour plot with view from bottom-left-back corner
(c) Vector plot with view from back

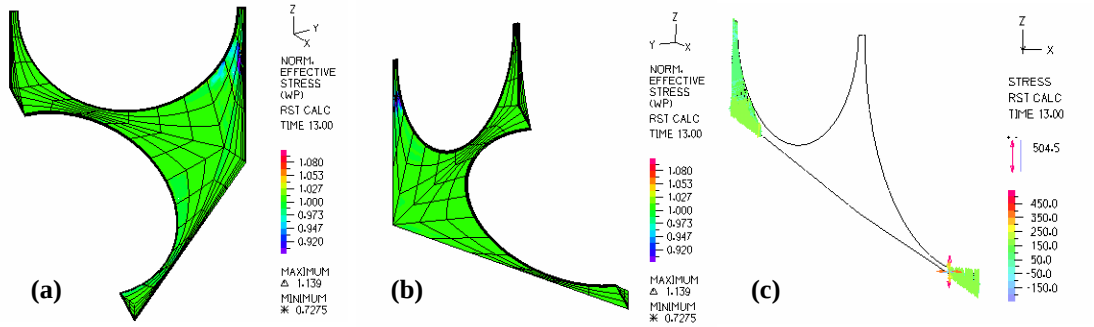

Figure K.6: Weaker phase (ϕ = 95%)
(a) Contour plot with view from top-right-back corner
(b) Contour plot with view from bottom-left-back corner
(c) Vector plot with view from back

K.2 EFFECTIVE STRESS DISTRIBUTION FOR THE CYLINDRICAL MODEL

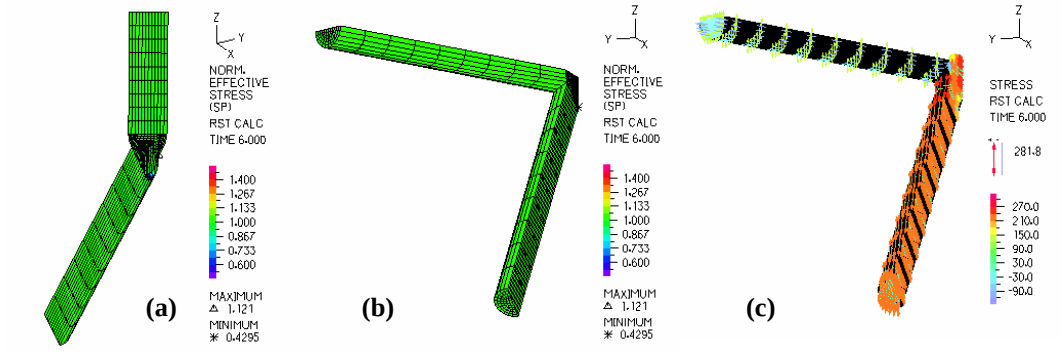

Figure K.7: Stronger phase (ϕ = 2%)
(a) Contour plot with view from top-right-back corner
(b) Contour plot with view from bottom-left-back corner
(c) Vector plot with view from bottom-left-back corner

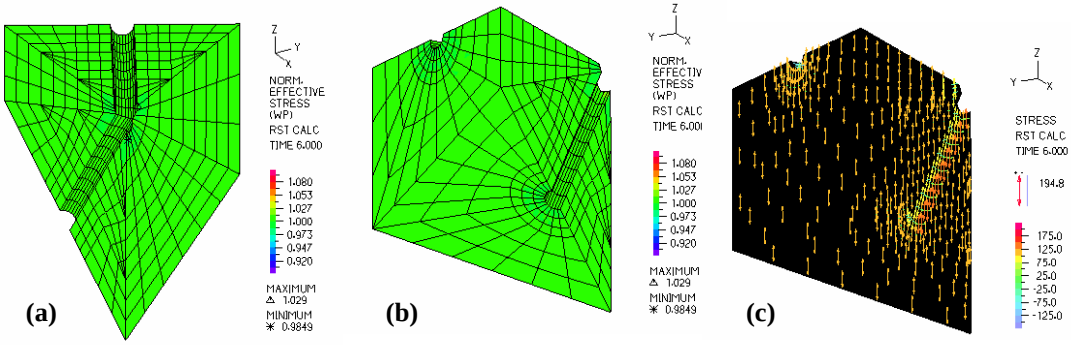

Figure K.8: Weaker phase (ϕ = 2%)
(a) Contour plot with view from top-right-back corner
(b) Contour plot with view from bottom-left-back corner
(c) Vector plot with view from bottom-left-back corner

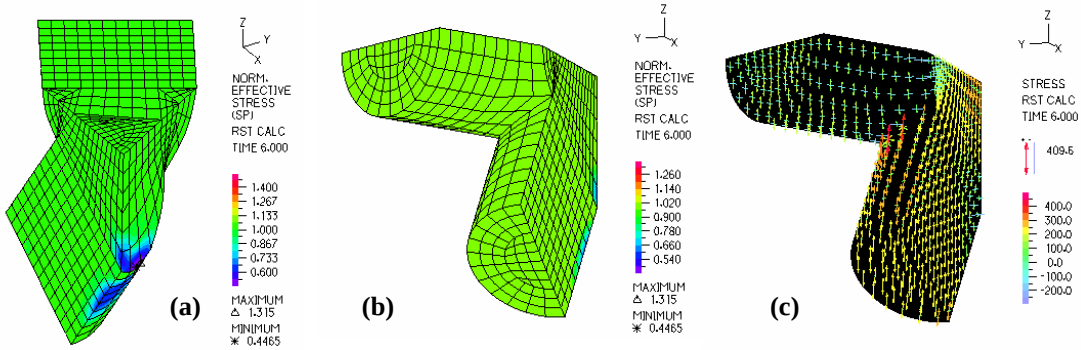

Figure K.9: Stronger phase (ϕ = 39%)
(a) Contour plot with view from top-right-back corner
(b) Contour plot with view from bottom-left-back corner
(c) Vector plot with view from bottom-left-back corner

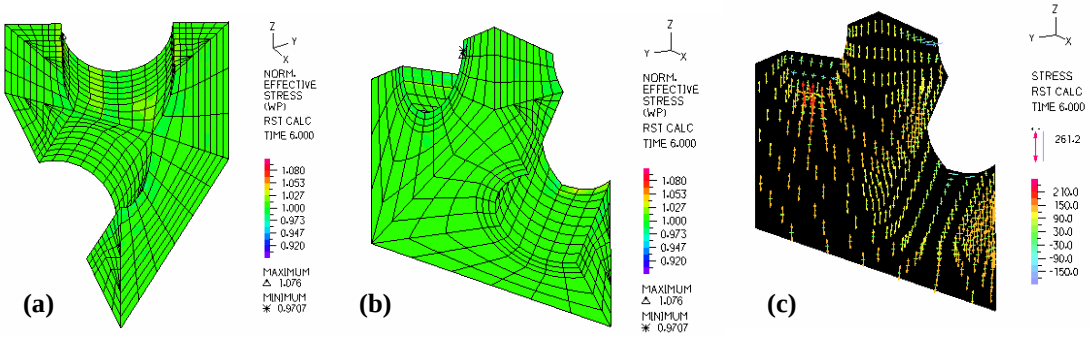

Figure K.10: Weaker phase (ϕ = 39%)
(a) Contour plot with view from top-right-back corner
(b) Contour plot with view from bottom-left-back corner
(c) Vector plot with view from bottom-left-back corner

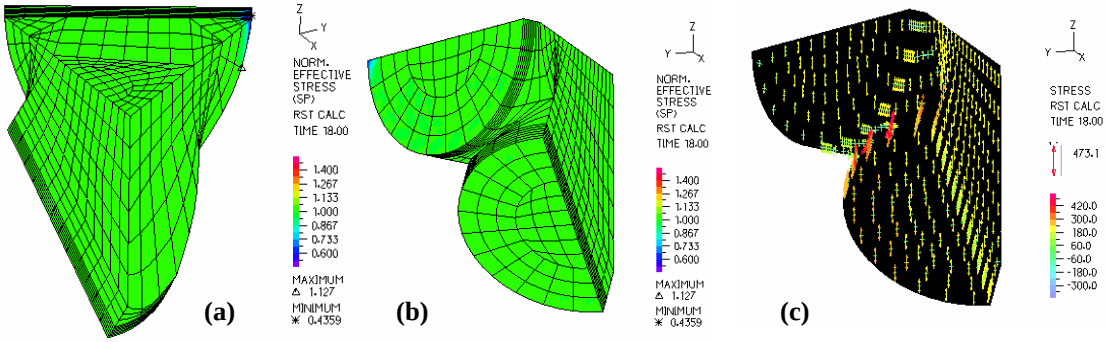

Figure K.11: Stronger phase (ϕ = 84%)
(a) Contour plot with view from top-right-back corner
(b) Contour plot with view from bottom-left-back corner
(c) Vector plot with view from bottom-left-back corner

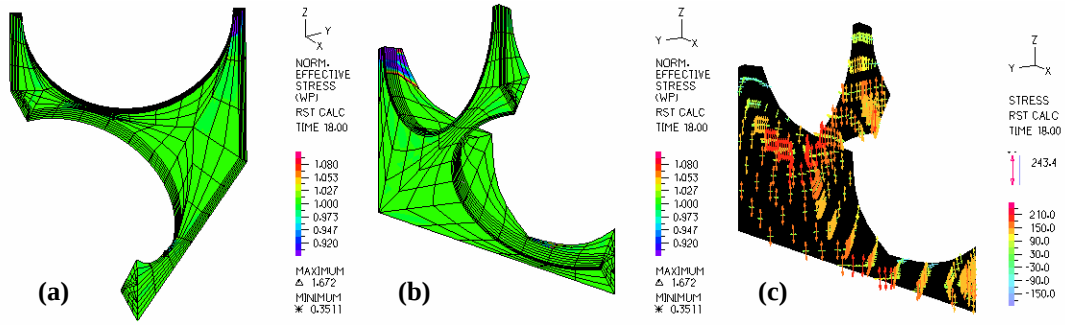

Figure K.12: Weaker phase (ϕ =84%)
(a) Contour plot with view from top-right-back corner
(b) Contour plot with view from bottom-left-back corner
(c) Vector plot with view from bottom-left-back corner